NANYANG TECHNOLOGICAL UNIVERSITY
SINGAPORE

THE GENETIC DISSECTION OF TRISOMY 21 and PARTIAL TRISOMY 21 CELLULAR PATHOLOGIES USING INDUCED PLURIPOTENT STEM CELLS

GILLIAN GOUGH

Lee Kong Chian School of Medicine

A thesis submitted to the Nanyang Technological University in partial fulfilment of the requirement for the degree of Doctor of Philosophy

2021

Statement of Originality

I hereby certify that the work embodied in this thesis is the result of original research, is free of plagiarised materials, and has not been submitted for a higher degree to any other University or Institution.

21/09/2021

Date

Gillian Gough

Supervisor Declaration Statement

I have reviewed the content and presentation style of this thesis and declare it is free of plagiarism and of sufficient grammatical clarity to be examined.

To the best of my knowledge, the research and writing are those of the candidate except as acknowledged in the Author Attribution Statement.

I confirm that the investigations were conducted in accord with the ethics policies and integrity standards of Nanyang Technological University and that the research data are presented honestly and without prejudice.

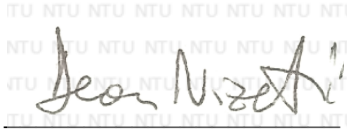

24/09/2021

Date

Prof. Dean Nizetic

26/09/2021

Date

Asst Prof. Jia Nee Foo

Authorship Attribution Statement

This thesis contains material from the following two papers published in the following peer-reviewed journals:

The data included in Chapter 5 are key components of figures 5-7 of Alic I, Goh PA, Murray A, Portelius E, Gkanatsiou E, Gough G, Mok KY, Koschut D, Brunmeir R, Yeap YJ et al. 2020. Patient-specific Alzheimer-like pathology in trisomy 21 cerebral organoids reveals BACE2 as a gene dose-sensitive AD suppressor in human brain. *Mol Psychiatry* doi:10.1038/s41380-020-0806-5.

For these I generated the *BACE2*Δ7 iPSC line and subsequent cerebral organoids, which are displayed in figure 5. This process included:

- gRNA selection, modification and cloning into the CRISPR/Cas9HF1 Plasmid.
- Plasmid validation, preparation, and transfection into iPSCs
- iPSC cell culture and clonal cell isolation
- Sequencing and analysis of insertions and deletions
- Western Blot and quantification of protein changes
- Cerebral organoid culture, fixing and media collection

Additionally, I contributed to data interpretation and analysis of supplementary figures 9-13, which include data generated by others as a result of the *BACE2*Δ7 reagent. The detailed contributions of all other co-authors are stated in the publication.

This thesis also contains material from Chapter 3 of the book “Preclinical Research in Down Syndrome: Insights for Pathophysiology and Treatments,” of which I was the first author.

Gough G, O'Brien NL, Alic I, Goh PA, Yeap YJ, Groet J, Nizetic D, Murray A. 2020. Modelling Down syndrome in cells: From stem cells to organoids. Prog Brain Res 251: 55-90.

All other chapters pressent the work not published yet at the point of the thesis submission.

21/09/2021

. . . . . .

Date

. . . . . .

Gillian Gough

Acknowledgements

Firstly, I would like to express my sincere gratitude to my advisor, Prof. Dean Nizetic, for the opportunity to pursue a PhD in his laboratory. His expertise in my PhD topic and related research have been invaluable. I am immensely grateful to him for the guidance and continued support that was provided throughout my candidature. I would also like to thank him for his input, patience, and helpful explanations throughout the many drafts of this thesis as well as other reports during my PhD candidature.

I would like to thank all members of the Nizetic lab for their constant support and guidance and for giving up hours of their personal time to assist with my experiments and questions. Dr. Aoife Murray, who kindly and very patiently answered all my questions and provided helpful advice, suggestions, and motivation throughout. I would like to thank her for sharing with me, her vast knowledge of iPSC, cerebral organoid and neuronal cultures as well as cloning and plasmid creation among many other things. Dr. Ivan Alic, for teaching me immunostaining, organoid cryopreservation and OCT embedding, and cryosectioning. I express my sincere gratitude to him for help with confocal microscopy and for being a constant source of motivation, reason and of course lab snacks! Yee Jie Yeap, for all her technical and administrative guidance and assistance during the entire project. I also appreciate our talks during cell culture and for keeping our lab a cheerful and entertaining place filled with quizzes, challenges, and lab activities. Dr. David Koschut for sharing with me his expertise in Western Blot and for guiding me in troubleshooting experiments.

I thank my thesis committee members for their precious time invested in guiding me through my candidature: Norris Ray Dunn, whose very early help with trouble shooting and the CRISPR/Cas9-HF1 plasmid was instrumental in the progression of this work. I would also like to thank him for ensuring I had a lab to work in during the COVID-19 pandemic as well as for his continued guidance and support. Thank you to my co-supervisor Jia Nee Foo, for her expertise and help with the SNP arrays and to Navin Kumar Verma and Karen Crasta for their helpful suggestions to improve my work.

I would also like to acknowledge LKC Medicine, the PhD programme director Prof. Ingham and the Graduate Programmes staff: Raymond, Edwin, and Zarifah. I thoroughly enjoyed the clinical attachment at CMC, Vellore, India, and I am grateful for the opportunity to bond with fellow PhD candidates whilst learning more about healthcare in other countries. A special thanks to my fellow PhD candidates for making the trip a great experience.

Last but not least, I wish to acknowledge the constant support, motivation and love from my mother, Denise, my father, Bill, my sister Natalie and my husband Chen Hui, who motivated me to travel halfway across the world to begin this journey in the first place. They were always one video call away when I needed a chat. Though miles apart they have given the strength and comfort that allowed me to continue pursuing my research career.

Table of Contents

Summary

Trisomy of human chromosome 21 (T21), which causes Down Syndrome (DS), is the most common autosomal trisomy in live born individuals. DS is characterised by distinct facial features, short stature, conditions of accelerated ageing, varying degrees of intellectual disability (ID) and Alzheimer's disease (AD). In fact, it is the most common genetic cause of both ID and AD. However, a paradoxical relationship between DS and AD exists: all individuals with DS and three copies of *APP* will develop AD-neuropathology by age 40 but 30% will not develop AD-like dementia. This suggests a role for other genes on chromosome 21 (HSA21) in modulating AD severity and onset.

For a clean dissection of the relationship between individual gene copy number and phenotypes related to neurodevelopment, accelerated ageing and AD, we sought to create a panel of genetically modified iPSCs with isogenic controls. CRISPR/Cas9 gene editing techniques were optimised to target pathologically relevant HSA21 genes (*APP*, *BACE2*, *DYRK1A* and *SOD1*) in iPSCs from patients with clinically diagnosed DS caused by either full or partial T21.

Chapter 3 presents the panel of isogenic iPSCs generated by various gene editing techniques such as CRISPR/Cas9 or stable integration of lentiviral fluorescent probes. The cell lines generated here have potential for a wide array of genotype to phenotype mapping studies. Chapter 4 focuses on the role of the gene dose of *DYRK1A* in neurodevelopment via 3D cerebral organoid differentiation and in accelerated ageing in undifferentiated iPSCs via the DNA damage/repair response. Chapter 5 focuses on the paradoxical relationship between AD and DS

with reference to trisomy correction of *BACE2* and provides evidence for a protective role against AD dementia. The results are discussed in Chapter 6 with conclusions and future recommendations in Chapter 7.

This work provides insight into new ways to use CRISPR/Cas9 gene editing techniques for genotype to phenotype correlation studies and potential phenotype mapping of DS phenotypes.

List of Figures

List of Tables

List of Abbreviations

Abbreviation	Definition
aCGH	Array Comparative Genome Hybridisation
AD	Alzheimer's Disease
AIF	Apoptosis Inducing Factor
ALS	Amyotrophic Lateral Sclerosis
APOE	Apolipoprotein E
APP	Amyloid Precursor Protein
ASF	Alternate Splicing Factor
Aβ	Amyloid beta
BACE (1/2)	Beta-site amyloid precursor protein-cleaving enzyme (1/2)
Bp	Base Pair
Cas9	CRISPR Associated Protein 9
CM	Conditioned Medium
CNS	Central Nervous System
CO	Cerebral Organoid
cpYFP	Circularly Permuted Yellow Fluorescent Protein
CRISPR	Clustered Regularly Interspaced Short Palindromic Repeats
CRO	Critical Region Only
CSF	Cerebrospinal Fluid
D21	Disomy 21
DMSO	Dimethyl sulfoxide
DIV	Days In Vitro
DS	Down Syndrome
DSBs	Double-Strand Breaks
DSCR	Down Syndrome Critical Region
dup*APP*	Duplication of the gene encoding the Amyloid Precursor Protein
DYRK1A	Dual Specificity Tyrosine Phosphorylation Regulated Kinase 1A
EB	Embryoid Body
EDTA	Ethylenediaminetetraacetic acid
EOAD	Early onset Alzheimer's Disease
FACS	Fluorescence Activated Cell sorting
FEOAD	Familial Early Onset Alzheimer's Disease
FISH	Fluorescence *in Situ* Hybridisation
GWAS	Genome-wide association studies
gRNA	Guide-RNA
hESC	Human Embryonic Stem Cells
H2AX	Histone H2A family member X
HR-DSCR	Highly Restricted- Down Syndrome Critical Region
HSA(number)	Homo Sapiens (Chromosome number)
HyPer-mito/cyto	Mitochondria/cytoplasm localized Hydrogen Peroxide sensor
ID	Intellectual Disability
InDels	Insertions or Deletions
iPSCs	Induced Pluripotent Stem Cells
IQ	Intelligence quotients
KO	Knock-out
LOAD	Late onset Alzheimer's Disease
MRD7	Mental Retardation Autosomal Dominant 7

Abbreviation	Definition
MRI	Magnetic Resonance Imaging
NHEJ	Non-Homologous End joining
NPCs	Neural Progenitor Cells
NSCs	Neural Stem Cells
PAM	Protospacer Adjacent Motif
PBMCs	Peripheral Blood Mononucleocytes
Pen/Strep	Penicillin/Streptomycin
PFA	Paraformaldehyde
PSEN1/2	Presenilin 1/2
PSM	Paralogous Sequence Mismatch
PSQ	Paralogous Sequence Quantification
pT21	Partial Trisomy 21
ROCK	Rho-associated protein kinase
ROS	Reactive Oxygen Species
RT	Room Temperature
RT-PCR	Reverse Transcription-Polymerase Chain Reaction
SDV	Slightly Deleterious Variants
SEM	Standard Error Mean
SNP	Single Nucleotide Polymorphism
SOD1	Superoxide Dismutase 1
SSC	Saline Sodium Citrate
T21	Trisomy 21
TAE	Tris-Acetate EDTA
TBS-T	Tris Buffered Saline with 0.1% Tween-20
TIDE	Tracking of InDels by Sequence Trace Decomposition
VTN	Vitronectin
WT	Wild-Type

Chapter 1

General Introduction

General Introduction

1.1. Trisomy 21

Approximately 45% of all human conceptions are estimated to fail before any signs of pregnancy appear and of those that become clinical pregnancies, a further 10-20% fail between weeks six-twelve of gestation (1, 2).

During the first trimester, 96% of miscarriages are due to sporadic chromosomal abnormalities (e.g., aneuploidy and polyploidy), which result from either meiotic, mitotic or fertilisation errors (1, 2). More specifically, autosomal aneuploidies are most frequently caused by maternal meiotic errors and the most common of these are trisomies (1).

Numerous studies using various techniques (such as: Fluorescent *in Situ* Hybridisation (FISH), Next Generation Sequencing, karyotype analysis by GTG banding, Quantitative Fluorescence PCR and Single Nucleotide Polymorphism (SNP) analysis, among others) have been conducted with the aim of identifying the cause of spontaneous abortion using cells and tissues collected from miscarried embryos (2-6).

The general consensus of these studies is that aneuploidies of chromosomes X, Y, 13, 15, 16, 18, 21 and 22 are the most frequent cause of first trimester miscarriages (2, 4). Regarding trisomies, triplication of chromosomes 16, 22 and 15 were the respective first, second and third most frequent causes of miscarriages during the first trimester. During the second trimester however, trisomy of chromosomes 18, 21 and 13 were the most frequent causes of

miscarriage (2, 4). Trisomy of human chromosome 21 (HSA21) most commonly reaches full term gestation and therefore is the most common autosomal trisomy in live born individuals (7).

Trisomy of HSA21 can be divided into four categories, depending on the size of the triplicated region. These are: whole-chromosome trisomies (T21), partial trisomies (pT21), micro-duplications, and single-gene duplications (8). T21 and pT21 are usually detectable by routine high-quality cytogenetic analysis whereas microduplications and single-gene duplications are not.

In most cases, the presence of extra genetic material from HSA21 causes Down Syndrome (DS; OMIM #190685) (9-11). Rare cases, however, of apparently healthy individuals without the phenotypic features of DS have been described with pT21 or micro-duplications (12, 13). Since DS is a polygenic gene-dose disorder it is unlikely that single-gene duplications will cause all phenotypic aspects of DS. However, HSA21 does harbour genes linked to monogenic disorders such as: Familial Early Onset Alzheimer's Disease (*APP* point mutation or gene duplication), DYRK1A-related intellectual disability syndrome (*DYRK1A* gene haploinsufficiency) and amyotrophic lateral sclerosis (*SOD1* gene mutation), among others (14-16).

Approximately 95% of DS cases are caused by nondisjunction during gametogenesis (17). This can either be due to maternal (95%) or paternal (5%) meiotic errors (18). In the oocyte, nondisjunction most frequently occurs during meiosis I (77.1% of cases). This is not surprising given the oocyte's extended period of arrest in prophase I between birth and ovulation. It has been shown that

the frequency of maternal meiotic errors increases with age, but the exact cause of nondisjunction remains unknown (19, 20).

The remaining 5% of DS cases can either be due to pT21 (triplication of a portion of HSA21 that is larger than 5 Mb), or microduplications (triplication of a portion of HSA21 that is shorter than 3-5 Mb). These events result from unequal crossovers during meiosis or segregation of balanced chromosomal rearrangements in the parents' gametes (8).

Of all DS cases, approximately 2% are mosaic. It has been predicted that 80% of mosaicism results from the loss of one copy of HSA21 in a trisomic zygote and the remaining 20% is likely due to mitotic nondisjunction in early foetal development (21).

Mosaic individuals are described as having either high- or low-grade mosaicism (22). The first, is characterised by an individual having 10-20% euploid cells and therefore obvious phenotypic features of DS, while the latter has been described in individuals with seemingly normal intelligence, subtle DS phenotypes or young-onset dementia (23, 24). As such, the frequency of low-grade mosaicism in the general population is yet to be determined.

1.2. Phenotypic features of Down Syndrome

DS has a wide range of phenotypic features that vary in both occurrence and severity among individuals (25). Features present in most individuals include: accelerated ageing, intellectual disability (ID), muscle hypotonia at birth, craniofacial dysmorphology, and the neuropathological changes commonly seen

in patients with Alzheimer's disease (AD; (8). Phenotypes such as heart defects, gastrointestinal tract defects, auto-immune conditions (including type I diabetes), susceptibility to infections and childhood leukaemia are only present in a subset of individuals with DS (8, 26).

Since the most common phenotypes include: ID, accelerated ageing and neurodegeneration, much of current research is focused on understanding the underlying biological mechanisms causing these in DS with the hope of developing targeted prenatal treatments to "normalise" brain development and postnatal treatments to improve cognition and delay the onset of AD. Some interventions include both DS-specific therapies but can also be expanded to include conditions involving HSA21 genes in non-DS individuals as well as conditions of accelerated ageing in the general population.

1.3. Accelerated Ageing in Down Syndrome

Individuals with DS display the phenotypic features of ageing much earlier than the general population (27). In a clinical setting, accelerated ageing has been observed as: general physical features (e.g. visual and hearing impairment, premature skin wrinkling and greying of hair), central nervous system (CNS) changes (e.g. Amyloid-β (Aβ) plaques, hyperphosphorylated tau, chronic oxidative stress and Alzheimer-like dementia), immune system changes (e.g. increased risk of autoimmune conditions and declining immune function) and endocrine system changes (e.g. thyroid disorders and early menopause) (28, 29).

1.4. Neuropathology in Down Syndrome

While the exact cause is only partially understood, T21 leads to abnormalities of the CNS that arise from a combination of abnormal neurodevelopment and the direct effect of HSA21 overexpression in neural tissues (30-34). Hence, cognitive impairment in DS is a complex phenomenon caused by both neurodevelopmental and neurodegenerative processes.

In fact, DS is the most common genetic cause of both ID and AD (35). ID in DS is accompanied by speech, learning and memory deficits and impairments in adaptive behaviour. Intelligence quotients (IQs) vary from mild to severe but the mean IQ in DS is 50 as opposed to 100 in the general population (36). AD in DS is evident by the presence of extracellular Aβ plaques and intracellular neurofibrillary tangles. These neuropathological hallmarks have been observed in virtually all adults with DS over the age of 40 and intracellular Aβ accumulation has even been reported in individuals with DS as young as 15 years old (37, 38). It has also been proposed that due to the fact that mosaicism for T21 often presents with absent or minimal manifestations of DS, it may be underdiagnosed as a cause of early-onset AD in the general population (22, 39).

1.4.1 Neurodevelopmental Aspects

Little is known about the phenotypic features of early brain development because research in this area is restricted to limited numbers of post-mortem brain samples. Clinical observations coupled with magnetic resonance imaging (MRI) studies have shown that both children and non-demented adults with DS have reduced brain volumes (40). This difference is first evident at 4-5 months of

gestation and becomes progressively more apparent at birth, where DS brains weigh approximately 12% less than euploid controls and have approximately 20-50% fewer neurons with lower neuronal density and distribution (40, 41). The difference in brain size between DS and euploid controls persists into adolescence (ages 10-20) with a 17% lower brain volume in DS (42).

After considering the overall reduced brain size in DS, MRI studies show a smaller volume of the hippocampus, with a reduction in granule cell density in the dentate gyrus, as well as smaller volumes of the cerebellum and white matter in the inferior brainstem (43, 44). In contrast, a larger volume of the parahippocampal gyrus and subcortical grey matter has been observed as well as significantly more cerebrospinal fluid, suggesting enlarged lateral ventricles (44, 45).

Hypocellularity and hypoplasia seen in early development are thought to arise from impaired proliferation of neural precursors and a number of studies in both human and DS mouse models have identified defects in neurogenesis, such as: reduced numbers of neurons in cultured DS neutrospheres (46) and DS foetal brains (47), a significant reduction in the number of dividing cells in the dentate gyrus and ventricular germinal matrix in DS foetuses at 17-20 weeks of gestation (48, 49), and increased cell death in the hippocampus (34). This defect in neural proliferation is thought to arise from alterations of the cell cycle of neuronal progenitors (49).

At a sub-microscopic level, abnormal brain development is thought to arise from both genetic and epigenetic differences in DS (33, 50, 51). The overexpression

and dysregulation of HSA21 genes not only directly alters neurodevelopment but also changes the way in which cells respond to and compensate for altered gene dosage.

HSA21 harbours numerous genes with known roles in common pathways altered in the brains of individuals with DS. An example of this is *DYRK1A*, which is known for its role in the transition from neural progenitor cells (NPCs) to neurons (52) and regulating dendrite development and dynamin dependent vesicle trafficking (53). . Interestingly, *DYRK1A* overdose has been implicated in the reduction of mature neurons in DS due to its ability to induce premature differentiation of neuronal progenitors (54).

Though histological studies on human neural tissues are limited, a body of work suggests that synaptic dysgenesis plays a major role in the manifestation of ID in DS children. Early histological studies on pyramidal neurons in the visual cortex of post-mortem DS brains described the DS visual cortex as having structurally irregular dendrites with poor dendritic spine density and branching (55). Another study by Becker and colleagues on the development of DS brains from infantile to juvenile (aged 4 months – 7 years old) showed increased dendritic length and intersections in infants below 6 months of age but these values dropped to significantly below normal by age 2 (56). Statistically, there was a 50% decrease in the total dendritic length per cell in layer 3 of the visual cortex. In contrast, dendritic arborisation in euploid controls increased by 65% from infantile to juvenile stages (56).

Other genes include: the oligodendrocyte transcription factors 1 and 2 (*OLIG1* and *2*), which are involved in regulation of development of oligodendrocytes, inhibitory neurons and the neural tube (30); *RCAN1,* whose overexpression is thought to regulate various cellular functions including synaptic activity, mitochondrial function and oxidative stress; and *SOD1,* which encodes the scavenger enzyme Cu, Zn-superoxide dismutase that converts superoxide radicals to hydrogen peroxide and oxygen (57).

The hydrogen peroxide generated by this process is further broken down by Glutathione peroxidase (GPX), an enzyme located on HSA3 (58). In DS however, the additional copy of *SOD1* may be responsible for increased oxidative damage due to hydrogen peroxide production in the absence of increased GPX (37, 57, 59). Interestingly, *RCAN1* is upregulated in response to increased levels of hydrogen peroxide, which in turn upregulates *SOD1* resulting in even more hydrogen peroxide production (60). This cycle may account for increased oxidative damage due to increased hydrogen peroxide production (61). The hypocellular phenotype observed in the brains of individuals with DS could be related to increased apoptosis during early development caused by increased levels of reactive oxygen species (ROS) (34, 62, 63).

It has been reported that neurons of patients with DS have a three- to four-fold increase in intracellular ROS and elevated levels of lipid peroxidation products (63). *In vitro* studies demonstrated that increased ROS plays a major role in neurodegeneration by causing apoptosis of cultured DS primary foetal neurons and astrocytes compared with euploid controls (63).

1.4.2. Neurodegenerative Aspects

The ageing DS brain exhibits a similar pattern of neurodegeneration to what is seen in the early stages of AD in the general population, however this occurs much earlier in DS (64). The identification of AD pathology in the brains of individuals with DS provided the first set of evidence for the involvement of *APP* in familial early onset AD (FEOAD) (65). This led to the isolation and sequencing of the Aβ-peptide (66-69) as well as mapping of APP to HSA21 (70-72). All individuals with DS and three copies of *APP* will develop Alzheimer's-like neuropathology by age 40. Interestingly, in the few reported cases of individuals with low-grade T21 mosaicism, most developed young onset dementia and AD despite presenting with either mild dysmorphology, mild ID or no apparent clinical manifestations of DS (24, 73-75). In addition, T21 was shown to sometimes arise in neurons and peripheral cells of euploid individuals and mouse models of both sporadic and familial AD (39). Likewise, duplication of *APP* (dup-*APP)* is a known cause of FEOAD in non-DS individuals with three copies of *APP*. All individuals with dup-*APP* will develop AD by age 60 with the median age of onset of clinical dementia being 41-51 years old (76, 77).

While *APP* gene duplication is essential for the development of AD neuropathology in DS (78, 79), the relationship between *APP* duplication and the development of AD in DS is paradoxical. Approximately 30% of DS individuals do not develop AD-like dementia by age 65, which suggests a role for other HSA21 genes in modulating its severity and onset in DS (76).

One such HSA21 gene is *BACE2*, which is a homolog of the β-site APP cleaving enzyme (BACE1) (80). Cleavage of APP by BACE1 and subsequently γ-secretase generates the Aβ-peptide. BACE2 is also able to cleave APP at this site but at a much lower affinity as it preferentially cleaves APP within the Aβ fragment at Aβ-19 (81-85). This led to the identification of BACE2 a potential anti-amyloidogenic θ-secretase (86).

Following this, BACE2 was identified as an avid Aβ-degrading protease (AβDP) as it was able to hydrolyse a synthetic Aβ peptide at an acidic pH (pH 3.5) in an *in vitro* situation (87). However, these studies were all carried out in cell lines artificially overexpressing APP and/or BACE2, or in enzymatic *in vitro* assays. This posed the unanswered question of whether any of these mechanisms are active *in vivo* in the human brain under physiological gene dose fluctuations.

1.5. Phenotypic variation in Down Syndrome

Variation among individuals with full T21 can be attributed to epigenetic factors, differences in the expression profile of genes on HSA21, transcriptome-wide variations, and the effects of T21 on the gene expression profile of the rest of the genome (33, 88-91).

While DS is the most common viable aneuploidy, it is important to note that only a fraction of T21 foetuses survive to term and approximately 31%-75% of these will spontaneously abort (92-94). This suggests a role for embryonic selection toward foetuses with genetic and epigenetic modifications favouring full term gestation (90). Popadin and colleagues confirmed this embryonic selection by showing that live born individuals with DS have increased variants on HSA21

and genome-wide that act towards slightly lowering the expression of HSA21 genes.

In addition, a reduction in the number of slightly deleterious variants (SDVs) on HSA21 as well as a decreased transcriptome-wide variation in the expression level of highly constrained genes was observed (90). These results led Antonorakis' group to propose the "Genetic Handicap Hypothesis," which in this context suggests that an individual with T21 will only be viable at birth if it's genome-wide burden of SDVs is sufficiently low. As such, discrepancies in an *in vitro* situation can be explained by the source of cells, which are either derived from living individuals or aborted foetuses that may have otherwise not reached full term gestation.

Variable numbers of trisomic cells in different tissues caused by mosaicism could also partially explain a highly variable clinical presentation of DS-like features among individuals. It has been proposed that elevated levels of Aβ disrupt the mitotic spindle leading to abnormal chromosome segregation and accumulation of aneuploid cell populations in various tissues (95). Hence, some individuals with T21 may have genetic variability caused by accumulation of mosaicism in some tissues.

While the phenotypic features of high-grade mosaicism are akin to full T21, those of low-grade mosaicism are often subtle and not commonly diagnosed until later in life. Hence only few such cases have been described in the literature (24, 73-75, 96, 97).

Another explanation for the high phenotypic variation in DS is a difference in the size and/or the gene composition of the triplicated region. Though rare in number, phenotypic variation is most apparent among different cases of microduplication and pT21. Clinical assessments on these individuals have been instrumental in identifying the genomic regions associated with specific DS phenotypes and hence the development of "phenotype maps" for genotype to phenotype correlations (98).

1.6. Genotype to Phenotype Correlations

Chromosome 21 is the smallest human autosome, making up 1-1.5% of the human genome (99). While the long arm (21q) contains approximately 231 genes (225 of which are protein-coding) and 184 pseudogenes, the short arm (21p) is considered genetically empty (100). This is proven by the fact that its absence is not associated with clinical phenotypes and the phenotypic features of T21 caused by centric fusion, which results in a loss of 21p, are indistinguishable to those caused by freely segregating T21 (101-103).

Early DS research, which was restricted to low resolution chromosome mapping, centred around the hypothesis that a single segment of dosage sensitive HSA21 genes are both necessary and sufficient to produce the whole phenotype of DS (104). This region, defined as the DS critical region (DSCR), is approximately 3.8-6.5 Mb and contains about 25-50 genes (Figure 1) (105-107). The notion that most DS phenotypes could be attributed to a single region was, however questioned following a series of publications (98, 108, 109).

First, by creating mice that were either trisomic (Ts1Rhr) or monosomic (Ms1Rhr) for the mouse ortholog of the DSCR, Olson and colleagues showed that triplication of this region was neither required nor sufficient to produce the phenotype of craniofacial dysmorphology that has been observed in mice carrying full T21 (Ts65Dn or Ts1Cje) (108). Using the same mouse model, they later showed that triplication of this region alone was not sufficient but was required to produce a phenotype of impaired hippocampal function as measured by electrophysiology and the Morris water maze test (109).

Further evidence that a single DSCR could not be responsible for all phenotypic features of DS came from studies on human cases of pT21 and microduplications (98, 102, 106, 110-114).

By correlating genotype to phenotype in 30 cases of pT21 using high resolution array comparative genome hybridization (aCGH), Lyle and colleagues mapped the major phenotypes of DS to specific regions of HSA21 (98). Though most phenotypes analysed in this study mapped slightly distal to the original DSCR between 37-44 Mb, which is also the most gene-rich region of HSA21 (99), features such as microcephaly, abnormal dermatoglyphics, short stature and furrowed tongue, require trisomy of genes in other regions.

Evidence that multiple regions of HSA21 can induce DS phenotypes was provided by eight pT21 cases involving the proximal segment of HSA21 that did not involve any of the DSCR genes (98, 115). For example: ID, which is a feature present in all individuals with DS (to greater or lesser extents), was mapped to two minimal regions (Figure 1). The first region is located at the proximal end of

HSA21, from the centromere to 26.96 Mb and does not overlap with the previously defined DSCR. The second region in which they also mapped hypotonia, is approximately 1 Mb in length and lies within the original DSCR from 37.94-38.64 Mb (98). In addition to this 1 Mb region, Lyle and colleagues mapped hypotonia to the q-terminal fragment from 46.5 onwards.

Neither ID minimal region described by Lyle and colleagues contains the dosage sensitive gene *DYRK1A*, which has been reported to contribute to ID in DS. In humans, there are currently two reported cases describing three individuals with microduplications involving part of the previously defined DSCR (Figure 1A & B). The first case, describes a familial 4.3 Mb duplication of 21q22.13-q22.2 in a mother and her 8 year-old daughter (106). The second is a smaller 2.56 Mb mosaic duplication at 21q22.13-q22.2 (111). Both reports describe patients presenting with ID and facial features of DS without major organ malformations. The duplicated region in these cases encompasses *DYRK1A*, but not *RCAN1* or *DSCAM*, which make up part of the originally proposed DSCR, thus pointing to the possible involvement of and perhaps a central role of *DYRK1A* in inducing the morphological and cognitive impairments in DS (106, 111).

A third minimal region involving *SOD1*, *SYNJ1* and *ITSN1* has also been proposed to contribute to ID in DS (112). In this report, both intellectual disability and distinct dysmorphic features of DS with no cardiac abnormalities were described in a child with a 2.78 Mb microduplication of chromosome 21q22.11 (Figure 1C). Aside from an earlier report on an 18 month old patient with a

microduplication involving *SOD1* (113), the genes in this region were not previously thought to contribute to the major DS phenotypes.

While all DS phenotypes cannot be restricted to a single region, studies are still ongoing to discover the smallest region of HSA21 responsible for the critical shared phenotypes of DS (102, 110). This region, which is shared by all DS diagnosed individuals with pT21, is now called the highly restricted DSCR (HR-DSCR). It is a 34 kb segment located at 21q22.13 and was identified based on a systematic reanalysis of all pT21 cases described between 1973 and 2015 (110). Interestingly the HR-DSCR maps within the original DSCR and is located at almost the exact same region as the second minimal ID region described by Lyle and colleagues.

These studies of phenotype mapping have identified the genes involved in certain DS phenotypes. An example of this is seen in Alzheimer's Disease (AD), which is present in all individuals with DS over the age of 40 (37, 76). The early incidence of AD-like neuropathology in DS is linked to triplication of the gene encoding the Amyloid Precursor Protein (APP) and its importance in this phenotype has been proven by two cases of elderly individuals (65-78 years old) with pT21 involving the telomeric segment of HSA21 from (but not including) *APP* (78, 79). In both cases, the patients presented with a clinical phenotype of DS but no post-mortem Alzheimer's-like pathology or dementia.

Additionally, assessment of pT21 cases has also provided evidence that not all HSA21 genes cause an abnormal phenotype when triplicated. For example, two cases of pT21 in apparently healthy individuals without DS phenotypes have

been described. The first report describes a young boy with a 5 Mb terminal duplication of HSA21, while the second report describes two prenatal cases and their healthy mothers all carrying pT21 (12, 13). The triplicated region in first case described by Su and colleagues consists of a 4.4 Mb region that slightly overlaps with the DSCR but does not include *DYRK1A*, ID1 or the HR-DSCR (Figure 1 E&F). Given that this region overlaps with the 5Mb terminal duplication described by Gijsbers and that all three affected patients did not present with DS-like facial dysmorphism or ID, it can be concluded that genes within the terminal 6 Mb of HSA21 do not contribute significantly to the DS phenotype.

The second prenatal case describes a mother and her infant both presenting with a 14.3 Mb duplication in the proximal segment of HSA21 (Figure 1G). The infant in this case had normal psychomotor development but presented with minor facial dysmorphism, which was absent in the mother (12). Hence, genes within this region may not be major contributors to DS pathogenesis.

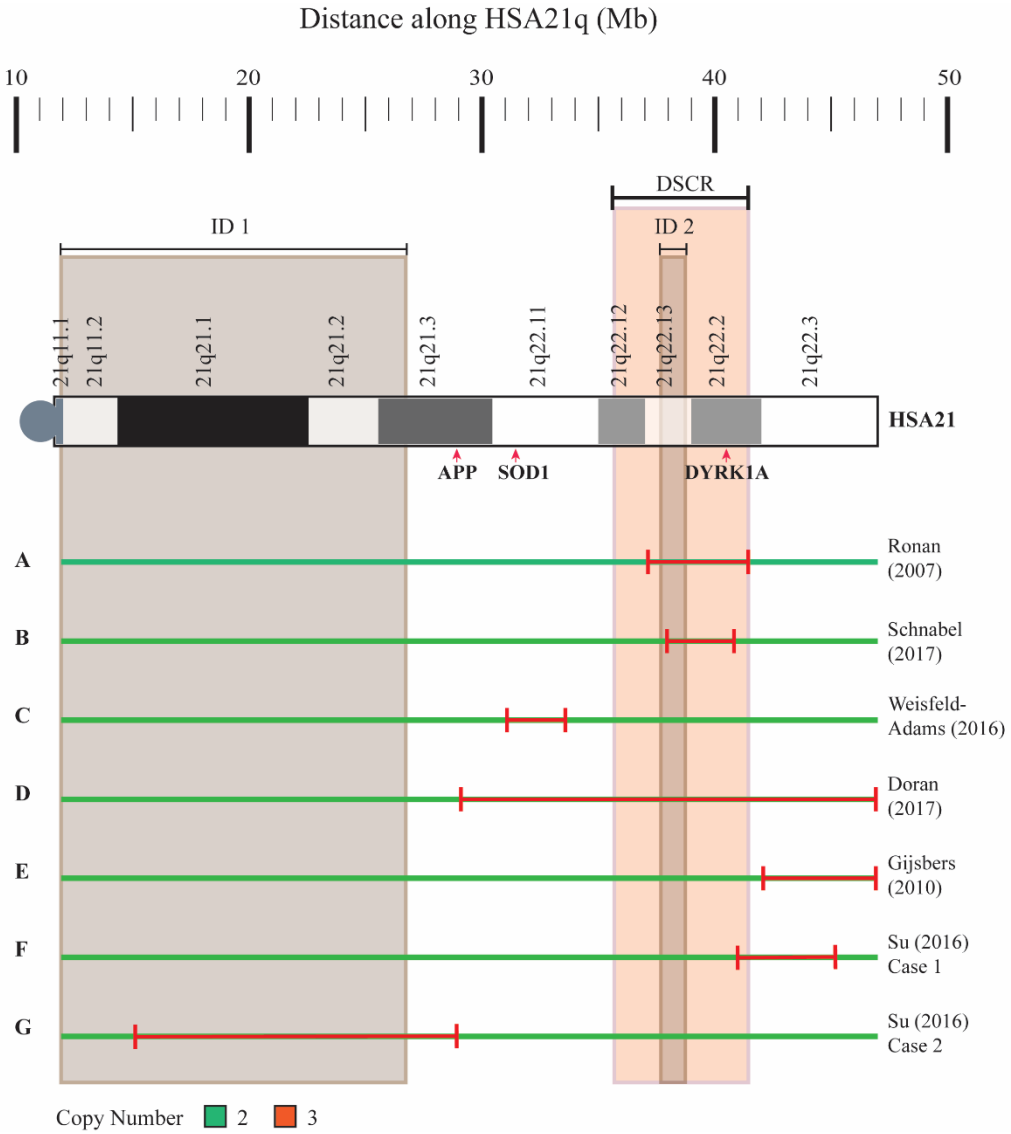

Figure 1: Genotype to Phenotype Correlations in Down Syndrome

A schematic diagram of genotype to phenotype correlations in DS based on a literature search of pT21 cases. The DSCR (**DSCR**, Orange box) represents the original minimal region responsible for most phenotypes of DS as defined by Delabar (1993). A subsequent reanalysis of 30 partial trisomy 21 cases by Lyle (2009) mapped intellectual disability to two distinct regions of chromosome 21 (**ID1 & ID2**, shaded in brown). A third minimal region for ID was proposed by Weisfeld-Adams (2016), but this is based on a single case of pT21 (**C**). Letters **A-G** represent individual human cases of pT21 referred to in this chapter with their reference on the right. Green lines indicate the disomic region and red bars represent the triplicated region in each patient.

1.7. Thesis Aims and Objectives

The aim of the work carried out during this PhD was to utilize the human induced pluripotent stem cell (iPSC) modelling to better understand how individual HSA21 genes and gene regions contribute to neurodevelopment, accelerated ageing and neurodegeneration in individuals with DS.

To do this, the following hypotheses were identified:

(1) A panel of iPSCs generated from individuals with T21, pT21 or microduplications and cellular phenotypes from them and their derivatives can be utilised to better understand the contribution of gene doses of *APP*, *BACE2*, *DYRK1A* and *SOD1* to DS phenotypes.

(2) Trisomy of BACE2 modulates APP processing in DS thereby protecting some individuals with T21 from developing AD-like dementia.

(3) Trisomy of genes within the DSCR play a role in the cellular features of accelerated ageing that are observed in cells and tissues from individuals with DS. More specifically, gene dose disruption of the DSCR gene *DYRK1A* is involved in accelerated ageing.

Chapter 2

Materials and Methods

Materials and Methods

2.1 Cloning and Bacterial Techniques

2.1.1 Guide-RNA Design

In collaboration with Dr Steven Havlicek, guide-RNAs (gRNAs) targeting two to three unique sites of either *APP, BACE2, DYRK1A* or *SOD1* were designed. The gRNAs were ordered as unmodified desalted oligonucleotides (IDT, Singapore), with overhangs compatible to those created by *BsmB1* restriction digest (Table 1). Efficiency and specificity of the gRNAs were confirmed using freely available CRISPR Guide RNA Design Software (https://www.benchling.com/crispr/). The Efficiency score is optimised for a 20 bp sequence (with a NGG PAM) and was calculated automatically based on the algorithm from (116). Specificity was calculated automatically based on the algorithm from (117). In both cases the score is given as a percentage and the higher the score the better the gRNA.

In preparation for cloning into the vector, 10 µM forward and reverse strands of each gRNA were annealed to one another in 15 µl final volume of 1x STE buffer (10x STE buffer: 1M Tris-HCL, 5M NaCl, 0.5M EDTA) in a Verti 96-well thermocycler (Applied Biosystems). Cycling conditions were as follows: 95°C for 5 min, -1°C/30s to a final temperature of 25°C and 4°C hold.

Annealed gRNAs were diluted 1:1000 in nuclease free H_2O (0.01 µM final concentration) prior to cloning into the pCAG-Cas9-HF vector.

Table 1: The gRNAs with overhangs compatible to a BsmBI digested vector

Gene	Target Site	Oligonucleotide Sequence (3'-5')	Efficiency	Specificity
SOD1 (1)	Exon 2	**F:** GCAGATGCTTCCCCACACCTTCAC **R:** AACGTGAAGGTGTGGGGAAGCAT	49.2	65.7
SOD1 (2)	Exon 2	**F:** GCAGGGATTCCATGTTCATGAGTT **R:** AAACAACTCATGAACATGGAATCC	32.7	71.1
BACE2 (1)	Exon 3	**F:** GCAGTGACGTCAAAGCCCTTGGAG **R:** AAACCTCCAAGGGCTTTGACGTCA	74.5	65.1
BACE2 (2)	Exon 3	**F:** GCAGGGAAGCTGGACGGGCTTCGT **R:** AAACACGAAGCCCGTCCAGCTTCC	43.8	82.7
DYRK1A (1)	Exon 7	**F:** GCAGGGGACCACATATCAATGGCA **R:** AAACTGCCATTGATATGTGGTCCC	69.0	72.5
DYRK1A (2)	Exon 7	**F:** GCAGACTGGAGAACCTCTGTTCAG **R:** AAACCTGAACAGAGGTTCTCCAGT	71.3	67.3
DYRK1A (3)	Exon 2	**F:** GCAGGGTGCAAGCCGAACAGATGA **R:** AAACTCATCTGTTCGGCTTGCACC	56.5	73.5
DYRK1A (4)	Exon 2	**F:** GCAGGCTGCTGGCCTTCAGATGGC **R:** AAACGCCATCTGAAGGCCAGCAGC	43.2	59.0
APP (1)	Exon 3	**F:** GCAGCATTGGTGATCTGCAGTTCA **R:** AAACTGAACTGCAGATCACCAATG	58.2	67.5
APP (2)	Exon 3	**F:** GCAGAACCAGTGACCATCCAGAAC **R:** AAACGTTCTGGATGGTCACTGGTT	46.8	69.0

2.1.2 Plasmid Vectors

High Fidelity CRISPR/Cas9 Plasmid

For CRISPR/Cas9 gene editing experiments, the pCAG-Cas9-HF plasmid was used (Figure 2). The plasmid, which was kindly provided by Dr Norris Ray Dunn, consists of the following components and promoters: (1) a hU6 promoter driving gRNA expression following insertion at a BsmB1 site; (2) a pCAG promoter driving the expression of hCsy4, hCas9-HF and blasticidin resistance; and (3) a bacterial promoter driving expression of the ampicillin resistance gene.

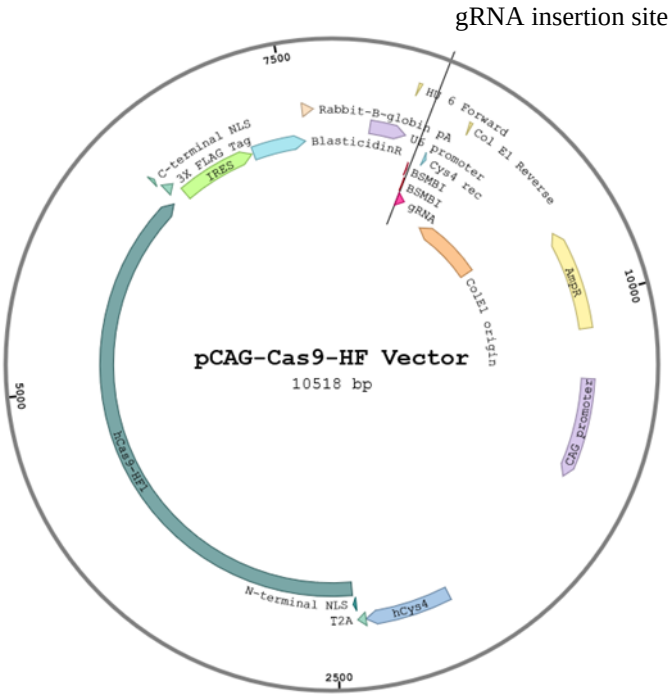

Figure 2: pCAG_Cas9HF Plasmid Map

The site for gRNA insertion lies within a BsmB1 restriction site and its expression will be driven by the hU6 promoter in transfected cells (top, purple). The pCAG promoter (right, purple) will drive the expression of Csy4, humanised High Fidelity Cas9 and blasticidin resistance. The expression of the ampicillin resistance gene (yellow) will be driven by the COL E1 promoter (Orange) in bacteria.

pGEM-T Easy Vector

To facilitate sequence analysis of PCR products, purified PCR products were ligated directly into the pGEM-T Easy Vector according to manufacturer's instructions (Figure 3; Promega #A1360). The vector contains a 3' thymidine overhang at the DNA insertion site, which is complementary to the 3' deoxyadenosine overhang created by standard polymerase during PCR.

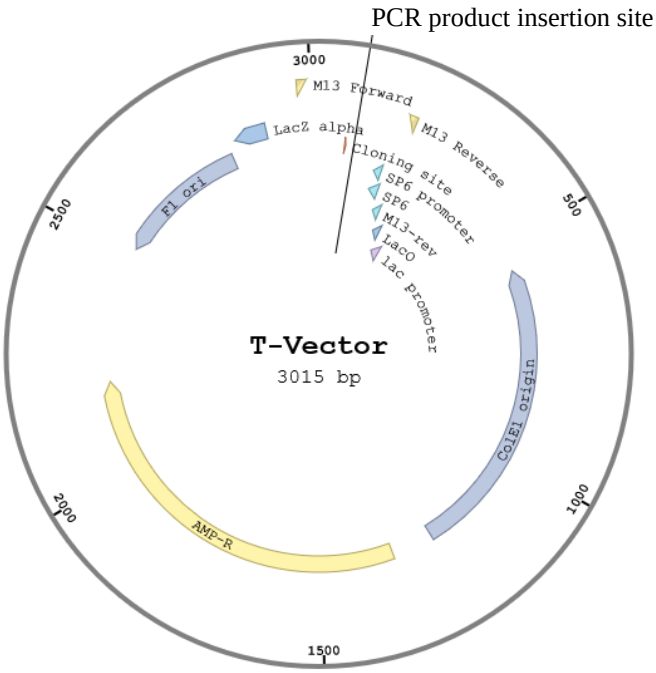

Figure 3: pGEM Easy T Vector Plasmid Map

The site for the insertion of the PCR product is marked by a 3' thymidine overhang, which is complementary to the 3' deoxyadenosine overhang created by the polymerase during PCR.

2.1.3 Plasmid Ligations

Double stranded annealed gRNAs were ligated into the pCAG-Cas9-HF vector. Ligations were carried out in a 10µl reaction with a final concentration of 0.02 µM gRNA, 20ng vector, T4 Polynucleotide Kinase; T4 DNA Ligase and 1X T4 Ligase Buffer (All from New England Biolabs) and incubated at 4°C overnight.

The amount of gRNA per reaction was calculated with the following formula:

$$ng\ of\ insert = \frac{ng\ of\ vector \times kb\ size\ of\ insert}{kb\ size\ of\ vector} \times insert{:}\ vector\ molar\ ratio$$

2.1.4 Expansion and Transformation of Chemically Competent Cells

All reagents were prechilled and incubation and centrifugation steps were carried out at 4 °C unless otherwise stated. 50 µl Top10 chemically competent cells (Thermo Fisher) were expanded overnight in Luria-Bertani (LB) Miller liquid broth (1st Base Asia) without antibiotics at 37°C in a 220 RPM shaking incubator. 500 µl overnight culture was transferred to 50 mL LB and further incubated for 2-3 hrs at 37°C in a 220 RPM shaking incubator. Bacteria were pelleted by centrifugation at 8000 RPM for 5 min and resuspended in a 5 mL solution containing 30 mM $CaCl_2$ before being redistributed into 1.5 mL prechilled Eppendorf tubes and pelleted. Pellets were resuspended in 30 mM $CaCl_2$ containing 10% glycerol and aliquoted as 25 µl stocks, which were stored at -80°C until use.

One 25 µl aliquot of chemically competent cells was used per transformation. Aliquots were thawed on ice, incubated with 2.5 µl ligated plasmid for 30 min, heat shocked at 42°C for 30 sec and incubated on ice for 2 min. Chemically competent cells were then incubated with 200 µl SOC (Thermo Fisher) at 37°C in a 220 RPM shaking incubator for 1hr 30min. Bacterial cultures were spread onto LB-agar Millar (1st Base Asia) plates supplemented with ampicillin (100 µg/ml) and incubated upside down at 37°C overnight.

2.1.5 Bacteria Screening and Selection by Colony PCR

PCR-based screening of vectors for the presence of the correct insert was carried out in 25µl PCR reactions using GoTaq DNA Polymerase and Buffers (Promega) according to the manufacturer's instructions. Cycling conditions comprised: 2 min initial denaturation at 95°C, [30 cycles of: denaturation at 95°C for 30 sec, 30 sec anneal, 1min/kb extension at 72°C] and a final 15min extension at 72°C. Vector specific primers flanking the insert were used and annealing temperatures were adjusted for each primer pair (Table 2).

Table 2: Vector-specific primer pairs for colony PCR

Plasmid	Plasmid region	Oligonucleotide Sequence (5'-3')	Ta (°C)	Size (Bp)
High Fidelity CRISPR/Cas9 Plasmid	hU6 - ColE1	**F:** GACTATCATATGCTTACCGT **R:** TCTGTGGATAACCGTATTAC	55	401
pGEM-T Easy Vector	M13	**F:** TGTAAAACGACGGCCAGT **R:** CAGGAAACAGCTATGACC	55	234+insert

For each PCR reaction, the DNA template was replaced by a single bacterial colony using a single sterile pipette tip to first to inoculate the PCR reaction and then a 100 µl LB starter culture containing ampicillin (100 µg/ml). The starter cultures were incubated at 37°C for the duration of the PCR reaction and

subsequent agarose gel electrophoresis (approx. 6 hours). Colonies with the correct product size after PCR amplification were used to inoculate 5ml bacterial cultures containing ampicillin, which were purified by miniprep (FavorPrep; Biotech Corp) according to the manufacturer's protocol. The purified plasmids were used for verification of the insert by Sanger sequencing (1st Base Asia).

All plasmids used for transfections were grown in 50 ml LB-ampicillin and purified with the Endotoxin Free MaxiPrep kit (Macherey-Nagel). Plasmid yields of ≥ 1 µg/µl were considered sufficient for iPSC transfection.

2.1.6 Restriction Digests

Restriction enzymes and buffers were obtained from NEB. All enzymes were inactivated at 80°C for 20 minutes.

For gRNA insertion, the pCAG-Cas9-HF plasmid was digested with the *BsmBI* restriction endonuclease at 55°C for 6 hours. Each 50 µl digestion contained: 1 µg purified vector, the required 1 X NEB buffer, and 10 U *BsmBI*. Digested and undigested plasmid were separated by gel electrophoresis on a 1% Tris-Acetate EDTA (TAE; 1st Base Asia) Agarose gel for 45 minutes. DNA was mixed with a 6 X loading dye containing Gel Red (Bioline #41003) prior to gel electrophoresis. The DNA band corresponding to digested vector was excised with a scalpel and extracted with the FavorGen gel purification kit (Biotech Corp) according to the manufacturer's instructions.

2.2 Cell Culture 1: HEK293T Cells and iPSCs

Appropriate ethics approval was obtained prior to the use of all human cells and tissues. Human subjects were participants in the "The London Down Syndrome Consortium (LonDownS): an integrated study of cognition and risk for AD in Down Syndrome" inter-disciplinary study, enrolled after informed consent, as per ethical approval 13/WA/0194, IRAS project ID:120344 see http://www.ucl.ac.uk/london-downsyndrome-consortium). For CRO1, the study was approved by the Ethical Research Committee of the Children's Hospital Zagreb, Croatia (University of Zagreb, School of Medicine).

All cultures were incubated at 37°C in a 5% CO_2 humidified incubator in 6-well plates (Corning) unless otherwise stated. For passaging, iPSCs were either disassociated as clumps using ReLeSR (Stem Cell Technologies) or as single cells using Accutase (SigmaAldrich) depending on their use. Rho Kinase/ROCK Inhibitor (Y-27632, StemCell Technologies) was added to media at a final concentration of 10 μM for up to 24 hrs after each passage.

2.2.1 General Media and Reagents

Culture media and reagents were purchased from Gibco, Life Technologies unless otherwise stated.

- **DMEM**: Dulbecco's Modified Eagle's Medium high glucose was used as base medium. Supplemented with 10% Foetal Bovine Serum, 1% Penicillin/Streptomycin and 1% L-Glutamine for the culture of HEK293T cells.

- **Transfection Media**: OptiMEM Reduced Serum media was used as base medium. Supplemented with either Lipofectamine 2000 (for HEK293T transfection) or Lipofectamine 3000 and P3000 reagent (for iPSC transfection). Lipofectamine reagents were purchased from Invitrogen.
- **dPBS:** Dulbecco's Phosphate Buffered Saline without calcium or magnesium was used for washing cells before dissociation and before collecting cell and organoid pellets.
- **mTESR:** mTESR1 Basal medium supplemented with 20% mTESR1 5x supplement (StemCell Technologies) and 1% Penicillin/Streptomycin was used for the culture of iPSCs.
- **E8:** Essential 8 Basal medium supplemented with 2% Essential 8 50x supplement, and 1% Penicillin/Streptomycin was used for the culture of iPSCs.
- **Matrigel:** hESC qualified (Corning, Life Sciences #3354277) Matrigel was diluted in DMEM Nutrient Mixture F-12 (DMEM F12) and used to coat plates for iPSC culture.
- **VTN:** Vitronectin (Life Technologies, #A14700) was diluted in dPBS (1:100) and used to coat plates for iPSC culture.
- **GTX:** hESC qualified (Life Technologies, #A1413301) Geltrex was diluted in DMEM F12 and used to coat plates for iPSC and NSC culture.
- **Erythroblast Differentiation Media:** StemSpan Serum-Free Expansion Medium II (SFEM II; StemCell Technologies) was used as basal medium supplemented with: 2 U/mL Human Erythropoietin, 50 µg/mL L-ascorbic

acid, 50 ng/mL Stem Cell Factor, 40 ng/mL IGF-1, 10 ng/mL IL-3, 0.4 ng/mL Dexamethasone, 1% L-glutamine and 1% MEM Non-Essential Amino Acids.

- **hESC Media:** DMEM F12 was used as a basal medium supplemented with 20% Knock Out Serum Replacement, 3% ES-quality fetal bovine serum, 1% GlutaMAX supplement, 1% MEM-Non-Essential Amino Acids and 50µM neat 2-mercaptoethanol (Life Technologies).

2.2.2 Cell counting

Cell counting reagents and equipment was purchased from Chemometec. To count cells, 1 µl Solution 18 AO-DAPI cell counting solution (#910-308) was added to 20 µl single cell suspension and 10 µl of this mixture was transferred to a single well of a NC-Slide A8^{TM} wells glass chamber (#942-0003). Cells were counted automatically using the Automated Cell Analyzer Nucleocounter, NC-250.

2.2.3 Erythroblast differentiation and Sendai Reprogramming

YA093 refers to a young male adult with DS caused by pT21 of a region spanning mid-*APP* to the telomere (Figure 8). With regard to genes of interest, YA093 has trisomy of *BACE2*, *DYRK1A* and *SOD1* but not *APP*. Patient blood sample was collected during routine tests in collaboration with the LonDowns Consortium (https://www.ucl.ac.uk/london-down-syndrome-consortium/) and consented surplus material was used to generate iPSCs. Peripheral blood mononuclear cells (PBMCs) were extracted by Ficoll-Hypaque density gradient centrifugation by Dr. Jurgen Groet (Queen Mary University London).

CRO1 refers to a young female individual with DS caused by a microduplication of a 4.8 Mb region overlapping the DSCR (Figure 8). With regard to genes of interest, CRO1 has trisomy of *DYRK1A* but not *SOD1*, *APP* or *BACE2*. Patient blood sample was collected during routine diagnostic tests by Prof. Ingeborg Barisic, Children's Hospital Zagreb, Croatia and consented surplus material was used to generate the iPSCs.

CRO1 and YA093 iPSC lines were generated from blood via erythroblast differentiation under the supervision of Dr. Jonathan Loh Yuin-Han (A*STAR). Extracted PBMCs were cultured in Erythroblast differentiation medium for 10 days to allow growth and expansion of erythroblasts. Erythroblasts were reprogrammed using the iPS 2.0 Sendai Reprogramming Kit comprising three reprogramming vectors containing the four Yamanaka factors: KOS (human Klf4 and human Oct3/4, Sox2), hc-Myc (human c-Myc) and hKlf4 (human Klf4) (CytoTune 2.0, Invitrogen, Thermo Fisher).

The resulting iPSCs were cultured in either mTESR1 on Matrigel-coated plates (YA093) or E8 on VTN coated plates (CRO1).

2.2.4 CRISPR/Cas9 Transfections in HEK293T and iPSCs

HEK293T cells were plated on Poly-D-Lysine coated wells and transfected at 70% confluency. Cells were transfected with 1µg of each complete High Fidelity CRISPR/Cas9 plasmid using Lipofectamine 2000 transfection reagents and then harvested 24 hrs after transfection. Genomic DNA from transfected HEK293T cells was used to assess the transfection and gene modification efficiencies of each gRNA as well as optimise PCR amplification of the target sites.

hiPSCs were transfected using Lipofectamine 3000 transfection reagents and 2.5 µg plasmid DNA per transfection.

2.2.5 Blasticidin Treatment

Successfully transfected iPSCs were selected 24 hrs after transfection by treatment with blasticidin. The optimal blasticidin concentration was 2 µg/ml for 48 hours in D21C3 and T21C5, and 8 µg/ml in CRO1. This concentration was determined by treating untransfected iPSCs with blasticidin at concentrations ranging from 0µg/ml to 8µg/ml at increments of 0.5µg/ml. The lowest possible concentration resulting in 100% cell death was used. Surviving iPSC colonies were grown for 14 days and then picked into individual wells of a 12 well plate. Picked colonies were expanded until there were sufficient cells for DNA isolation, cryopreservation, and maintenance in culture.

2.2.6 Clonal Isolation of iPSCs

Colonies with a mutation as indicated by Sanger sequencing were harvested by incubation with Accutase (Life Technologies) for 5-10 min until a single cell suspension was achieved. The cells were counted and plated at 500 cells/cm^2 in a 6-well plate for clonal cell expansion. Individual colonies were picked into 12 well Matrigel or Vitronectin coated plates approximately 14 days after seeding and expanded for DNA isolation, cryopreservation, and maintenance in culture.

2.2.7 Cryopreservation of iPSCs, HEK293T and Erythroblasts

HEK293T cells were cryopreserved at a density of 1x10^7 cells per cryovial in DMEM containing 10% Dimethyl sulfoxide (DMSO, Sigma, D2650).

Erythroblasts were cryopreserved at a density of $1x10^6$ cells per cryovial in SFEM II containing 10% DMSO. Clumps of iPSCs from half a 6 well were either vitrified in StemCell Keep™ (Abnova #U0021) or cryopreserved in Bambanker™ serum-free cell freezing medium containing 10% DMSO (Lymphotec Inc) according to each respective manufacturer's instructions.

2.2.8 HyPer and GFP Viral Packaging in HEK293T

HEK293T cells were plated in 1 mL DMEM without penicillin/streptomycin (pen/strep) and transfected with plasmids containing the components needed to create 3rd generation lentiviral constructs.

Transduced plasmids consisted of: (1) 1.6 µg pFUGW lentiviral backbone containing eGFP (Addgene #14883) or a modified version containing either the mitochondria-localised hydrogen peroxide sensor (HyPer-Mito) or the cytoplasm-localised hydrogen peroxide sensor (HyPer-Cyto) instead of eGFP; (2) the lentiviral packaging plasmids (1.2 µg Addgene #12251 & 0.8 µg #12253), and (3) 1.6 µg of the lentiviral envelope expressing plasmid (Addgene #12259) in 250 µl OptiMEM medium supplemented with 6 µl P3000. The plasmid/OptiMEM mixture was mixed with 250 µl OptiMEM containing 7 µl Lipofectamine 3000 and the total 500 µl was added to the wells in a dropwise fashion. Media was replaced after 6-hour incubation at 37°C in a humidified incubator.

Media was collected and pooled 24 and 48 hrs after transduction, centrifuged to remove cell debris, aliquoted and stored at -80ºC until needed for iPSC transduction.

2.2.9 Generating Stably expressing GFP and HyPer iPSC Lines

Packaged lentiviral particles for stably expressing eGFP, HyPer-Mito or HyPer-Cyto were transduced into isogenic T21C5 and D21C3 iPSCs. iPSCs were plated on Matrigel-coated wells of a 6-well plate in mTesR1 supplemented with 20% lentivirus-containing HEK293T supernatant. Following transduction, the iPSCs were passaged 4-5 times before being subject to Fluorescence Activated Cell Sorting (FACS).

2.2.10 Fluorescence Activated Cell Sorting

All centrifugation steps were at 1200 RPM at 4ºC for 10min. Each well of a 6 well plate containing approximately $2x10^6$ iPSCs was dissociated to single cells and washed in PBS before being resuspended in 100 µl filter sterilised FACS Buffer (1x PBS supplemented with 5% BSA and 2 mM EDTA). For staining, 100 µl iPSC suspension was incubated with 5 µl of either mouse anti-human TRA-1-81 conjugated to BV510 or the mouse IgMκ Isotype control conjugated to BV570 (both antibodies from BD Horizon) on ice for 15 min in the dark and then washed twice to remove unbound antibody. Labelled iPSCs were resuspended in 500µl FACS buffer and sorted under sterile conditions using the FACSAtria Fusion (BD Biosciences) with the help of Manisha Cooray (Flow Cytometry Assistant Manager, LKC Medicine).

For HyPer or eGFP tagged cells, double positive iPSCs expressing both eGFP/HyPer and TRA-1-81 were collected into FACS tubes containing mTESR1 and 10µM ROCK inhibitor (RI). The gating strategy was kept constant for both

cell lines to avoid unwanted bias. Cells collected by FACS were centrifuged, resuspended in fresh media containing RI and plated onto Matrigel coated plates.

2.3 Cell Culture 2: iPSC Differentiation and Inhibitor Treatment

Embryoid bodies (EBs) or cerebral organoids were transferred to new plates using sterile wide orifice P1000 filtered tips when required.

2.3.1 Germ Layer Differentiation for Pluripotency Validation

CRO1 iPSCs at 80% confluency were dissociated into single cells, PBS rinsed and counted before being resuspended at 9,000 cells per 150µl HESC media (supplemented with 4ng/ml bFGF (Peprotec, Gene-ethics Asia) and 50µM RI). The cell suspension was plated in a 96-well round-bottomed ultra-low attachment plate at 150µl per well. The plate was centrifuged at 200xg for 5min to aid EB formation and incubated at 37ºC for three days. On day three, 50% spent media was replaced with fresh HESC media (no bFGF or RI). The EBs were fed bi-weekly for a total of seven days to allow self-directed differentiation into cells of the three embryonic germ layers (endoderm, mesoderm and ectoderm).

On day seven, each EB was transferred to a geltrex-coated coverslip in a 24 well plate in HESC media. The EBs were fed bi-weekly for a further seven days, until the EB attached to the coverslip and the cells began to migrate out of the EB.

After a total of 14 days in culture (7 days suspension plus 7 days adherent culture), coverslips were fixed for immunofluorescence analysis of the three germ layers (See section 2.7.3).

2.3.2 Generation of Neural Stem Cells from iPSCs

Neural stem cells were generated using the PSC Neural Induction protocol (gibco, life technologies). Briefly, iPSCs were plated on VTN coated wells at $3x10^5$ cells per well in E8. After 24 hours, media was changed to complete PSC Neural Induction Medium, and cells were monitored and fed every 2 days before being harvested. NSCs were expanded on day 7 of neural induction and propagation was continued for at least 4 passages before cells were plated on coverslips, fixed, and stained for the markers of neural stem cells.

2.3.3 Generation of Cerebral Organoids from iPSCs

Cerebral organoids were generated as described (118). Briefly, EBs were generated as in 2.3.1 until day six. On day six, induction of primitive neuroepithelia was initiated by transferring EBs of approximately 500-600 μm to a 24 well ultra-low attachment plate containing 500 μl neural induction medium. The EBs were fed bi-weekly until visible signs of neuroepithelium development was observed (clearing of the outer ectoderm with a distinction between the outer bright and inner dark tissues, and radial organisation of the outer ectoderm).

At approximately 10 days *in vitro* (DIV) the neuro-EBs were embedded in Matrigel and transferred to 60 mm ultra-low attachment dishes in organoid differentiation medium (without vitamin A) for four days (thereafter vitamin A was included in the differentiation media). The plates were incubated in a 37ºC tissue culture incubator on an orbital shaker at 85 RPM for up to three months, whilst being fed every 3-4 days.

2.3.4 Treatment of iPSCs and Cerebral Organoids with DYRK1A Inhibitors

Both undifferentiated iPSCs and cerebral organoids were treated with the same concentrations of either harmine (Sigma #286044) or ID8 (Adipogen, #AG-CRI-3655) dissolved in DMSO.

100mg harmine powder (molecular weight: 212.25g/mol) was weighed out and dissolved in 15.7 ml DMSO to produce a 30 mM stock solution. This was further diluted to produce a 1.5 mM working solution (1:20) which was used at a final concentration of 300 nM in media. 1 mg ID8 powder (MW: 298.3g/mol) was weighed out and dissolved in 67 µl DMSO to produce a 50 mM stock solution. This was diluted in media at a final concentration of 10 µM. The total DMSO concentration in drug treated and the vehicle controls did not exceed 0.02% in either case.

2.4 Genomic DNA analysis of CRISPR/Cas9 Targeted cells

2.4.1 Genomic DNA Extraction

All pellets harvested for DNA were rinsed in PBS before being stored at -20ºC. DNA was extracted using the FavorPrep Genomic DNA purification kit (Biotech Corp) as per the manufacturer's instructions.

2.4.2 PCR Amplification of the CRISPR/Cas9 Target Region

PCR was carried out on genomic DNA as in 2.1.4. For primer optimisation, two primer pairs flanking each gRNA target site were designed and tested on targeted HEK293T genomic DNA. Primer pairs were selected for their ability to amplify

a single PCR product, of the expected size, when visualised by agarose gel electrophoresis (Table 3).

5 µl of a 25 µl PCR product was used for gel electrophoresis (1.5% TAE/Agarose gel) and the remaining 20 µl was purified (FavorPrep, Biotech Corp). The purified PCR products were either analysed with a T7 endonuclease assay (for gRNA efficiency tests) or sent for Sanger sequencing (for identification of insertions or deletions (indels) in targeted iPSCs).

Table 3: The most optimal primer pairs for amplifying the selected target sites

No.	Target Site	Sequence (5'-3')	Ta (°C)	Size (Bp)
1.	*APP* Exon 3	**F:** GCATGTCAACATGATGCTC **R:** CAGAGTGGCAATGTGCTG	55	513
2.	*BACE2* Exon 3	**F:** GACACGGCAACCTTATCTTC **R:** ACTGTCTCCAAGAACAGCC	56	732
3.	*DYRK1A* Exon 7	**F:** CCGTATTCGTAGTCTAATGTTG **R:** CTAACTGTTCTCCTTCATGAGTAG	56	528
4.	*SOD1* Exon 2	**F:** GAGCAGTTAAGCAGCTTGC **R:** GGAGGTCGAGGAGGATAGAC	55	618

2.4.3 gRNA Gene Modification Efficiency Test

Three gRNA pairs for each gene were assessed for their efficiency in causing indels at the target site by transfection of HEK293T cells. The efficiency of CRISPR/Cas9 to cause mutations by non-homologous end joining was analysed with a T7 endonuclease assay (NEB, M03025).

The T7 Endonuclease recognizes and cleaves non-perfectly matched DNA. The DNA fragments were visualized by gel electrophoresis and quantified as a

percentage of the total DNA/lane with the BioRad gel imaging software. The percentage of gene modification was calculated by the following formula:

$$\%\ Gene\ modification = 100 \times (1 - (fraction\ cleaved)\text{^}0.5\ )$$

2.4.4 Sanger Sequencing and Tracking of Indels by Sequence Trace Decomposition (TIDE) Analysis

All sequencing was performed by First Base Asia. Purified PCR products were either sent directly for sequencing or cloned into the pGMT-Easy T vector prior to sequencing. Sequence files were analysed in Mutation Surveyor V3.1.0 or uploaded to the Tracking of InDels by Sequence Trade Decomposition (TIDE) webtool for analysis. TIDE, developed by (119) uses a decomposition algorithm on a pair of sequences uploaded by the user (edited and unedited) to identify major induced mutations at a CRISPR-SpCas9 target site. The software accurately determines the frequency of mutations in the cell population. For example, a heterozygous mutation in disomic cells would be displayed as a sequence trace with 50% normal and 50% mutated sequence. For trisomic cells, 33.3% would be expected per allele.

2.4.5 Paralogous Sequencing

To assess whether a cell line is disomic or trisomic, “Touchdown PCR” was carried out on 20 ng genomic DNA using the method and primers flanking a paralogous sequence mismatch (PSM) as described (120).

Pyrosequencing of the purified PCR products was carried out on the PyroMark Q48 Autoprep (Qiagen) according to the manufacturer’s instructions. For each

gene the primer running in the opposite direction to the sequencing primer was biotinylated to aid binding of the strand to the Pyromark Q48 Beads. Sequencing data was analysed and the PSM was quantified using the PyroMark Q48 Autoprep 2.4.2 software. The PSM ratio would be 1:1 in the case of disomy and 1.5:1 in the case of trisomy.

To identify whether the pT21 region of CRO1 was excised, the above method was adapted to quantify a G/G/C SNP in *DYRK1A* Exon 7 of CRO1. The SNP could be quantified as either 2:1 in WT CRO1 cells, 1:1 in the case of excision of the allele containing the G or 0:1 in the case of excision of the allele containing the C.

Table 4: Primers used for PCR amplification of Paralogous genes

No.	HSA21 Locus	Reference Chromosome	Forward and Reverse Primer Sequences (5'-3)	Ta (°C)
1.	*ITSN*	HSA5	**F:** ATTTATTGCCATGTACACTT **R:** GAATCTTTAAGCCTCACATAG[B]	57
2.	*GABPA*	HSA7	**F:** CTTACTGATAAGGACGCTC[B] **R:** CTCATAGTTCATCGTAGGCT	57
3.	*DYRK1A* G SNP	*DYRK1A* C SNP	**F:** GCCATTGATATGTGGTCC **R:** GATTAAGTAGACATCTTTGCC[B]	51

[B] - Biotinylated primers

Table 5: Sequencing Primers for Paralogous Sequencing

No.	HSA21 Gene locus	Primer Sequence (5'-3)
1.	*GABPA*	TCACCAACCCAAGAAA
2.	*ITSN*	ACCAAGAAAGATGGTGAC
3.	*DYRK1A*	TACAAATTCTGTTTTCATAATT

2.4.6 Single Nucleotide Polymorphism analysis

Purified Genomic DNA from clonal cell lines at a minimum of 40 ng/μl in a total volume of 10 μl was sent for analysis by SNP array. Samples were run on Illumina OmniExpress v1.1 chips in collaboration with the lab of Jia Nee Foo (Asst. Prof, LKC Medicine). Data analysis was performed in Genome Studio 2.0 software.

2.5. Gene expression analysis

2.4.7 RNA Extraction and cDNA Synthesis

Total RNA was isolated from iPSCs using TRIzol™ Reagent (Invitrogen), and the RNA extraction kit (Zymogen) following manufacturer's instructions. Genomic DNA was removed by DNase treatment. RNA integrity was checked by 2% TAE/agarose gel electrophoresis. Concentration and purity of RNA was evaluated with a NanoDrop 3000 spectrophotometer. The minimum quality for samples used was: 260/280 nm absorbance ratios between 1.8 and 2.2 and 260/230 nm absorbance ratios above 1.8. Complementary DNA (cDNA) was reverse transcribed from 200 ng total RNA with Reverse Transcriptase (Applied Biosystems) according to the manufacturer's instructions.

2.4.8 Reverse Transcription-PCR (RT-PCR)

RT-PCR was performed according to the following PCR conditions: 95°C for 3 minutes followed by 35 cycles at 95°C for 35 seconds, 55°C for 40 seconds, and 72°C for 45 seconds and a final extension at 72°C for 7 minutes.

Table 6: Primers used for RT-PCR amplification of Sendai virus

Direction	**Primer Sequences (5'-3)**	**Tm (ºC)**	**Ta (ºC)**
Forward	GGATCACTAGGTGATATCGAGC	61.4	55
Reverse	ACCAGACAAGAGTTTAAGAGATATGTATC	61.0	

2.6. Protein Analysis

2.4.9 Whole Cell Lysate Extraction and Quantification

iPSC pellets of approximately $2x10^6$ cells were resuspended in 150 µl RIPA buffer (Sigma) containing protease inhibitor cocktail (PIC) and incubated on ice for 10 min. After incubation, the suspension was centrifuged at 1 300 RPM for 10 min at 4ºC and supernatants were transferred to new Eppendorf tubes.

Standards were generated with the Pierce™ BCA Protein Assay Kit (ThermoFisher Scientific) according to the manufacturer's instructions and colorimetric quantification was carried out using Synergy H1 plate reader and Gen5 3.3 Software (BioTek, Winooski, US).

2.4.10 Western Blot

Normalised whole lysates of CRISPR/Cas9 edited and unedited iPSCs were separated by SDS-PAGE in a 10% acrylamide gel. Voltage was first set at 75V for 20 min to ensure proteins were running correctly followed by 100V for 1.5 hrs. Separated proteins were transferred to a 0.45µm nitrocellulose membrane according to the manufacturers protocol (Bio-Rad) at 100V for 1hr.

Before antibody staining, membranes were blocked in 5% non-fat milk in Tris buffered saline with 0.1% Tween-20 (TBS-T) for 1 hr at room temperature (RT).

Primary and secondary antibodies are listed in Tables 7 and 8. To remove unbound antibody membranes were rinsed three times at 10 min each in TBS-T after incubation with each antibody. The same membranes were stripped and re-probed with anti-β-actin for loading controls. Stripping was carried out using Thermo-Fisher stripping solution according to the manufacturer's instructions.

Western blots were developed using the Pierce™ ECL Western Blotting Substrate kit (ThermoFisher) according to the manufacturer's instructions and imaged on a Bio-Rad ChemiDoc.

2.7. Immunostaining and Microscopic Analysis

2.7.1. Fixation of Cells and Organoids

Cells were either plated in 96 well imaging quality plates (Greiner) or on coverslips coated with appropriate matrix. Cells were fixed in 4% paraformaldehyde (PFA) for 10 min at RT for immunocytochemistry (ICC) analysis or for 2 min at RT for Alkaline Phosphatase staining. After fixation, cells were rinsed three times with PBS to remove residual PFA.

For immunohistochemistry (IHC) analysis cerebral organoids (COs) were fixed in 4% PFA for approximately 24 hours at 4ºC and thereafter rinsed three times with PBS. For cryoprotection, PBS-rinsed COs were placed first in 10% sucrose/PBS followed by 30% sucrose/PBS for 24 hours each and then embedded in OCT (Fisher Scientific). OCT embedded COs were sectioned by cryostat into 20 μm thick slices and mounted on Superfrost Plus slides (Fisher Scientific) for immunostaining. Cryosectioning was conducted with the help of Dr. Ivan Alic (Research Fellow, LKC Medicine).

2.7.2. Fluorescent in Situ Hybridisation

FISH was performed on fixed iPSCs and organoid cryosections and following methods as previously published (121). PBS rinsed slides were rehydrated and incubated for 20 min in 10 mM sodium citrate buffer at 80ºC and thereafter allowed to cool. Slides were then incubated in 2x Saline Sodium Citrate (SSC) for 5 min followed by 50% formamide in 2x SSC for 1h. After incubation, slides were covered with a previously prepared hybridization chamber and incubated with 10 µl of the XA 13/18/21 Probe (D-5607-100-TC, MetaSystems Probes). Incubation steps, which were carried out in the dark, consisted of 45ºC for 2h, 80ºC for 5 min and 37ºC for 2 days. After incubation, slides were rinsed three times with 2x SSC at 37ºC for 15 min each and then rinsed twice with 0.1x SSC at 60ºC for 5 min each on the shaker. Thereafter slides were equilibrated for 2 min in 2x SSC at 37ºC, counter stained with DAPI for 10 min, and covered with DAKO Fluorescent Mounting Medium.

2.7.3. Staining, Immunocytochemistry and Immunohistochemistry

Fixed cells or PBS-rinsed CO slices on slides were permeabilised with 0.2% Triton X-100 and 3% donkey serum in PBS for 1hr at RT. Thereafter cells or sections were stained with primary antibody overnight at 4ºC followed by secondary antibodies for 2 hrs at RT (Tables 7 and 8). After each incubation, unbound primary and secondary antibody was removed by 3x PBS rinses. Antibodies were diluted in 1% donkey serum with 0.2% Triton X-100/PBS prior to use. Nuclei were counter-stained with either DAPI (1:8000, Sigma) or DRAQ5 (1:117, Abcam) for 10 min at RT, washed 3x in PBS and mounted with DAKO

fluorescent mounting medium. Negative controls consisting of secondary antibody only were carried out for each antibody.

iPSCs were stained with Alkaline Phosphatase (Merk) according to the manufacturer's instructions. Briefly, PBS-rinsed fixed iPSCs were incubated with 2:1:1 ratio of FRV: Naphthol As-B1: H_2O for 15 min at RT in the dark. Cells were then rinsed once in PBS and brightfield images were captured on an EVOS FLc microscope (Life Technologies).

For staining with AmyloGlo (TR-300-AG, Biosciences), PBS-rinsed CO slices on slides were first incubated in 70% ethanol for 5 min at RT, washed in Milli Q water for 2 min at RT and then incubated with 1:100 AmyloGlo solution (1:100 in PBS) in the dark for 10 min at RT. Slides were then washed in 0.9% saline solution for 5 min at RT and counterstained with DRAQ5 for 10 min at RT.

Thiolfavine S (T1892, Sigma) staining was performed according to (122). PBS-rinsed CO slices were incubated with Thiolfavine S solution (1:100 in PBS) in the dark for 10 min at RT, differentiated in 80% ethanol and counterstained with DRAQ5 for 10 min at RT.

To increase the signal of insoluble Aβ material, fixed T21C5Δ7 (96 DIV) organoid slices were treated with 87% formic acid (Sigma) for 10 min at RT. Formic acid was removed and slices were rinsed three times with PBS before immunostaining as described above.

2.7.4. Stains and Antibodies

Primary antibodies for immunofluorescence (IF), Immunohistochemistry (IHC) and western blot (WB) are listed in Table 7. Fluorescent conjugated secondary antibodies were obtained from ThermoFisher Scientific (IF and IHC) and HRP secondary antibodies were from Abcam (WB) and are listed in Table 8.

Table 7: Primary antibodies for immunofluorescence, immunohistochemistry and western blot

Antibody/ Stain	**Species**	**Clone**	**Cat No.**	**Source**	**Dilution**	
					IF/IHC	**WB**
3R-Tau	mouse	8E6/C11	#05-803	Millipore	1:500	1:1k
4R-Tau	mouse	1E1/A6	# 05-804	Millipore	1:500	1:1k
AIF	Rabbit	D39D2	#5318	Cell Signaling	1:400	N/A
APP/ Aβ	mouse IgG1	6E10	803001	Biolegend	N/A	1:1k
Aβ	mouse IgG2b	4G8	800701	Biolegend	1:200	N/A
Aβx-40	mouse IgG2a	BA27	014-26923	Wako	1:500	N/A
Aβx-42	mouse IgG1	BC05	010-26903	Wako	1:500	N/A
BACE2	rabbit IgG	Polyclonal	AB5670	Abcam	N/A	1:500
Beta-Actin	rabbit IgG	Polyclonal	ab8227	Abcam	N/A	1:10k
Brachyury	Rabbit IgG	D2Z3J	#81694	Cell Signaling	1:600	N/A
BRN2	goat IgG	D2Z3J	SC-6029	Santa-Cruz	1:250	N/A
Conformationally altered Tau	mouse IgG	TG3	N/A	Peter Davies (Alzforum)	1:100	1:1000
Ctip2	rat IgG2a	25B6	Ab18465	Abcam	1:100	N/A
Doublecortin	goat	C-18	sc-8066	Santa Cruz	1:200	N/A
DYRK1A C-terminal	rabbit IgG	Polyclonal	ab180910	Abcam	10 µg/ml	N/A
DYRK1A N-terminal	rabbit IgG	Polyclonal	ab65220	Abcam	1:500	N/A
FOXA-2	Goat IgG	Polyclonal	AF2400	R&D Systems	5-15 µg/ml	N/A
FOXG1	rabbit IgG	Polyclonal	ab18259	Abcam	1:400	N/A
GFAP	chicken IgY	Polyclonal	ab4674	Abcam	1:2k	N/A
GFAP	rat IgG2a	2.2B10	13-0300	ThermoFisher Scientific	1:1k	N/A

Table 7 continued: Primary antibodies for immunofluorescence, immunohistochemistry and western blot

Antibody/ Stain	Species	Clone	Cat No.	Source	Dilution	
					IF/IHC	WB
Hyper-phosphorylated Tau	mouse IgG	AT8	MN1020	ThermoFisher Scientific	1:500	N/A
MAP2	chicken IgY	Polyclonal	ab5392	Abcam	1:1k	N/A
Nestin	mouse IgG1	10C2	ab22035	Abcam	1:200	N/A
OCT-4	rabbit	Polyclonal	#2750	Cell Signaling	1:400	N/A
Pax6	rabbit IgG	Polyclonal	901301	Biolegend	1:200	N/A
REELIN	mouse IgG1κ	142	mab5366	Chemicon (Merck)	1:300	N/A
SATB2	IgG	Polyclonal	ab34735	Abcam	1:200	N/A
SMA	Rabbit IgG	Polyclonal	ab5694	Abcam	1:200	N/A
SOX2	Rabbit IgG	Polyclonal	Ab97959	Abcam	1:500	N/A
SSEA-4	mouse IgG3	Polyclonal	#4755	Cell Signaling	1:500	N/A
TBR1	rabbit IgG	Polyclonal	ab31490	Abcam	1:500	N/A
TRA-1-60	mouse IgM	Polyclonal	#4746	Cell Signaling	1:1k	N/A
TRA-1-81	mouse IgM	Polyclonal	#4745	Cell Signaling	1:250	N/A
Tubulin β-3 (TUBB3)	Rabbit IgG	Poly18020	802001	Biolegend	1:1000	N/A
γH2AX	mouse	JBW301	05-636	Millipore	1:100	N/A

Table 8: Secondary antibodies for IF and WB

Antibody	Conjugate	Cat. No	Dilution
Donkey anti-Mouse IgG (H + L)	Alexa Fluor 488	A-21202	1:1 000
Donkey anti-Mouse IgG (H + L)	Alexa Fluor 555	A-31570	1:1 000
Donkey anti-Mouse IgG (H + L)	Alexa Fluor 647	A-31571	1:500
Donkey anti-Rabbit IgG (H + L)	Alexa Fluor 488	A-21206	1:1 000
Donkey anti-Rabbit IgG (H + L)	Alexa Fluor 555	A-31572	1:1 000
Donkey anti-Rabbit IgG (H + L)	Alexa Fluor 647	A-31573	1:500
Donkey anti-Goat IgG (H + L)	Alexa Fluor 555	A-21432	1:1 000
Goat anti-Mouse IgG2b (H + L)	Alexa Fluor 488	A-21141	1:500
Goat anti-Mouse IgM (H + L)	Alexa Fluor 568	A-21043	1:500
Goat anti-Rat IgG (H + L)	Alexa Fluor 568	A-11077	1:1 000
Goat anti-Chicken IgY (H + L)	Alexa Fluor 633	A-21103	1:500
Goat anti-Rabbit IgG (H + L)	HRP	ab97051	1:10 000
Goat anti-Mouse IgG (H + L)	HRP	ab97023	1:10 000

2.7.5. Microscopy and Image Analysis

Brightfield images were captured on an EVOS FLc microscope (Life Technologies) and fluorescence was captured on a Zeiss LSM-800 inverted confocal microscope with the help of Dr. Ivan Alic. Image analysis was performed either by ImageJ or IMARIS software (BITPLANE, An Oxford Instruments Co., Zurich, Switzerland).

FISH: images were captured by confocal microscope with Airyscan using 63x oil-immersed objective. HSA21 specific probe was labelled in the red spectrum and the HSA13 specific probe was labelled in the green spectrum. Quantification of spots was performed by IMARIS on more than 500 nuclei from eight different Z-stacks. For each probe, nuclei were classified as having 1, 2, 3 or > 3 signals. Damaged or overlapping nuclei were not included in scoring.

A similar quantification was performed for γH2AX on more than 3 000 nuclei from two independent experiments.

HyPer-Mito: HyPer-Mito iPSCs plated on coverslips were imaged in two wavelengths (488 and 405) and fluorescence intensity at each wavelength was calculated using IMARIS. Ratiometric quantification of the 488/405 signals was calculated for D21C3 vs T21C5 and a 2-tailed t-test was used to calculate statistical significance.

Chapter 3

Creating a Toolkit for Genetic Dissection of Trisomy 21 Cellular Pathologies

Results: Creating a toolkit for genetic dissection of trisomy 21 cellular pathologies

3.1. Construction of the CRISPR-SpCas9-HF1 plasmids and gRNA efficiency tests

Clustered Regularly Interspaced Short Palindromic Repeats and their associated endonuclease 9 (CRISPR/Cas9) is a ribonucleoprotein complex that forms part of the bacterial and archaeal adaptive immune response (123). Cas9 derived from *S. pyogenes* (SpCas9) can be used as a RNA-guided genome editing endonuclease since it can target any 20bp dsDNA sequence that immediately precedes a 3'-NGG protospacer adjacent motif (PAM) (123).

In this work, a modified High-Fidelity version of the SpCas9 endonuclease (SpCas9-HF1) was co-expressed with a custom gRNA sequence in cultured iPSCs. The high-fidelity variant contains an alteration within one of the four residues that are in direct contact with the phosphate backbone of the target DNA. This alteration reduces the amount of energy available to SpCas9 after gRNA binding, which ensures it has a lower ability to cleave mismatched off-target sites, whilst retaining enough energy for high on-target activity (124).

Once inside the cell nucleus, the gRNA directs SpCas9-HF1 to the target site by Watson-Crick base-pairing. Upon recognition of the PAM, SpCas9-HF1 introduces a site-specific double-strand break (DSB) approximately 3 bp upstream of the PAM site prompting the cell to begin its DNA repair process (125-127). In this case, DNA repair occurs via non-homologous end-joining

(NHEJ), which is error-prone and typically results in insertions or deletions (indels) at the target site (Figure 4).

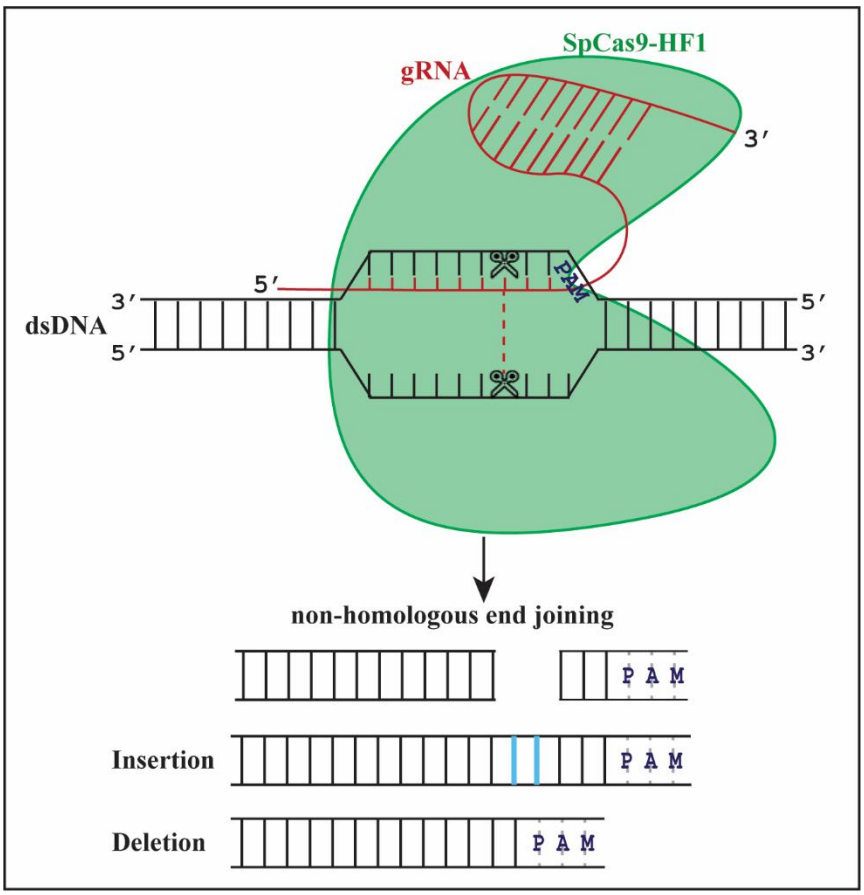

Figure 4: CRISPR/Cas9 genome editing: repair by non-homologous end joining

A schematic diagram depicting the gRNA-SpCas9-HF1 complex and subsequent Watson-Crick base pairing between the target double stranded DNA (dsDNA) and the gRNAs complementary target region (red). Upon gRNA/dsDNA binding, the SpCas9-HF1 endonuclease cleaves the dsDNA three bp upstream of the PAM site. This cleavage initiates DNA repair by non-homologous end joining, which results in insertions or deletions at the target site. The schematic diagram was adapted from (124).

The gRNAs used in this thesis were designed using freely available online tools and selected for their ability to target sequences in early exons of the target gene with no off-target abilities. Correct orientation and successful cloning of the gRNA oligonucleotides in the pCAG-Cas9-HF vector was confirmed by PCR amplification and Sanger sequencing with primers flanking the insertion site (Figure 5A).

The efficiency of Cas9 cleavage at each target site was determined according to the percentage of on-target indels generated following transfection of HEK293T cells. Indels were identified by PCR amplification followed by a series of denaturation and annealing cycles to provoke the formation of heteroduplex strands. These were digested by the T7-endonuclease, which recognises and cleaves imperfectly annealed DNA. Agarose gel electrophoresis of the resulting products demonstrated a pool of full length and cleaved DNA fragments and the genome modification efficiency was calculated according to the following formula: % Gene modification = $100\times(1-(\text{fraction cleaved})^{0.5})$. For each target site, DNA from two different transfections (samples 1 and 2) were analysed alongside their respective negative control in which the T7-endonuclease was not present during digestion.

For each of the four genes, at least one plasmid achieved a gene modification efficiency of greater than 10%, which is sufficient for modification of iPSCs (Figure 5B).

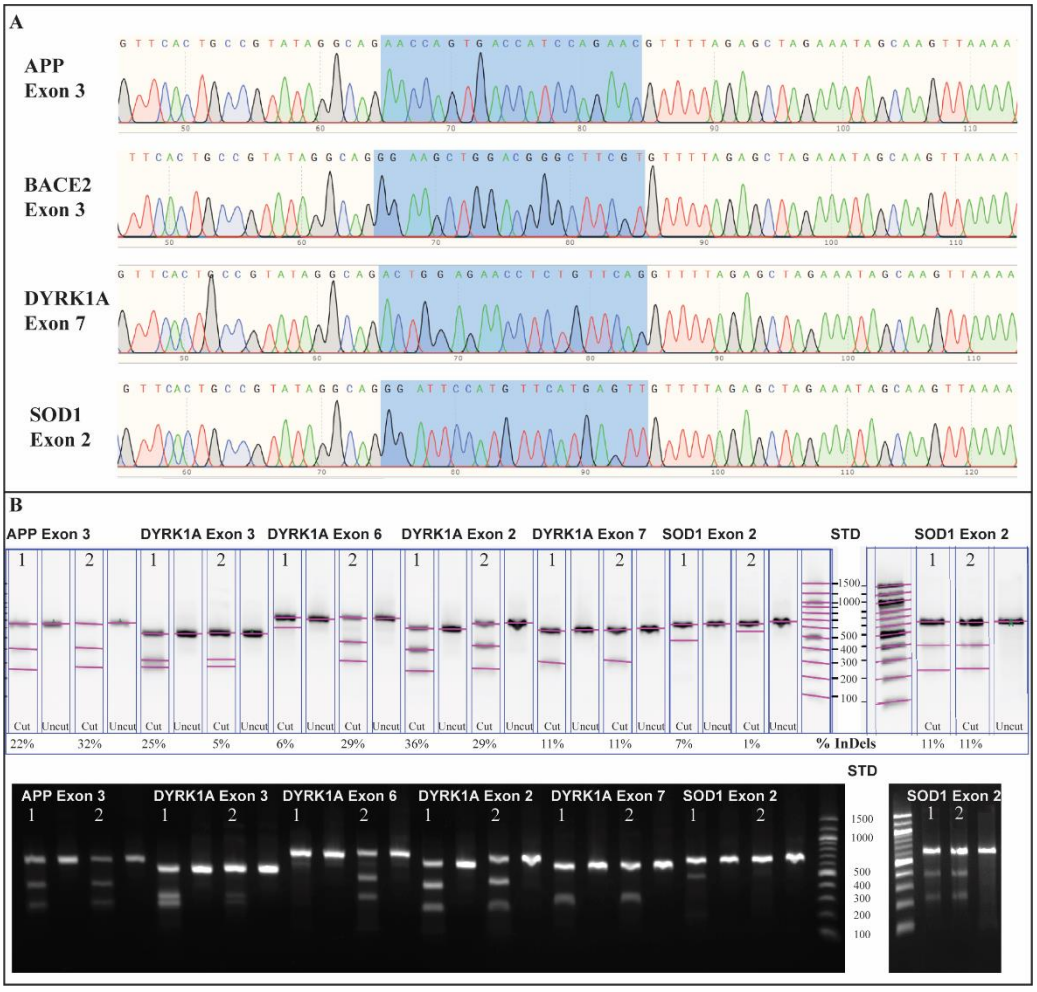

Figure 5: Construction and efficiency of CRISPR-SpCas9-HF1 Plasmids

A: Sanger sequencing results showing cloning and correct orientation of gRNA sequences within the pCAG-Cas9-HF vector plasmid. Only the four selected gRNAs (one per gene) are displayed and were selected for transfection into iPSCs based on their efficiency in HEK293T cells. The gRNA sequence is highlighted in blue.

B: Agarose gel electrophoresis of T7-endonuclease digested PCR products from transfected HEK293T genomic DNA. In the analysis gel (top panel), bands are demarcated by pink lines automatically identified by Image Lab Software (Bio-Rad). Two DNA samples **(1 & 2)**, representing two separate transfections were run adjacent to their respective uncut control (T7 endonuclease negative reaction). The percentage of gene modification for each transfection (**% indel**s) was calculated according to the manufacturer's formula and is displayed in the panel below the analysis gel. For clarity, the originally imaged agarose gels (without band markers and an inverted colour scheme) are displayed below.

3.2. Validating genotype and pluripotency of isogenic iPSCs

CRISPR/Cas9 genome editing was performed on two iPSC lines created from fibroblasts of a patient with constitutional mosaicism (128). These iPSC lines (D21C3 and T21C5) are isogenic with the sole difference between them being the presence of a third copy of HSA21 in T21C5. The trisomic cells reproduce previously described T21-related cellular differences in differentiation, ageing, neurodegeneration, abnormalities in mitochondrial size and number as well as increases in DNA double-strand breaks in neurons (128). HSA21 copy number was validated by interphase FISH using MetaSystems fluorescent probes localising to either HSA21 or HSA13 and counter stained with DAPI. Quantification of nuclei with either 1, 2, 3 or >3 spots was performed automatically using IMARIS software (Figure 6).

The D21C3 iPSCs were disomic for both HSA21 and HSA13, with 93.2% and 95.3% of nuclei displaying two spots for each respective probe. Fewer than 5% of nuclei in this cell line showed greater than or less than two positive signals for either probe. The T21C5 iPSCs were disomic for HSA13 (94.4% nuclei) and trisomic for chromosome 21 (92.92% nuclei). Again, fewer than 5% of nuclei were present in other quantities.

Disomy in D21C3 and trisomy in T21C5 iPSCs was further confirmed by SNP analysis and no other major chromosomal copy number abnormalities were present (Figure 7).

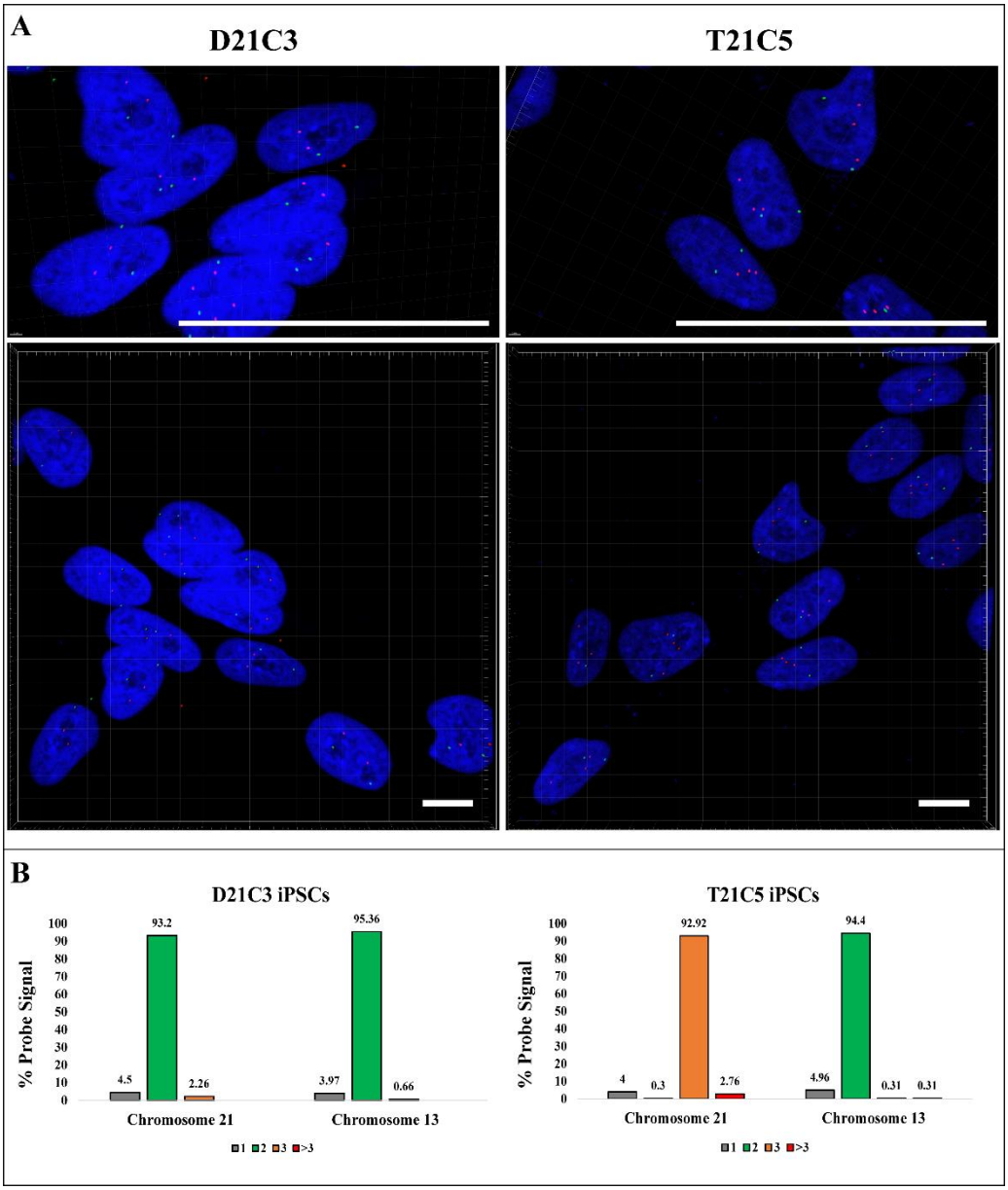

Figure 6: Fluorescent in Situ Hybridisation of isogenic iPSCs

A: Interphase nuclei FISH on D21C3 and T21C5 iPSCs. Fixed cells were probed with MetaSystems Probes for HSA21 (red) and HSA13 (green) and counter stained with DAPI (blue). Fluorescence was captured on Zeiss LSM-800 inverted confocal microscope and processed in IMARIS. Scale bars represent 50 µm.

B: Quantification was performed automatically on 10-13 figures per Z-stack using IMARIS software. Nuclei were counted as having either 1, 2, 3 or >3 spots out of n>500 nuclei per cell line.

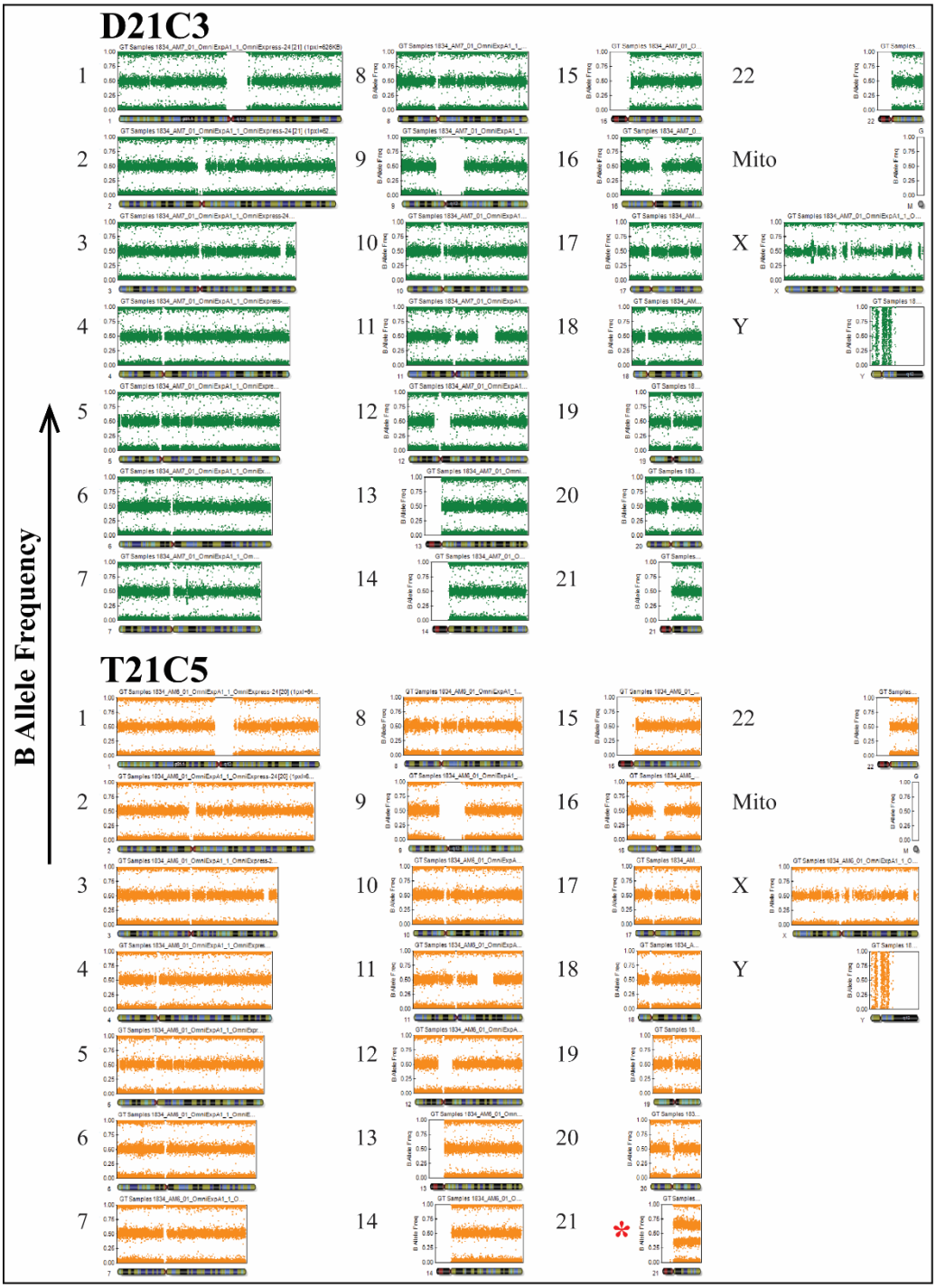

Figure 7: SNP array of isogenic iPSCs

SNP arrays of genomic DNA from D21C3 (green) and T21C5 (orange) iPSCs showing the normalised allelic intensity ratio of the A and B alleles (B-allele frequency). HSA21 B-allele frequencies indicative of trisomy (AAA, AAB, ABB and BBB) were present in T21C5 but absent in D21C3 iPSCs (red asterisk). No other major copy number variations were observed in other chromosomes.

3.3. iPSCs from individuals with partial trisomy 21

Allelic variance, epigenetics and differences in the size and/or the gene composition of the triplicated region are contributing factors to the high levels of phenotypic variation among individuals with DS.

Studies of genotype to phenotype mapping have relied on mouse models of DS and clinical data from humans with pT21 to identify individual dosage sensitive genes or combinations thereof that are responsible for specific DS phenotypes (98, 108, 109, 114, 129).

To allow for high throughput disease modelling, iPSCs were created from two individuals with DS and either pT21 or a HSA21 microduplication. The first iPSC line, called Young Adult 093 (YA093), was created from a male individual with DS caused by pT21 of a region spanning from mid-APP to the telomere (Figure 8C). The second iPSC line, called Critical Region Only 1 (CRO1), was created from a female infant with DS caused by a microduplication of a 4.8 Mb region overlapping the DSCR (Figure 8D).

In both cases consented surplus blood sample collected during routine diagnostic testing was used for PBMC extraction and subsequent erythroblast expansion. CRO1 iPSCs were subject to further genome modification by CRISPR/Cas9 to generate isogenic counterparts necessary for genotype to phenotype studies involving the DSCR. The making of YA093 iPSCs will be discussed below. CRO1 iPSC creation, validation and genome editing is presented in Chapter 4.

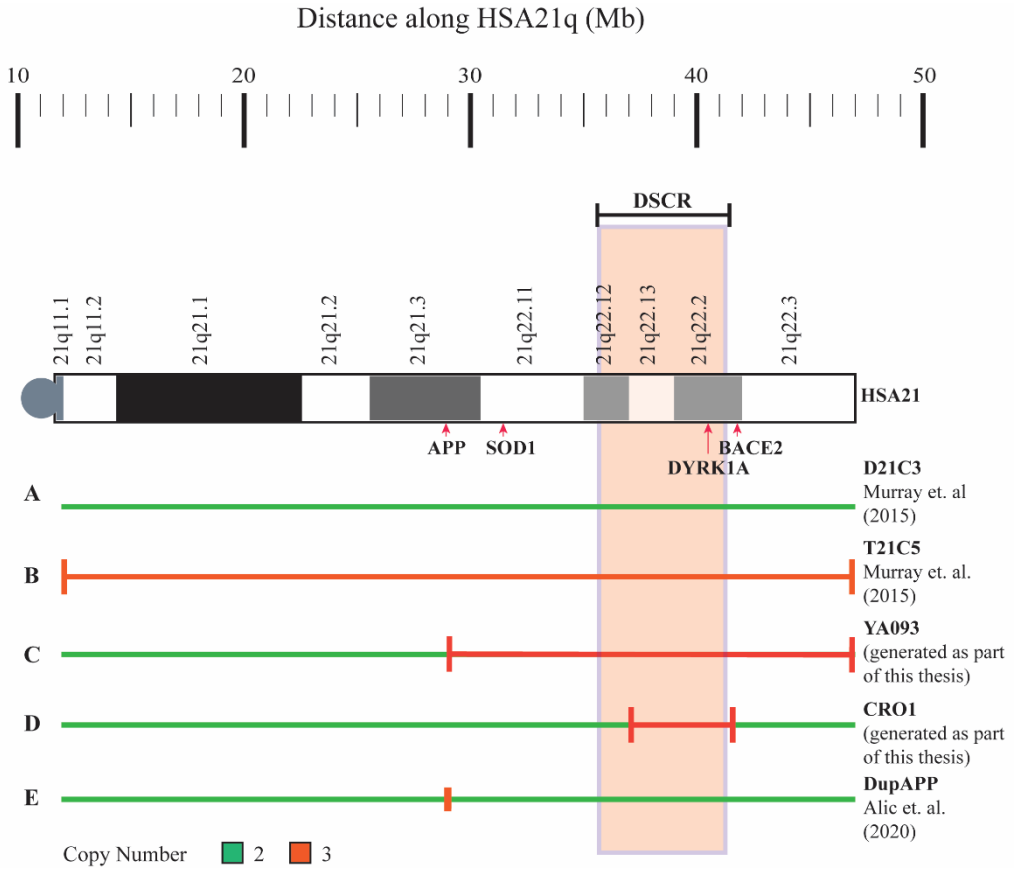

Figure 8: Schematic diagram of the genotypes of iPSCs used in this research.

DSCR (Orange Box): The originally defined minimal region responsible for most phenotypes of DS as defined by Delabar (1993). Genotypes of cells used in this work are indicated below HSA21. Green lines indicate normal disomic gene copy number. Red lines indicate the trisomic region. The original source of the iPSCs is listed on the right.

A&B: isogenic iPSCs generated in the Nizetic lab and published in (130).

C: YA093 iPSCs with pT21 of a region from mid APP to the telomere generated and described in this chapter.

D: CRO1 iPSCs with a microduplication of a region overlapping the DSCR. This region spans from DOPEY2 to PCP4, encompassing the DSCR gene DYRK1A but not DSCR1 (RCAN1) or DSCAM.

E: iPSCs from an euploid individual with a microduplication of *APP* that were generated in the Nizetic lab, published in (131) and utilised in Chapter 5 of this thesis.

To generate the YA093 iPSCs, the small population of erythroblasts within the PBMCs was successfully expanded over a 10-day culture period. The cultures comprised mostly small T-cells and a few monocytes during the first four days of culture. However, the media favours erythroblast proliferation leading to the expansion of large round erythroblasts with a slightly yellow halo (Figure 9A). The erythroblasts were reprogrammed by transiently overexpressing the four "classical" Yamanaka factors using a non-integrating Sendai RNA Virus. iPSCs were selected for based on the morphological features of iPSCs: round cells with large nuclei, prominent nucleoli and scant cytoplasm that grow in colonies with distinct boarders. By passage 7 the picked colonies stained positively for alkaline phosphatase, which is a marker of undifferentiated cells (Figure 9A).

RT-PCR gene expression analysis of undifferentiated passage 7 iPSCs showed complete removal of Sendai virus from clones one and two but not from clone three. This was likely due to the early age (passage number) of the iPSCs and would be diluted out of the cytoplasm in future passages (Figure 9B). Pluripotency of the iPSCs that had lost Sendai virus was confirmed by positive staining for: stage specific embryonic antigen-4 (SSEA-4), tumour-related antigens (Tra)-1-60 and 1-81 and the transcription factor Oct-4, which is involved in the maintenance of pluripotency and self-renewal (Figure 10).

SNP analysis of genomic DNA from YA093 iPSCs confirmed that they retained the duplication spanning from mid *APP* to the telomere that was observed in the patient and no other major chromosomal copy number variations were present (Figure 11).

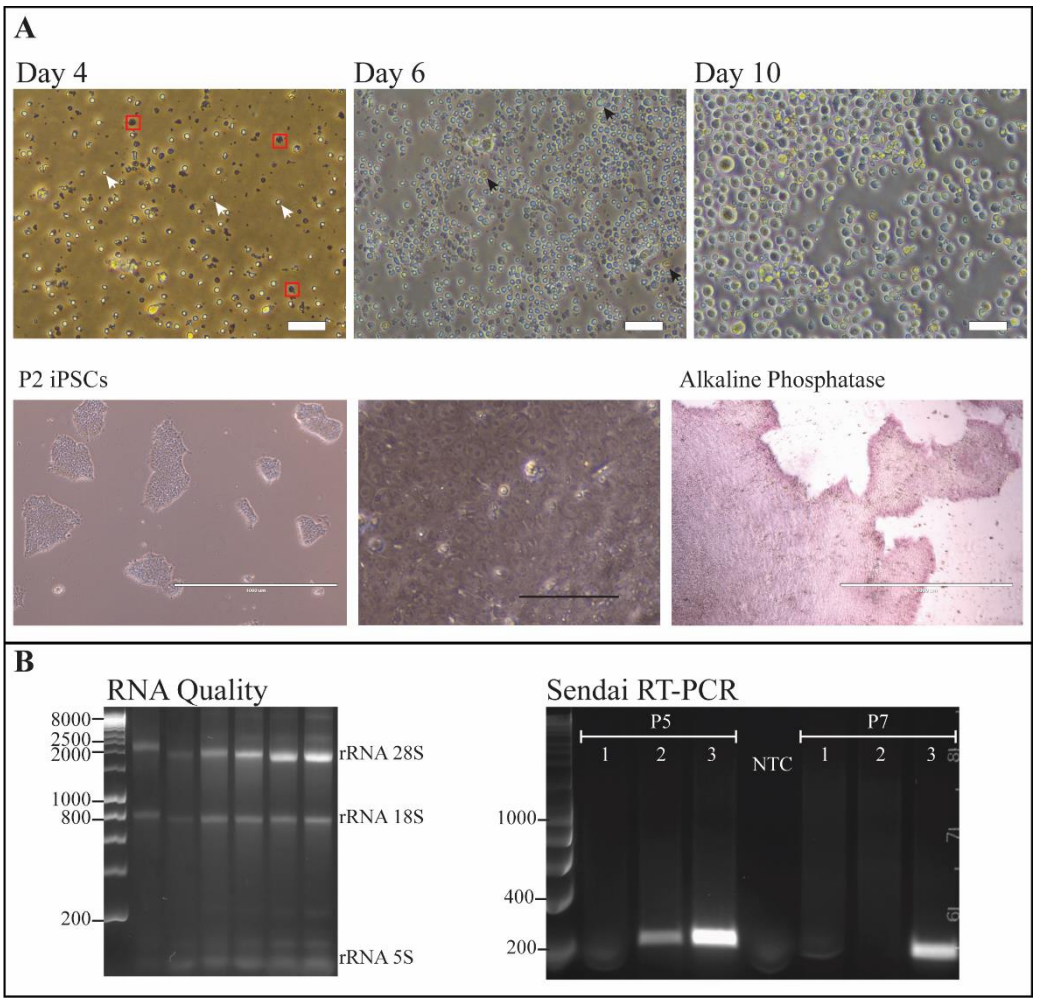

Figure 9: Generating YA093 iPSCs and confirming Sendai removal

A: Expansion of the erythroblast fraction of PBMCs over a 10-day period. **Day 4:** PBMCs are mostly comprised of small T-Cells (white arrows), and monocytes (red box). Debris was present, indicating cell death, which was eventually removed via successive media changes. **Day 6:** erythroblasts (black arrows) expand as T-cells begin to die off. **Day 10:** Successful erythroblast differentiation is seen by many large erythroblasts with a slightly yellow halo. Thick white scale bars represent 50µm. **P2 iPSCs:** iPSCs generated by erythroblast reprogramming display the common morphological features such as growth in colonies with borders (scale bar represents 1000µm). At higher magnification the iPSCs display the common morphological features including large nucleus with prominent nucleolus and scant cytoplasm (scale bar represents 100µm). The cells stained positively with alkaline phosphatase at passage 7 (scale bar represents 1 000µm).

B: RNA extracted from Passage 7 iPSCs was of good quality as determined by agarose gel electrophoresis. RT-PCR for a Sendai virus-specific transcript confirmed complete removal of the virus from clones 1 and 2 by this stage.

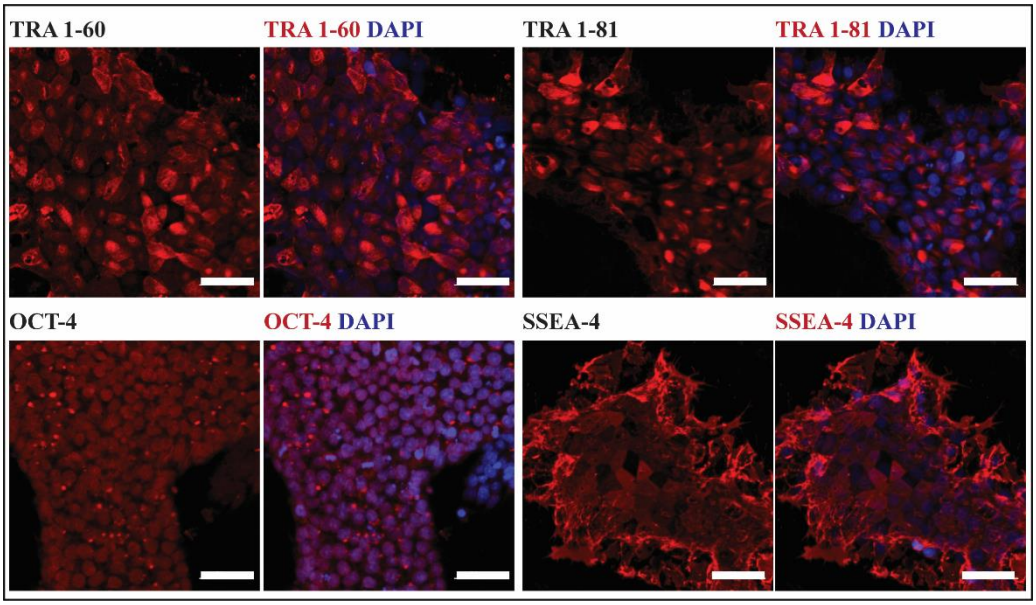

Figure 10: YA093 Pluripotency staining

Representative confocal images of YA093 erythroblast-derived iPSCs immunostained for pluripotency markers. Tra 1-60, Tra 1-81 and SSEA4 are localised to the cell surface, and OCT4 is nuclear. DAPI was used as a nuclear counter stain. Scale bars represent 50µm.

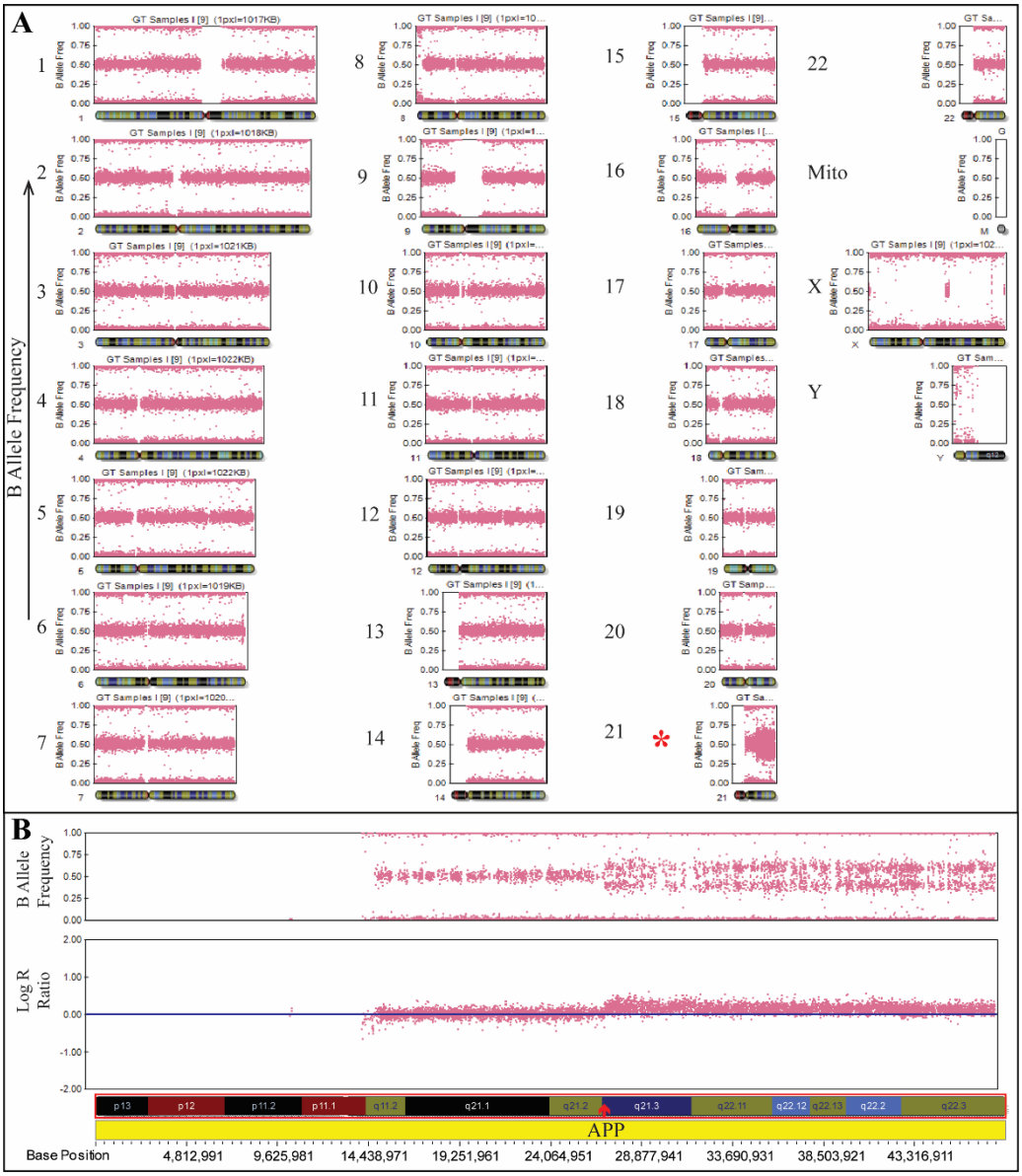

Figure 11: SNP Analysis of YA093 iPSC genomic DNA

A: The normalised allelic intensity ratio of the A and B alleles (B-allele frequency) of genomic DNA from YA093 iPSCs. The presence of a partial duplication of HSA21 is indicated by the presence of AAA, AAB, ABB and BBB frequencies (red asterisk). No other major copy number variations were observed in other chromosomes.

B: Enlarged B-allele frequency and Log R ratio of HSA21. The SNP array for HSA21 in this run was particularly messy as seen in the B-allele frequency. The HSA21 Log R ratio, which measures the copy number changes relative to the reference genome, indicates a $\log_2$ ratio of greater than zero from mid *APP* to the telomere and therefore confirms the presence of pT21 in YA093 iPSCs.

3.4. *APP* CRISPR/Cas9 targeting in isogenic T21 and D21 iPSCs

In non-DS individuals, *APP* duplication causes FEOAD. Conversely, absence of its triplication in individuals with DS caused by distal pT21 or microduplications do not develop AD pathology, which is otherwise present in all individuals with DS (78, 79, 132).

To further study the molecular contributions of APP and its metabolites to AD pathogenesis in DS, the aim was to generate isogenic T21C5 iPSCs with a reduced *APP* gene dose or D21C3 iPSCs with a complete knock-out (KO) of *APP*. Isogenic D21C3 and T21C5 iPSCs were transfected with CRISPR/Cas9 plasmids targeting *APP* exon 3 and successfully transfected iPSCs were selected with blasticidin treatment.

Successful uptake of the plasmid DNA and cell survival after blasticidin treatment was observed in the disomic D21C3 iPSCs but not in the T21C5 iPSCs (Figure 12). Twenty of the surviving colonies were picked for further analysis. Of these, successful on-target genome modification was observed in two parental colonies, one of which (D21C3 *APP* 2) was further sub-cloned by limiting dilution to generate two purified clonal cell lines. The remaining parental colonies produced a wild-type (WT) sequence and were not purified further.

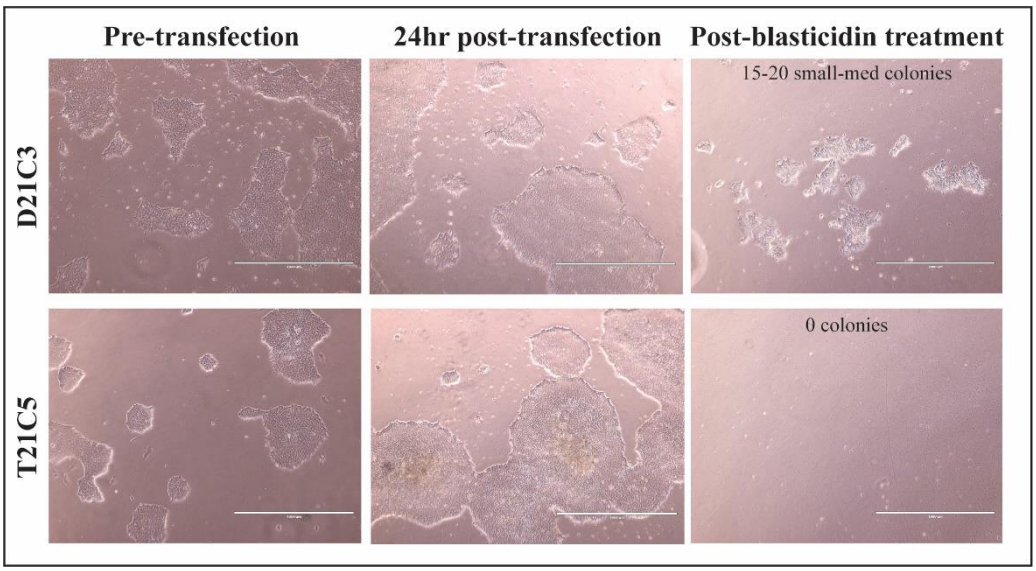

Figure 12: APP CRISPR targeting in D21C3 and T21C5 iPSCs

D21C3 and T21C5 iPSCs transfected with the *APP* CRISPR/Cas9 plasmid were treated with blasticidin for 48 hours to remove untransfected cells and enrich the transfected cell population. D21C3 successfully produced colonies post blasticidin treatment. Twenty of these were picked and sequenced to identify mutations.

Within the D21C3 *APP* 2 parental colony, two clones with on-target mutations were purified and the mutations were confirmed via Sanger sequencing and sequence trace decomposition analysis using the TIDE webtool.

The cell lines, named according to their mutations within *APP* exon 3 are D21C3 *APP KO*Δ16Δ2, which has a deletion of 16 base pair (bp) on one allele and a deletion of 2bp on the other and D21C3 *APP KO*Δ35Δ5, which has a deletion of 35bp on one allele and a deletion of 5 bp on the other (Figure 13A). All 4 deletions cause frame shifts, which lead to premature stop codons (Figure 13B).

This was confirmed by *in silico* analysis of translation and mapped to the cystine rich domain of the APP protein (Figure 14A&B). APP KO was further validated by western blot of iPSC lysates probed with the c-terminal antibody (6E10) (Figure 14C). Maintenance of pluripotency after CRISPR/Cas9-targeting was confirmed by immunofluorescence, using the pluripotency markers previously described (Figure 15).

Since the TIDE graphs did not display the 50:50 ratio that is expected in a disomic cell line, FISH was performed on cerebral organoids generated from these iPSCs for genotype confirmation (Figure 16).

Analysis was performed as in 3.2. In both cases, the iPSCs were disomic for both HSA21 and HSA13, with ≥90% of nuclei displaying two spots for each respective probe. In addition, fewer than 5% of nuclei in either cell line displayed greater than or less than two positive signals for either probe (Figure 16).

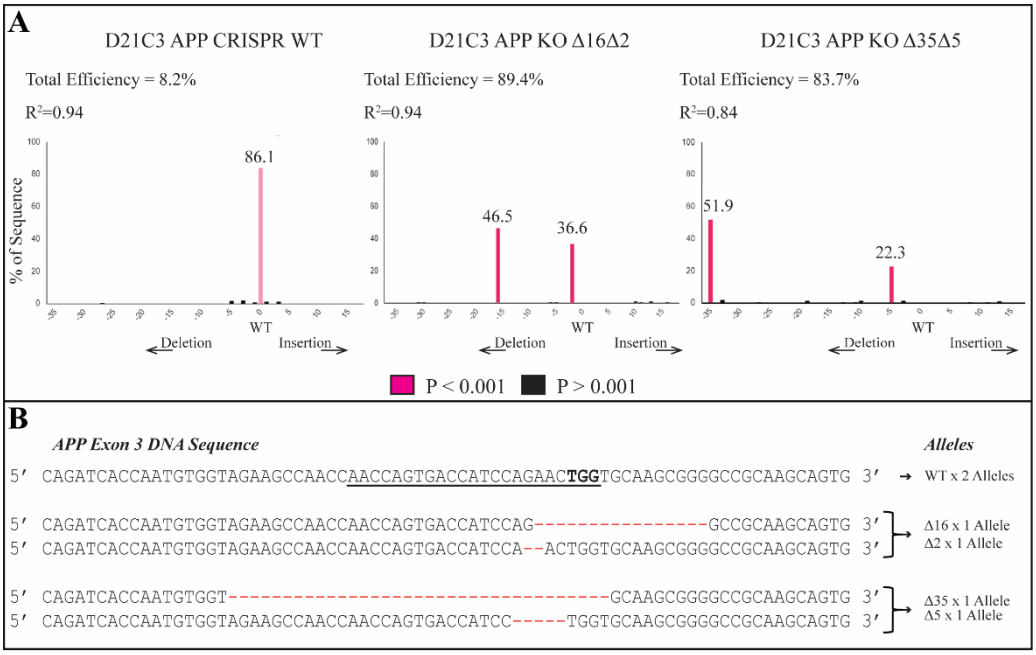

Figure 13: Identification of mutations in the D21C3 APP KO cell lines

A: Graphs generated by the Tracking of InDels by Sequence Trace Decomposition (TIDE) webtool. The graphs display the percentage of the sequence that corresponds with either wild type (**WT**) or a specific indel. D21C3 APP CRISPR WT refers to a clonal cell line that received the CRISPR/Cas9 plasmid but both alleles retained WT sequence. A ratio of 50:50 would be expected for cell lines with two alleles, but the sequences were messy as seen by smaller black peaks, which may explain deviation from this ratio.

B: The sequence of a region of *APP exon 3* is shown for each cell line. The deletion on each individual allele is indicated by red dashes. In the WT sequence, the gRNA sequence is underlined with the PAM in bold.

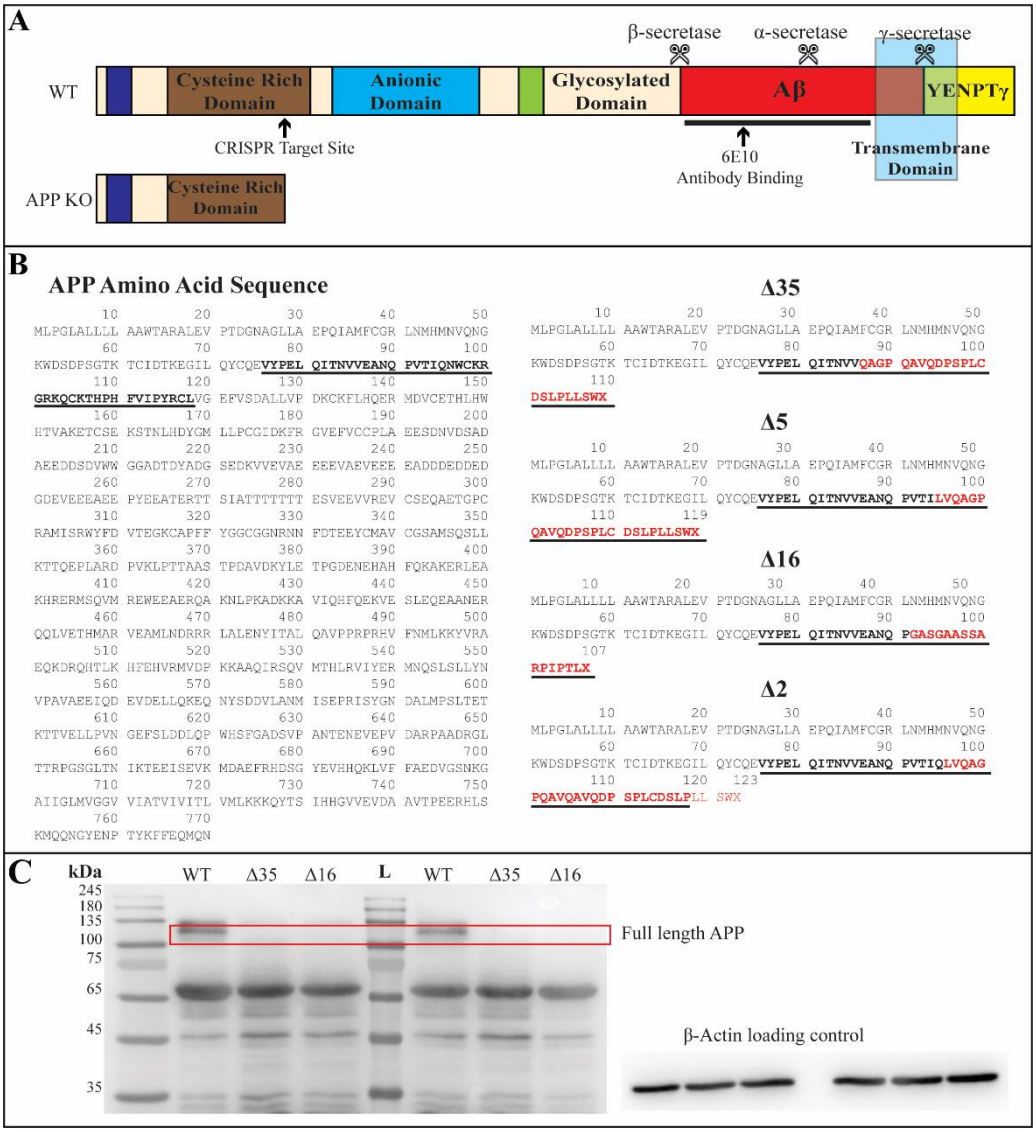

Figure 14: Protein analyis of the D21C3 APP KO cell lines

A: Schematic representation of the protein domain structure of human APP (top). The region in which a premature stop codon would cause a truncated protein falls within exon 3, which codes part of the cystine rich domain.

B: Amino acid sequences arising from WT and mutant alleles. The sequence encoded for by exon 3 is underlined. For each deletion, the resulting amino acid changes are shown in red.

C: Western Blot on iPSC lysates probed for human APP with the c-terminal antibody (6E10). Technical replicates were run on the same gel, separated by a protein ladder (L). The 6E10 antibody recognises both full length APP (Red box) and its metabolites. β-actin was used as a loading control.

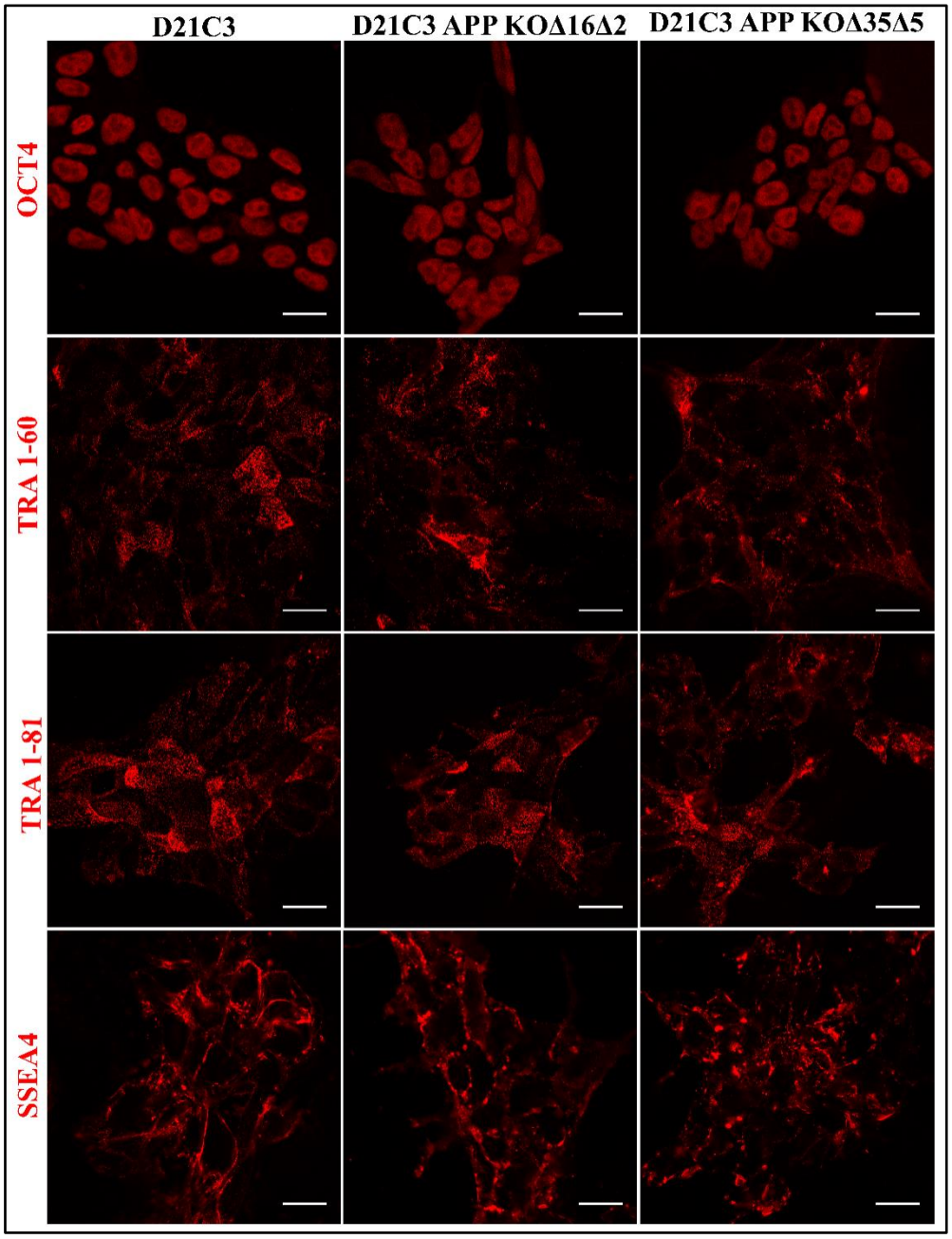

Figure 15: Pluripotency staining of D21C3 APP KO iPSCs

Representative confocal images of the parental D21C3 and the CRISPR/Cas9 edited (D21C3 *APP KOΔ16Δ2* and *APP KOΔ35Δ5*) iPSCs immunostained for markers of pluripotency. Tra 1-60, Tra 1-81 and SSEA4 are localised to the cell surface, and OCT4 is nuclear. Scale bars represent 20µm.

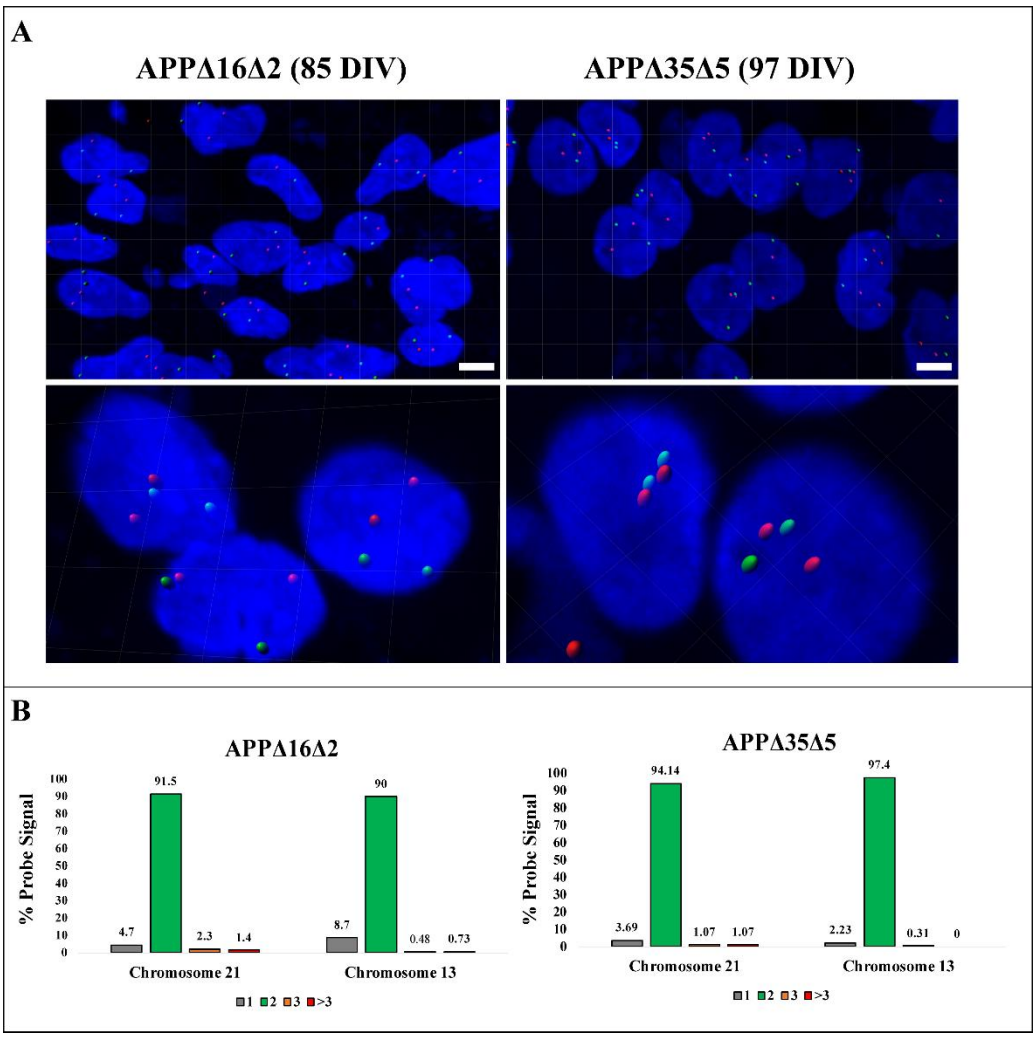

Figure 16: FISH analyis of the D21C3 APP KO cell lines

A: Interphase nuclei FISH on D21C3 *APP KOΔ16Δ2* and *APP KOΔ35Δ5* cerebral organoid slices. Fixed cells were probed with MetaSystems Probes for HSA21 (red) and HSA13 (green) and counter stained with DAPI (blue). Fluorescence was captured on Zeiss LSM-800 inverted confocal microscope and processed in IMARIS. A zoom in of the nuclei showing "Spots" as identified by IMARIS are displayed in the bottom row. Scale bars represent 50 µm.

B: Quantification was performed automatically on 10-13 figures per Z-stack using IMARIS software. Nuclei were counted as having either 1, 2, 3 or >3 spots out of n>500 nuclei per cell line.

3.5. *BACE2* CRISPR/Cas9 targeting in isogenic T21 and D21 iPSCs

BACE2 is a homologue of the gene encoding the widely studied APP cleaving enzyme *BACE1* (β-secretase). The role of BACE2 in APP proteolysis is not fully understood, but reports suggest that in addition to having a β-secretase cleavage ability, it may also prevent Aβ formation (86).

Isogenic D21C3 and T21C5 iPSCs were transfected with CRISPR/Cas9 plasmids targeting *BACE2* exon 3 and selected for by blasticidin treatment. Successful uptake of the plasmid DNA and cell survival after treatment was observed in both D21C3 (with >20 surviving colonies) and T21C5 (with two surviving colonies) (Figure 17).

Twelve colonies from the D21C3 line and both colonies from the T21C5 line were picked and assessed for mutations. No mutations were present in any D21C3 iPSC colonies.

A single T21C5 colony (T21C5 *BACE2* colony 2.3) was identified as having an on-target mutation and was sub-cloned by limiting dilution to produce purified clonal cell lines. One of these purified clonal cell lines harboured a heterozygous mutation on a single allele, thus reducing *BACE2* copy number from three copies to two copies (disomic *BACE2* while maintaining the rest of the chromosome in trisomy). The results relating to the generation and validation of this cell line iPSCs will be discussed in Chapter 5.

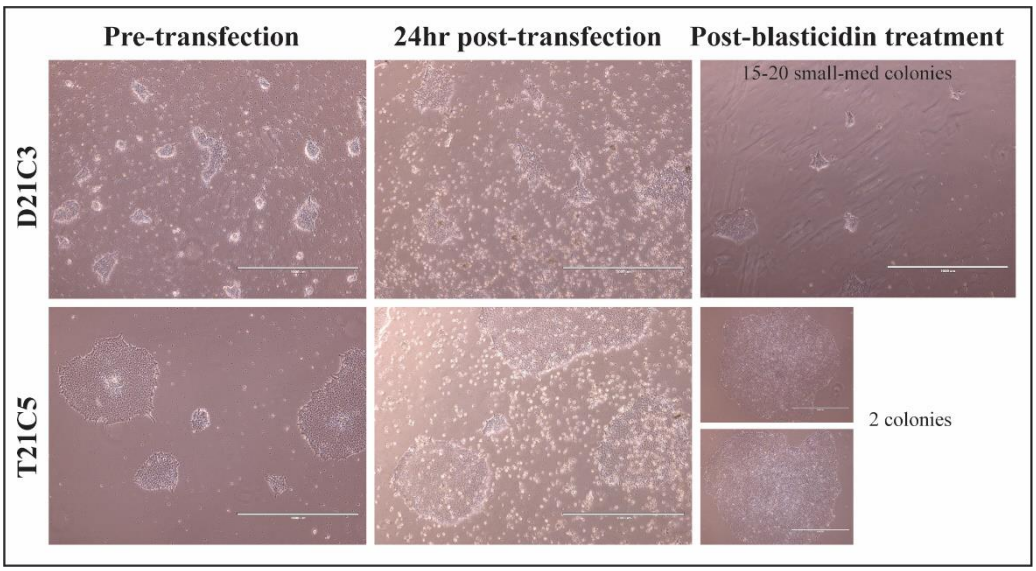

Figure 17: BACE2 CRISPR targeting in D21C3 and T21C5 iPSCs

D21C3 and T21C5 iPSCs transfected with the *BACE2* CRISPR/Cas9 plasmid were treated with blasticidin for 48 hours to remove untransfected cells and thus enrich the transfected iPSC population. Both D21C3 and T21C5 iPSC lines successfully produced transfected colonies, which were picked and sequenced to identify on target mutations.

3.6. *DYRK1A* CRISPR/Cas9 targeting in isogenic T21 and D21 iPSCs and the CRO1 iPSCs

The Dual Specificity Tyrosine Phosphorylation Regulated Kinase 1A (DYRK1A) displays a 1.5-fold increase in expression levels in DS (133). This kinase phosphorylates numerous targets involved in a range of biological processes, including cell cycle progression, gene transcription, mRNA splicing and brain development among others (134-136). Its excess (as seen in DS) has been linked to intellectual disability (137) whereas its deficit (as seen in DYRK1A haploinsufficiency syndrome) has been linked to intellectual disability, microcephaly, autism and epilepsy (138-140).

To better understand the underlying molecular changes attributed to its triplication, D21C3, T21C5 and CRO1 iPSCs were targeted with the *DYRK1A* exon 7 CRISPR/Cas9 plasmid. Three clones with different *DYRK1A* copy numbers were produced from T21C5 iPSCs, a single KO cell line was produced from D21C3 iPSCs, and two *DYRK1A* reduced clonal cell lines were generated from CRO1. Cell lines pertaining to CRO1 iPSCs will be discussed in Chapter 4.

Exon 7 encodes a region within the kinase domain, hence if a truncated protein is present, a premature stop codon at this site would render the kinase function of DYRK1A non-functional (Figure 18A).

CRISPR/Cas9 targeting of T21C5 iPSCs produced two trisomic *DYRK1A* knock out cell lines, which are referred to as T21C5 *DYRK1A* KO 1 & 2 and one heterozygous DYRK1A KO, which reduces DYRK1A copy number from 3 to 1.

Sanger sequencing of the target site in each clonal cell line revealed that T21C5 *DYRK1A* KO 1 has a single nucleotide insertion on two alleles and a single nucleotide deletion on the third allele, T21C5 *DYRK1A* KO 2 has a deletion of 4 nucleotides one allele and insertions of 1 and 2 nucleotides on the remaining two alleles respectively and T21C5 *DYRK1A* het has one normal allele and 1 and 2 nucleotide insertions on the other two respective alleles (Figure 18B).

TIDE analysis of the PCR-amplified target sites confirmed the presence of these mutations. In addition, TIDE and SNP analysis confirmed that all three iPSC lines maintained their trisomy (Figure 18C). SNP arrays for the full genome were compared with the parental T21C5 iPSC line and were identical in all four samples indicating no major off target effects.

To ensure preservation of pluripotency after CRISPR/Cas9-targeting the T21C5 *DYRK1A* het and T21C5 *DYRK1A* KO 1 iPSCs were stained for the pluripotency markers as previously described (Figure 19).

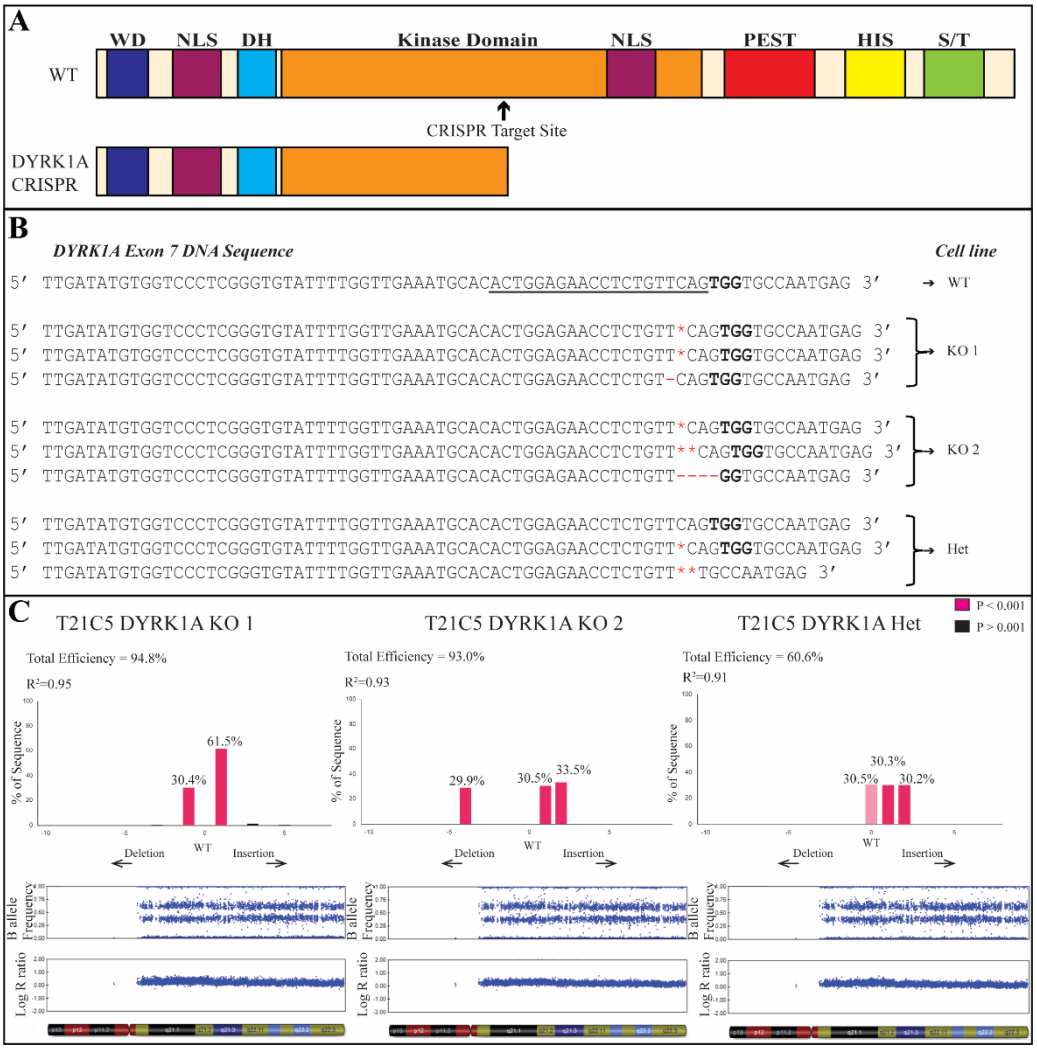

Figure 18: Trisomic DYRK1A Het and KO iPSCs

A: A schematic representation of the protein domain structure of human DYRK1A (Top) adapted from (141). The region in which a premature stop codon would prevent further translation is indicated below the full-length protein. Exon 7, which was targeted by CRISPR/Cas9, falls within the kinase domain. **WD**: binding motif to adaptor WD40 repeat domain proteins, **NLS**: Nuclear Localising Signal, **DH**: DYRK Homology region, **PEST**: Proline-glutamic acid-serine-rich domain, **HIS**: consecutive histidine repeat, **S/T**: Serine/Threonine rich domain.

B: *DYRK1A* exon 7 sequence indicating the gRNA (underlined) and the PAM site (bold). For each of the CRISPR/Cas9 edited iPSC lines, deletions are indicated by red dashes and insertions are indicated by red asterisks. Both *DYRK1A* KO1 and KO2 have mutations on all three alleles and *DYRK1A* Het has two mutated and one normal allele.

C: TIDE analysis of the PCR amplified *DYRK1A* exon 7 target sites in T21C5 *DYRK1A* *DYRK1A*-targeted iPSCs. Graphs indicate the percentage of sequence corresponding to each mutation. In all three cases, mutations make up approximately one third of the total sequence trace, which is expected in trisomic cells. The corresponding HSA21 SNP array below confirms T21 was maintained in all three cell lines.

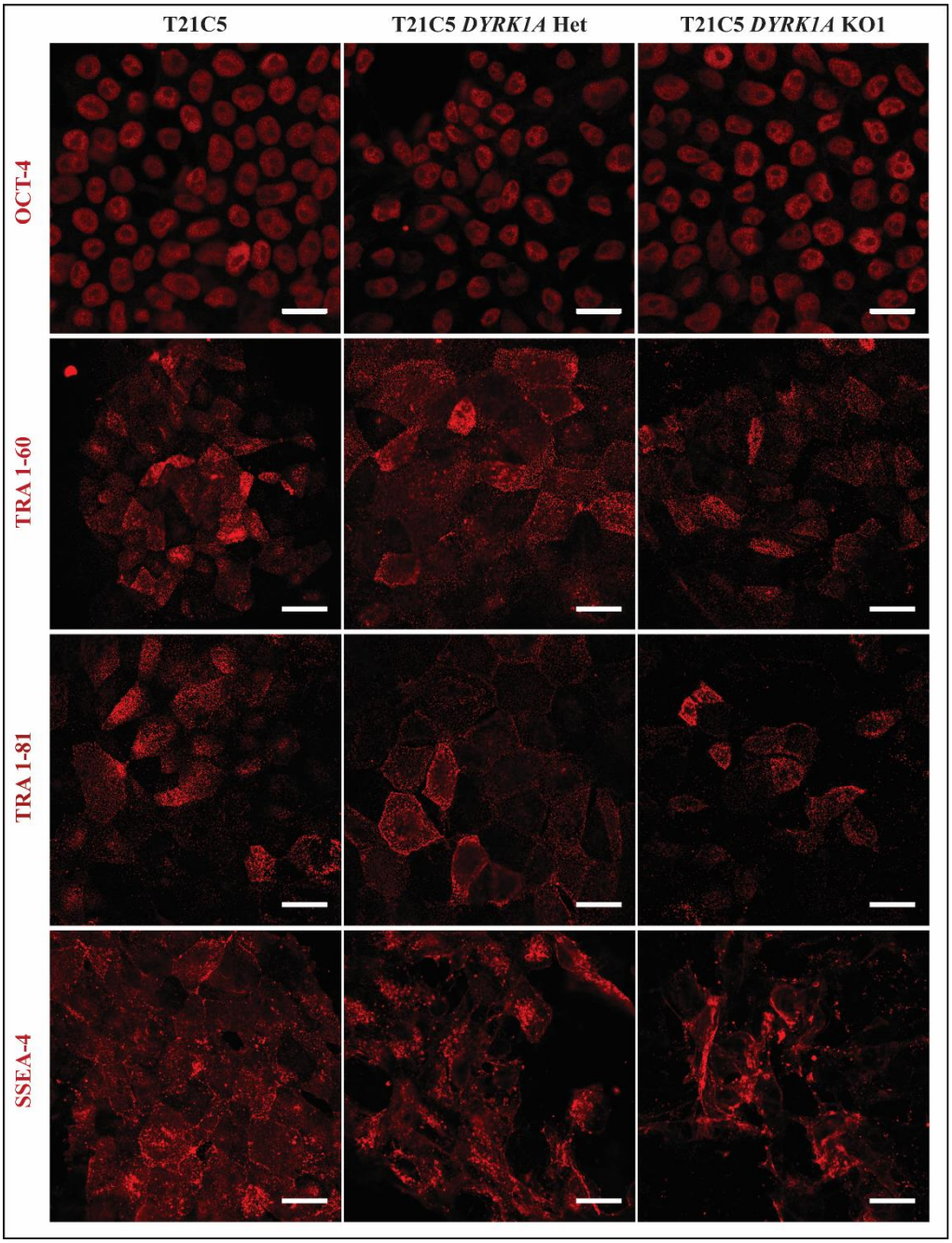

Figure 19: Pluripotency T21C5 DYRK1A het and T21C5 DYRK1A KO 1 iPSCs

Representative confocal images of the parental T21C5 and the CRISPR/Cas9 edited (T21C5 DYRK1A het and T21C5 DYRK1A KO1) iPSCs immunostained for markers of pluripotency. Tra 1-60, Tra 1-81 and SSEA4 are localised to the cell surface, and OCT4 is nuclear. Scale bars represent 20µm.

Next, to identify whether this isogenic system allows for further study of human neurodevelopment in DS, the parental T21C5 iPSCs, T21C5 *DYRK1A* het and T21C5 *DYRK1A* KO 1 iPSCs were differentiated into NSCs according to the protocol outlined in Chapter 2-2.3.2 as well as COs according to the protocol outlined in Chapter 2-2.3.3. Successful differentiation into NSCs was achieved in all three cell lines as indicated by positive staining for SOX2, Nestin and Pax6, which are markers of neural stem cells (Figure 20A).

Additionally, the T21C5 *DYRK1A* het and T21C5 *DYRK1A* KO 1 iPSCs were able to form COs with SOX2 positive NSCs and Tubulin β-3 (TUBB3) positive neurons at 30DIV (Figure 20B).

Both NSCs and COs demonstrate some differences in the presence, patterns and morphology/distribution of markers of neural differentiation as a function of *DYRK1A* dose.

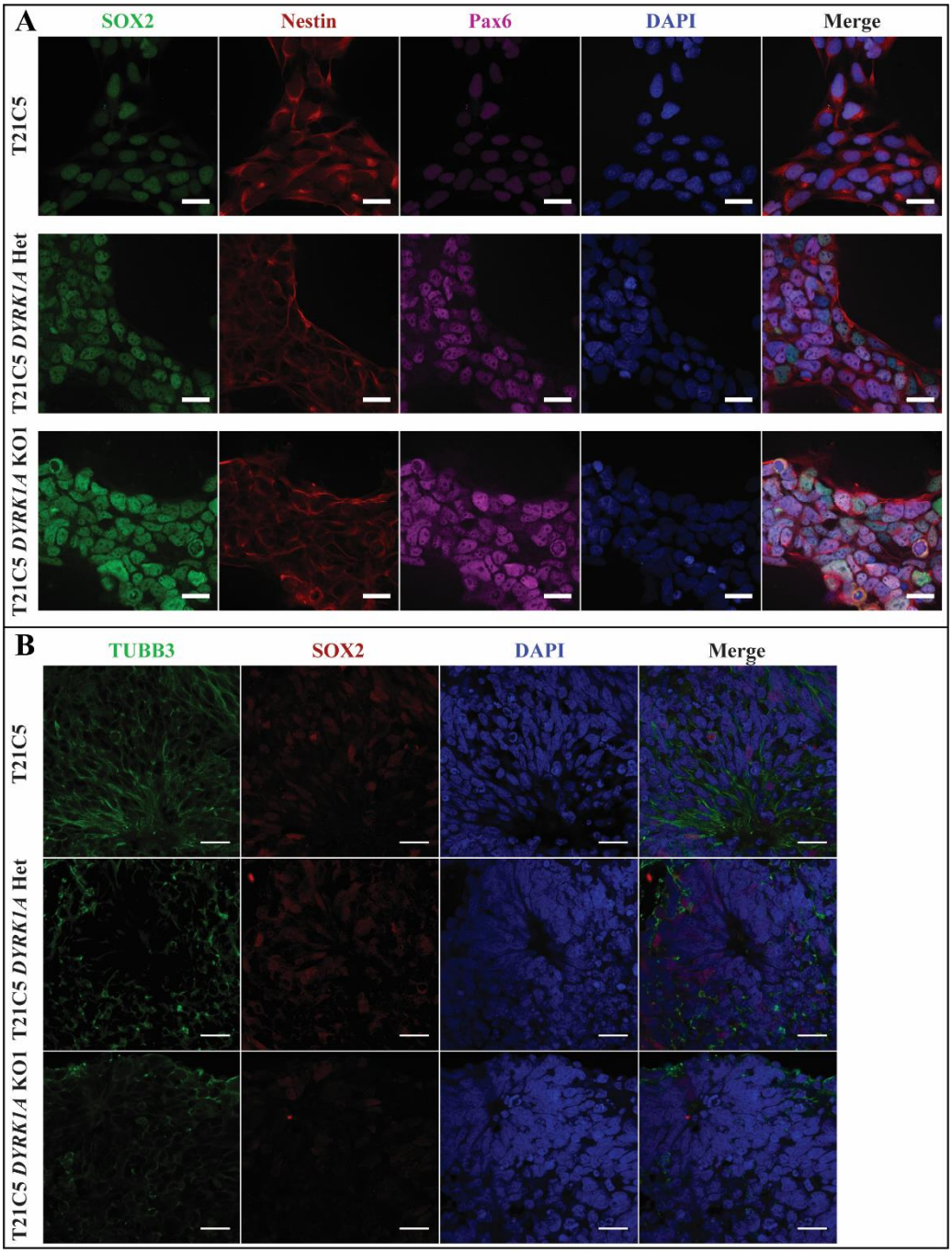

Figure 20: Neural differentiation of isogenic T21C5 and CRISPR/Cas9 edited DYRK1A iPSCs

A: Representative confocal images of the parental T21C5 and the CRISPR/Cas9 edited (T21C5 DYRK1A het and T21C5 DYRK1A KO1) iPSCs immunostained for the NSC markers SOX2, Nestin and Pax6. DAPI was used as a nuclear stain. Scale bars represent 20µm.

B: Representative confocal images of 30DIV COs generated from the parental T21C5 and the CRISPR/Cas9 edited iPSCs stained for SOX2 and TUBB3. DAPI was used as a nuclear stain. Scale bars represent 20µm.

CRISPR/Cas9 targeting of D21C3 iPSCs produced a disomic knockout cell line (hereafter referred to as D21C3-*DYRK1A* KO). This cell line contains an on-target single base pair insertion on both alleles, which leads to non-sense amino acid changes. Sanger sequence analysis identifies these as an insertion of a thymine on one allele and an adenine on the other. TIDE analysis indicated that 99.5% of the sequence trace contained a single base pair insertion, confirming that both alleles were edited, and no other mutations were present in this region (Figure 21A).

SNP analysis of this iPSC line revealed a culture-induced duplication of chromosome 17, rendering the cell line not suitable for further use. (Figure 21B).

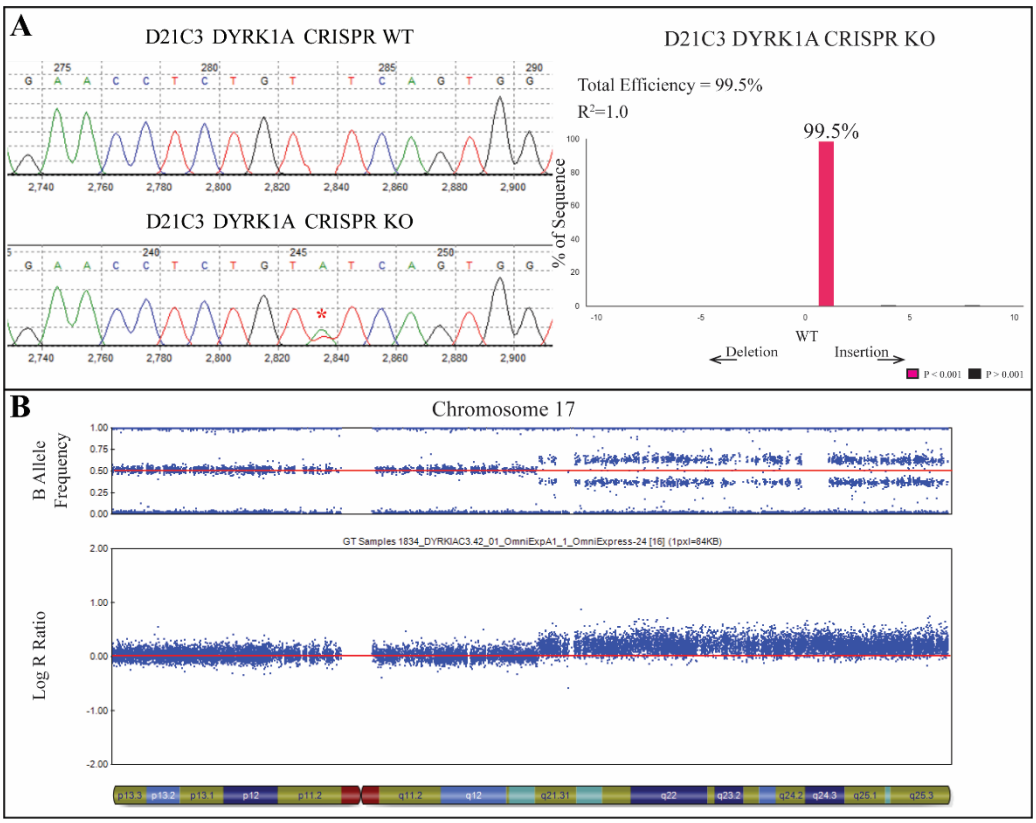

Figure 21: Disomic DYRK1A CRISPR KO validation

A: Sanger sequencing of the PCR amplified *DYRK1A* exon 7 target site and subsequent TIDE analysis. This cell line contains a single base pair insertion (Red asterisk), which causes non-sense amino acid changes. TIDE analysis revealed that a single base pair insertion is present in 99.5% of the sequence trace.

B: SNP analysis of genomic DNA extracted from D21C3 *DYRK1A* KO iPSCs revealed an acquired duplication of chromosome 17, which was likely caused by culture-induced cellular stress. This is indicated by the presence of AAA, AAB, ABB and BBB alleles in the B-allele frequency of HSA21 as well as a $\log_2$ ratio of greater than zero from mid HSA17 to the telomere.

3.7. *SOD1* CRISPR/Cas9 targeting in isogenic HyPer tagged T21 and D21 iPSCs

SOD1 encodes the scavenger enzyme Cu, Zn-superoxide dismutase, which is known for its ability to convert superoxide radicals to hydrogen peroxide and oxygen (57). Since individuals with DS have 3 copies of this gene, it has been proposed that increased SOD1 levels result in overproduction of hydrogen peroxide, which may be a contributing factor to the observed increased oxidative damage in DS (61).

To better study the differences in hydrogen peroxide levels between D21C3, T21C5 and iPSCs with genetically altered levels of *SOD1*, the isogenic iPSCs were tagged with stably expressing Hydrogen Peroxide (HyPer) sensors. These are genetically encoded fluorescent probes that allow one to detect changes in intracellular hydrogen peroxide (H_2O_2) levels.

HyPer was derived from insertion of the circularly permuted yellow fluorescent protein (cpYFP) into the regulatory domain of the bacterial transcription factor OxyR (142). It is excited by wavelengths of 400-420 (blue spectrum) and 488-500 nm (green spectrum), which correspond to the protonated and deprotonated form of cpYFP respectively (143). Upon exposure to H_2O_2, the cpYFP domain becomes deprotonated resulting in a proportional decrease in the blue spectrum excitation peak and an increase in the green spectrum excitation peak.

For the purpose of this work, HyPer was localised to either the mitochondria (HyPer-Mito) or the cytoplasm (HyPer-Cyto). In parallel, iPSCs were tagged with eGFP, which was a positive control for transduction efficiency.

Transduced iPSCs expressing eGFP or HyPer were purified by FACs. HyPer cells were sorted based on their excitation in the green spectrum. To ensure only undifferentiated iPSCs were collected, Tra-1-81 was used as a counter stain and double positive live cells were collected for expansion and cryopreservation. The gating strategy remained constant between disomic and trisomic cell lines to avoid selection bias (Figure 23A). Confocal microscopy of the transduced iPSCs confirmed successful tagging as well as correct localisation of each of the HyPer sensors (Figure 22B).

Correct localisation of HyPer-Mito was further confirmed by counter staining iPSCs with the mitochondrial protein: apoptosis-inducing factor (AIF) (Figure 23).

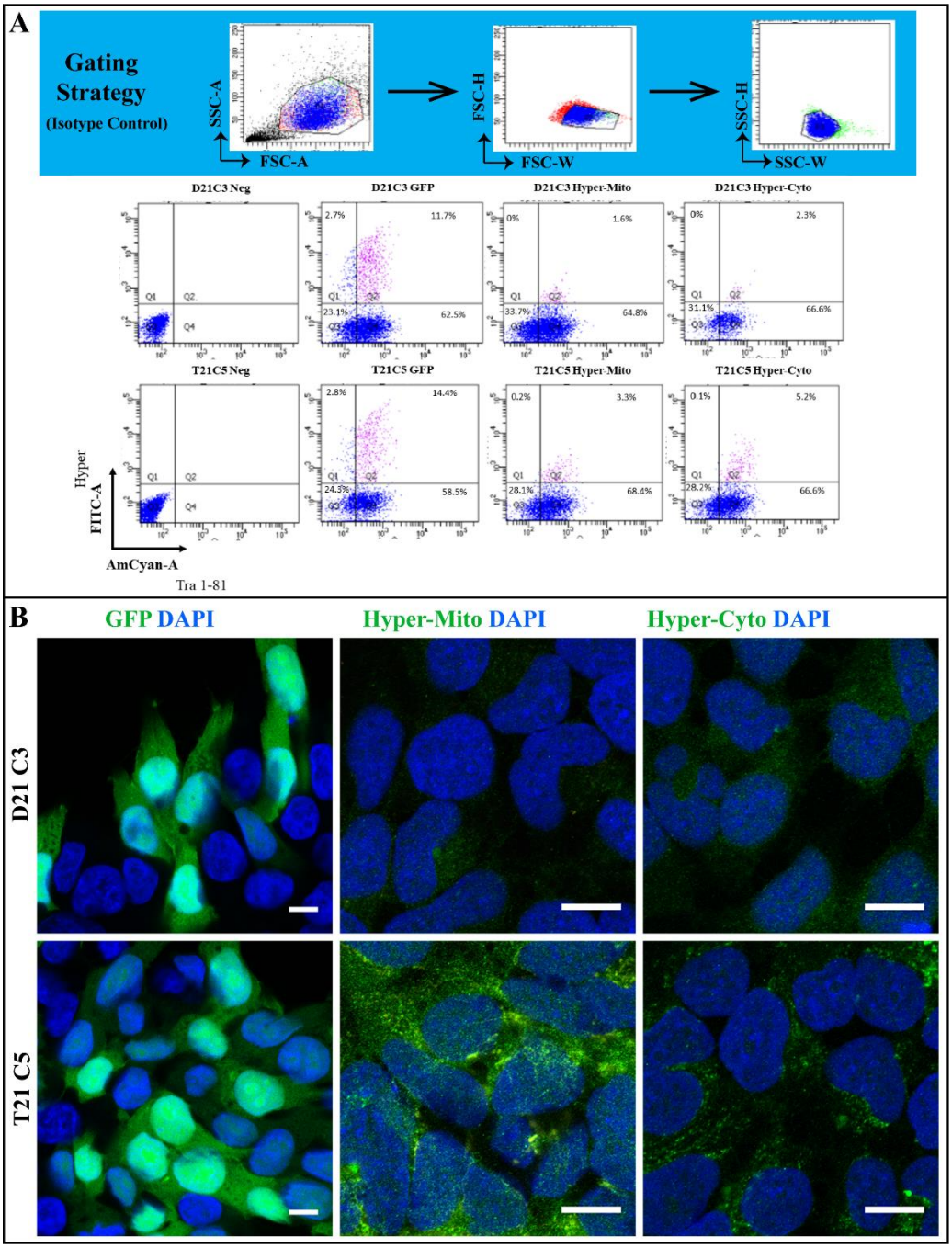

Figure 22: Confirming the presence and localisation of GFP and HyPer proteins in iPSCs

A: Fluorescence activated cell sorting of HyPer and eGFP tagged iPSCs. iPSCs were stained with the pluripotency marker Tra-1-81 and sorted for double positive expression. The gating strategy (blue panel) remained constant for both cell lines to prevent selection bias. First, the live cell population was selected based on size and complexity (FSC-A vs SSC-A). Next doublets were excluded by FSC-H vs FSC-A and SSC-A vs SSC-H. Acquired cells were collected and plated on Matrigel coated plates.

B: To confirm successful tagging, GFP and HyPer signal was assessed by fluorescence microscopy on fixed iPSCs. Fluorescence signal is not present in all cells as images were captured prior to FACS sorting. Scale bars represent 10µm.

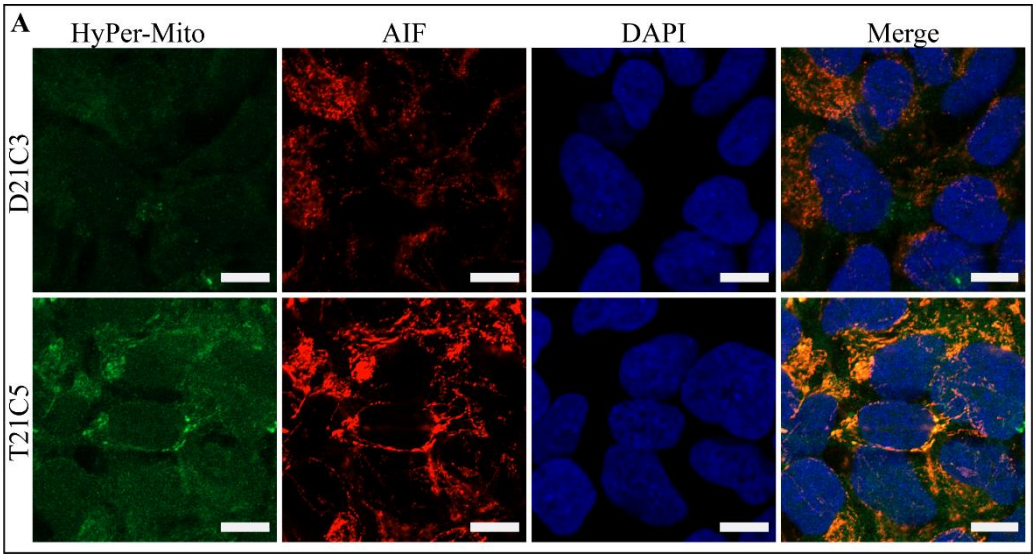

Figure 23: HyPer-Mito colocalization with the mitochondrial protein: AIF

A: Representative fluorescent images of HyPer-Mito co-stained with the mitochondrial protein: Apoptosis-Inducing Factor (AIF). Co-localisation of HyPer-Mito and AIF indicates mitochondrial localisation of HyPer fluorescence.

Since initial images showed increased HyPer-Mito signal in T21C5 compared with D21C3 iPSCs, further ratiometric analysis was performed and baseline differences in H_2O_2 levels between cell lines was investigated.

HyPer fluorescent protein was excited by wavelengths of 405 nm (blue) and 488 nm (green). Since DAPI falls within the blue spectrum, nuclei were counter stained with DRAQ5 (647 nm). The mean fluorescent intensities of the total green and blue volumes were quantified automatically by IMARIS. The ratiometric quantification of the fluorescence excited by the 488 nm and 405 nm lasers (488/405) revealed that T21C5 iPSCs contained significantly higher mitochondria localised H_2O_2 levels compared with D21C3 iPSCs ($P<0.001$). Statistical significance was calculated by a 2-tailed t-test (Figure 24). HyPer-Cyto was not studied further.

This is, to our knowledge, the first demonstration that this predicted cellular phenotype (increased mitochondria localised H_2O_2) can be reproduced and therefore modelled in undifferentiated iPSCs.

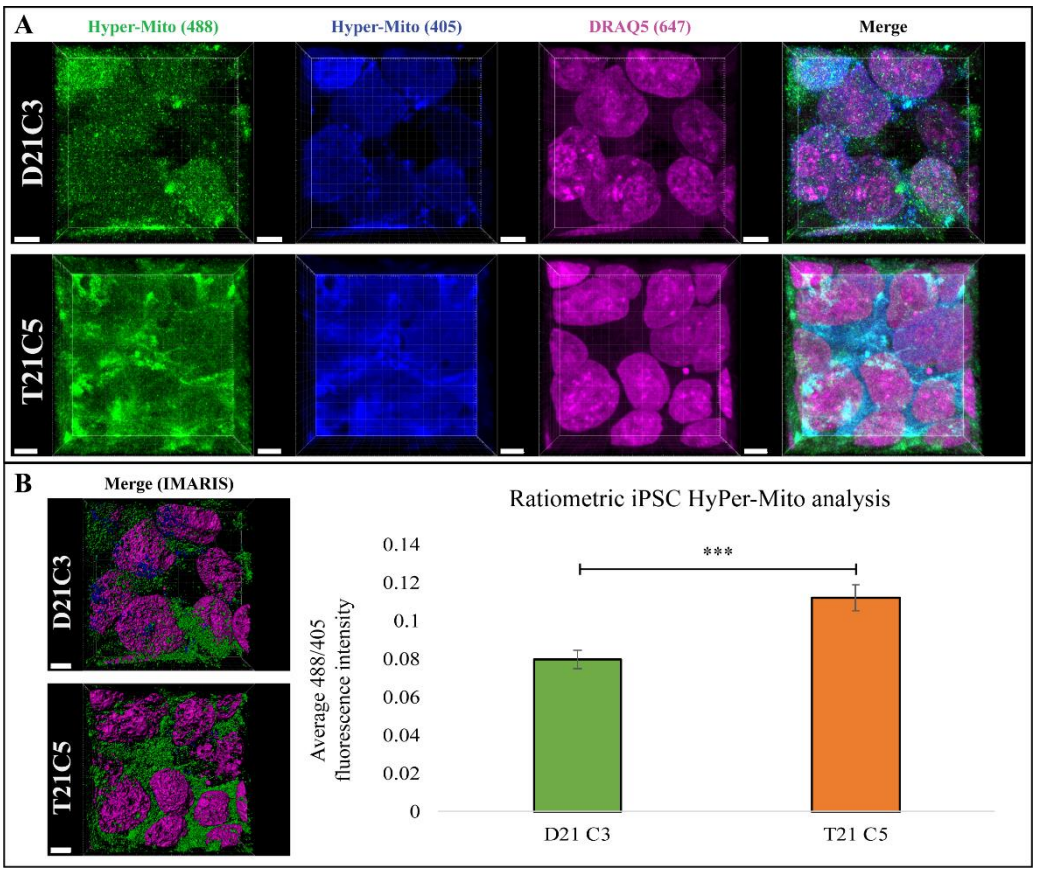

Figure 24: Ratiometric analysis of HyPer-Mito in isogenic iPSCs

A: Representative confocal images of D21C3 and T21C5 iPSCs stained with the nuclear dye DRAQ5. HyPer fluorescence was excited at wavelengths of 488 and 405 nm. Scale bars represent 5µm.

B: Images were processed in IMARIS for quantification of the mean fluorescence intensity of the total green (488) and blue (405) "surfaces" (Right). More than 5000 cells were analysed from a total of 10 images from three experiments. For each cell line, a ratiometric calculation of the signal intensities (488:405) was performed as specified for this sensor. T21C5 iPSCs contained significantly more mitochondria localised H_2O_2 compared with D21C3 iPSCs. Statistics were calculated using a 2-tailed t-test. Scale bars represent standard error.

Both D21C3 and T21C5 HyPer-tagged iPSCs were targeted with the *SOD1* exon 2 CRISPR/Cas9 plasmid but only D21C3 produced a genetically modified clone (hereafter referred to as D21C3 *SOD1*Δ6). This clone has a heterozygous 6bp deletion of exon 2 that removes two amino acids (Figure 25).

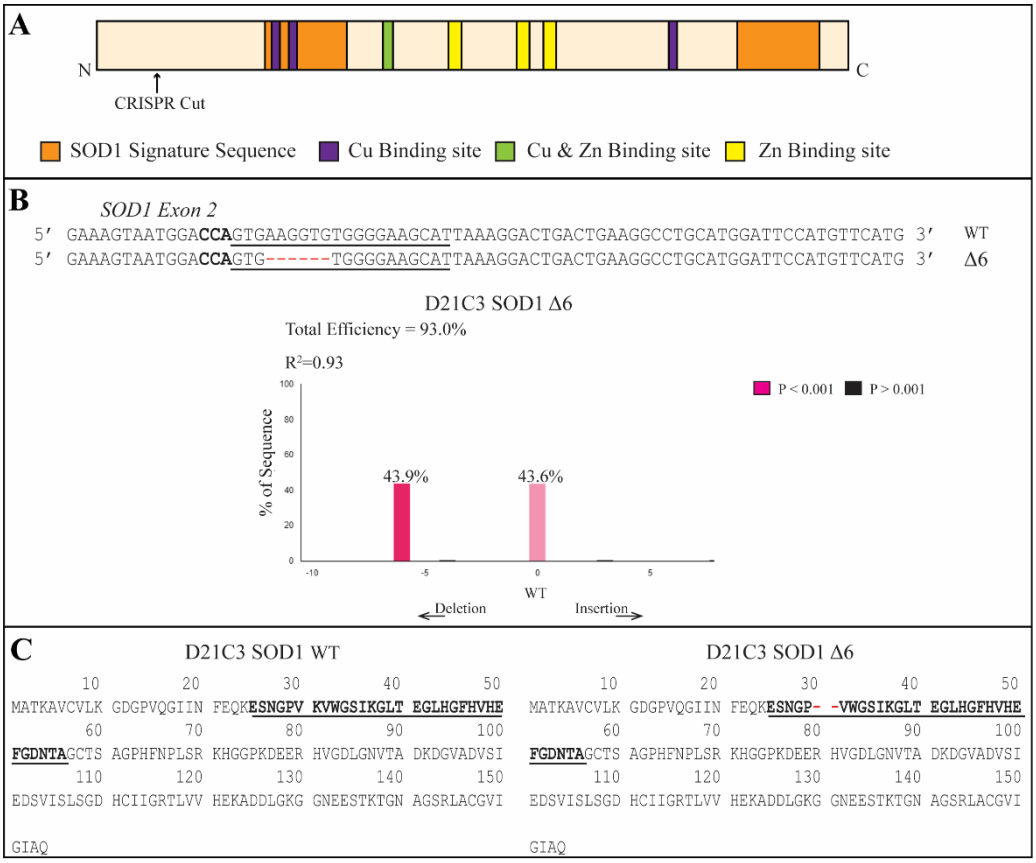

Figure 25: SOD1 CRISPR/CAS9 in D21C3 HyPer-Mito iPSCs

A: A schematic representation of the protein domain structure of mammalian SOD1 identified using the UniProtKB database (https://www.uniprot.org/uniprot/P00441). Exon 2 is located before any major Cu/Zn bunding sites.

B: The DNA sequence of *SOD1* exon 2 (top) showing the WT and edited (Δ6) sequences. The gRNA is underlined with the PAM site in Bold. The deleted nucleotides are replaced with the red dashes. Sanger sequencing of the PCR amplified target site analysed by TIDE indicates 43.9% of the sequence harbours the 6bp deletion while 43.6% of the sequence remains WT.

C: *In silico* analysis of the amino acid sequence produced by the WT and edited DNA sequences. Exon 2 is underlined. The two deleted amino acids in D21C3 *SOD1*Δ6 are indicated by red dashes.

3.8. Summary and Discussion

For a clean dissection of the relationship between gene copy number and phenotypes related to neurodevelopment, accelerated ageing and Alzheimer's Disease, a panel of genetically modified iPSCs with isogenic controls were generated. CRISPR/Cas9 gene editing techniques were optimised to target relevant HSA21 genes (*APP, BACE2, DYRK1A* and *SOD1*) in iPSCs from individuals with clinically diagnosed DS. These iPSCs provide a toolkit for further genetic dissection of T21-related cellular pathologies. This system was first employed on a unique set of isogenic iPSCs from an individual with constitutional mosaicism for T21 (D21C3 and T21C5) (128). Additional iPSCs were generated from two individuals with DS caused by pT21 to further dissect the contribution of gene segments to HSA21-related pathologies.

The main goal of CRISPR/Cas9 modification was to generate a cell line in which a single copy of the gene of interest was edited, reducing its gene dose to disomic levels. This was achieved for *BACE2* and the iPSCs were studied further (Chapter 5). The generation of iPSCs with gene KO's were a by-product of working towards this aim and these cell lines are useful tools for investigating gene function. All iPSC lines described in this chapter are listed in Figure 26 and their potential use is outlined below.

For each cell line studied further in this thesis (BACE2 and DYRK1A), the top 10 off-target sites of that gRNA (as identified using the freely available webtool: CCTOP (144)) was amplified and screened for mutations. These data are presented in the Appendix.

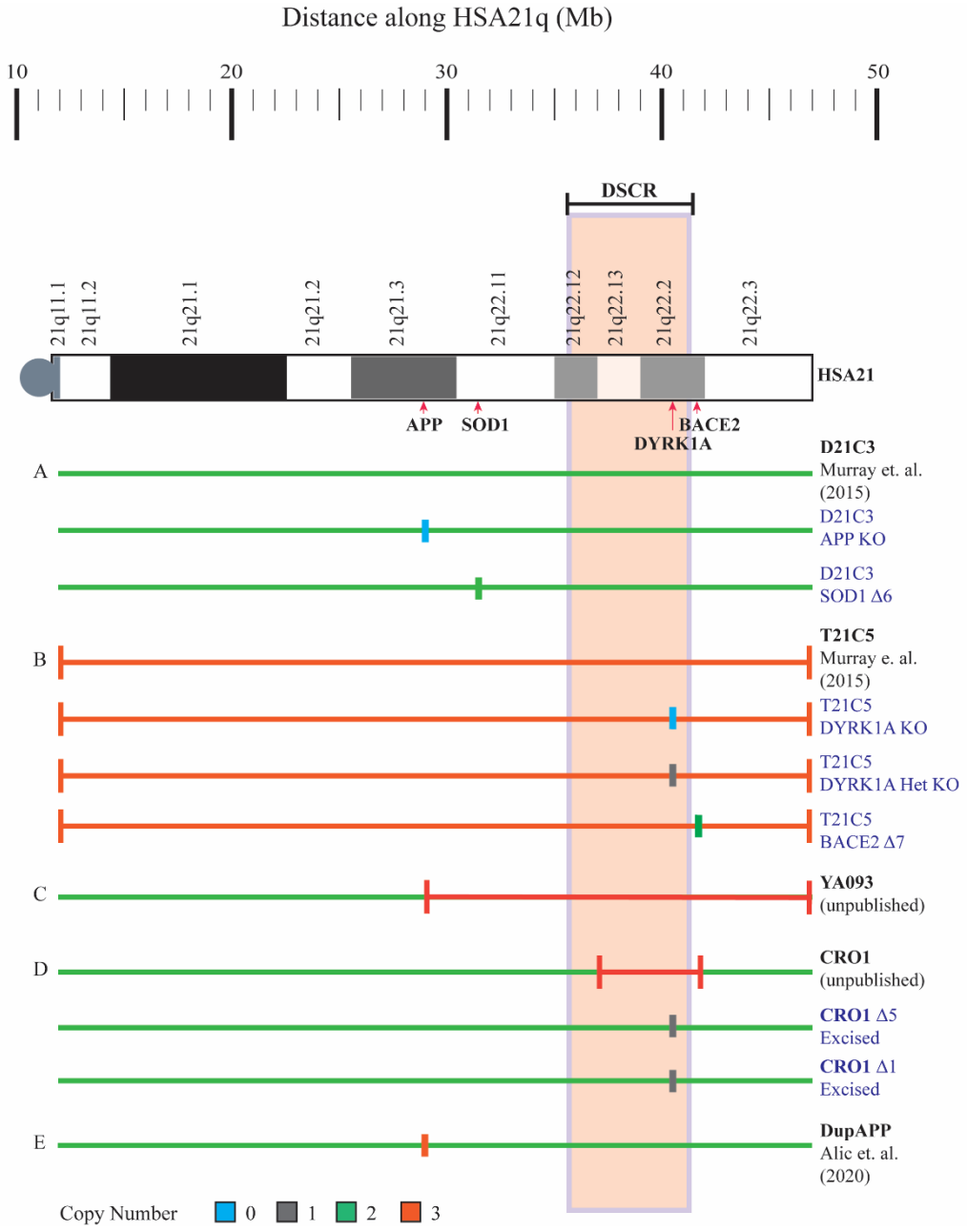

Figure 26: Full list of iPSCs created

Parental iPSC lines (**A-E)** are shown below HSA21 with their isogenic CRISPR/CAS9 edited cell lines below them. Parental D21C3 and T21C5 iPSCs are isogenic. **DSCR** (Orange Box): The originally defined minimal region responsible for most phenotypes of DS as defined by Delabar (1993). Green lines indicate normal disomic gene copy number. Red lines indicate the trisomic region. Individual gene copy number is marked by a colour-coded vertical line at the gene region.

3.8.1. Disomic APP Knockout iPSCs

The Amyloid Precursor Protein is a single pass transmembrane protein with a large extracellular domain. It is produced in large quantities by neurons, but metabolised rapidly at either the cell surface or the trans-Golgi network (145). As a major contributing factor to AD, therapeutic approaches aim to inhibit APP cleavage and therefore reduce Aβ-peptide build up (146). However, little is known about the function of APP and its metabolites or how their reduction will affect the ageing brain. Both full-length APP and its metabolites have roles in various biological processes, including neuronal stem cell proliferation and differentiation, neurite outgrowth and synaptogenesis, cholesterol metabolism and regulating cerebral blood flow under hypoxic conditions (147-150). Most of this knowledge has come from analysis of cells and tissues of *App*$^{-/-}$ mice.

For example, manganese-enhanced MRI studies, which detect axonal transport dynamics via visualisation of Mn^{2+} transport, showed that *App*$^{-/-}$ mice have axonal transport deficits within the CNS (151). App has also been shown to modulate neural network activity in the prefrontal cortex of anaesthetized WT and *App*$^{-/-}$ mice (152). *App*$^{-/-}$ mice displayed significantly longer UP-states caused by impaired $GABA_BR$ signalling, reduced expression of glutamine synthetase and lower tissue GABA content (152). Furthermore, cultured hippocampal neurons derived from *App*$^{-/-}$ mice display fewer neuronal branching, reduced synapses and reduced and abnormal axons (153).

Since overall brain development, structure, neuronal density and dendrite morphology differ greatly between rodents and humans, it would be interesting

to study these features in neurons and glia derived from human *APP*$^{-/-}$ iPSCs. 2D neuronal cultures and 3D cerebral organoids have been generated by others using these iPSCs and work beyond the scope of this thesis is currently underway.

3.8.2. Isogenic iPSCs with altered DYRK1A copy number

Both disomic and trisomic *DYRK1A KO* iPSCs have been presented, however, the D21C3 *DYRK1A-/-* iPSCs are not suitable for further use due to their acquired HSA17 duplication. While the desired *DYRK1A* reduction from three to two copies was not produced, a reduction in copy number from three to one was generated in trisomic iPSCs. Future work to generate a *DYRK1A* trisomy reduction is still necessary. This could be done either by targeting T21 iPSCs with a less efficient gRNA or retargeting the T21C5 *DYRK1A Het* iPSCs with a gRNA specific to the 2bp insertion to correct this mutation.

DYRK1A has important roles in neurodevelopment, adult brain function and neurodegeneration (136). Its *Drosophila* ortholog *minibrain (mnb)*, so named because its mutation caused a reduction in brain size, provided the first set of evidence for its involvement in neurodevelopment (154).

DYRK1A is dosage sensitive with detrimental effects when imbalanced. For example, heterozygous mutations of *DYRK1A* in humans cause mental-retardation autosomal dominant 7 (MRD7, OMIM #614104), an autism spectrum disorder characterised by microcephaly, intellectual disability, facial dysmorphism and seizures. Excess *DYRK1A*, as seen in DS is associated with structural and functional brain changes and DS related cognitive and motor deficits. In addition, *DYRK1A* dysregulation during normal aging is involved in

the development of neurodegenerative conditions like Alzheimer's and Parkinson's diseases (155).

Homozygous knockout of *Dyrk1a* is lethal in mice, making it difficult to fully understand its function in mammalian brain development or autism spectrum disorders (156). *Dyrk1a* KO zebrafish are viable and recapitulate phenotypes such as microcephaly caused by neuronal cell death during brain development and autism spectrum disorders like that seen in individuals with *DYRK1A* haploinsufficiency (157).

However, many aspects of early neurodevelopment (such as organisation of progenitor zones) are unique to humans and would benefit from human cellular models (158). The ability of the T21C5 *DYRK1A KO* iPSCs to generate NSCs and early COs highlight the potential for further study of these phenotypes in both 2D neural stem cell cultures and 3D cerebral organoids and prove that *DYRK1A* is not essential for early neural fate determination in DS. These CRISPR/Cas9 edited T21 iPSC lines, whereby the dose of *DYRK1A* was reduced from 3 to either 1 or 0, demonstrate differences in the presence, patterns and morphology or distribution of markers of neural differentiation as a function of DYRK1A dose.

Hence, the *DYRK1A* iPSCs generated here could facilitate the increasing research on *DYRK1A* inhibition for the prevention of neurodevelopmental defects in DS (159) and are useful tools to study the biological effect that *DYRK1A* reduction has on DS neurodevelopment as well as whether its overexpression is necessary to regulate other overexpressed genes on HSA21.

3.8.3. Euploid iPSCs with a heterozygous SOD1 mutation

In euploid individuals, heterozygous mutations of *SOD1* cause amyotrophic lateral sclerosis (ALS), a neurodegenerative disease characterised by death of both upper and lower motor neurons in the brain, brainstem and spinal cord (160).

The mutation created in our *SOD1* iPSCs does not lead to a stop codon, instead it deletes two amino acids from the N-terminal of the protein. A literature search revealed an ALS patient with a 6 bp deletion just 3 bp upstream of the deletion described in D21C3 Δ6 iPSCs (161) (Figure 27).

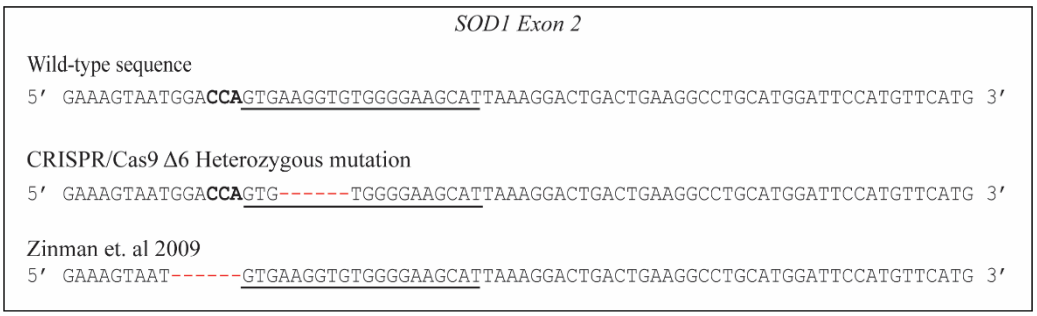

Figure 27: Comparison of mutations in D21C3 SOD1 Δ6 and a previously reported clinical case

The CRISPR/Cas9 provoked mutation in D21C3 SOD1 Δ6 is displayed in the middle row and the patient-specific 6bp deletion as described in (161) is indicated below. The gRNA used for CRISPR/Cas9 targeting is underlined with the PAM site in bold. In both cases deletions are indicated by red dashes.

While ALS is typically transmitted in an autosomal dominant manner, this patient's mutation is recessive as seen by heterozygous deletions in eight healthy and unaffected family members aged 48-85 years. These family members did however produce lower levels of SOD1 as identified by western blot analysis of white blood cells and lumbar spinal cord samples (161). The authors attributed

this to enhancement of the naturally occurring alternative splicing of *SOD1* exon 2 mRNA by the deletion.

In addition, researchers identified that SOD1 enzyme activity in erythrocytes was reduced by 50% in the homozygous patient and 30% in the heterozygous family members. Further study on our iPSCs is required to determine if alternate splicing of exon 2 is favoured as a result of the 6 bp deletion, as well as whether SOD1 protein and activity levels are reduced.

3.8.4. The cellular phenotype of increased mitochondrial H_2O_2 levels caused by T21 is detectable in undifferentiated iPSCs stably expressing HyPer

Aside from being available for CRISPR/Cas9 genome editing of genes related to oxidative stress, the HyPer tagged iPSCs are useful for studying the global effect that the supernumerary copy of HSA21 has on intracellular H_2O_2 production. Ratiometric analysis of HyPer allows one to quantify the average intracellular H_2O_2 concentration independent of the amount of reporter protein expressed in each cell line (142)

Ratiometric comparisons of HyPer-Mito between D21C3 and T21C5 indicated significantly more mitochondrial H_2O_2 in T21 iPSCs. While this is consistent with reports of increased oxidative stress in T21 foetal fibroblasts (162) and primary foetal neurons and astrocytes (63), increased oxidative stress has not previously been reported in embryonic stem cells. The source of the increased oxidative stress in T21 cells remains unconfirmed but SOD1 remains a target for future studies. Hence, generating trisomy reduction of *SOD1* in T21C5 HyPer-Mito and HyPer-Cyto tagged cells is still required.

Nevertheless, our result here also establishes a potential model for the accurate and rapid pharmacological screening, aimed at detecting the compounds capable of correcting the H_2O_2 overproduction in T21 mitochondria.

For studies beyond the scope of this thesis, the iPSCs were differentiated into neural stem cells (NSCs) and subsequently 2D neurons to determine differences in H_2O_2 levels throughout neural development.

3.9. Limitations

In an ideal situation, the aim was to create isogenic T21 iPSCs in which a single copy of the gene of interest was edited. This would produce a cell line in which the individual gene's dose is normalised while maintaining the rest of the chromosome in trisomy.

Though this is possible, a number of factors need to be considered. First, gRNAs must be carefully selected for optimal efficiency. If the gRNA is highly efficient, many on target mutations are possible but these may occur on different chromosomes within a single cell (as in the case of the *DYRK1A* and *APP* gRNAs). If the gRNA is less efficient, trisomy reduction is much more attainable but as a rare occurrence because the number of unedited cells far exceed the number of edited cells (as in the case of *BACE2* and *SOD1* gRNAs). Other factors such as Cas9 activity or the delivery method used may affect the efficiency of CRISPR targeting (127).

Another factor to consider is the genotype of the target cell line. The additional copy of HSA21 make identifying individual mutations by sequence trace alone

difficult. Sequences are especially difficult to decipher when there is a different mutation on each of the three alleles. The TIDE webtool offers a way around this but only mutations within the range of the PCR product can be identified and larger mutations, off target effects or chromosomal rearrangements are hidden from this analysis. This issue seems more prominent in cells with intra chromosomal pT21, like CRO1 which will be discussed in Chapter 4.

Chapter 4

Trisomy of Genes Within DSCR is Linked to Accelerated Cellular Ageing

Results: Gene dose within the DSCR is linked to accelerated cellular ageing

4.1. Genetic dissection of the DSCR

Mouse models of DS have been invaluable sources of information about the underlying mechanisms associated with cognitive, developmental, and age-related abnormalities in DS and mouse models with partial trisomy of different regions of mouse orthologs to HSA21 have been important for DS phenotype mapping (108, 129). For example, the use of the Ts1Rhr mouse model, which carries a 4.2 Mb duplication of 33 genes and 1 non-coding RNA on mouse chromosome 16 (Mmu16) orthologous to the DSCR provided important evidence that some but not all DS phenotypes map to a single region of HSA21 (108, 109).

In humans, duplication of just the DSCR has only been reported in two individuals with clinically diagnosed DS (106, 111). A third individual with DS and a microduplication involving the DSCR was recently identified (163) and iPSCs from this patient were generated and utilised within this thesis project (CRO1). The patient carries a 4.083 Mb duplication of HSA21 consisting of approximately 31 genes within 21q22.13 and 21q22.2. This duplicated region is nearly the exact region that is duplicated in the Ts1Rhr mouse model (Figure 28). However, of the orthologous genes found on HSA21 and MMU16, the duplication present in the TS1Rhr mouse includes an additional 4 genes at the centromeric end (*CBR3, C21Orf5*, *AK009785* and *KIAA0136*) as well as an additional 3 genes at the telomeric end (*DSCAM*, *BACE2* and *Mx1*) that are not

duplicated within CRO1 (108). Both models are missing the DSCR gene *RCAN1*.

At the time of examination, the patient (aged 3 years) displayed signs of dysmorphic facial features of DS, intellectual disability, developmental delay, and congenital abnormalities (163). The Ts1Rhr mouse model on the other hand has been associated with cognitive dysfunction, craniofacial abnormalities (though this is distinct from what is seen in Ts65Dn and Ts1Cje mice) and a smaller brain and cerebellum size (108, 164, 165).

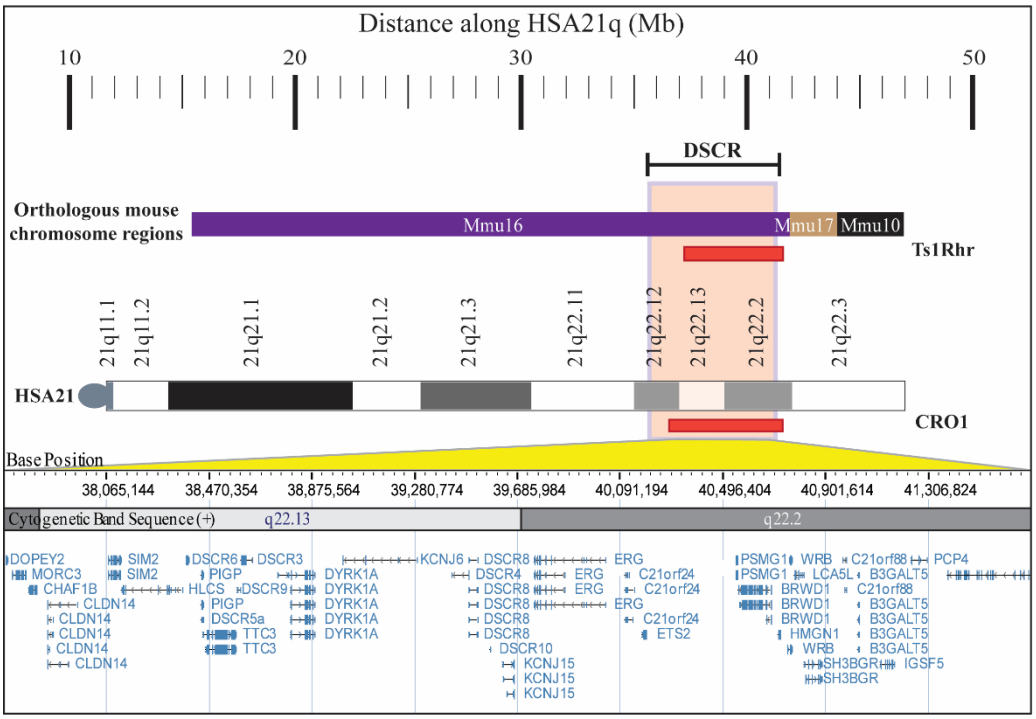

Figure 28: Graphical representation of the CRO1 microduplication with reference to the Ts1Rhr mouse model of DS

Mouse chromosome regions orthologous to HSA21 are located on chromosomes 16, 17 and 10. The duplicated regions within the Ts1Rhr mouse and the human CRO1 iPSC models are indicated by the red bars below the respective chromosome regions. In both cases a region overlapping the DSCR is duplicated but without duplication of RCAN1. A zoom in of the CRO1 duplicated region is indicated below. This region includes 31 genes spanning from *DOPEY2* to *PCP4* (inclusive).

4.2. Targeting *DYRK1A* Exon 7 in CRO1 iPSCs

To dissect the DSCR, iPSCs were generated from a blood sample taken during routine clinical examination (CRO1: Critical Region Only) and the iPSCs were subjected to CRISPR/Cas9 genome modification of *DYRK1A* with the aim of editing one out of three copies.

Initial sequence analysis led to the identification of two clones, each with a single deletion of 1 bp and 5 bp respectively (Figure 29A). *In silico* analysis of DNA translation revealed that the 1 and 5 bp deletions in *DYRK1A* exon 7 produce nonsense amino acids followed by a premature stop codon within the kinase domain (Figure 29B).

TIDE analysis confirmed these deletions, however at an unexpected mutation to WT ratio of 1:1 was observed in both clones. The equal percentage of WT and mutated sequence within the PCR product indicated the presence of only two copies of *DYRK1A* as opposed to the expected three copies (Figure 29C).

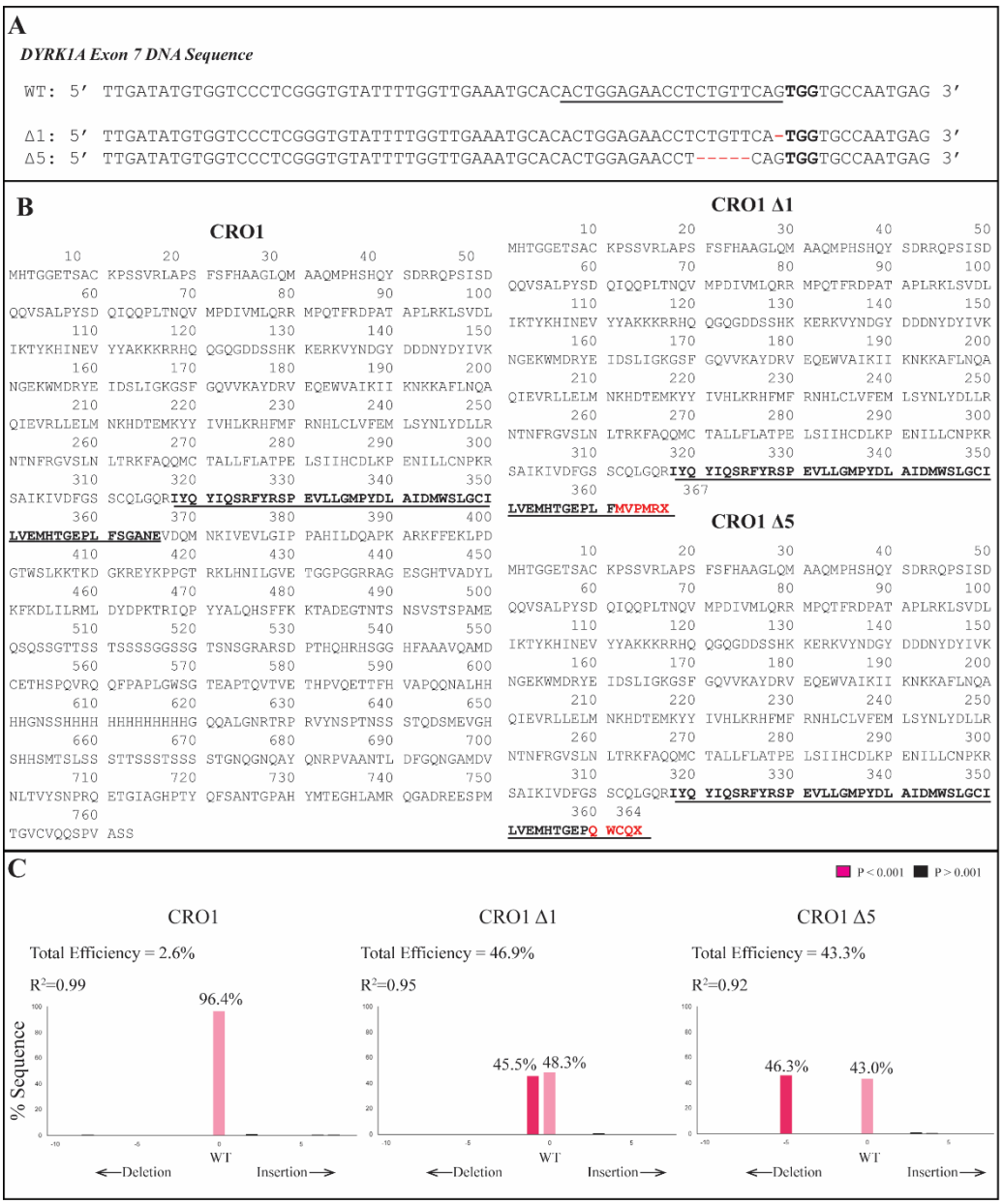

Figure 29: DYRK1A targeting of CRO1 iPSCs

A: A portion of the DNA sequence from *DYRK1A* exon 7 is shown. In the WT sequence (top), the gRNA is underlined, and the PAM is shown in bold. The two CRISPR/Cas9 edited cell lines (CRO1Δ1 and CRO1Δ5) are shown below WT and their respective 1 and 5 bp deletions indicated by red dashes.

B: *In silico* analysis of *DYRK1A* DNA translation reveals that the 5 bp and 1 bp deletions in exon 7 (**underlined**) cause nonsense amino acids followed by premature stop codons (**red**).

C: Graphs displaying TIDE analysis of the PCR amplified *DYRK1A* target site in CRO1 iPSCs. CRO1 represents a WT sequencing CRISPR/Cas9-targeted clone. In both CRO1Δ1 and CRO1Δ5 the mutation to WT ratio is 1:1 indicating loss of one of the copies of *DYRK1A*.

4.3. Designing a pyrosequencing assay to identify T21 excision

A G/G/C SNP (rs2835772) downstream of the *DYRK1A* target site was identified in CRO1 and subsequent sequence analysis of the CRISPR/Cas9 modified clones indicated that aside from having one WT and one mutated allele, both clones had lost one allele. The corresponding deleted nucleotide of the SNP was a C in CRO1Δ1, leaving behind G/G and a G in CRO1Δ5 leaving behind G/C (Figure 30).

Since Sanger sequencing is not quantitative, a new assay was designed to accurately quantify the relative ratios of this SNP. An elegant method, termed paralogous sequence quantification (PSQ) was developed by Deutsch et al. to quantify the trisomic status of the most frequently occurring human trisomies (T21, T18 and T13). The method relies on a comparison of paralogous sequences on the chromosome being tested for trisomy with another chromosome, containing a distinguishing SNP. For example, the HSA21 genes *GABPA* and *ITSN* have such paralogous sequences on HSA5 and HSA7 respectively.

PCR amplification of the paralogous region surrounding the SNP by a single pair of primers (one of which is biotinylated) results in amplification from both chromosomal locations. Since each amplicon differs only by the known SNP, it is possible to determine the chromosomal origin of the resulting PCR products. Pyrosequencing can then be used to accurately quantify the relative ratio of each SNP within the amplicon. During a sequencing reaction, pyrophosphate (PPi) is released in an equimolar quantity to the amount of nucleotide incorporated. Enzymes in the pyrosequencing reaction then convert PPi to ATP, which in turn

drives a luciferin conversion to produce light. The amount of light produced is directly proportional to the amount of a given nucleotide incorporated in the sequencing reaction, making such a method highly quantifiable.

The PSQ method was adapted to develop a pyrosequencing assay that would enable quantification of the nucleotides of the rs2835772 SNP and therefore confirm the presence of a large deletion involving one of the three copies of *DYRK1A*.

The assay designed differed slightly in that the paralogous sequence mismatch was in the duplicated region of HSA21 itself. As such instead of 1:1 for disomic or 1:1.5 for trisomic SNPs, a 1:1 or 0:1 ratio was expected for disomic SNPs or a 1:2 ratio if the SNP was retained in trisomy (Figure 31A).

Pyrosequencing of the parental CRO1 served as a control and confirmed a C:G SNP ratio of 1:2 as indicated by 34% C and 66% G. Pyrosequencing of CRO1Δ1 revealed loss of the copy of *DYRK1A* harbouring a C SNP, as indicated by 9% C and 91% G. Pyrosequencing of CRO1Δ5 on the other hand revealed loss of the copy of *DYRK1A* harbouring a G SNP, as indicated by 53% C and 47% G (Figure 31B).

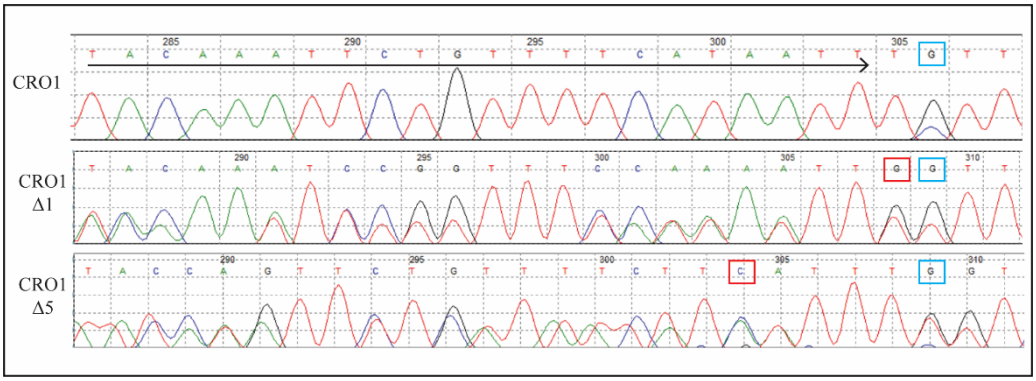

Figure 30: SNP identification in CRO1

Sequence trace of the intron after *DYRK1A* exon 7 where the SNP rs2835772 is located. The **blue box** indicates the position of the SNP on a WT allele. On the mutated alleles of CRO1Δ1 and CRO1Δ5, this nucleotide shifts 1 and 5 bp to the left respectively. The remaining nucleotide is indicated by a **red box**. In both cases the nucleotide corresponding to a third copy of *DYRK1A* is absent.

Figure 31 (next page): Pyrosequencing assay to confirm loss of one copy of DYRK1A

A: Sequence alignment of each allele (**#1-3**) for designing the pyrosequencing assay. **Green boxes** indicate the position of the primers for PCR amplification and the **blue box** indicates the position of the sequencing primer for pyrosequencing. The encircled region shows the SNP used for quantification. The intron/exon junction is marked with a red line and the gRNA target site (purple) with its adjacent PAM (bold) is indicated within the exon.

B: CRO1 WT indicates an unedited CRISPR/Cas9 targeted cell line. Trisomy of *DYRK1A* is indicated by a C:G ratio of 1:2. This ratio is altered in CRO1Δ1 and CRO1Δ5, indicating loss of a copy of *DYRK1A* from the target site onwards.

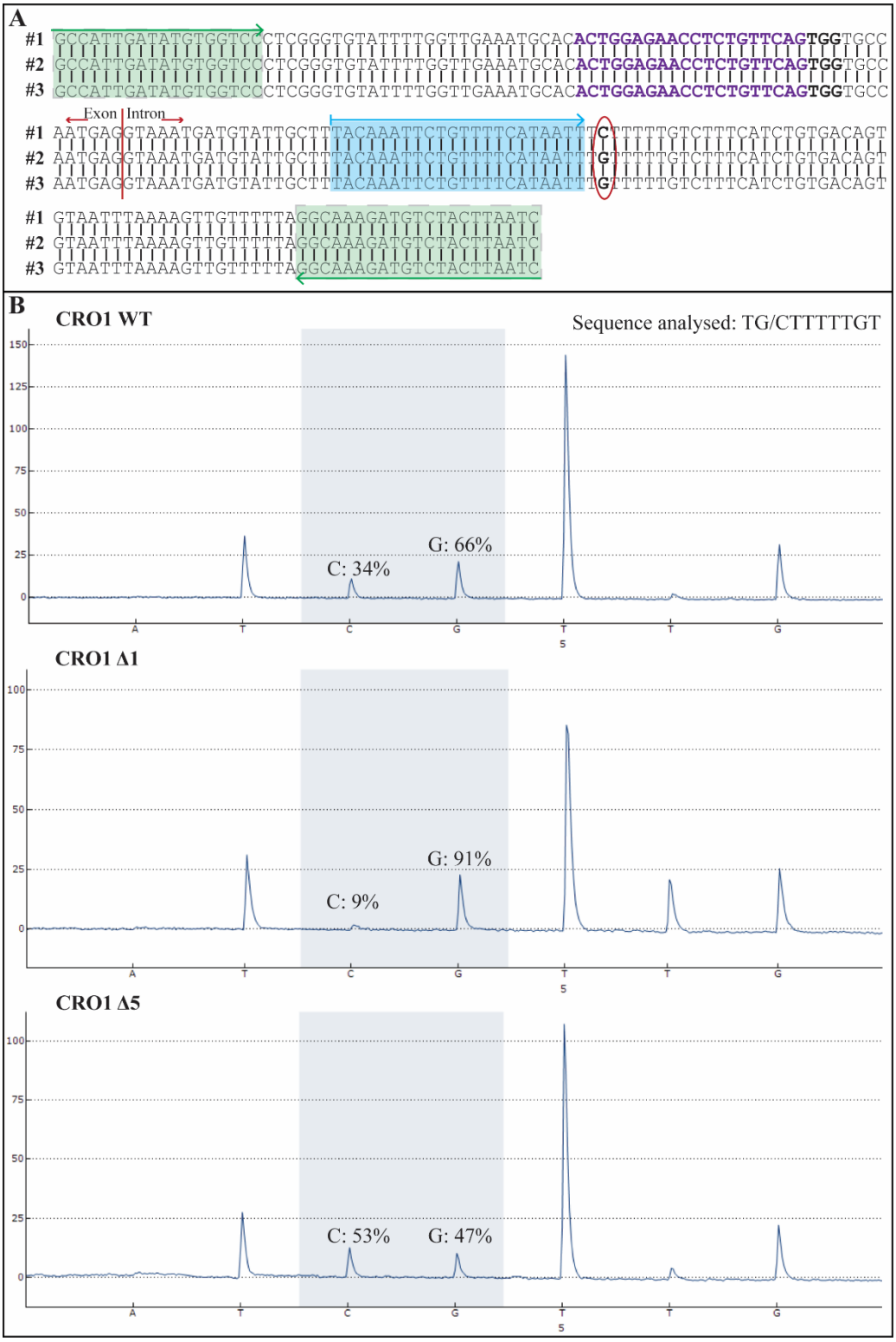
A
#1 GCCATTGATATGTGGTCCCTCGGGTGTATTTTGGTTGAAATGCACACTGGAGAACCTCTGTTCAGTGGTGCC
#2 GCCATTGATATGTGGTCCCTCGGGTGTATTTTGGTTGAAATGCACACTGGAGAACCTCTGTTCAGTGGTGCC
#3 GCCATTGATATGTGGTCCCTCGGGTGTATTTTGGTTGAAATGCACACTGGAGAACCTCTGTTCAGTGGTGCC
Exon
Intron
#1 AATGAGGTAAATGATGTATTGCTTTACAAATTCTGTTTTCATAATTTCTTTTTGTCTTTCATCTGTGACAGT
#2 AATGAGGTAAATGATGTATTGCTTTACAAATTCTGTTTTCATAATTTGTTTTTGTCTTTCATCTGTGACAGT
#3 AATGAGGTAAATGATGTATTGCTTTACAAATTCTGTTTTCATAATTTGTTTTTGTCTTTCATCTGTGACAGT
#1 GTAATTTAAAAGTTGTTTTTAGGCAAAGATGTCTACTTAATC
#2 GTAATTTAAAAGTTGTTTTTAGGCAAAGATGTCTACTTAATC
#3 GTAATTTAAAAGTTGTTTTTAGGCAAAGATGTCTACTTAATC
B
CRO1 WT
Sequence analysed: TG/CTTTTTGT
C: 34%
G: 66%
CRO1 Δ1
C: 9%
G: 91%
CRO1 Δ5
C: 53%
G: 47%

4.4. Investigating loss of pT21 in CRO1 CRISPR

Since the pT21 in CRO1 is intrachromosomal, it is possible that two copies of *DYRK1A* approximately 4.8 Mb apart were simultaneously cleaved by CRISPR/Cas9. It was therefore hypothesised that, cleavage at both target sites caused the first half of the first copy of *DYRK1A* to join with the second half of the second copy of *DYRK1A*. This caused excision of the region between the two target sites of the duplicated chromosome. While *DYRK1A* in the normal chromosome remained unedited, the copy within the excised chromosome was subject to non-homologous end joining, resulting in the Δ5 and Δ1 mutations (schematic in Figure 32A).

Analysis of CRO1Δ1 and CRO1Δ5 by SNP genotyping confirmed excision of the region of pT21 in both clones, hereafter referred to as CRO1(corrected)Δ1 and CRO1(corrected)Δ5. No other major chromosomal rearrangements were present.

However, based on pyrosequencing analysis, different loci have been excised in CRO1Δ1 and CRO1Δ5 corresponding to the loss of either a C or a G nucleotide, respectively. This cannot be explained by excision alone and is likely the result of additional crossover events or rearrangements in one of the clones.

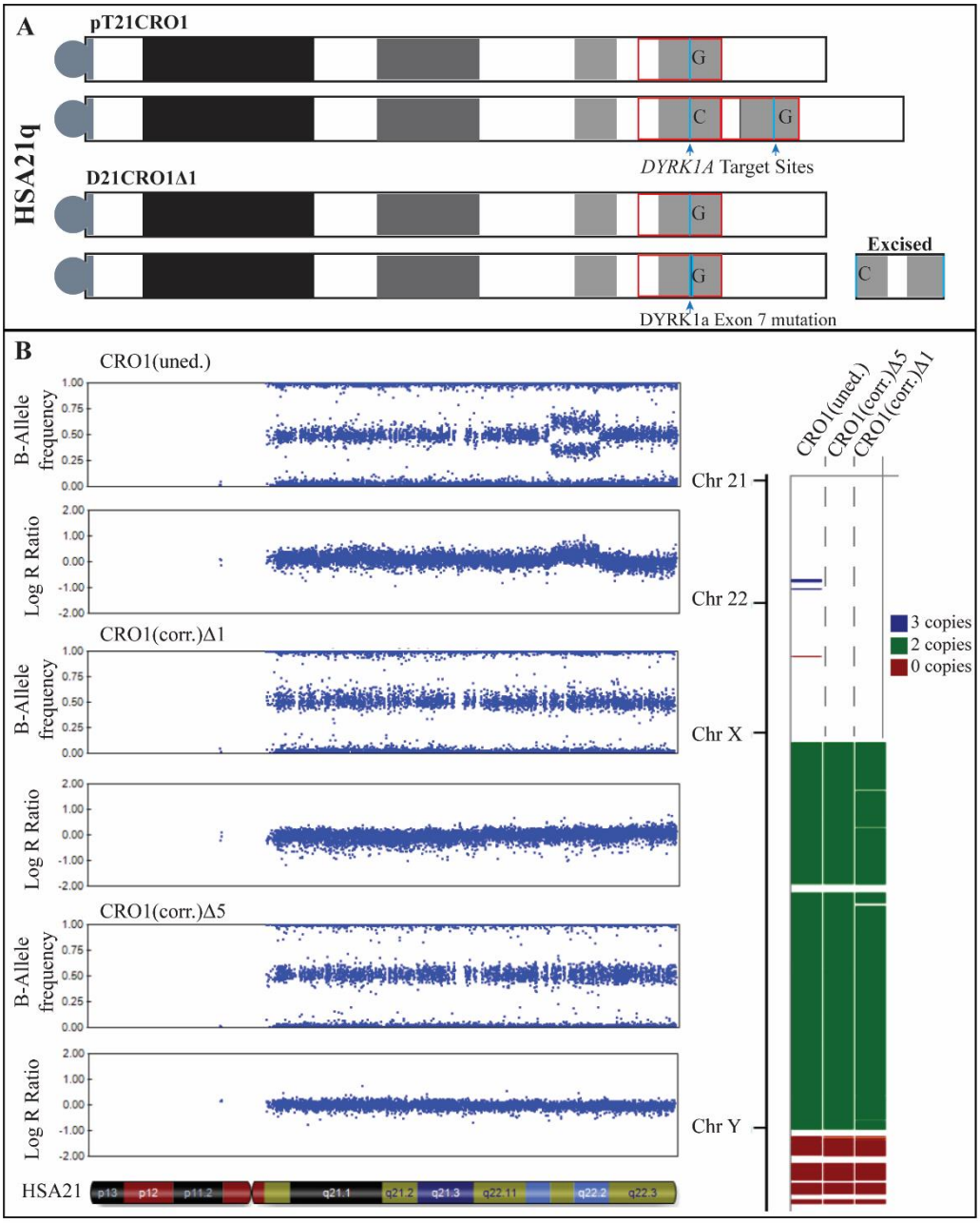

Figure 32: SNP array confirms excision of the DSCR in CRO1Δ1 and Δ5

A: The **red box** indicates the region of HSA21 duplicated in CRO1. This region encompasses the *DYRK1A* target site (**blue line**). It was hypothesised that CRISPR/Cas9 cleavage at both target sites of the chromosome containing the duplication caused excision of the region between cleavage sites. The remaining target site was subject to non-homologous end joining, which caused the 1 bp deletion. The SNP identified for paralogous sequencing is depicted downstream of the target site.

B: SNP analysis of genomic DNA from untargeted parental CRO1 and the DYRK1A CRISPR/Cas9 targeted CRO1Δ1 and CRO1Δ5 iPSCs. The B-allele frequency and Log R ratio of HSA21 (left) confirms excision of the 4.8Mb duplication that is present in the parental CRO1 cell line. Excision was also confirmed by copy number variant analysis (right).

4.5. Validating iPSC status of CRO1 Cell lines

To ensure correct reprogramming as well as preservation of pluripotency after CRISPR/Cas9-targeting the iPSCs were stained for the pluripotency markers as described in (Chapter 3-3.3).

Alkaline phosphatase staining of the CRO1 pre-CRISPR/Cas9 parental cell line confirmed the presence of undifferentiated iPSCs. All three cell lines displayed positive staining for the pluripotency markers: SSEA-4, Tra-1-60 and 1-81 and the transcription factor Oct-4 (Figure 33).

In addition, the CRO1 iPSC lines were able to form embryoid bodies (EBs) containing all three germ layers as shown by positive expression of Nestin (neuroectoderm), FOXA2 (endoderm) and SMA and Brachyury (mesoderm) (Figure 34).

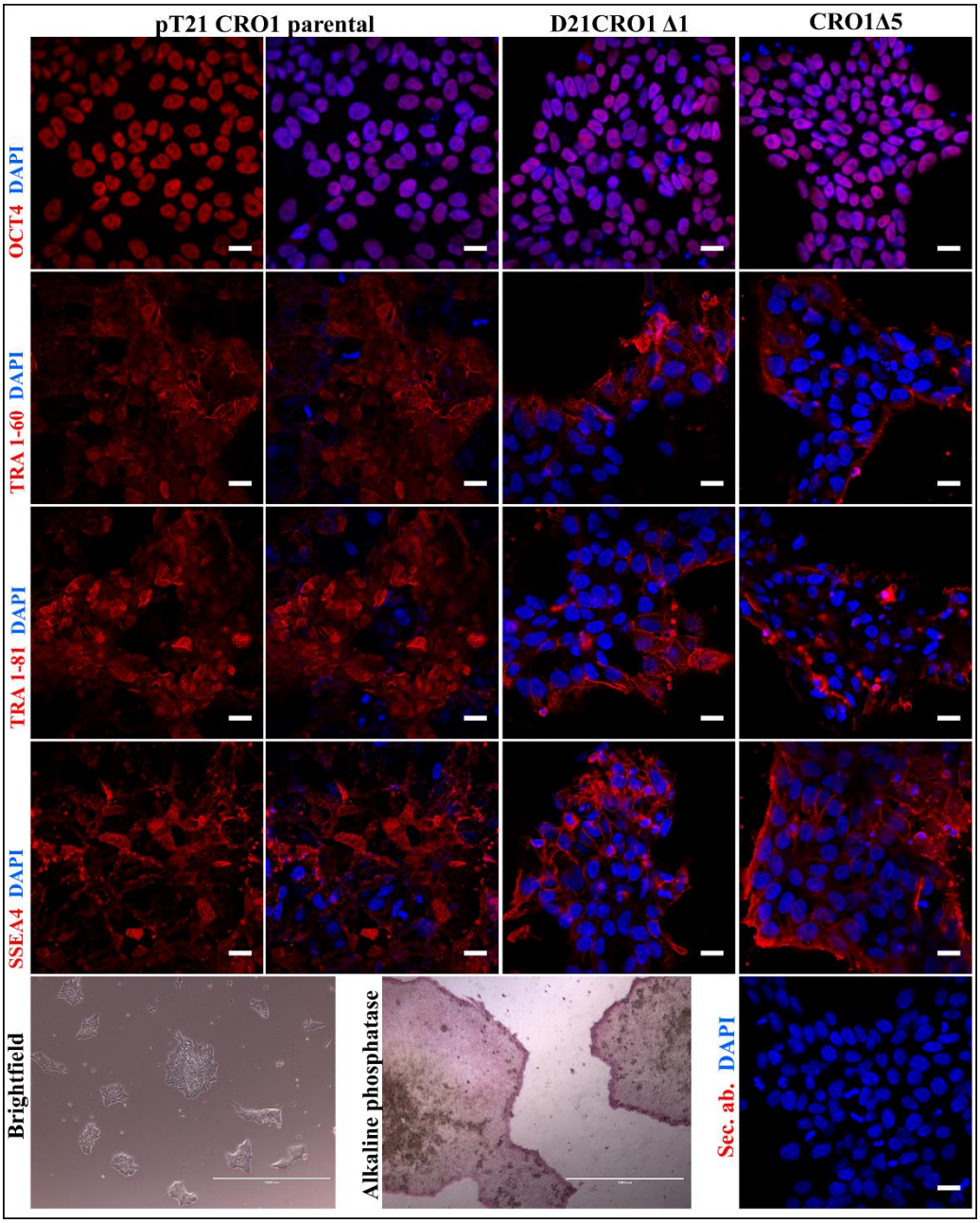

Figure 33: CRO1 untargeted and CRISPR/CAS9 iPSCs display the characteristic features of undifferentiated iPSCs

Top Row: CRO1 parental, CRO1Δ1 and CRO1Δ5 iPSCs were immunostained with the pluripotency markers: Oct-4, TRA-1-60, TRA-1-81 and SSEA4 and counter stained with DAPI. All three lines displayed positive staining for each marker. Scale bar represents 20 µm.

Bottom Row: (1) Representative brightfield image of CRO1 parental iPSCs indicating characteristic morphology and colony formation. Scale bar represents 1 000 µm. **(2)** Representative brightfield image of positive alkaline phosphatase staining of parental CRO1 iPSCs. Scale bar represents 1 000 µm. **(3)** Secondary only control for immunofluorescence staining.

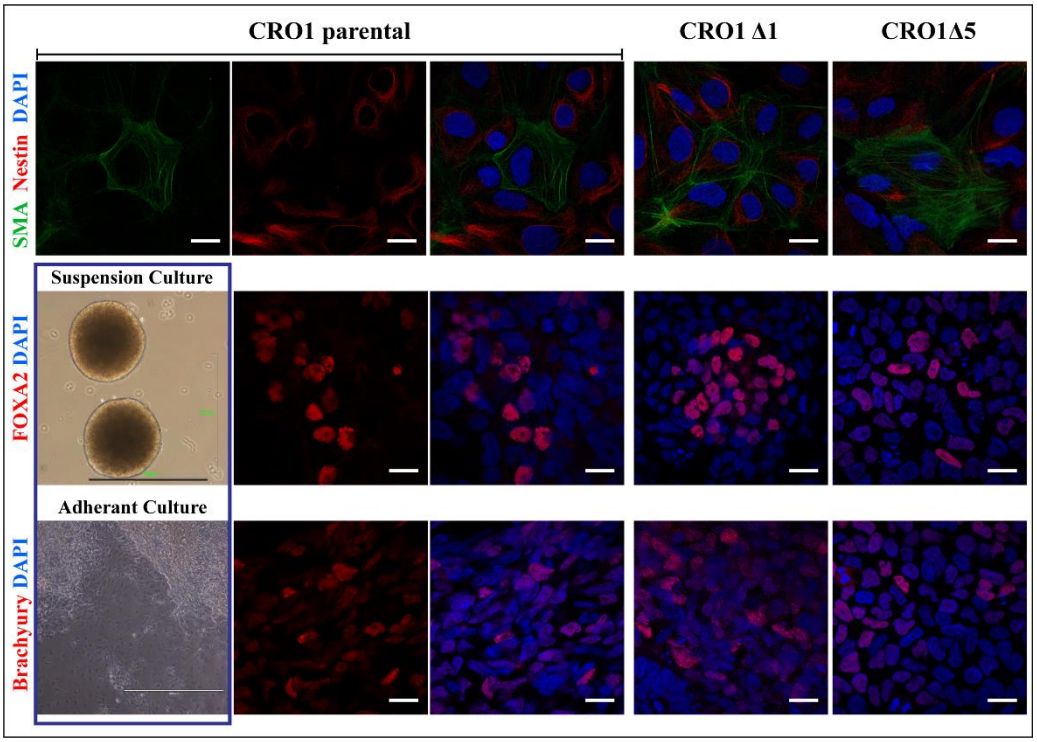

Figure 34: CRO1 untargeted and CRISPR/CAS9 iPSCs form cells from all three germ layers

Blue Box: EBs were formed over a 14-day culture period, which consisted of seven days in suspension to promote EB formation followed by seven days on VTN-coated coverslips to promote cell migration out of the EB. Scale bars represent 100 µm (suspension) and 400 µm (adherent).

Immunofluorescence: All three CRO1 iPSC lines formed cells from each of the three embryonic germ layers: ectoderm (FOXA2), mesoderm (SMA and Brachyury) and endoderm (Nestin). Scale bar represents 20 µm.

4.6. T21 is associated with increased DNA double strand breaks

The formation of phosphorylated H2AX (γH2AX) is an early cellular response to DNA double strand (DSBs) breaks, indicative of accelerated cellular ageing. Previously published work (128) reported more γH2AX puncta in T21 iPSC-derived neurons compared with their isogenic D21 counterparts (Figure 35A&B). The same phenotype was observed by western blot analysis of immunoprecipitated histone material from lysates of undifferentiated iPSC of the same system (Figure 35C). This is to our knowledge, the first demonstration of this cellular phenotype at the level of undifferentiated iPSCs in T21 or pT21.

To further dissect this, genes within the DSCR were investigated for their role in accelerated cellular ageing in DS. Immunofluorescence labelling for γH2AX revealed significantly more γH2AX foci in CRO1 iPSCs when compared with CRO1Δ1 and CRO1Δ5 (Figure 36A). Both D21CRO1Δ1 and CRO1Δ5 iPSCs, which each have 1 functional copy of *DYRK1A* behaved similarly suggesting that the difference in γH2AX expression was the result of *DYRK1A* gene dosage.

Next, to determine if this effect could be caused by the decrease in kinase function of DYRK1A, the parental CRO1 iPSCs were treated with the selective DYRK1A inhibitors: Harmine and ID8. For both inhibitors, the treatment reduced γH2AX expression relative to the DMSO treated vehicle control. No significant difference was observed between CRO1 untreated and the DMSO control. Fewer γH2AX foci were observed at both high (500 μM) and low (10 μM) concentrations of ID8, indicating that γH2AX expression was dependent on *DYRK1A* dosage (Figure 36).

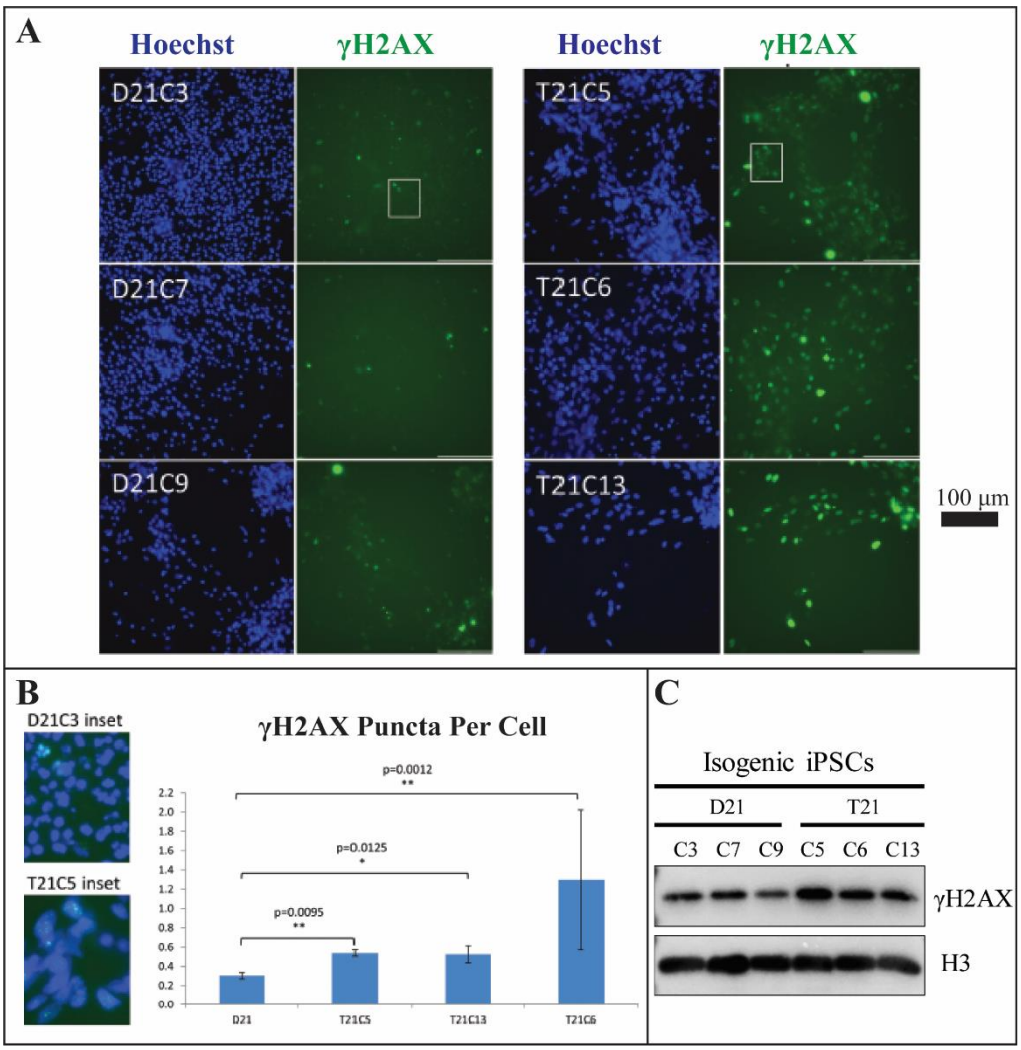

Figure 35: γH2AX staining in isogenic D21 and T21 iPSCs and iPSC-derived neurons

A & B: Figure from (128). (A) Isogenic iPSC derived neurons stained for the presence of DNA damage (γH2AX) and counter stained with the nuclear marker Hoechst. Scale bars represent 100 µm. (B) The T21 neurons contain significantly more γH2AX puncta than the D21 neurons, indicative of increased DNA damage. Quantification was performed on three wells per cell line and a minimum of 6000 cells were analysed each. Statistical significance was calculated with a Student's t-test and error bars represent SEM.

C: Nizetic Lab unpublished data. Western Blot analysis of isolated histones from the isogenic iPSCs indicates increased γH2AX in trisomic iPSCs. Histone 3 (H3) was used as a loading control.

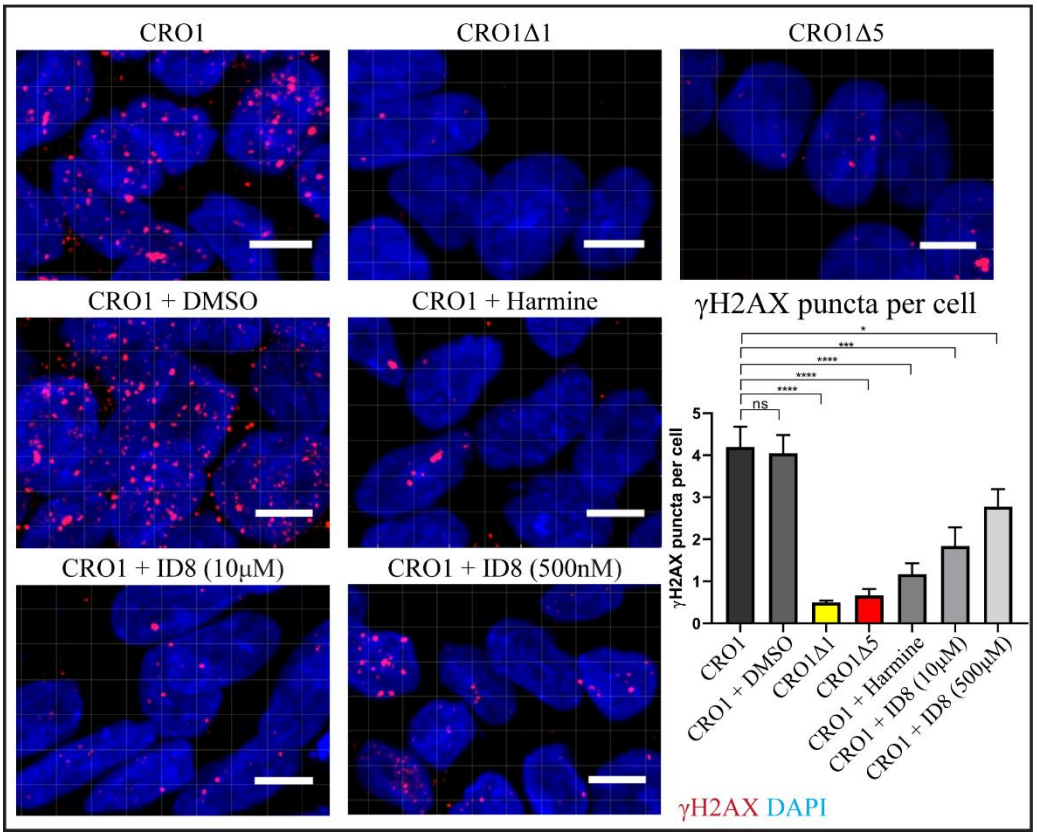

Figure 36: γH2AX staining in isogenic CRO1 iPSCs

Immunofluorescence: Representative fluorescent images of CRO1 WT and CRISPR/Cas9 edited iPSCs stained with anti-γH2AX. Prior to fixation, separate wells of CRO1 WT iPSCs underwent 48 hr treatment with selective *DYRK1A* inhibitors or a DMSO vehicle control. The final concentration of DMSO was 0.02%. Scale bars represent 5 μm.

Graph: Untreated and DMSO treated CRO1 displayed similar levels of γH2AX foci with no significant difference between them. Cells with lower levels of DYRK1A, both by genome modification and selective chemical inhibition displayed significantly less γH2AX foci. Quantification of γH2AX foci was performed automatically using IMARIS. The number of spots within n>3 000 DAPI positive nuclei from two independent experiments consisting of three wells each were counted per cell line. Statistical significance was calculated by one-way ANOVA followed by Holm-Sidak's multiple comparisons test using GraphPad Prism 6.0. software. Statistical significance was defined as $P < 0.05$ (*), $P < 0.01$ (**), $P < 0.001$ (***) and $P < 0.0001$ (****).

4.7. Cerebral organoids generated from isogenic CRO1 iPSCs differ in size and development of cortical folds

To investigate the role of *DYRK1A* in phenotypes related to neurodevelopment, ageing and neurodegeneration, cerebral organoids (COs) were generated from CRO1, CRO1Δ1 and CRO1Δ5 iPSCs. Early cerebral organoid development differed between the cell lines in terms of size and development of organoid cortical folds (Figure 37).

CRO1Δ1 and CRO1Δ5 iPSCs formed smaller EBs from the same starting number of cells when compared with CRO1 WT. In addition to a smaller starting EB size, the neuro-EBs from the CRISPR/Cas9 edited cells became smaller as the newly formed surrounding neuroectoderm detached and formed multiple smaller neuro-EBs.

Despite their smaller size, CRO1Δ1 and CRO1Δ5 NSC containing neuro-EBs (which contain only one copy of *DYRK1A*) displayed faster growth as well as a better ability to generate organoid cortical folds when compared with CRO1 (which contain three copies of *DYRK1A*).

Average total organoid surface area was quantified on bright-field images using ImageJ software of n= 7 to 12 CO images per cell line from two separate CO batches. 24 COs were generated from each of the three cell lines per batch and a panel of CO images were captured at the same time point for both batches. The surface area of COs from the CRISPR cell lines were compared to those of the parental CRO1 cell line at three time points: day 3, which represents EBs prior

to neural induction, day 10, which represents neuro-EBs after 4 days of neural induction and day 14, which represent COs during neural expansion and differentiation. On day 3, EBs from both CRISPR cell lines were highly significantly smaller than CRO1 EBs ($P<0.0001$). On day 10, both CRO1Δ1 and CRO1Δ5 neuro-EBs were significantly smaller than CRO1 neuro-EBs with $P<0.0001$ and $P<0.1$, respectively. On day 14, however, only CRO1Δ1 was significantly smaller ($P<0.0001$) and there was no significant difference between CRO1 and CRO1Δ5. Statistical significance was calculated with a two-tailed T-test.

The organoid cortical folds were manually traced using Adobe Illustrator to quantify fold differences between the CRISPR clones and the parental CRO1 cell line. For each organoid image, the percentage of black pixels (representing rosette folds) vs the percentage of white pixels were quantified per 10 000 cm^2. Statistical significance of $P<0.0001$ was achieved for each respective CRISPR clone to the parental CRO1 cell line. Statistical significance was calculated by a Dunnett's multiple comparisons test in GraphPad Prism.

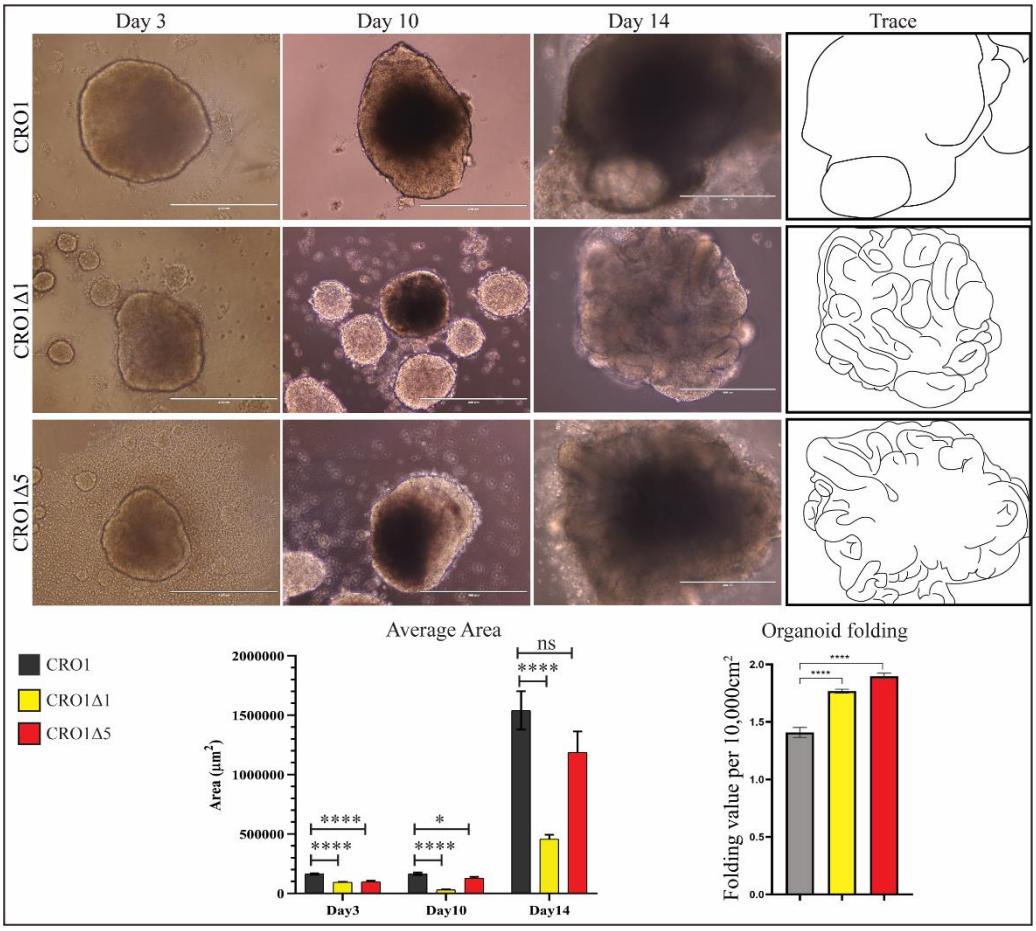

Figure 37: Early Cerebral organoid development using CRO1 iPSCs

Representative bright-field images of COs generated in parallel. **Day 3:** EBs prior to neural induction. Starting cell number was consistent per line. CRISPR/Cas9 edited iPSCs generated significantly smaller EBs. **Day 10:** EBs after 4 days in neural induction medium. Clearing of the outer surface indicates the formation of neural ectoderm. **Day 14:** Cerebral organoids display radial organisation of neuroectoderm into organoid cortical folds. A simplified schematic outline is drawn to the right. Scale bars represent 400 µm.

Graphs: Average organoid surface area on bright-field images and organoid folding value per 10 000 cm^2 on image traces were calculated using ImageJ software of n= 7-12 images per cell line from two batches of COs. Error bars: SEM. Statistical significance was defined as $P < 0.05$ (*), and $P < 0.0001$ (****).

4.8. CRO1 corrected iPSCs generate neurons with reduced DYRK1A expression

DYRK1A expression was measured by immunostaining with both N- and C-terminal antibodies. Reduced expression of DYRK1A was observed in CRO1Δ1 and CRO1Δ5 COs compared with that of CRO1 and this was consistent for both antibodies (Figure 38). The reduced expression in CRO1Δ1 and CRO1Δ5 COs was uniformly distributed throughout the CO as seen by lower magnification of sections stained with the C-terminal antibody (Figure 39A).

Quantification of DYRK1A expression in MAP2 positive neurons was performed automatically using IMARIS software. For both antibodies, MAP2 normalised DYRK1A was significantly lower in CRO1Δ1 and CRO1Δ5 compared with CRO1.

Figure 38 (next page): DYRK1A expression in DIV63 Cerebral Organoids

Representative confocal images of histological sections from DIV 63 CRO1, CRO1Δ1 and CRO1Δ5 COs. Neurons are labelled with MAP2. Scale bars represent 10 μm.

A: Nuclear expression of DYRK1A as labelled with the N-terminal antibody. Lower expression is visible in CRO1Δ1 and CRO1Δ5 sections (refer to Figure 39B).

B: Expression of DYRK1A labelled with the C-terminal antibody. Lower expression is visible in CRO1Δ1 and CRO1Δ5 sections (refer to Figure 39B).

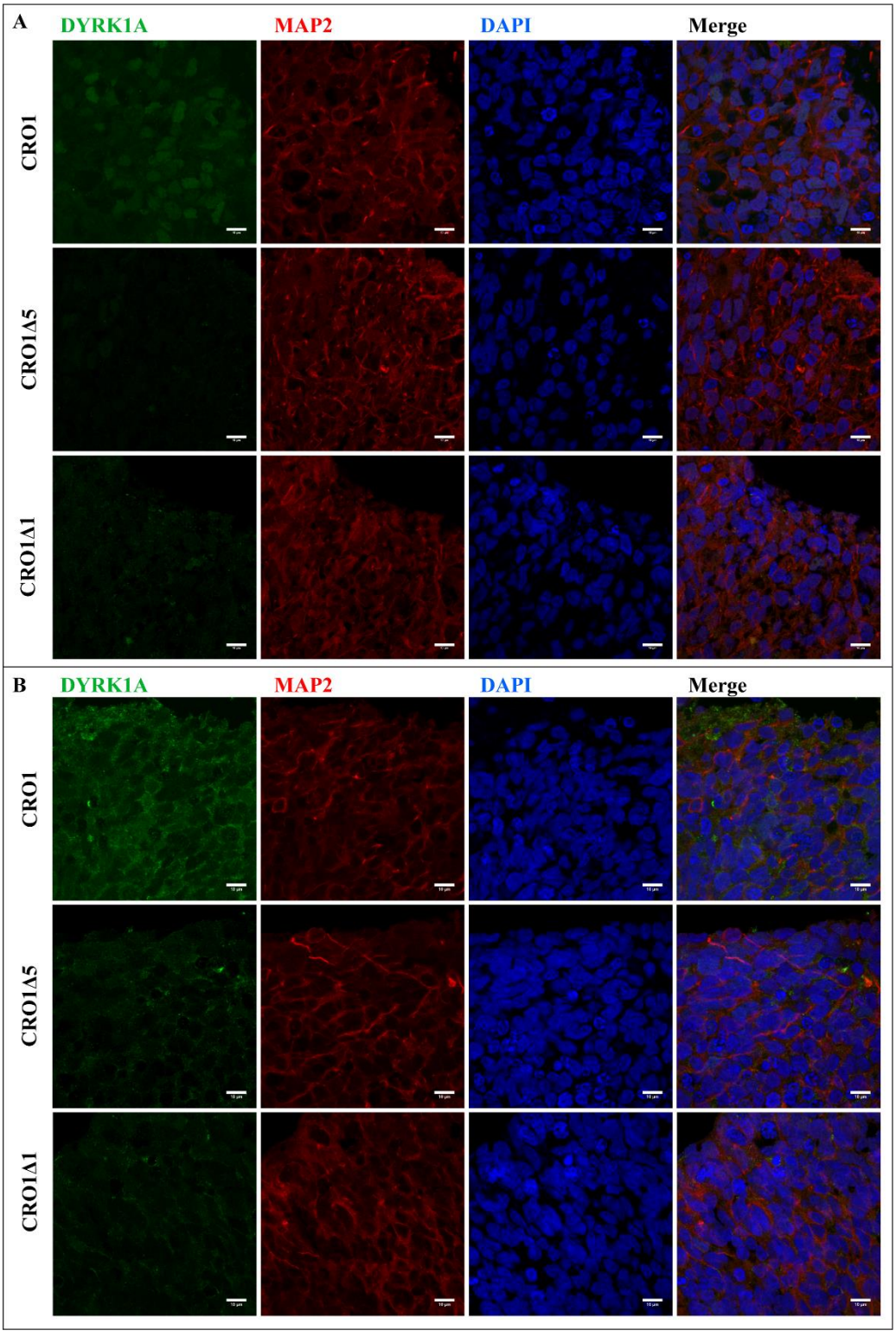
A
DYRK1A
MAP2
DAPI
Merge
CRO1
CRO1Δ5
CRO1Δ1
B
DYRK1A
MAP2
DAPI
Merge
CRO1
CRO1Δ5
CRO1Δ1

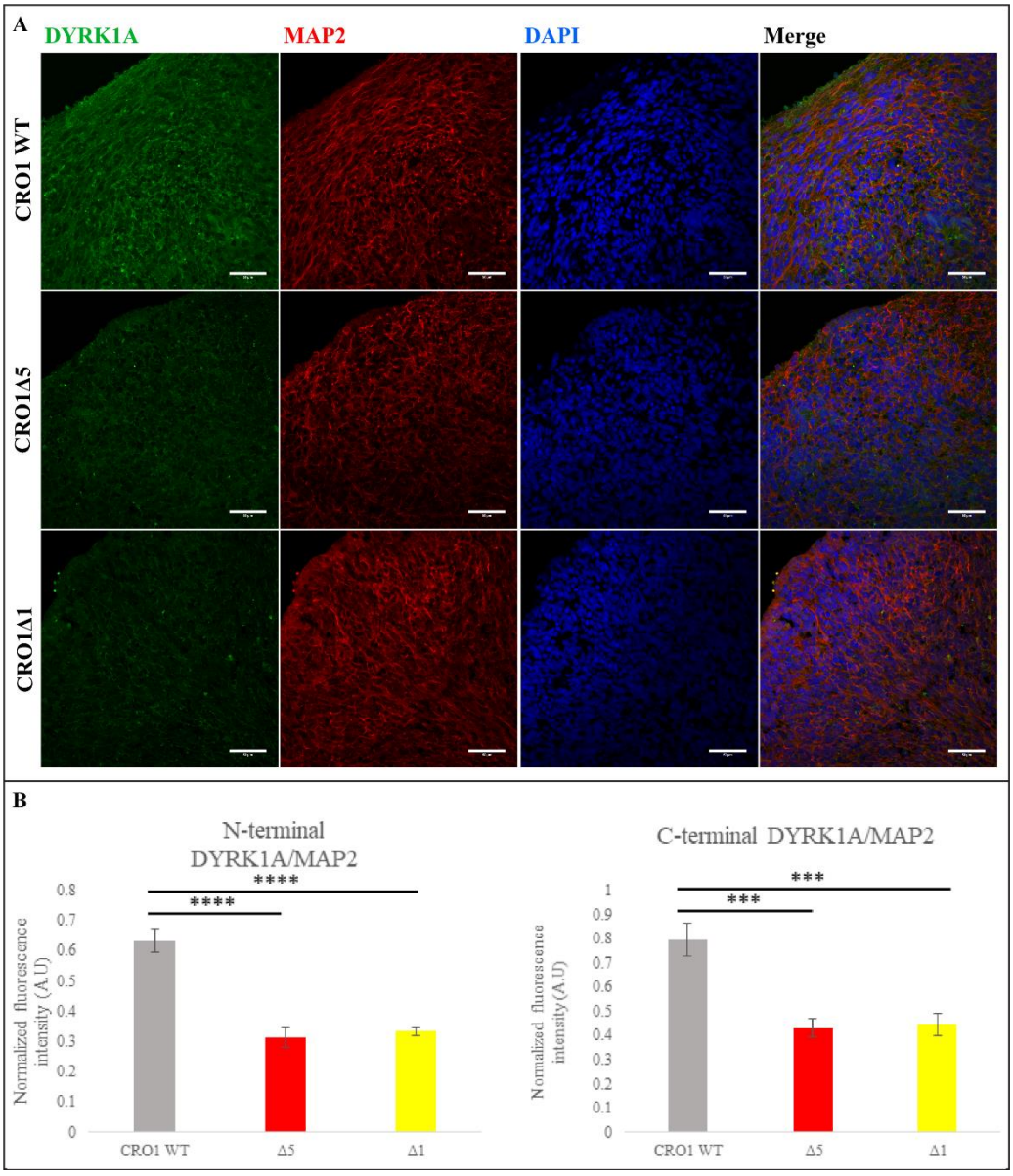

Figure 39: DYRK1A Expression in COs

A: Representative confocal images indicating uniform distribution of DYRK1A in histological sections of DIV 63 CRO1, CRO1Δ1 and CRO1Δ5 COs labelled with the C-terminal *DYRK1A* antibody. Neurons are labelled with anti-MAP2. Scale bars represent 50 µm.

B: Quantification of DYRK1A expression normalised to MAP2. DYRK1A expression is significantly lower in CRO1Δ1 and CRO1Δ5 sections with both antibodies. Statistical significance is defined as: *** (P<0.001) **** (P<0.0001).

4.9. CRO1 iPSCs generate COs containing all six distinct cortical layers

During differentiation into COs, iPSCs from each CRO1 cell line were able to self-organise and acquire distinct identities, as a cellular model surrogate to what is seen in the developing human cerebral cortex.

COs were fixed after 63 days *in vitro* (DIV) and immunostained for the cortical layer markers: FOXG1 (forebrain marker), REELIN (layer I), BRN2 (layers II-III), SATB2 (layers II-IV) and TBR1 and Ctip2 (layers V-VI). Neurons and glia were stained with MAP2 (mature neurons), 3R-Tau (all neurons) and GFAP (astrocytes).

All three cell lines were able to form neurons expressing REELIN, FOXG1 and Ctip2 (Figure 40).

Late-born upper-layer neurons stained with SATB2, appeared slightly higher in CRO1Δ1 and CRO1Δ5 compared with CRO1. Due to the young age of the COs, astrocytes were not visible (Figure 41). We have, however observed astrocytes in CRO1 COs older than DIV 100 (not shown).

Likewise, the presence of immature neurons expressing TBR1 and superficial layer neurons expressing BRN2 could be observed in each of the three cell lines (Figure 42).

We can therefore confirm that CRO1 and its derivative CRISPR cell lines express representative markers of neurons in all 6 cortical layers.

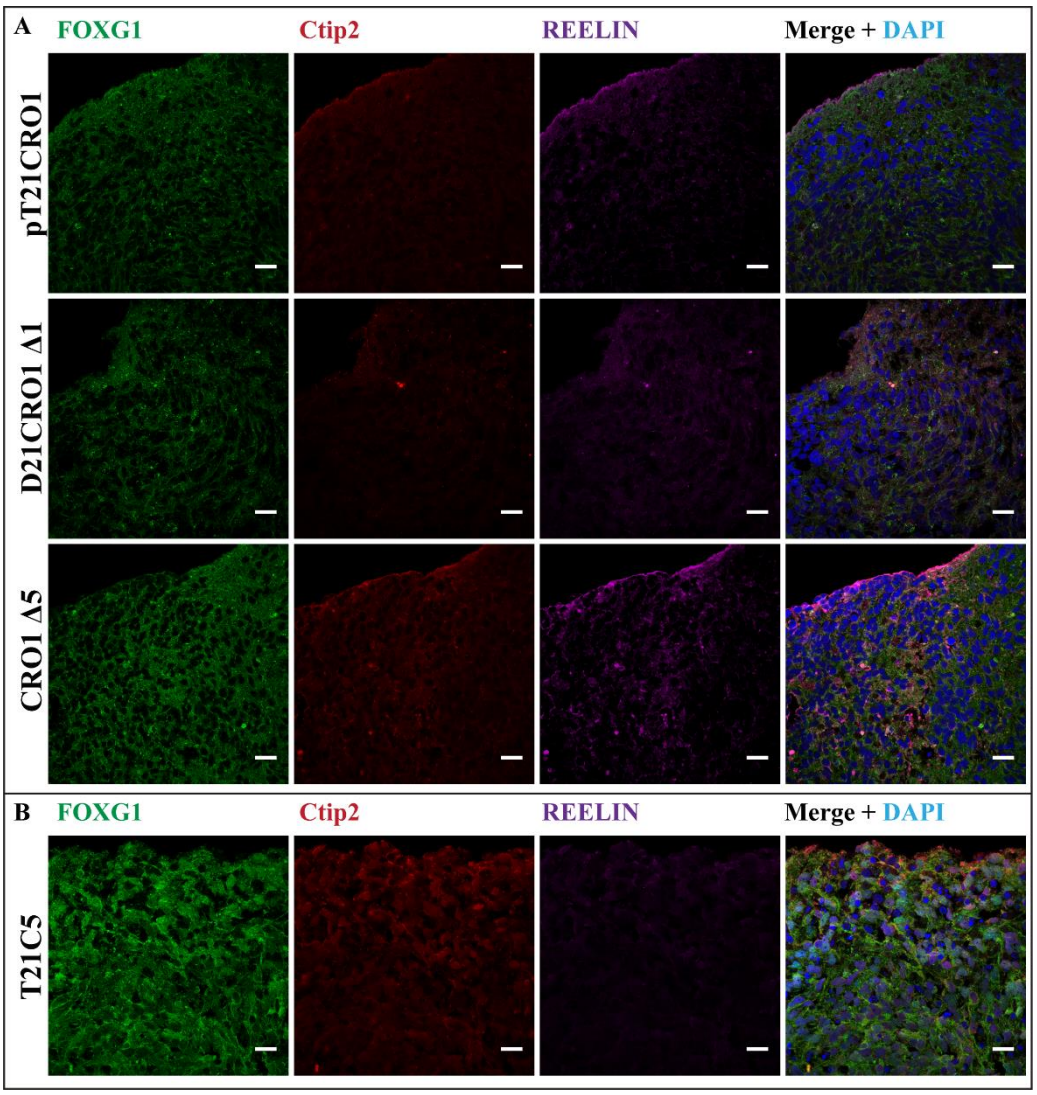

Figure 40: FOXG1, REELIN and Ctip2 expression in CRO1 iPSC-derived COs

Representative confocal images of histological sections of COs. Sections were stained with FOXG1 (forebrain neurons), REELIN (cortical layer I) and Ctip2 (cortical layers V-IV). Scale bars represent 20 µm

A: DIV 63 CRO1, CRO1Δ1 and CRO1Δ5 COs.

B: DIV 100 T21C5 COs for comparison.

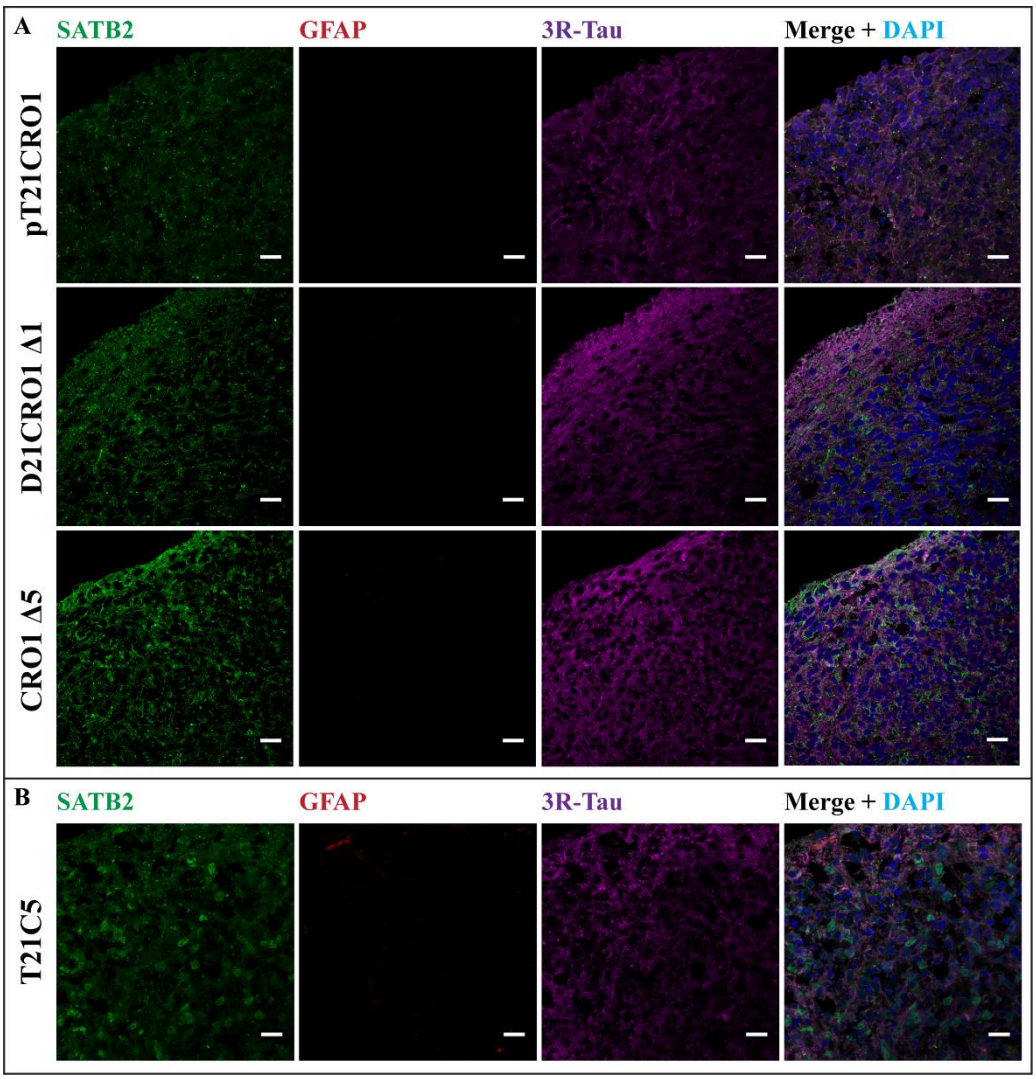

Figure 41: SATB2, GFAP and 3R-Tau expression in CRO1 iPSC-derived COs

Representative confocal images of histological sections of COs stained with SATB2 (cortical layers III-IV), GFAP (astrocyte marker) and 3R-Tau (general neuron marker). Scale bars represent 20 µm

A: DIV 63 CRO1, CRO1Δ1 and CRO1Δ5 COs. No GFAP positive cells are visible due to the young age of the COs.

B: DIV 100 T21C5 COs for comparison. Few astrocytes are visible by GFAP staining (top left corner).

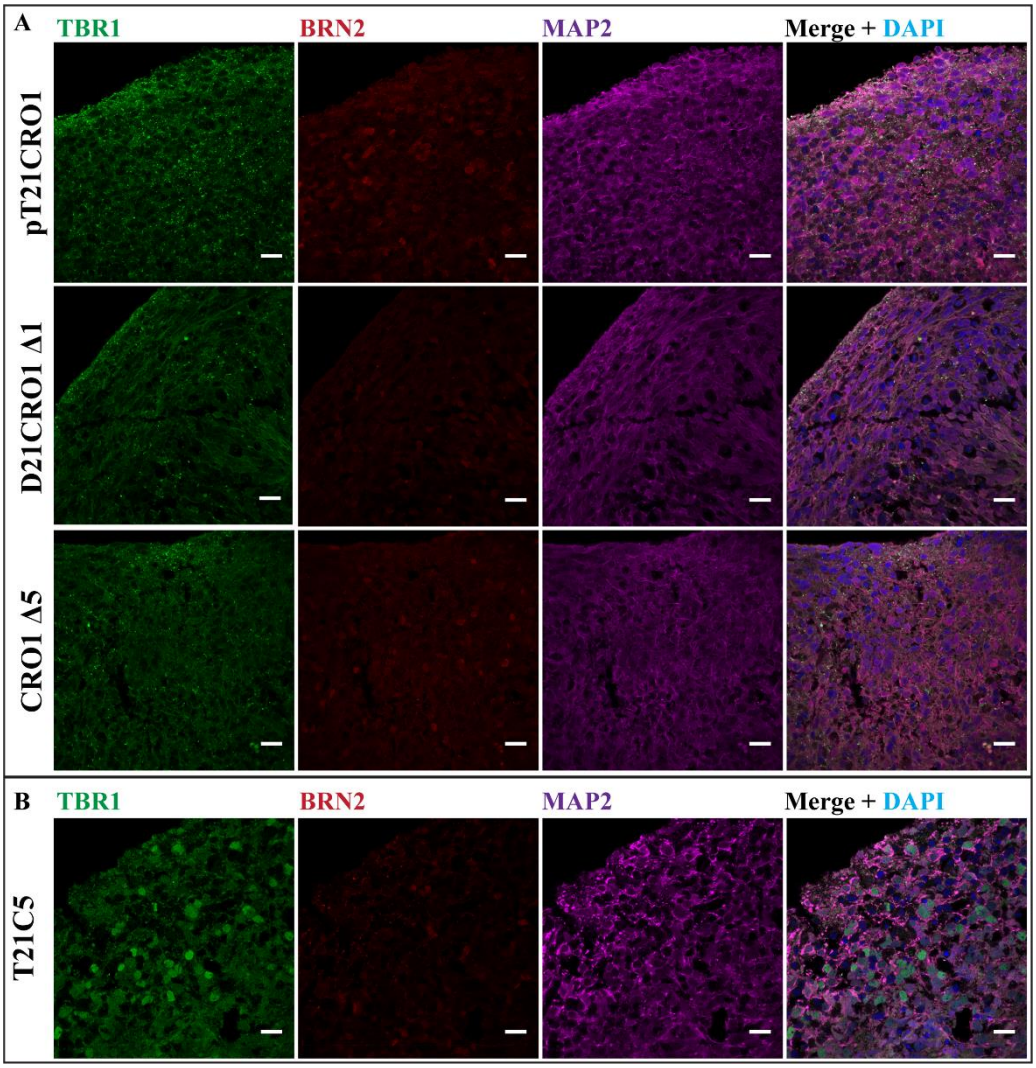

Figure 42: TBR1, BRN2 and MAP2 expression in CRO1 iPSC-derived COs

Representative confocal images of histological sections of COs stained with TBR1 (layers V-VI), BRN2 (cortical layers II-III) and MAP2 (general neuron marker). Scale bars represent 20 µm

A: DIV 63 CRO1, CRO1Δ1 and CRO1Δ5 COs.

B: DIV 100 T21C5 COs for comparison.

4.10. Summary and discussion

In this chapter a unique human iPSC line with pT21 of the DSCR has been described. This iPSC line, herein referred to as CRO1, is nearly exactly the human counterpart to the extensively studied Ts1Rhr mouse model and could therefore help bridge the species gap in "phenotype mapping" studies.

Isogenic counterparts of CRO1 were created by CRISPR/Cas9 genome editing of *DYRK1A* exon 7. All three CRO1 iPSC lines were characterised as pluripotent stem cells via the expression of pluripotency markers and their ability to differentiate into cells of the three embryonic germ-layers.

Though the aim was to reduce *DYRK1A* copy number from three to two, the entire micro-duplicated region was excised, in addition to producing an edited copy of *DYRK1A*. These iPSCs are therefore isogenic models of partial trisomy of the DSCR and are useful tools to better understand whether dosage sensitive genes in the DSCR contribute to DS phenotypes.

One such phenotype is the development of B cell acute lymphoblastic leukaemia (B-ALL), which is 20 times more common in individuals with T21 and in which polysomy 21 is the most frequently observed somatic aneuploidy (166-168). Research into this phenotype currently relies on the use of mouse models and work involving the Ts1Rhr mouse has pointed to the potential involvement of H*mgn1* (167). Overexpression of *Hmgn1*, which is located at 21q22, was identified as a contributor to early passage B-cell hyperproliferation *in vitro* and promotes B-ALL *in vivo* but further work is required to determine the underlying

mechanism (167). The human CRO1 isogenic iPSC model has potential for further dissection of this phenotype once reliable protocols for the differentiation of B-lineage progenitors from iPSCs are established.

In addition, CRO1Δ1 and CRO1Δ5 iPSCs are potential models of *DYRK1A* haploinsufficiency syndrome, which is observed in euploid individuals with the autism spectrum disorder, MRD7 (138, 169, 170). Like DS, individuals with *DYRK1A* haploinsufficiency present with structural brain abnormalities, eye defects, microcephaly at birth, intellectual disability, developmental delay, short stature, and distinct facial features (170).

4.10.1. DYRK1A overdose contributes to increased DNA damage in DS

It has been proposed that Down Syndrome is a segmental progeroid syndrome since affected individuals suffer from age-related conditions much earlier than the general population (27). It is unclear what exactly causes accelerated ageing, both in DS and the general population, but two theories exist (reviewed in Studer et al. 2015). The first suggests that ageing is a developmentally controlled process involving regulation of tissue homeostasis, repair, and defence responses. The second suggests that ageing is caused by an accumulation of damage due to an altered energy metabolism, increased ROS or increased DNA damage. Whether accelerated ageing in DS is the result of disrupted repair and defence mechanisms, an accumulation of damage or a combination of both remains to be identified.

In DS, the extra genetic material from HSA21 has been reported as a contributing factor to the accumulation of DNA damage and therefore accelerated ageing by

at least two mechanisms: (1) T21 leads to increased oxidative stress and mitochondrial dysfunction (63), and (2) triplicated HSA21 genes, for example, ubiquitin-specific-peptidase 16 (*USP16*) cause altered cellular responses to DNA damage and impair DNA repair mechanisms (171-173).

USP16 encodes the enzyme that controls the ubiquitin state of H2A and its triplication was first identified as a contributor to DNA damage accumulation in hematopoietic stem cells of the Ts65Dn mouse model of DS when compared with a pT21 mouse model of DS that lacks *USP16* triplication (Ts1Cje mouse) (173).

Similar phenotypes of mitochondrial dysfunction and increased dsDNA breaks in DS were observed in human T21 iPSC-derived neurons when compared with their isogenic euploid counterparts (128). However, accumulation of dsDNA breaks in undifferentiated iPSCs has not previously been shown to correlate with the dose and phosphorylation activity of a gene associated with aneuploidy.

It has been shown that ectopic expression of the reprogramming factors increases the levels of phosphorylated histone H2AX, one of the earliest cellular responses to DNA double strand breaks (DSBs), and a direct role of the homologous recombination (HR) DDR pathway in pluripotency reprogramming has been found (Simara et al., 2017, Gonzalez et al., 2013). However, no specific gene dose effects associated with aneuploidy had previously been shown to affect the γH2AX-foci accumulation in iPSCs.

Using the isogenic CRO1 iPSCs and their genetically modified counterparts described this chapter, we show that triplication of genes within the DSCR are

contributors to DNA DSB accumulation and that this phenotype can not only be modelled but also reversed in undifferentiated iPSCs by DSCR correction. Increased DNA damage in CRO1 is independent of USP16, since this gene is located at position 21q21.3 and is not duplicated in CRO1. In addition, the increased DNA damage in CRO1 could not be explained by the triplication of either *APP* or *SOD1* (both of which have their overdoses linked to increased ROS and cellular toxicity) since neither gene is within the CRO1 micro-duplicated region. This result shows the usefulness of our system in dissecting the role of candidate gene overdoses to the overall T21 phenotypes.

A typical hallmark of accelerated ageing is the accumulation of DNA DSBs, which is always followed by phosphorylation of histone H2A family member X (H2AX) generating γ-H2AX (174). A reduction in the number of γ-H2AX foci was evident following chemical inhibition of DYRK1A kinase activity in iPSCs, which suggests that *DYRK1A* triplication is either a contributor to endogenous DNA damage or that its overdose hinders DNA repair mechanisms. Further work is required to identify the molecular mechanisms by which *DYRK1A* overdose contributes to an accumulation of γ-H2AX foci in CRO1. However, we cannot exclude the possible synergistic action of other gene trisomies within the DSCR.

To completely eliminate this possibility, a version of CRO1 with a perfectly excised DSCR and two remaining copies of *DYRK1A* would need to be produced.

Two recent reports have linked DYRK1A to the DNA damage/repair process (175, 176). Both groups reported that DYRK1A associates with the E3 ubiquitin ligase RFN169 using antibody-based affinity purification coupled with mass

spectrometry. Upon formation of DSBs RFN169, which is a promoter of homology directed repair (HDR), competes with a promoter of NHEJ, the p53-binding protein 1 (*53BP1*), for binding to the H2A ubiquitin marks near the sites of DNA damage (175, 177-180).

By studying the effects of *DYRK1A* KO and chemical inhibition on the maintenance of 53BP1 expression and its subsequent recruitment to DNA damage loci, Guard and colleagues identified that DYRK1A kinase activity was necessary for 53BP1 recruitment after induction of DNA damage by ionizing radiation (IR) and 53BP1 expression decreased with lower levels of DYRK1A in a dose dependent manner (175). However, overexpression of DYRK1A was also found to suppress 53BP1 accumulation and co-localisation with γH2AX at IR-induced DSBs (176).

In addition to regulating 53BP1, DYRK1A forms a complex with RNF169 and phosphorylates it at various sites, one of which alters its ability to displace 53BP1 from sites of DNA damage (176). This complex formation is thought to be required for recruitment of DYRK1A to sites of DNA damage following IR.

Both groups observed a possible role for DYRK1A in cell survival following DSB induction by IR, though this is controversial. Guard noted that DYRK1A expression decreased in WT HeLa cells after IR and genetic KO of *DYRK1A* increased cell survival in response to DNA damage (175). On the contrary, Roewenstrunk reported that depletion of DYRK1A by lentiviral shRNA knockdown lowered the number of surviving cells as well as reduced long-term recovery from DNA damage (176).

Nevertheless, these reports support the hypothesis that DYRK1A correction in CRO1 iPSCs is related to the observed decrease in γ-H2AX foci. To induce DNA damage in our experiments, CRO1 iPSCs were treated with either mitomycin C or a range of H_2O_2 concentrations (not shown). This served mainly as a positive control for γH2AX staining and quantification of cell survival was not performed. Future experiments could involve similar clonogenic survival assays by inducing DNA DSBs in both CRISPR/Cas9 edited and inhibitor treated CRO1 iPSCs. This may provide further insight about whether over- or under- expression of *DYRK1A* protects against or increases the probability of DNA damage induced cell death.

In addition, T21C5 DYRK1A CRISPR/Cas9 targeted cell lines (refer to Chapter 3-3.6), particularly T21C5 *DYRK1A* KO and T21C5 *DYRK1A* het and their parental T21C5 isogenic counterpart, could be included in these experiments. Although they are not isogenic comparisons to CRO1 iPSCs, they may provide evidence whether alteration of *DYRK1A* copy number alone influences the DNA damage/repair process or if other duplicated DSCR genes are responsible for this phenotype.

4.10.2. DYRK1A gene dose affects Cerebral Organoid development

As with the human cerebral cortex, each of the three CRO1 isogenic iPSC lines were able to generate COs containing cells from all 6 distinct cortical layers. *DYRK1A* staining confirmed the expected protein level reductions in both CRO1Δ1 and CRO1Δ5 and neither haploinsufficiency nor overexpression of *DYRK1A* prevented *in vitro* formation of any cortical layers. A more in-depth analysis of early layer formation as well as analysis of individual layer

composition was beyond the scope of this work and is therefore left to future experiments.

During early cerebral development, CRO1Δ1 and CRO1Δ5 produced significantly smaller COs compared with CRO1, which differed by trisomy of the DSCR and three copies of *DYRK1A*. This result was consistent with clinical observations in individuals with microcephaly caused by *DYRK1A* haploinsufficiency syndrome (169, 170, 181) as well as in *mnb* mutant Drosophila (154) and *Dyrk1a* $^{+/-}$ mice (156).

Differences between cell lines were also observed in the radial organisation of neuroepithelia. In all cases, organoid cortical fold formation resembled features of the embryonic neural tube with a distinct lumen by light microscopy. In CRO1 COs, however, fewer clearly defined neural organoid cortical folds were present at 14 DIV.

Further research is required to identify whether this is because of delayed or reduced NSC proliferation and therefore delayed rosette formation or because of premature differentiation of NPCs into neurons. While CRO1Δ1 and CRO1Δ5 COs displayed faster growth during the early stages of neural induction, these COs remained smaller in size throughout their development (up to 63 DIV). Microcephaly related to *DYRK1A* haploinsufficiency has previously been attributed to increased neuronal cell death in *dyrk1a* KO zebrafish (157) and *Dyrk1a*$^{-/+}$ mice (182). This may also be the case in our system but further experiments to assess and quantify activated Caspase-3 levels are required.

Neural rosettes generated *in vitro* can recapitulate properties of radial glia by generating intermediate cell types organised roughly into progenitor zones akin to the ventricular and subventricular zones of the developing CNS (183-185). The neuroectodermal cells within rosettes require high activation of the Notch signalling pathway for maintenance of pluripotency and its absence has been found to cause a loss of rosette organisation and promote early differentiation to more restricted cell types including neural crest cell fates (184, 185). Thus, active vs inactive Notch states determine whether NSCs will gain CNS or non-CNS fates respectively (184).

In mice, both *DYRK1A* haploinsufficiency and overexpression have been modelled with important (and sometimes similar) phenotypes, particularly in brain development and behaviour.

During early embryonic brain development in the mouse, *Dyrk1A* mRNA is asymmetrically segregated between two daughter neural progenitor cells (NPCs) and its expression is thought to induce the switch from proliferative to neurogenic cell divisions (136, 186). *Dyrk1A* overexpression has been shown to cause a reduction in NPC proliferation and premature neuronal differentiation but the mechanism by which this arises is not clearly defined (54, 187). Conversely, haploinsufficiency of *Dyrk1A* causes failure of NPCs to exit the cell cycle and begin differentiation into neurons, which leads to apoptotic cell death (52, 54). In both cases, fewer mature neurons are generated.

In DS, impaired proliferation of neural precursors manifests as hypocellular and disorganised neurodevelopment and has been attributed to reduced brain volumes

and ID. Affected areas include: delayed and disorganised cortical lamination, smaller and hypocellular dentate gyrus, a hypomorphic cerebellum, delayed myelination and synaptic dysgenesis, which most likely results from alterations in dendritic spine length, density, morphology and complexity (19, 30, 31, 188).

Though histological studies on human neural tissues are limited, a body of work suggests that synaptic dysgenesis plays a major role in the manifestation of ID in DS children. Early histological studies on pyramidal neurons in the visual cortex of post-mortem DS brains described the DS visual cortex as having structurally irregular dendrites with poor dendritic spine density and branching (55). Another study by Becker and colleagues on the development of DS brains from infantile to juvenile (aged 4 months – 7 years old) showed increased dendritic length and intersections in infants below 6 months of age but these values dropped to significantly below normal by age 2 (56). Statistically, there was a 50% decrease in the total dendritic length per cell in layer 3 of the visual cortex. In contrast, dendritic arborisation in euploid controls increased by 65% from infantile to juvenile stages (56).

Similarly, dysregulated brain development may be responsible for ID in *DYRK1A* haploinsufficiency syndrome since pyramidal neurons in both *Dyrk1a*$^{+/-}$ and Ts65DN mice appear smaller with fewer dendritic spines, shorter basal dendrites and smaller dendritic arbours compared with normal controls (169, 189, 190). A similar feature of impaired dendrtitiogenesis was observed in mice transgenic for *Dyrk1A* (191). Additional work to assess dendritogenesis impairments in isogenic CRO1 CO's could clarify *DYRK1A's* role in dendritogenesis. COs from

all three cell lines have been fixed at different time points throughout development and could be further utilised for this purpose.

Some pathways affected by *DYRK1A* overexpression in DS could also be studied further. These include: (1) suppression of the NFATc transcription factors, which are necessary for axonal outgrowth and regulation of genes involved in cell survival, proliferation and differentiation (105, 192), (2) altered transcript levels of neuron-restrictive silencer factor (NRSF/REST) chromatin remodelling complex and its target molecules: Nanog and SOX2 (91, 193) and (3) attenuation of Notch signalling by phosphorylation of Notch, which triggers NPC differentiation to neurons (136, 194).

It is important to note, CRO1 and its CRISPR/Cas9 isogenic counterparts differ by trisomy of the DSCR in addition to *DYRK1A* gene dose, therefore, corrected DSCR genes may also be responsible for differences in NPC proliferation and rosette formation. Potential genes related to neural development that are duplicated within CRO1 are listed in Table 9.

Table 9: Duplicated DSCR genes that have roles in neurogenesis

Gene Name	Description	Reference
SIM2	A regulator of neurogenesis that is involved in CNS development	(195)
TTC3	E3 ubiquitin-protein ligase that regulates neuronal differentiation via actin remodelling and Golgi organisation	(196)
ETS2	A transcription factor that regulates genes involved in development and apoptosis.	(197)
PCP4	Purkinje cell protein 4 is plays an important role in synaptic plasticity and may have roles in ventricle formation.	(198)

4.11. Limitations

Though a simple and clean trisomy reduction of *DYRK1A* was not achieved, the unforeseen event of pT21 excision shed light on new ways to use genome editing techniques for microduplication correction in cultured cells. A caveat of this, however, is that non-homologous end joining is error prone and commonly causes indels at the target site, which in this case, produced segmental trisomy "corrected" cells with heterozygous gene mutations.

Upon identification of pT21 correction, attempts were made to identify clones with normal euploid gene copy number but without the presence of an indel at the *DYRK1A* target site. This was however a laborious task as the clones picked after CRISPR/Cas9 genome editing comprise a mixture of both edited and unedited iPSCs, which require further sub-cloning for purification.

Whether or not a colony is sub-cloned relies on sequence analysis and identification of indels within the mixed cell population. Since both "excised corrected" and parental CRO1 iPSCs would produce the WT *DYRK1A* exon 7 sequence, it was difficult to identify which clones to sub-clone or the number of sub-clones to screen.

An attempt at sub-cloning a WT-sequencing colony was made and a total of 12 sub-clones were picked. Unfortunately, excision of the 4.8 Mb region cannot be identified by sequence analysis alone and would require identification by SNP analysis, which is costly on a large scale.

The unique pyrosequencing assay described in this chapter was used to quantify the *DYRK1A* exon 7 SNP, but all clones were identical to CRO1 indicating no excision was present. Nevertheless, this highlights a potential future use of the pyrosequencing assay that has not been described elsewhere.

Despite not being a perfectly excised model of partial trisomy of the DCSR, this isogenic iPSC system, coupled with selective chemical DYRK1A inhibition makes it possible to identify whether a given phenotype is the result of the DSCR as a whole or *DYRK1A* gene dose.

DYRK1A inhibition with Harmine and ID8 in COs, however, is only feasible in "developed" COs since DYRK1A is required for neuron formation. Evidence for this can be found in studies on *Dyrk1A*$^{-/-}$ mice which are not viable at birth (156) as well as failure to neurally induce iPSCs treated with ID8 (199). As such, current follow up studies on COs involve treatment of CRO1 iPSC-derived organoids from DIV 30-90 and these will focus on phenotypes related to ageing and AD, for example Tau pathology.

Chapter 5

The paradoxical relationship between T21 and Alzheimer's Disease

The paradoxical relationship between T21 and Alzheimer's Disease

5.1. APP Duplication and Neurodegeneration in DS

Like many other organ systems in DS, the CNS is subject to accelerated ageing and most individuals develop early signs of the neuropathological changes commonly seen in the non-DS population with AD (200). These changes include accumulation of extracellular Aβ-plaques, the formation of intracellular neurofibrillary tangles, synaptic loss, and death of neuronal cells.

The main component of Aβ-plaques is the Aβ-peptide, which is a biproduct of APP processing by various secretases (65, 201). Not surprisingly, amyloid plaques are only present in DS individuals with either T21 or pT21 that includes *APP*, but not in DS individuals with pT21 of a region that does not include *APP* (78, 79).

APP proteolysis can either follow the non-amyloidogenic pathway (producing a soluble p3 fragment) or the amyloidogenic pathway (producing either the Aβ-40 or Aβ-42 fragments that tend to aggregate, causing soluble aggregates that appear to be toxic to the neurons, and eventually fall out of solution altogether) (Figure 43).

The non-amyloidogenic pathway begins with α-secretase cleavage in the middle of the Aβ-domain at Aβ-16 or -17 followed by γ-secretase cleavage. If this does not happen, cleavage of APP at Aβ-1 by the β-site APP cleaving enzyme 1 (BACE1 or β-secretase) liberates the C99 fragment, so called because it consists of the C-terminal 99 amino acids (aa).

C99 is then progressively trimmed by γ-secretase to produce Aβ peptides of different lengths (the most common being Aβ-40 or -42) and the APP intracellular domain (AICD) (202). BACE1 can also cleave APP at Aβ-11, which produces a C89 fragment that is processed by γ-secretase in the same way, producing a truncated Aβ-peptide (203) (Figure 43).

Both Aβ-40 and -42 are involved in the formation of amyloid plaques but Aβ-42 is more amyloidogenic due to its higher cellular toxicity and increased ability to form fibrils (204).

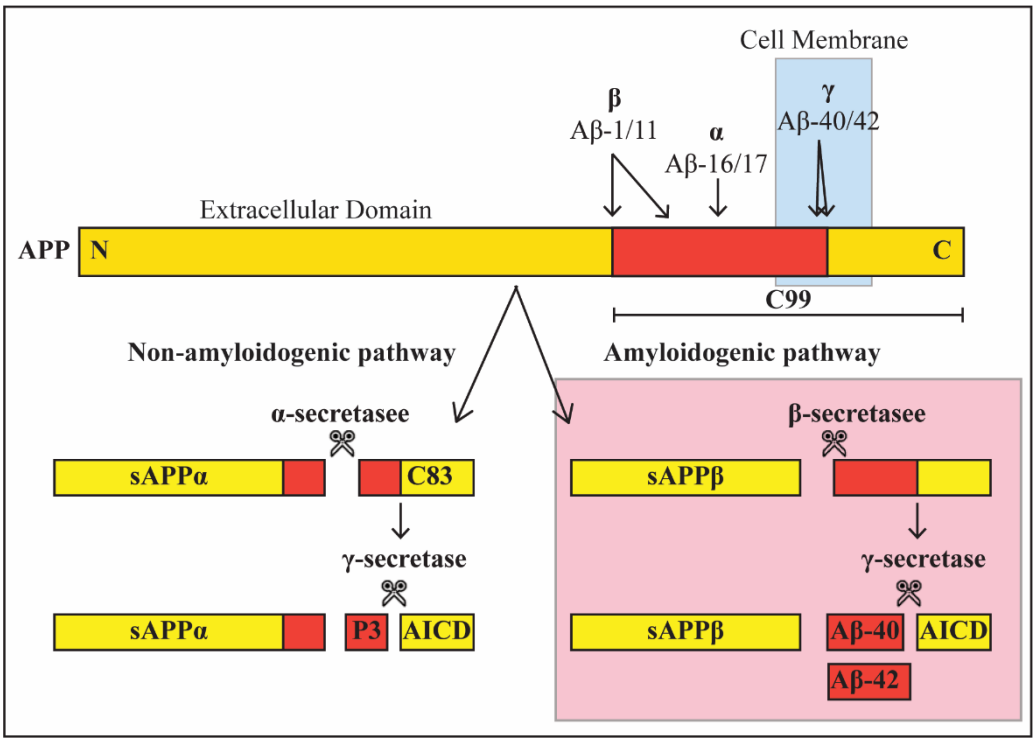

Figure 43: Amyloidogenic and non-amyloidogenic processing of APP

Simplified schematic representation of APP cleavage based on the above in text references. Cleavage by α-secretase followed by γ-secretase at the cell membrane leads down the non-amyloidogenic pathway. Here a soluble p3 peptide is produced. Cleavage by β-secretase followed by γ-secretase at the cell membrane leads down the amyloidogenic pathway, resulting in the formation of an insoluble Aβ peptide. AICD: APP intracellular domain.

The presence of an additional copy of *APP* in T21 causes increased APP expression and subsequent increased Aβ production and deposition. The same feature is observed in non-DS individuals with *APP* duplication alone (dup-*APP)* and in individuals with pT21 that includes *APP* (76).

This phenotype was recapitulated *in vitro* using 2D neurons derived from isogenic T21 and euploid iPSCs (128). The T21 iPSC-derived neurons displayed higher levels of total amyloid staining and increased deposition of Aβ-containing material both in and around T21 neurons (128). Furthermore, 3D COs generated from D21C3 and T21C5 iPSCs of the same isogenic system recapitulate this phenotype with significantly more APP staining in T21 (Figure 44).

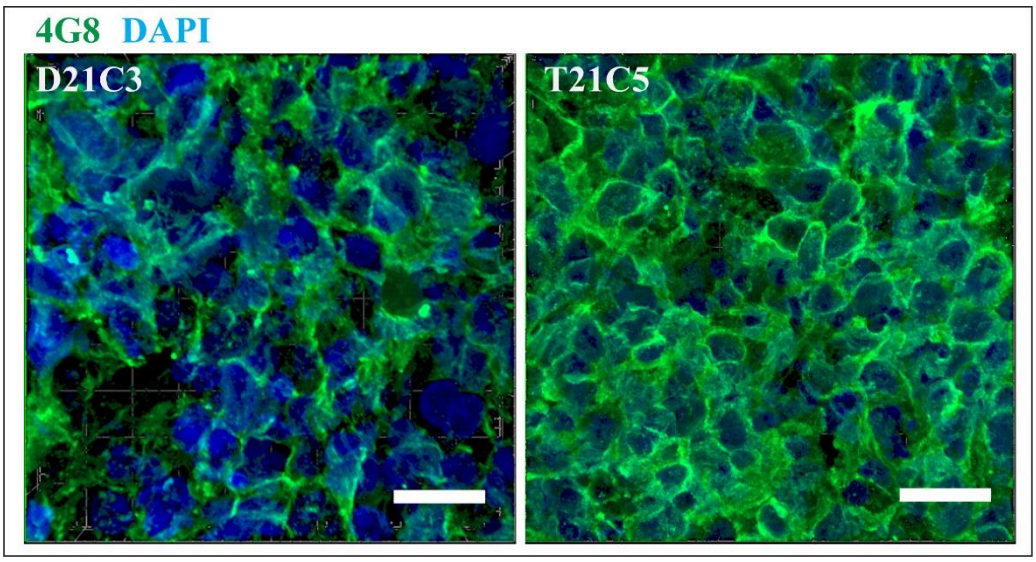

Figure 44: APP expression in D21 vs T21 Cerebral organoids

Comparison of APP between isogenic euploid (D21C3) and DS (T21C5) iPSC-derived cerebral organoids at DIV 100. Immunostaining with 4G8 detects both full length APP and Aβ but does not detect non-pathological metabolites, which are formed by cleavage within the antibody epitope. Scale bars represent 10 µm. Image adapted from (131)

The amyloid hypothesis proposes that an imbalance between production and clearance of Aβ, leads to its accumulation and is the driving force behind AD pathogenesis (14). This hypothesis holds true for individuals with mutations of the *APP* gene that favour APP cleavage by β- or γ-secretases (205, 206), individuals with dup-*APP*, which increases overall APP and therefore Aβ levels (76), and individuals with presenilin mutations that enhance the amyloidogenic processing of APP (207). The amyloid hypothesis is however controversial because not all elderly patients with Aβ-plaques develop the cognitive decline observed in AD (208).

A similar paradox has been observed in individuals with DS. Like dup-*APP*, all individuals with DS and three copies of *APP* develop Aβ pathology. However, despite 100% of individuals with dup-*APP* developing AD-like dementia by age 65, approximately 30% of individuals with DS and three copies of *APP* do not develop AD-dementia (76). This confounding effect has been recapitulated in COs generated from different individuals with DS and an individual with dup-*APP* using iPSCs previously generated in the Nizetic lab and published within the enclosed paper (131).

For example, 100 DIV iPSC-derived COs from a non-DS male with familial early onset AD caused by dup-*APP* (APOE 3/3) displayed AD-like amyloid pathology visualised with AmyloGlo. Likewise, iPSC-derived COs from a male individual with DS (QM-DS3) who is of the APOE 3/4 genotype displayed AD-like amyloid pathology at 100 DIV. The APOE status of an individual can influence their risk developing AD. Compared to APOE3, APOE4 is associated with increased AD

risk and APOE2 is associated with reduced AD risk. QM-DS3 iPSCs were reprogrammed from hair follicles collected from the patient at age 37, one year after diagnosis of early onset AD dementia.

Some COs, however, do not develop amyloid pathology. These include T21C5 iPSC-derived COs from an individual with mosaic DS and unknown dementia status (APOE 3/4) and iPSC derived COs from YA093, which was generated and described in Chapter 3-3.3 from a patient with DS caused by pT21 that does not include *APP* (Figure 45).

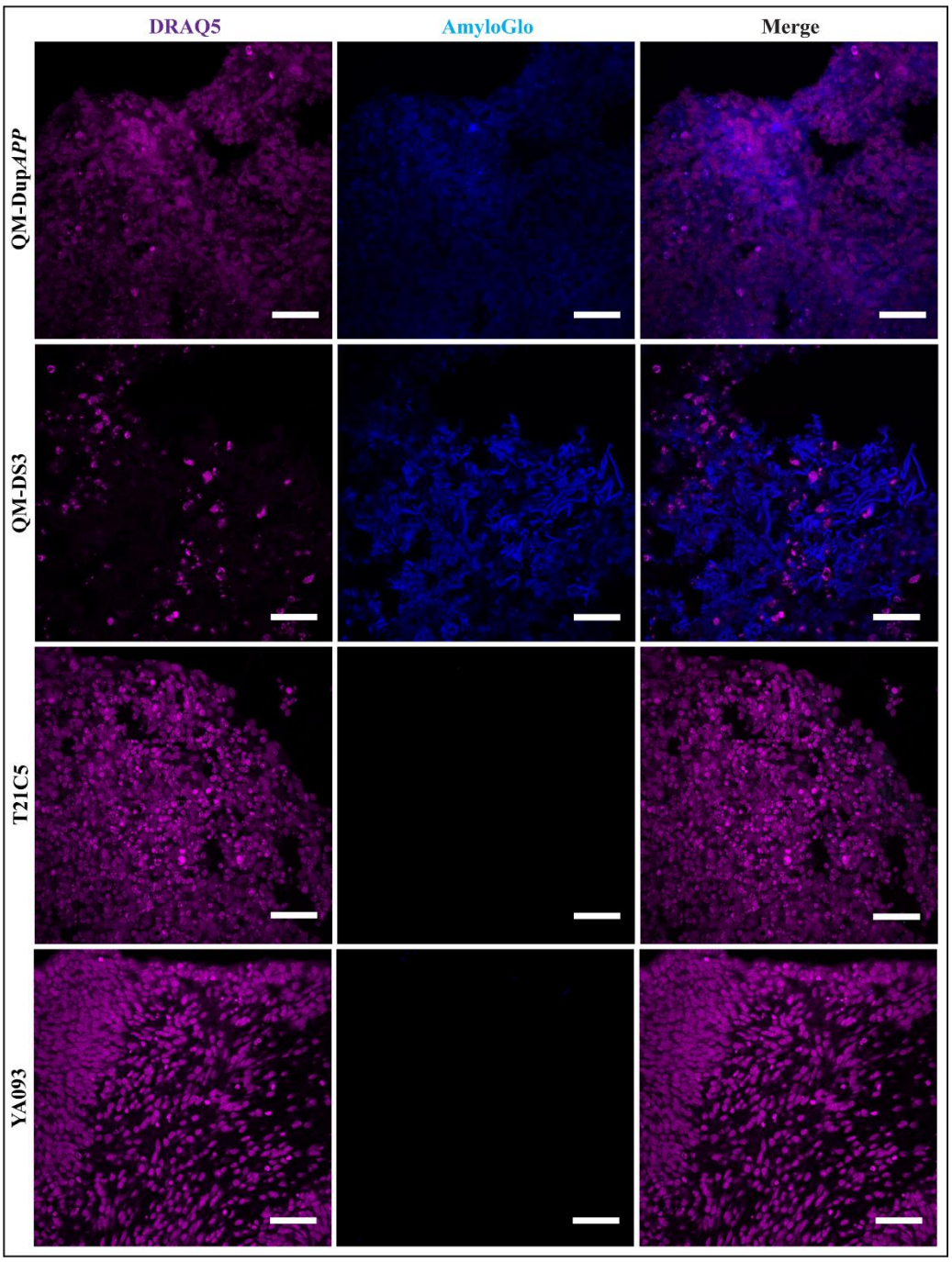

Figure 45: Amyloid-like pathology in COs generated from individuals with DS

AmyloGlo positive aggregates can be seen in DIV 100 COs from Dup-APP (compact plaques) and QM-DS3 (diffuse plaques). COs of the same age generated from T21C5 and YAO93 do not display AmyloGlo positive Aβ-plaques. DRAQ5 was used to label nuclei. Scale bars represent 20 µm. Parts of this figure have been published in (131)

To further understand the paradoxical relationship between *APP* triplication and the development of AD pathology, we sought to identify whether other trisomic genes on HSA21 modulate APP processing by either preventing the formation or increasing the clearance of Aβ and therefore protecting some individuals with DS from developing AD dementia.

A candidate gene is *BACE2*, which is a homolog to *BACE1* located on chromosome 11. The role of BACE2 in APP proteolysis is not yet fully understood but data previously generated in the Nizetic lab on the Aβ-peptide profiles of conditioned media (CM) from T21, dup-*APP* and euploid COs indicated that triplication of *BACE2* produces double the amount of non-amyloidogenic peptides with BACE2 cleavage signatures relative to the total amyloidogenic peptides. Non-amyloidogenic peptides with BACE2 cleavage signatures, were defined as: Aβ1-19 (putative θ-secretase cleavage product) and Aβ1-20 and Aβ1-34 (putative products produced from Aβ degradation by BACE2) whereas amyloidogenic peptides were defined as: Aβ1-38, Aβ1-39, Aβ1-40 and Aβ1-42. No significant difference was observed in this ratio between D21 and dup-*APP (131)*.

A similar pattern was seen *in vivo* by analysis of CSF from individuals with DS compared with age matched controls and provoked the hypothesis that genetic correction of *BACE2* trisomy in DS iPSCs would remove the protective mechanisms that prevent the formation of amyloid pathology in DS.

5.2. Targeting *BACE2* exon 3 in T21C5 iPSCs

T21C5 iPSCs were targeted with the *BACE2* exon 3 CRISPR/Cas9 plasmid with the aim of editing a single copy of *BACE2* while maintaining the rest of the chromosome in trisomy.

CRISPR/Cas9 targeted iPSCs were enriched by blasticidin treatment and the two surviving colonies were expanded for cryopreservation and DNA analysis by Sanger sequencing. A single clone (Clone 2.3) harboured an on target seven bp deletion and was colony purified by limiting dilution. Five sub-clones expanded from single cells were picked (Clone 2.3, sub-clones 1-5) and one of these contained a seven bp deletion (Figure 46A). This purified cell line was renamed (T21C5Δ7).

Maintenance of HSA21 trisomy was confirmed by SNP analysis, and no other major chromosomal rearrangements were visible following CRISPR/Cas9 genome modification (Figure 46B). Sequence trace decomposition by TIDE identified 65.3% of the sequenced PCR product contained WT sequence and 25.4% contained a seven bp deletion (Figure 46C).

Pluripotency in the T21C5Δ7 iPSCs was assessed by immunofluorescence after CRISPR/Cas9-targeting. The cells displayed positive staining for each of the four markers of pluripotency (OCT4, Tra-1-60, Tra-1-81 and SSEA4) (Figure 47).

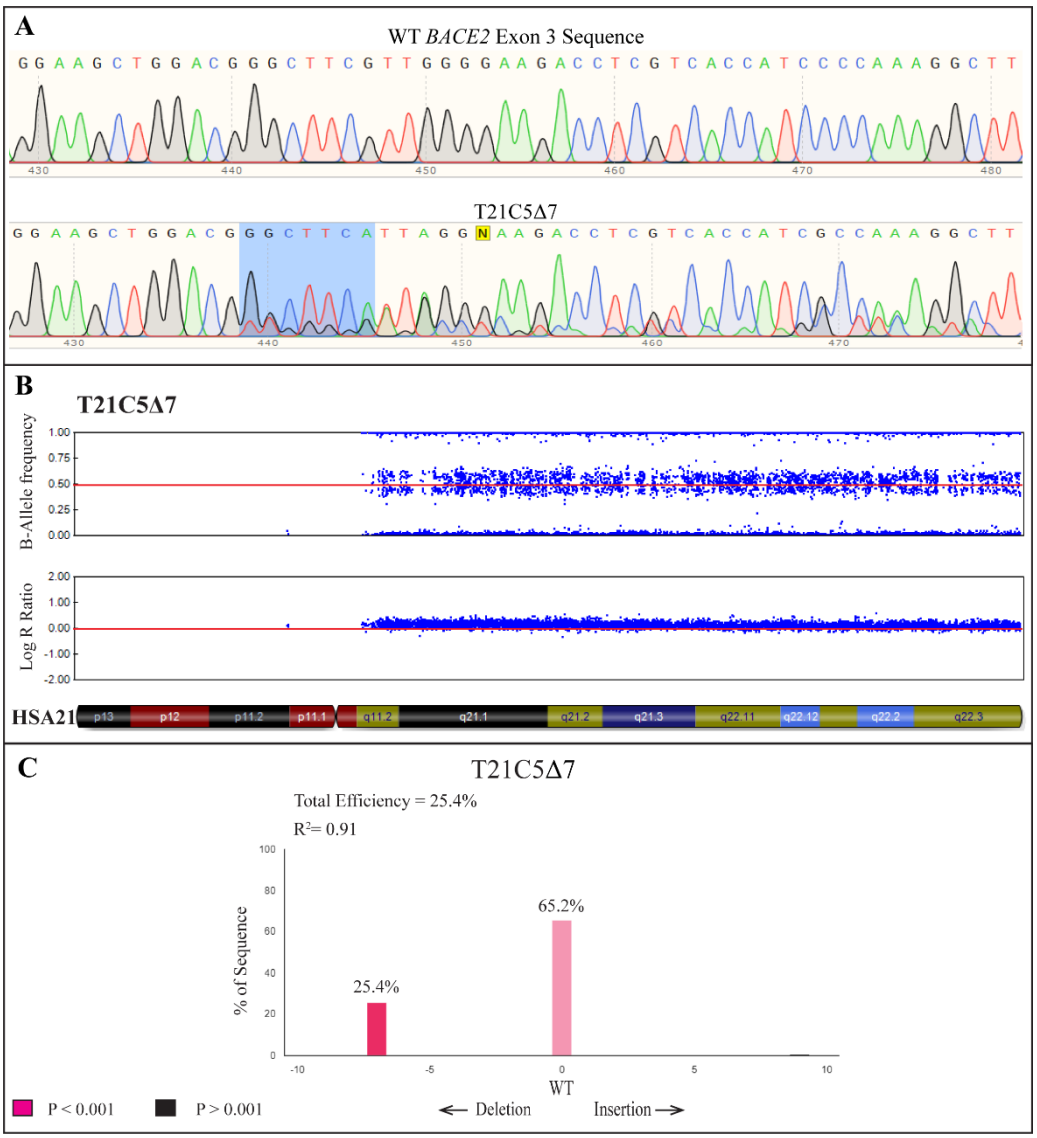

Figure 46: BACE2 targeting in T21C5 iPSCs

A: Sanger sequencing analysis of the PCR amplified *BACE2* exon 3 target site. **Top:** The WT sequence. **Bottom:** T21C5Δ7 sequence with the seven deleted nucleotides highlighted in blue. Two peaks represent the presence of both WT and edited sequence trace.

B: SNP analysis of HSA21 on genomic DNA from T21C5Δ7 iPSCs. HSA21 was maintained in trisomy as indicated by B-allele frequencies for AAA, AAB, ABB and BBB alleles and a $\log_2$ ratio of greater than zero.

C: Graph generated by the TIDE webtool. WT sequence was retained in 65.2% of the sequence trace whereas 25.4% contained the 7bp deletion.

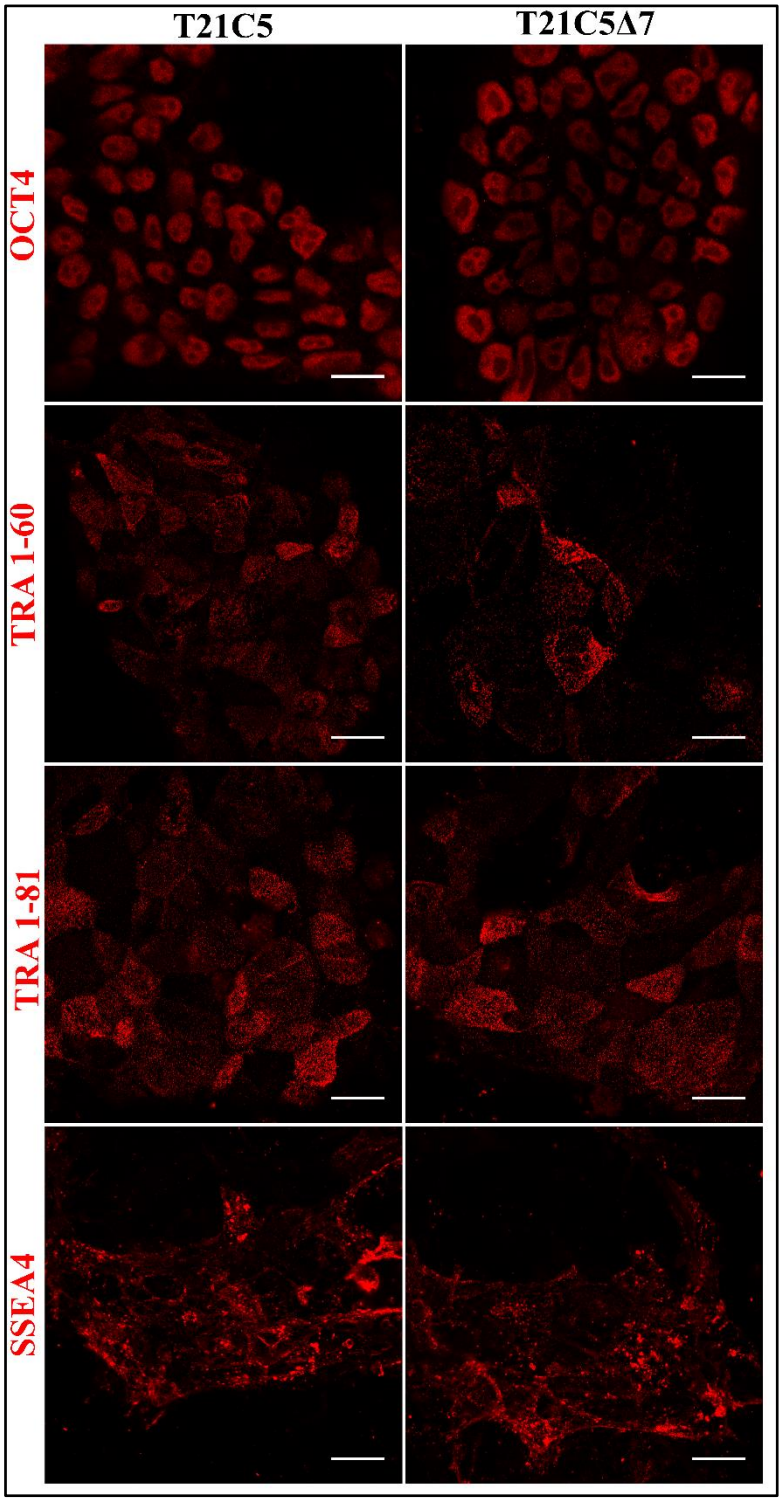

Figure 47: Pluripotency staining of the parental T21C5 and CRISPR-targeted T21C5Δ7 iPSCs

Representative confocal images of the parental T21C5 and the CRISPR/Cas9 edited T21C5Δ7 iPSCs immunostained for markers of pluripotency. Tra 1-60, Tra 1-81 and SSEA4 are localised to the cell surface, and OCT4 is nuclear. Scale bars represent 20µm.

5.3. Confirmation of single allele targeting

Since Sanger sequencing is not a quantitative analysis method, we developed a unique assay using restriction digest to quantify the number of alleles modified by CRISPR/Cas9. A single HpyCH4IV restriction site (ACGT) was identified in the WT PCR product and cleavage of this 732bp product would produce two smaller products of 439 and 293 bp respectively. The seven base pair deletion, however, created a second *de novo* HpyCH4IV restriction site. Digestion of PCR amplified DNA from the Δ7 allele produces three cleavage products of 439, 32 and 254 bp respectively (Figure 48A).

As expected, WT cell lines: parental D21C3, T21C5, and its sub-clones 1-4 did not produce the additional band of 254bp. Both the mixed parental T21C5 2.3 cell line as well as sub-clone 5 (T21C5Δ7) produced the band at 254bp but this was fainter in the mixed parental cell line (Figure 48B)

Bands were quantified using ImageJ. Since all three alleles will produce the 439bp band despite the presence or absence of the seven bp deletion, this served as an internal control and the 293 and 254 bp fragments were normalised to it. This revealed that the 293 bp band was equivalent to 60% of the 439 bp band (ratio of 2:3). The 32bp fragment is too small to resolve by agarose gel electrophoresis (Figure 48C).

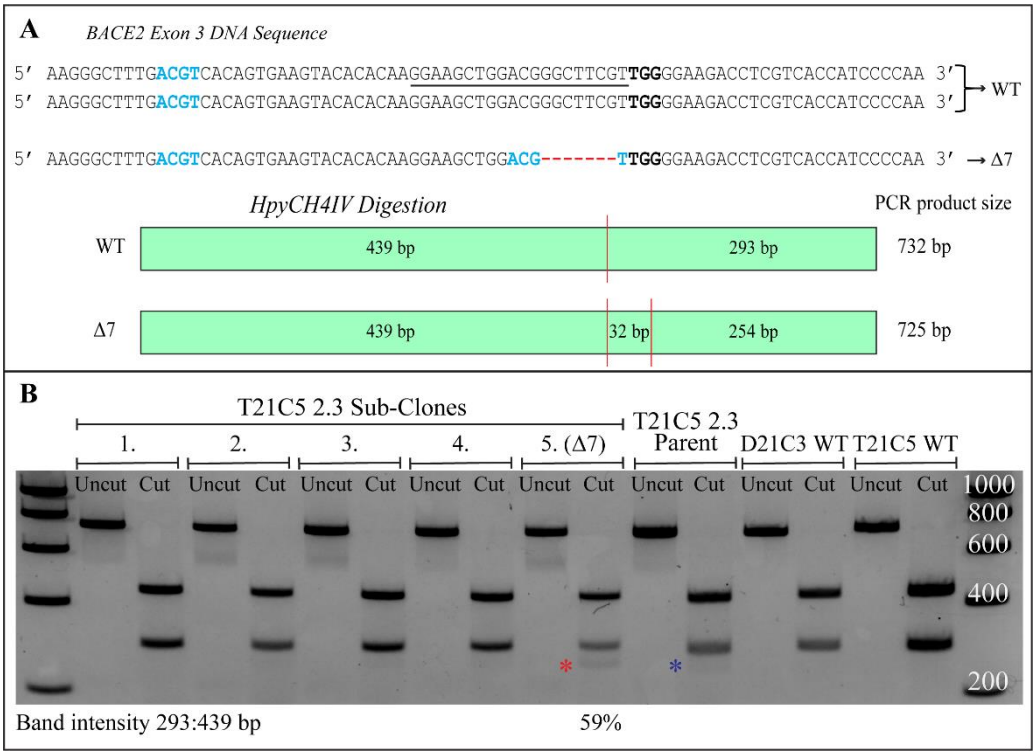

Figure 48: HpyCH4IV *restriction digest of BACE2 CRISPR/Cas9-targeted iPSCs*

A: Top: A segment of the PCR-amplified *BACE2* exon 3 target site. The gRNA (underlined) and its adjacent PAM site (bold) is indicated on the WT allele. The seven bp deletion (red dashes) creates a second *de novo* HpyCH4IV restriction site (ACGT, blue). Bottom: A schematic representation of the HpyCH4IV digested 732 bp PCR product. Red lines indicate HpyCH4IV restriction sites.

B: Agarose gel electrophoresis of full the length 732 bp PCR product (uncut) and the HpyCH4IV digested PCR product (cut). T21C5 2.3 colony purified sub-clones are labelled 1-5. Only sub-clone 5, which is T21C5Δ7 produces the 254 bp cleavage product (red asterisk). This band is also faintly visible in the unpurified T21C5 clone 2.3 (blue asterisk).

5.4. BACE2 Protein analysis

The CRISPR/Cas9 target site lies within the protease domain of BACE2 (Figure 49A). *In silico* analysis of DNA translation in T21C5 and T21C5Δ7 revealed that the 7bp deletion produces nonsense amino acids followed by a premature stop codon (Figure 49B)

Immunoblotting for the C-terminal of human BACE2 was performed in duplicate (n=2) using iPSC lysates from T21C5Δ7 and T21C5 unedited iPSCs (representative western blot displayed in Figure 49C). The same experiment was independently validated on an additional n=2 samples.

Intensities of the β-actin normalised bands were calculated on a total of n=4 blots using ImageJ software. The total actin normalised BACE2 signal was reduced by approximately 35% in T21C5Δ7 compared with unedited T21C5 iPSCs (Figure 49D). Statistical significance (P=0.0468) was calculated by unpaired t-test using GraphPad Prism Software 6.0.

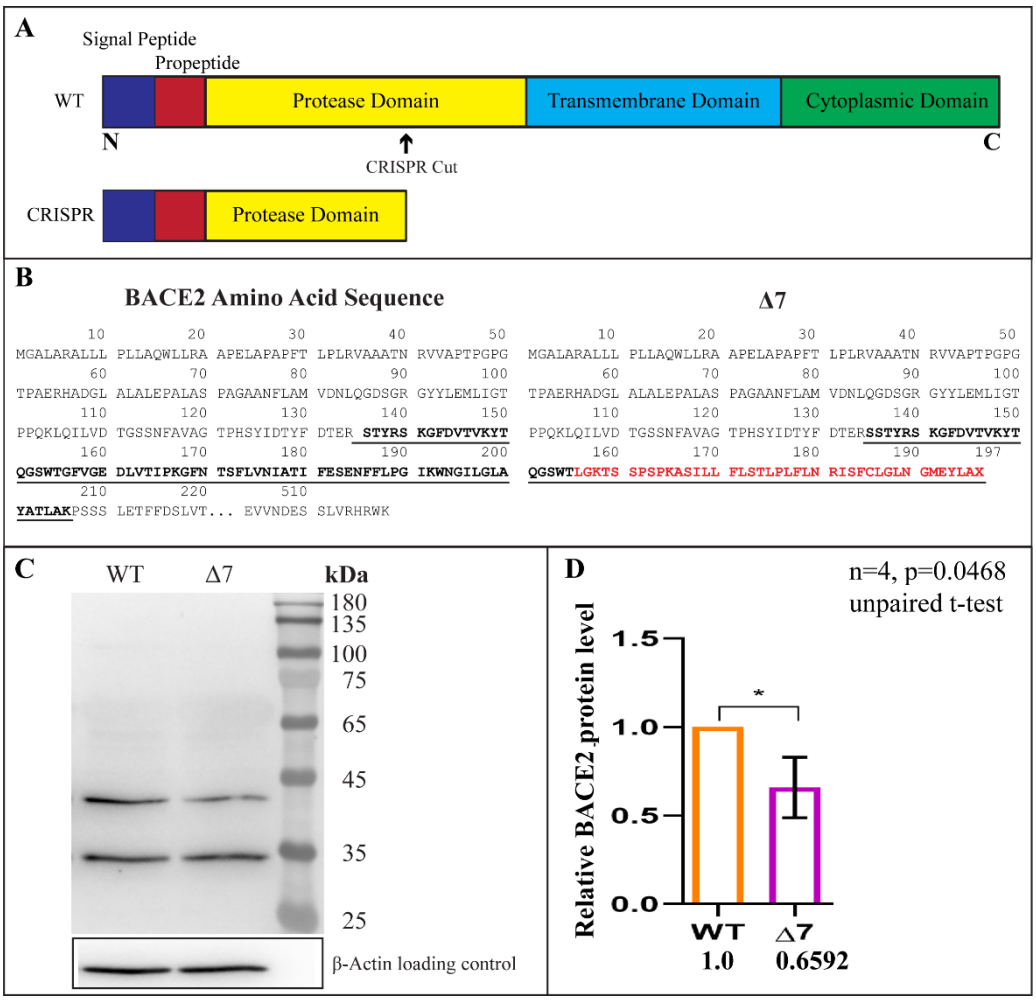

Figure 49: The 7bp BACE2 exon 3 deletion reduced BACE2 protein levels

A: A Schematic representation of the protein domain structure of human BACE2 produced using the UniProtKB database (https://www.uniprot.org/uniprot/Q9Y5Z0). The region in which a premature stop codon would cause a truncated protein falls within the protease domain.

B: Simplified amino acid sequences of *in silico* translated WT and Δ7 DNA sequences. Exon 3 is underlined, and nonsense amino acids caused by the 7 bp deletion are shown in red.

C &D: Representative western blot of WT and Δ7 iPSC lysates probed with the BACE2 C-terminal antibody (C) and the combined average reduction in BACE2 signal calculated on n=4 western blots (D). Two isoforms of BACE2 are visible just below 45 and 35 kDa respectively. β-actin was used as a loading control. Western blots were verified in two independent experiments and the combined BACE2 signal was reduced by 35% in T21C5Δ7 hiPSC lysates compared with T21C5. Error bars: standard error, P values: unpaired t-test. Data published in (131)

5.5. Normalisation of BACE2 copy number provokes AD-like pathology and skews the non-amyloidogenic Aβ peptide ratios in Cerebral Organoids

Reduction of *BACE2* copy number from three to two in T21C5 iPSCs provoked early AD-like pathology in COs by 48 DIV. No pathology was visible in the parental T21C5 COs (Figure 50A&B). Amyloid pathology was visualised with two different amyloid specific dyes: Thioflavin S, which stains both β-amyloid plaques and neurofibrillary tangles (209) and AmyloGlo, which is a newer highly specific marker of amyloid plaques (210).

By 96 DIV, amyloid pathology in T21C5Δ7 COs was denser and accompanied by large scale cell death and neuronal loss. This is indicated by the reduction in DRAQ5 positive nuclei surrounding amyloid plaques. The same pathology was absent in COs generated from the parental T21C5 iPSCs at the same or older organoid age (100 DIV).

Quantification of the number of DAPI positive nuclei was performed on eight representative figures from the same z-stack in a total of three COs per condition. T21C5Δ7 COs displayed less nuclei compared with T21C5 parental COs and this was significantly reduced at 96 DIV ($p=0.0001$). Significantly less nuclei were also observed when comparing 96 DIV with 48 DIV in the T21C5Δ7 cell line ($p=0.001$) (Figure 50C).

Conditioned media (CM) from the parental T21C5 and T21C5Δ7 COs (48DIV) was collected, and IP-MS was performed by a specialist collaborator.

CM from T21C5Δ7 COs, which contain disomic levels of BACE2, contained significantly less putative BACE2-AβDP products (Aβ1-20 & Aβ1-34) as well as significantly less total BACE2-related non-amyloidogenic peptides (Aβ1-19, Aβ1-20 & Aβ1-34) relative to amyloidogenic peptides (Aβ1-38, Aβ1-39, Aβ1-40 & Aβ1-42). Statistics were calculated by a two-tailed t-test and error bars represent standard error (Figure 50D).

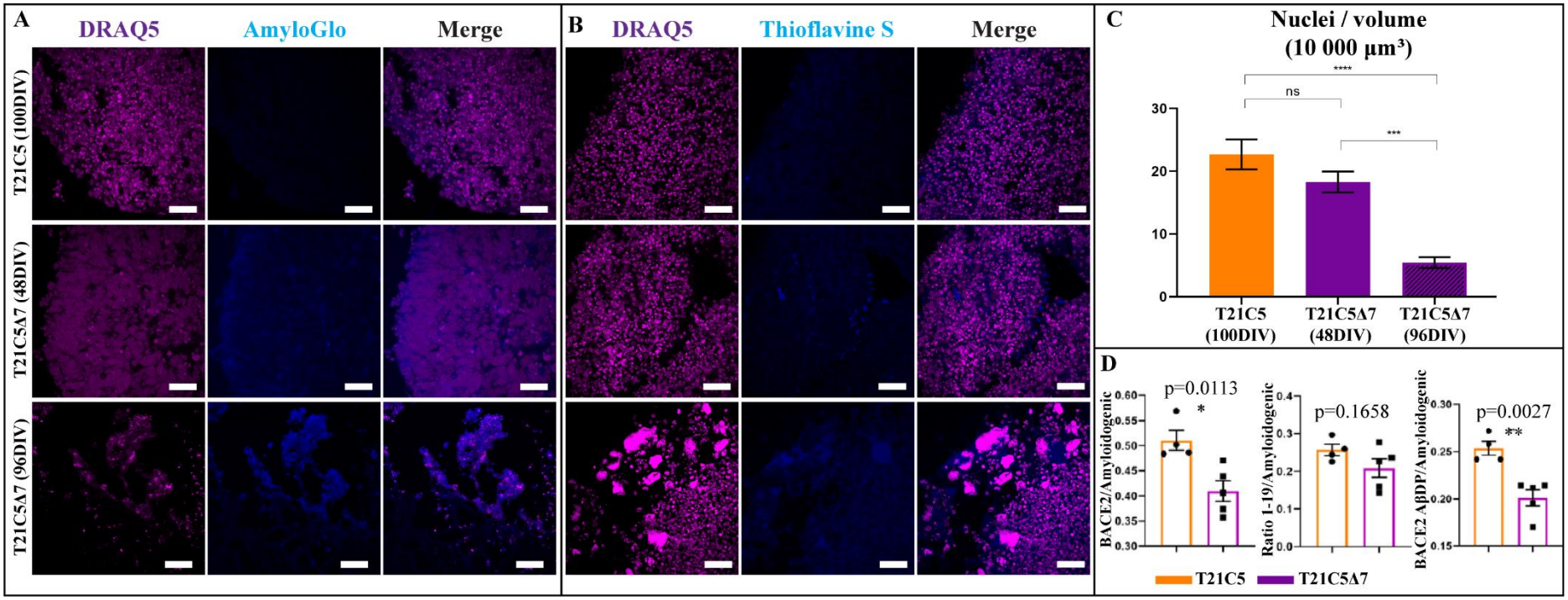

Figure 50: Amyloid pathology in T21C5 vs T21C5Δ7

Representative histological sections of T21C5 and T21C5Δ7 COs stained with DRAQ5 (nuclear dye) and the amyloid specific dyes: AmyloGlo (**A**) or Thioflavine S (**B**). T21C5 COs did not show any signs of pathology at 100DIV. T21C5Δ7 displayed amyloid pathology as early as 48 DIV and a large amount of cell death by 96 DIV. Scale bars represent 10µm. (**C)** Quantification of the number of DAPI positive nuclei was performed by IMARIS on eight representative figures from each z-stack in a total of three COs per condition. Statistical significance was calculated by standard one-way ANOVA followed by Tukey's multiple comparison test. Error bars: SEM. Modified from the figures published in (131). (**D)** Non-amyloidogenic peptides with BACE2 cleavage signatures/amyloidogenic peptide ratios after IP-MS on CM from T21C5 and T21C5Δ7 COs. P-values: two-tailed t-test. Error bars: SEM.

5.6. Increased detection level of Aβ-deposits following antigen retrieval by formic acid

Antigen retrieval by pre-treatment of fixed histological sections with formic acid is a widely used method to enhance the detection level of Aβ-deposits and is essential for detection of highly aggregated and insoluble Aβ material (211, 212).

To confirm that the plaques in T21C5Δ7 COs were aggregated amyloidogenic material, histological sections of COs were treated with 87% formic acid prior to immunostaining with either Thioflavin S and the Aβ-40/-42 end specific antibodies (BA27/BC05) or Thioflavin S and the Aβ specific antibody (4G8).

This procedure drastically increased staining with the aforementioned antibodies in the T21C5Δ7 COs and therefore confirmed the presence of insoluble extracellular Aβ deposits (Figure 51).

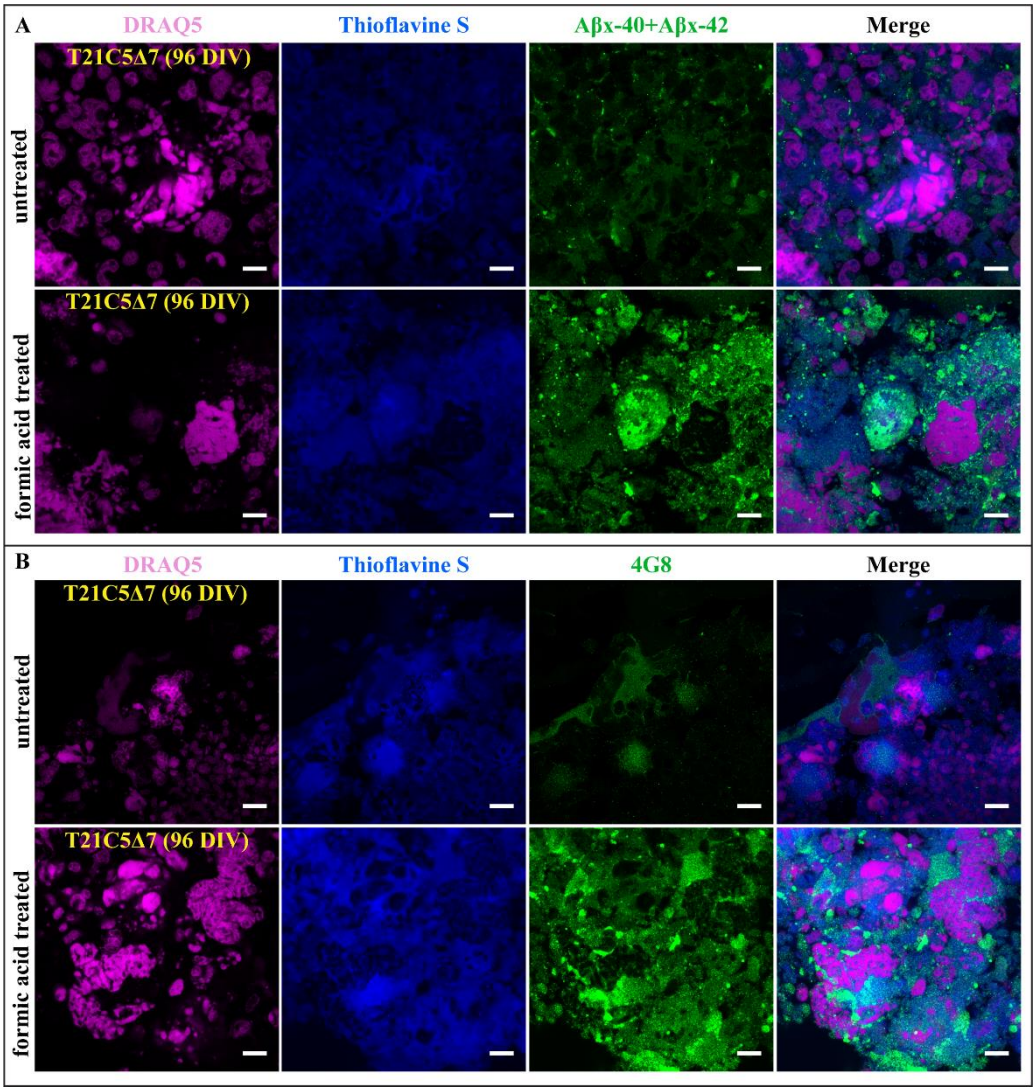

Figure 51: Increased detection level of Aβ-deposits following antigen retrieval by formic acid

Representative histological sections of DIV 96 COs untreated or treated with 87% formic acid. Pre-treated sections were stained with either Thioflavin S and Aβ-40/-42 end specific antibodies (**A**) or Thioflavin S and 4G8 (**B**). In both cases, pre-treatment with formic acid loosened highly aggregated Aβ-peptides, which exposed the antibody binding epitopes and enhanced the signal. The plaques produced by T21C5Δ7 COs are therefore insoluble Aβ material. Scale bars represent 10µm.

5.7. Hyperphosphorylated and conformationally altered Tau species are present in T21C5Δ COs

Hyperphosphorylated tau was recognised by immunohistochemical staining with AT8 (213, 214). Positive staining was observed in T21C5Δ7 COs at both 48 and 96 DIV. More AT8-positive aggregates were however present in older 96 DIV COs. At higher magnification, hyperphosphorylated tau is intraneuronal as indicated by AT8 positive staining in both the neural soma and neurites (Figure 52A).

Conformationally altered or pathological forms of Tau were visualised by immunofluorescence with the TG3 antibody (215). The parental T21C5 COs did not contain conformationally altered Tau whereas both 48 and 96 DIV T21C5Δ7 COs did (Figure 52B). As with the hyperphosphorylated tau, conformationally altered tau increased with CO age.

The relative increase in conformationally altered Tau in T21C5Δ7 COs compared with T21C5 unedited COs was independently verified by western blot with the same antibody in 83DIV COs (Figure 52D). A total of four western blots were done using lysates from a pool of three COs each and bands were quantified by standard densitometry and normalised to their corresponding β-actin value. Samples were then normalised to the parental T21C5 value for each blot (n=4) and statistical significance was calculated using a Student's T-test.

T21C5Δ7 COs contained significantly more conformationally altered Tau (p=0.0127) despite the presence of fewer neurons as indicated by a lower signal of the general neuronal marker, 3R-Tau (Figure 52Figure 52 (next page): BACE2 reduction in T21C5Δ7 provoked the formation of both conformationally altered and hyperphosphorylated Tau in COs

D).

Immunohistochemical staining with Gallyas revealed the presence of neuritic plaque-like features (positive intraneuronal signal with plaque-like associated neurites) in 96 DIV T21C5Δ7 but not the parental T21C5 COs (Figure 52C). A section from the brain of an AD patient was used for comparison as a positive control.

Figure 52 (next page): BACE2 reduction in T21C5Δ7 provoked the formation of both conformationally altered and hyperphosphorylated Tau in COs

A: Positive immunohistochemical staining with AT8 (hyperphosphorylated tau) indicates the presence of plaque-like structures at 48 DIV. A whole organoid slice (left) displaying a plaque-like structure (arrow), scale bar = 500 μm. Zoom in of three different z-slices (Z1-3, 1 μm interval), scale bar = 20 μm. AT8 positive neurites from a section of a T21C5Δ7 96 DIV CO (right). Scale bar = 10 μm.

B: TG3 immunofluorescence displaying conformationally altered tau (red) in COs from T21C5Δ7 at 48 and 96 DIV but not in T21C5 parental at 100 DIV. DAPI was used as a counter stain. Increased TG3 positive neurons are present in T21C5Δ7 at 96 DIV. Scale bars represent 50 μm.

C: Gallyas staining of 100 DIV T21C5 parental COs and human AD brain showing negative and positive signal respectively (top). T21C5Δ7 COs display neurons with strong signal and plaque-like associated neurites (bottom). Scale bars represent 50 μm.

D: Representative western blots of lysates from T21C5 and T21C5Δ7 COs at 83DIV (n=4 each) probed with TG3 (conformationally altered tau) and 3R-Tau (general 3 repeat tau). Lysates from human AD tissue from a 75-year-old is shown for comparison. The relative amount of pathologically conformed Tau was calculated by normalisation of the band signal intensities to the β-actin loading control. T21C5Δ7 displayed significantly higher levels of TG3 compared with T21C5 ($p=0.0127$). Blot reproduced from (131) .

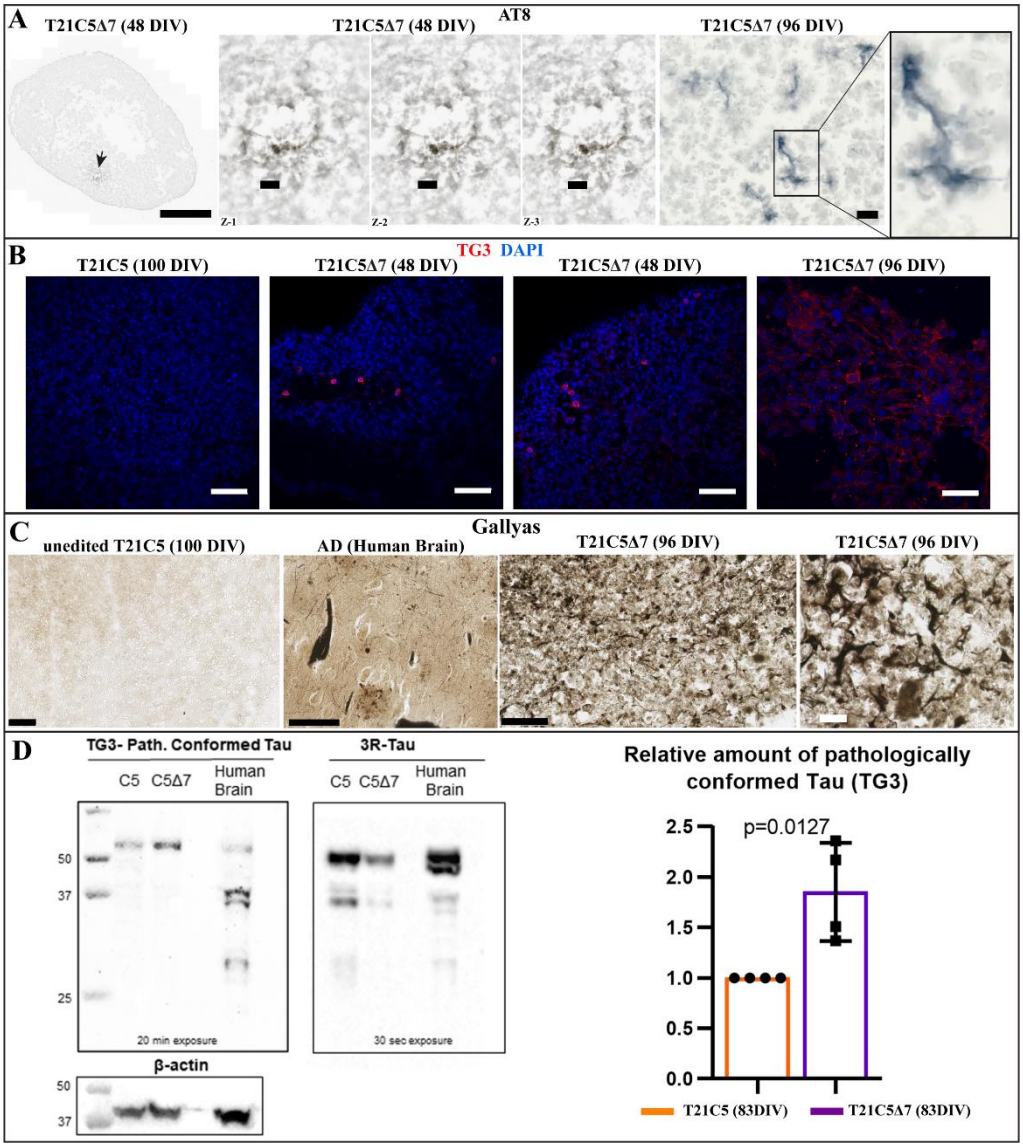
A
T21C5Δ7 (48 DIV)
AT8
T21C5Δ7 (48 DIV)
T21C5Δ7 (96 DIV)
Z-1
Z-2
Z-3
B
TG3 DAPI
T21C5 (100 DIV)
T21C5Δ7 (48 DIV)
T21C5Δ7 (48 DIV)
T21C5Δ7 (96 DIV)
C
Gallyas
unedited T21C5 (100 DIV)
AD (Human Brain)
T21C5Δ7 (96 DIV)
T21C5Δ7 (96 DIV)
D
TG3- Path. Conformed Tau
C5 C5Δ7 Human Brain
3R-Tau
C5 C5Δ7 Human Brain
50
37
25
20 min exposure
30 sec exposure
β-actin
50
37
Relative amount of pathologically conformed Tau (TG3)
p=0.0127
2.5
2.0
1.5
1.0
0.5
0.0
T21C5 (83DIV)
T21C5Δ7 (83DIV)

5.8. Summary and Discussion

AD is a condition characterised by progressive and irreversible neurodegeneration. It is the sixth-leading cause of death and the most common cause of dementia in elderly patients (216, 217). AD is typically associated with advanced age in the general population, but it can also occur below the age of 60 and is therefore subdivided into two categories: early onset AD (EOAD) or late onset AD (LOAD).

EOAD is a rare form, that is most commonly familial (FEOAD). At present, highly penetrant mutations that cause FEOAD have been identified in three genes: presenilin 1 and 2 (*PSEN1* and *PSEN2*), which are the catalytic components of the γ-secretase complex and make up 6% and 1% of cases respectively, and *APP* mutations or deletions, which make up 1% and 3% of cases respectively (217, 218). These mutations, however, account for only 10-15% of FEOAD cases, leaving the majority with an undetermined cause (217, 219).

Aside from duplications of *APP*, which increases the amount of substrate available to produce the Aβ-peptide, most known mutations alter APP proteolysis in such a way that production of insoluble Aβ is favoured (217, 220). It is therefore not surprising that almost 50% of the drug candidates for AD currently in clinical trials aim to inhibit Aβ production via β- or γ- secretase modulation (202).

The β-secretase, which is responsible for the first step in APP proteolysis emerged as an attractive candidate for therapeutic prevention of Aβ production

following two important discoveries: (1) reports of FEOAD in a Swedish family with a pathological mutation in *APP* that enhances β-secretase cleavage (221) and (2) the identification of a protective mutation in *APP* adjacent to the β-cleavage site that prevents β-secretase activity (222).

Still, little success has been achieved in clinical trials for BACE1 inhibitors, with high failure rates evident in late stage clinical trials due to poor specificity, poor efficacy or toxicity despite favourable outcomes in preclinical animal studies (223). Nevertheless, BACE1 remains a major therapeutic target for AD but less is known about its homolog, BACE2, which is often cross-inhibited by β-secretase inhibitors.

It is therefore important to identify the similarities and differences between these enzymes as well as investigate the consequences, if any, of BACE2 inhibition during AD treatment.

5.8.1. Uncovering the role of BACE2 in AD

The two enzymes, BACE1 and BACE2 share approximately 75% homology (80) but have very different expression patterns in the human body. BACE1 is highly expressed in both the brain and pancreas with lower levels present in other organs whereas BACE2 is most highly expressed in the kidney but can also be found at variable levels in most peripheral tissues (81, 82). Both enzymes, however, have equal expression levels in the human brain and like BACE1, BACE2 possess a β-secretase function albeit at a much lower level (81-85). Other differences have been observed in the APP processing abilities of the two enzymes (for clarity,

Figure 53 provides a simplified schematic summary of the key APP cleavage sites that will be discussed after).

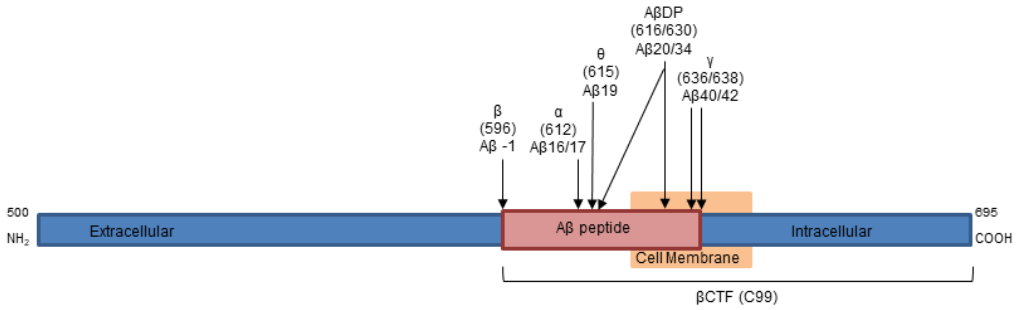

Figure 53: Simplified schematic representation of APP695 (aa500 to C-terminal)

Figure modified and reproduced with permission from (131). APP695 is the isoform predominantly expressed in neurons. Cleavage sites for each secretase (β: BACE1, α: ADAM10, θ: BACE2, γ: gamma secretase complex) are indicated with the respective amino acid in parenthesis. The Aβ peptide position is indicated for sites within this region. We investigated whether BACE2 physiologically acts as a dose sensitive θ-secretase and Aβ-degrading protease (indicated as AβDP).

Both BACE1 and BACE2 preferentially cleave the Swedish mutant APP peptide over a WT peptide in *ex vitro* enzymatic assays but cellular studies (in a stably expressing Swedish mutant APP cell line) revealed that BACE2 preferentially cleaves at positions $A\beta_{19/20}$ over the β-cleavage site (224). As such, BACE2 was labelled an alternate α-secretase that prevents Aβ formation. Later reports, however, identified BACE2 as a unique non-amyloidogenic θ-secretase that cleaves the C99 fragment at position $A\beta_{19}$ (86, 225).

Consistent with the anti-amyloidogenic findings, a report on enzymatic activities of BACE1 and BACE2 in homogenised tissue from the frontal cortex of AD-affected individuals vs age-matched controls indicated that Aβ levels correlated

significantly with the amount of BACE1 but not BACE2 and suggested that while BACE1 accounts for most Aβ production, BACE2 is not likely to be a contributor to its pathological formation in AD (81).

In line with work from Abdul-Hay and colleagues, in which they showed that at a low pH, BACE2 could degrade a synthetic Aβ-peptide at $A\beta_{20}$ and $A\beta_{34}$ we identified that BACE2 could function as an Aβ-degrading protease (AβDP) under normal physiological conditions both *in vitro* using CO conditioned media and *in vivo* using CSF from patients with DS vs dup*APP* and age-matched euploid controls (131).

Under normal circumstances, Aβ is a biproduct of APP metabolism that can be measured in cell culture conditioned medium (CM), CSF and plasma. With this in mind, CM from COs generated in three independent experiments were subject to analysis by immunoprecipitation in combination with mass spectrometry and the ratio of non-amyloidogenic peptides with BACE2 cleavage signatures ($A\beta_{1-19}$ and $A\beta_{1-20}$ and $A\beta_{1-34}$) vs the total amyloidogenic peptides ($A\beta_{1-38}$ and $A\beta_{1-39}$ and $A\beta_{1-40}$ and $A\beta_{1-42}$) was calculated. Both ratios for θ-secretase and AβDP cleavage products to the amyloidogenic peptides were 2-fold higher in the T21 COs vs the isogenic euploid controls or dup*APP*.

By comparison, the ratio of α-secretase anti-amyloidogenic cleavage products ($A\beta_{1-16}$ and $_{1-17}$), which are generated by a non HSA21-encoded enzyme, vs the total amyloidogenic peptides showed no difference between T21, D21 and dup*APP*. The fact that the ratio of BACE2 cleavage products was increased but

α-secretase cleavage products were not provided evidence that BACE2 is gene-dose-sensitive (Figure 1a of the enclosed Mol Psych paper) .

The fact that BACE2 triplication is responsible for the skewed anti-amyloidogenic peptide ratios in DS was further confirmed in *in vivo* studies using CSF from patients with T21 vs age-matched controls. These results mirrored that of the CM results (131).

5.8.2. BACE2 triplication protects against the development of AD-dementia in DS

The gene-dose-sensitive protective function of *BACE2* was further validated by way of CRISPR/Cas9 genome modification in T21C5 iPSCs. Correction of *BACE2* trisomy (*BACE2* disomy while maintaining the rest of the chromosome in trisomy) was achieved by creating a 7bp deletion within *BACE2* exon 3 and 27% - 34% reduction in protein levels was confirmed by western blot.

COs from T21C5Δ7 generated both extracellular neuritic or senile plaques (consisting of aggregated insoluble Aβ) and intracellular neurofibrillary tangles (consisting of hyperphosphorylated tau). Both of which are reproducibly absent from T21C5 iPSC-derived COs.

Peptide ratios in T21C5Δ7 CM was further investigated (131). A significant decrease in AβDP cleavage products ($A\beta_{1-20}$ and $_{1-34}$) as well as total BACE2-related non-amyloidogenic peptides ($A\beta_{1-19}$, $A\beta_{1-20}$ and $A\beta_{1-34}$) was observed relative to amyloidogenic peptides. This confirms that BACE2 triplication is responsible for their over-production in DS and suggests that some individuals

with trisomy of both *APP* and *BACE2* have reduced Aβ production and/or increased Aβ clearance (compared to individuals with DupAPP alone), protecting them from developing AD.

The same protective effects of *BACE2* trisomy were, as expected, not present in in dup-*APP* CM, possibly explaining why 100% of these individuals but only 70% of individuals with DS develop AD-dementia despite both having an additional copy of *APP*. Overall, the data suggest that in DS, the trisomy of BACE2 imparts a protective mechanism that partially counteracts the pathogenic effect trisomy of APP. As both genes also show the natural variation of expression levels in normal population, the data suggest that fluctuations in this expression level have the potential to modulate the severity and age-of-onset of AD in both DS and non-DS (general) population.

To support this, evidence from genome-wide association studies (GWAS) indicate that polymorphisms in *BACE2* are associated with individual differences in Aβ peptide levels (226, 227). Furthermore, certain haplotypes of *BACE2* have been associated with EOAD in adults with DS (228) as well as LOAD in elderly adults in the general population (229, 230).

Altogether these findings open further avenues for future study that could potentially identify a genetic cause explaining some of the remaining fraction of undetermined EOAD cases, as well as some of the LOAD risk pathogenesis.

5.8.3. T21C5Δ7 iPSC line is a potential resource for future AD research

The mechanisms surrounding Aβ clearance as well as the involvement of BACE2 in this process have, until now, been less studied. As a result, much of the therapeutic focus is being placed on prevention of Aβ formation via BACE1 inhibition. Here and in both preliminary and the follow up studies discussed above, we have shown that BACE2 can degrade Aβ in both patients with DS and COs grown *in vitro.* BACE2 therefore possesses both amyloidogenic and anti-amyloidogenic properties but further research is required to identify its predominant function. These iPSCs, along with cerebral organoids generated from them may aid future research in this area.

Aside from many unknowns surrounding Aβ clearance, the exact mechanisms by which Aβ accumulation causes neurotoxicity is controversial and requires further study (202). Not only did trisomy reduction of *BACE2* provoke formation of Aβ-plaques, but tau pathology was also observed in COs supporting the amyloid hypothesis, which suggests that the oligomerisation and aggregation of Aβ is the cause of the molecular and cellular changes that lead to neuronal dysfunction and dementia (14). However, the underlying molecular mechanisms responsible for the formation of tau pathology following *BACE2* reduction and the subsequent increase in Aβ-deposition requires further study.

This isogenic BACE2 iPSC model could therefore be a resource for *in vitro* generation of Aβ-pathology that can be further dissected to identify how altered APP processing or decreased Aβ degradation affect the kinase and phosphatase activity that leads to the formation of pathologically altered and

hyperphosphorylated tau. On another note, the use of cerebral organoids for AD disease modelling may provide an *in vitro* format for pre-clinical human drug studies that overcome translational limitations of rodent AD models.

Current drug therapies for AD only relieve symptoms despite neurological changes associated with the condition beginning as early as 20 years prior to the onset of the first symptoms (202, 231, 232). There is therefore a great need to develop treatment strategies aimed at preventing or delaying the development of AD pathology in addition to improving Aβ clearance and preventing its accumulation.

5.9. Limitations

AD is a complex condition involving interaction between both neuronal and non-neuronal cell types. A key component of AD and many other neurodegenerative disorders is neuroinflammation, which cannot be modelled in our COs due to the lack of vasculature and therefore a lack of microglia. Astrocytes develop but only in late-stage COs (typically older than 100 DIV). To better study the neuroinflammatory response and associated neuronal damage, recent advances have been made with the development of 3D triculture systems involving neurons, astrocytes and microglia (233).

In addition, the lack in vasculature often results in poor nutrient diffusion, low oxygenation, and increased cell death in the centre of the organoid, this is especially apparent in larger and/or older organoids. Without vascularization, maturation of neuronal cells is limited, which in turn limits the formation of synapses (234). To overcome these issues, chimeric models using vascularization

from the mouse brain are being developed (235, 236). Nevertheless, the COs generated here were useful for the study of our particular hypothesis since neuroinflammation and synaptic activity were beyond the scope of this thesis.

While off target mutations are always an issue with CRISPR/Cas9 experiments, this limitation was overcome by extensive testing and characterisation of the generated T21C5Δ7 cell line. In addition to sequence analysis by Sanger sequencing, TIDE analysis, restriction digest and SNP analysis, the top 10 off target sites for the BACE2 exon 3 gRNA were identified using the freely available webtool: CCTOP (144). DNA from both T21C5Δ7 and the parental T21C5 iPSCs was PCR amplified and then sequenced by Sanger sequencing. No differences in the sequences were found, indicating no off target effects at these sites in T21C5Δ7.

Chapter 6

General Discussion

General Discussion

6.1. CRISPR/Cas9 genome modification to generate a toolkit for the genetic dissection of DS-related cellular pathologies

A detailed understanding of the mechanisms by which the extra genetic material from HSA21 is associated with the phenotypic changes commonly found in people with DS and their cells is limited by the fact that relevant phenotypes occur in cells and tissues that are not accessible, such as the CNS.

Primary cells can be harvested directly from patients during routine clinical examinations, but their use *in vitro* is limited by low cell numbers, culture induced cellular changes and senescence. Primary human embryonic stem cells (hESC) on the other hand, have the potential for high-throughput disease modelling due to their ability to self-renew but their availability is limited, and they are not necessarily patient specific, nor can they be correlated with clinical data. Alternatively, induced pluripotent stem cells (iPSCs) can be derived from most cells acquired during routine clinical examinations and like hESC, iPSCs can be differentiated into most cell types for the purpose of disease modelling, tissue engineering, drug testing or cellular based therapies.

By coupling iPSCs with CRISPR/Cas9 genome modification of selected genes, isogenic controls were generated to overcome the limitation of genotypic differences between T21 and euploid individuals and hence reducing the need for comparisons of larger cohorts of individuals. This is especially important when considering the “Genetic Handicap Hypothesis,” which in this context would

suggest euploid individuals may have a higher burden of genome wide SDVs compared with living trisomic individuals.

A major goal of this thesis was to use CRISPR/Cas9 genome modification techniques to generate a toolkit of patient-derived iPSCs with isogenic controls that allow for a genetic dissection of T21-related cellular pathologies. The preferred outcome was to modify a single copy (out of three) of either *APP*, *BACE2*, *DYRK1A* or *SOD1*, thereby reducing the genes copy number from three to two.

The CRISPR approach used here relied on chance as there was no way of determining the number of alleles (if any) that would be targeted. As discussed in Section 3-6, the limiting factor is the efficiency of the gRNA, which should be carefully selected to ensure that it is not so efficient that it causes many on-target mutations on multiple alleles (as in the case of the *DYRK1A* and *APP* gRNAs) yet not too inefficient that the probability of identifying an edited clone is decreased (as in the case of *BACE2* and *SOD1* gRNAs). Fortunately, this approach was possible as neither of the four genes of interest on HSA21 are thought to be parentally imprinted (237, 238). Hence the work was not limited to targeting a specific allele. At present, only one gene on HSA21 is known to be imprinted: DSCAM (239). This would however not affect the phenotypes studied here as it does not fall within the duplicated region of CRO1, nor is it one of the four targeted genes.

That said, future work in this area may benefit from allele-specific targeting to ensure single gene mutations with a highly efficient gRNA as opposed to

homozygous KOs. Some interesting technological advances have been made in the field of CRISPR/Cas9 genome-editing since the start of this PhD project. One approach relies on the identification of a SNP within the gene of interest that either enables identification of an allele-specific PAM site or an allele-specific-gRNA (240, 241). Although the guide-specific approach offers a wider range of target sites to choose from, it was shown to lack the ability to distinguish between alleles (240). The PAM-specific approach, on the other hand confers greater specificity for the allele of interest but it is limited by the need for a specific genotype (for example, NGG as in the case of the SpCas9) (240). It is important to note that possible failure of the guide-specific approach could be attributed to the use of the normal SpCas9 endonuclease, which has a lesser ability to discriminate between single base pair differences in gRNA sequences compared with the high-fidelity version used here (124).

To tackle this approach, future work could make use of more recently developed gRNA design tools that incorporate patient-specific genetic variation into gRNA design, such as the AlleleAnalyzer (242). This tool allows one to identify areas in which the reference genome differs from the patient-specific genome. This not only increases the efficacy of the gRNA but could also increase the chances of single allele-targeting. Unfortunately, this tool was not available at the start of this PhD project.

6.2. A toolkit of modified T21 and pT21 iPSCs

A panel of isogenic iPSC lines were generated by CRISPR/Cas9 genome modification of either *APP, BACE2, DYRK1A* or *SOD1* that when compared with their unedited isogenic trisomic or disomic counterparts enable identification of individual gene dose differences. Additionally, isogenic T21 and D21 HyPer-Mito or HyPer-Cyto stably transduced cells were generated to uncover oxidative stress differences caused by the additional whole copy of HSA21. These iPSCs provide a proof of principal that increased cellular H_2O_2 caused by T21 can be modelled in undifferentiated iPSCs. Coupled with CRISPR/Cas9 genome modification, HyPer stably expressing cell lines allow one to study the contribution of the gene of interest to cellular H_2O_2 levels. At present only a heterozygous mutation of *SOD1* in euploid HyPer-mito expressing iPSCs was generated. Although the cells are not relevant for DS research, the cells are a useful resource to model the contribution of SOD1 to mitochondrial H_2O_2 and further investigate the role of SOD1 in ALS pathogenesis.

Genotype to phenotype mapping of HSA21 genes by clinical analysis of pT21 cases has been an important source of knowledge for linking genomic imbalances to individual phenotypes. Due to the rarity of cases, only one iPSC line from a patient with pT21 has been published thus far but *in vitro* cellular phenotypes were not studied further (243). Adding to this for future genotype to phenotype mapping studies, two sets of iPSCs from two different cases of pT21 have been generated and described in Chapters 3 (YA093) and 4 (CRO1).

In vitro clinical comparisons of different cases of pT21 are limited by two important factors: firstly, the endpoints of each duplicated segment are unique to each individual, which adds complexity to comparisons between individuals (244), secondly, phenotypes unrelated to HSA21 gene duplications may be involved since most pT21 is caused by chromosomal translocations that are often associated with other unbalanced non-HSA21 genomic rearrangements (114, 244).

For genotype to phenotype studies involving the DSCR, CRO1 iPSCs and its genetically modified isogenic counterparts were used to study the DNA damage phenotype. In the genome edited cell lines, the entire micro-duplicated region was successfully excised with CRISPR/Cas9, thereby producing isogenic models of partial trisomy of the DSCR. All three cell lines should contain the same genomic rearrangements found in the patient. One caveat, however, is that the CRISPR/Cas9 modified cell lines contain an artifact of DSCR excision, which lies within *DYRK1A* exon 7. Here, a non-sense mutation causes a heterozygous *DYRK1A* KO. *DYRK1A* gene dose differences can, however, be confirmed or ruled out with the added use of DYRK1A specific chemical inhibition in the unedited CRO1 cell line. Additionally, comparisons of WT CRO1 with CRO1Δ1 and CRO1Δ5 can be further scrutinized by assessment of the same phenotype using the isogenic D21C3, T21C5, T21C5DYRK1A-Het and T21C5DYRK1A KO iPSCs. In doing so, one could deduce whether the given phenotype is caused by *DYRK1A*, other DSCR genes or genes in other regions of HSA21.

The ability of iPSCs to differentiate into a wide array of cell types was utilised to model neurodevelopment and AD by cerebral organoid differentiation. During CO development, iPSCs spontaneously differentiate and self-organise into layers of the developing cerebral cortex, which broadly resemble different regions of the brain. These include ventricle-like cavities with a surrounding ventricular zone and distinct inner and outer sub-ventricular zones (245). COs are therefore superior to 2D neuronal cultures as they provide cells with the three-dimensional spatial cues that are necessary to better recapitulate human brain development *in vitro*. The effect of DSCR excision and *DYRK1A* reduction on early brain development was studied using this 3D system. More specifically, differences in total organoid size and organoid cortical folds were quantified between cell lines and consistent with previous studies, *DYRK1A* gene dose was identified as an important factor in NSC induction.

Aside from early neurogenesis, 3D organoid models generated from FEOAD (caused by a *PSEN1* mutation) and DS iPSCs have recently been proven to recapitulate features of AD pathology (216). Studies of AD pathogenesis had previously relied on the use of transgenic mouse models with knock-in of *APP* or *PSEN1* genes carrying familial mutations (234). These are however, limited by their translational potential, which is evident by the number of therapeutic compounds with favourable pre-clinical results in mice but failed clinical trials in humans (246).

Additionally, it is difficult to study the relationship between Aβ accumulation and Tau hyperphosphorylation in these models as they do not develop Tau

pathology without the integration of Tau mutations (234, 247). The COs generated from T21C5Δ7 do however, recapitulate both major hallmarks of AD: amyloid plaques and neurofibrillary tangles, opening avenues for further study on the relationship between these phenotypes.

Additionally, CO sections from 48 and 96 DIV indicate a progressive accumulation of Aβ and conformationally altered Tau leading to extensive neuronal loss by 96 DIV. In our organoid system, the triad of AD-like pathologies appears to be consequentially linked; inhibition of the production of Aβ prevents not only the extracellular amyloid plaque like accumulations but also the conformationally altered Tau and neuronal loss phenotypes. This build-up of AD-like pathological features in T21C5Δ7 COs may aid future studies aimed at identifying the underlying molecular changes that lead to toxicity and neuronal loss in late-stage AD.

6.3. Alzheimer's Disease and accelerated brain ageing

Though AD is considered a condition displaying one type of accelerated ageing in the general population, its underlying cause in DS is more likely genetic imbalance rather than simply accelerated ageing. This is because individuals with DS will only develop AD if they have *APP* triplication. Hence, *APP* triplication is essential for the development of early onset AD even in conditions of accelerated AD, such as DS (78, 79, 244).

However, the combined effects of accelerated ageing and *APP* triplication could speed up AD onset in DS (37, 244). Since EOAD occurs in most but not all individuals with DS, other polymorphic genes both on HSA21 and genome-wide

with biological roles in AD pathology have been proposed to influence the age of onset of AD (226, 244).

Additionally, a large percentage of EOAD in the general population has no known genetic cause, highlighting the importance of identifying other genes involved in its progression. As discussed in Chapter 5, the ability of BACE2 to both prevent Aβ formation as well as directly degrade it could prevent its build up in individuals with DS. However, 70% of the individuals with DS who have triplication of both *APP* and *BACE2* develop AD-dementia, suggesting the protective effects of BACE2 are more complex than simply having three copies of the gene.

Evidence of individual genotype specific factors have been described in two studies associating polymorphisms in *BACE2* with LOAD in the general population (229) and EOAD in DS (228). *BACE2* polymorphisms are thought to be related to the age of onset of AD-dementia (228), which could play a role by either enhancing the protein's pathogenic role (e.g., β-cleavage abilities) or diminishing its protective role (e.g., θ-site cleavage or Aβ degradation abilities). However, the effect of individual SNPs on BACE2 function is yet to be studied.

Nevertheless, impairments in BACE2 could account for some of the EOAD cases with an unknown genetic cause. BACE1 and BACE2 are members of the aspartic protease family (248). It is therefore important to consider the possible negative side effects of BACE2 inhibition during therapeutic inhibition of its homolog, BACE1. Likewise, the effect of human immunodeficiency virus (HIV) antiretroviral treatments on BACE2 should be considered since many of these

drugs target the HIV protease, which is a member of the same family and shares structural homology with BACE1 (249).

Still, identification of FEOAD gene mutations is important to understand the underlying molecular mechanisms leading to AD pathogenesis, which is important to develop clinical strategies aimed at delaying or slowing down AD progression. Much work, however, remains to be done to identify these mutations.

6.4. Understanding biological ageing via trisomy 21

Normal biological ageing is characterised by the dysregulation of various cellular pathways including: the DNA damage and repair response, mitochondrial dysfunctions, chromatin dysfunction and disorganisation, and increased ROS among others (250). All of these are dysregulated in cells and tissues from individuals with DS. T21 therefore, provides a unique model to study age-related pathologies by allowing researchers to narrow the focus down to a specific chromosome or chromosome regions as in the case of the DSCR in CRO1.

Features of accelerated ageing, such as age-related DNA CpG methylation patterns have been observed at both foetal and early post-natal stages in the blood and brains of both human and mouse models of DS (29, 51). These DNA CpG methylation patterns are considered an “epigenetic clock” that can be correlated with chronological age (244, 251).

Interestingly, the authors observed that individuals with DS displayed accelerated ageing during foetal and early post-natal development but there was no evidence

of accelerated epigenetic ageing during adult life, suggesting a higher initial epigenetic starting age is established early on but the rate of epigenetic ageing remains constant throughout (51, 244).

This points to the possibility that a portion of the accelerated ageing observed in DS stems from a developmentally controlled process with the first features appearing in stem and progenitor cells. Consistent with this, a body of work indicates that stem cell dysregulation is responsible for the development of blood and testicular cancer in DS (252). Likewise, our findings in in Chapter 4 provides evidence that features of accelerated ageing, such as increased DNA damage, can be examined at the level of embryonic stem cells DS iPSCs. In addition, we have shown that correction of the DSCR can reverse this phenotype. We have also highlighted the potential involvement of DYRK1A kinase activity in the DNA damage/repair process by way of DYRK1A chemical inhibition.

Further investigation to identify the molecular mechanisms controlling stem cell ageing and how this predisposes one to age-related conditions may therefore provide insight into both conditions of accelerated ageing such as DS and Hutchinson Gilford Progeria as well as normal biological ageing. Furthermore, understanding how and why cells age will facilitate the development of therapeutic targets to prevent onset or delay the progression of age-related conditions.

An example of this is AD, whereby current treatments are palliative and cannot currently prevent or stop its progression.

6.5. T21-related phenotypes: potential for further study

The first set of iPSCs with T21 were reprogrammed from fibroblasts of two male patients with DS (253). Since then, many reports describing the generation of T21 iPSCs from various starting cell types and using different reprogramming methods have been published [Reviewed in: (254)]. In most reports, the effect of T21 on phenotypes such as myeloid leukaemia, neurogenesis and Alzheimer's disease-related pathologies were evaluated against age matched euploid controls.

The iPSCs generated here provide a toolkit of modified isogenic T21 and D21 iPSCs that allow further study of DS cellular phenotypes beyond those already discussed, while reducing the need for large cohorts of individuals due to variations in genotypic backgrounds.

For example, the *DYRK1A* modified iPSCs from both the isogenic and CRO1 system may provide insight to the molecular mechanisms underlying the reduced incidence of angiogenesis-related solid tumours or the increased number of vascular abnormalities in DS. Aside from its role in neurogenesis, *DYRK1A* overexpression is involved in disrupted angiogenesis, impaired cardiac development and a decreased risk of solid tumours in DS individuals at all age groups (252, 255, 256). Interestingly, high levels of *Dyrk1a* were observed in the developing heart of euploid mice (257) and more recently, *DYRK1A* was shown to play a role in cardiac remodelling via regulation of ASF and cardiomyocyte hypertrophy via regulation of NFAT (258, 259).

In addition, individuals with *DYRK1A* haploinsufficiency syndrome have presented with congenital heart defects (260) and *Dyrk1a*$^{-/-}$ zebrafish exhibited cerebral haemorrhage and defects in angiogenesis of central arteries in the developing hindbrain (261). Here, researchers identified that *dyrk1a* plays a role in angiogenesis and cerebral vasculature formation via regulation of calcium signalling in *Dyrk1a*$^{-/-}$ zebrafish (261).

Chapter 7

Concluding Remarks

Concluding Remarks

DS, neurodevelopment, AD and accelerated ageing are all complex conditions brought on by imbalances in multiple genes and cellular processes. Whether accelerated ageing in DS is the result of disrupted repair and defence mechanisms, an accumulation of damage or a combination of both remains to be identified but studies of these processes may provide insight into normal biological ageing and related conditions. The results presented in this thesis generate a platform for cellular modelling aimed at detection, as well as genetic and mechanistic dissection of the cellular and molecular mechanisms underpinning these processes. The main conclusions can be summarised as:

1. A panel of hiPSC lines was generated. These allow isogenic comparisons interrogating the roles of gene doses of individual genes and chromosomal segments thought to be most relevant for the pathomechanisms of DS.
2. The first human isogenic model of the partial trisomy of DS critical region (DSCR) was generated by excising the entire region from one chromosome and correcting it to disomy. This is a proof of principle that CRISPR/Cas9 technology can be used to interrogate segments of the chromosome in trisomy.
3. A proof of principle for the capability of these cellular models to dissect the roles of trisomies of the chromosomal segment and several individual HSA21 genes for cellular phenotypes (underpinning neurodevelopmental

derangements, mitochondrial ROS metabolism defects, accelerated ageing and AD-like neurodegeneration) was shown.

4. It has been demonstrated for the first time that the cellular phenotypes of increased accumulation of mitochondrial H_2O_2, as well as increased accumulation of DNA double-strand break repair foci caused by T21, are visible in undifferentiated iPSCs.
5. Trisomic overdose of DYRK1A kinase activity has been identified as one of the causes of the increased accumulation of DNA double-strand break repair foci, independent of the actions of other HSA21 candidate genes outside of the DSCR (such as RCAN1, RUNX1, USP16 and SOD1).
6. The role of *BACE2* trisomy as a dose-dependent repressor of AD-like pathology in cerebral organoids has been uncovered, providing a formal proof on an isogenic human iPSC model for the observations made through the analysis of Aβ peptide profiles and genetic studies.

7.1. Future work

Possible future experiments relevant to each cell line have been mentioned and discussed in their respective chapters.

7.2. Papers and Talks during my PhD candidature

- I presented Chapter 1 as a poster at the first LKC Medicine Research Retreat (2017).
- I presented work from Chapter 4 as part of an Organoids seminar hosted by STEMCELL Technologies (November 2019).
- I presented work from Chapter 4 in the LKCMedicine Scientific Seminar Series via Zoom (June 2020).
- A manuscript involving work from Chapter 5 has been published in Molecular Psychiatry (131), which is enclosed in Appendix II.
- I co-wrote a book chapter entitled: *Modelling Down Syndrome in cells: from stem cells to organoids*, which has been published in Progress in Brain Research (254) and enclosed in Appendix II.

Bibliography

1. Hardy K, Hardy PJ. 1(st) trimester miscarriage: four decades of study. Transl Pediatr. 2015;4(2):189-200.

2. Jia CW, Wang L, Lan YL, Song R, Zhou LY, Yu L, et al. Aneuploidy in Early Miscarriage and its Related Factors. Chin Med J (Engl). 2015;128(20):2772-6.

3. Andrews T, Dunlop W, Roberts DF. Cytogenetic studies in spontaneous abortuses. Hum Genet. 1984;66(1):77-84.

4. Dai R, Xi Q, Wang R, Zhang H, Jiang Y, Li L, et al. Chromosomal copy number variations in products of conception from spontaneous abortion by next-generation sequencing technology. Medicine (Baltimore). 2019;98(47):e18041.

5. Gug C, Ratiu A, Navolan D, Dragan I, Groza IM, Papurica M, et al. Incidence and Spectrum of Chromosome Abnormalities in Miscarriage Samples: A Retrospective Study of 330 Cases. Cytogenet Genome Res. 2019;158(4):171-83.

6. Xu J, Chen M, Liu QY, Hu SQ, Li LR, Li J, et al. Detecting trisomy in products of conception from first-trimester spontaneous miscarriages by next-generation sequencing (NGS). Medicine (Baltimore). 2020;99(5):e18731.

7. Wellesley D, Dolk H, Boyd PA, Greenlees R, Haeusler M, Nelen V, et al. Rare chromosome abnormalities, prevalence and prenatal diagnosis rates from population-based congenital anomaly registers in Europe. Eur J Hum Genet. 2012;20(5):521-6.

8. Antonarakis SE, Lyle R, Dermitzakis ET, Reymond A, Deutsch S. Chromosome 21 and down syndrome: from genomics to pathophysiology. Nat Rev Genet. 2004;5(10):725-38.

9. Lejeune J, Turpin R, Gautier M. [Mongolism; a chromosomal disease (trisomy)]. Bull Acad Natl Med. 1959;143(11-12):256-65.

10. Jacobs PA, Baikie AG, Court Brown WM, Strong JA. The somatic chromosomes in mongolism. Lancet. 1959;1(7075):710.

11. Epstein CJ. The consequences of chromosome imbalance. Am J Med Genet Suppl. 1990;7:31-7.

12. Su MT, Kuan LC, Chou YY, Tan SY, Kuo TC, Kuo PL. Partial trisomy of chromosome 21 without the Down syndrome phenotype. Prenatal diagnosis. 2016;36(5):492-5.

13. Gijsbers AC, van Haeringen A, Bosch CA, Hansson K, Verschuren M, Bakker E, et al. A subtle familial translocation t(3;21)(p26.3;q22.3): an apparently healthy boy with a 3p deletion and 21q duplication. Cytogenet Genome Res. 2010;128(4):245-9.

14. Hardy J, Selkoe DJ. The amyloid hypothesis of Alzheimer's disease: progress and problems on the road to therapeutics. Science. 2002;297(5580):353-6.

15. Ruaud L, Mignot C, Guët A, Ohl C, Nava C, Héron D, et al. DYRK1A mutations in two unrelated patients. European Journal of Medical Genetics. 2015;58(3):168-74.

16. Orrell RW, Marklund SL, deBelleroche JS. Familial ALS is associated with mutations in all exons of SOD1: a novel mutation in exon 3 (Gly72Ser). J Neurol Sci. 1997;153(1):46-9.

17. Brigida AL, Siniscalco D. Induced pluripotent stem cells as a cellular model for studying Down Syndrome. J Stem Cells Regen Med. 2016;12(2):54-60.

18. Antonarakis SE, Petersen MB, McInnis MG, Adelsberger PA, Schinzel AA, Binkert F, et al. The meiotic stage of nondisjunction in trisomy 21: determination by using DNA polymorphisms. Am J Hum Genet. 1992;50(3):544-50.

19. Salehi A, Mobley WC, Pohlman B. Encyclopedia of Neuroscience. Subject Classification: Disease and DysfunctionGenetic/chromosomal disorders: Disease and Dysfunction: Genetic/chromosomal disorders: Article Titles: D. 2009:627-34.

20. Oliver TR, Feingold E, Yu K, Cheung V, Tinker S, Yadav-Shah M, et al. New insights into human nondisjunction of chromosome 21 in oocytes. PLoS Genet. 2008;4(3):e1000033.

21. Richards BW. Investigation of 142 mosaic mongols and mosaic parents of mongols; cytogenetic analysis and maternal age at birth. J Ment Defic Res. 1974;18(3):199-208.

22. Hulten MA, Jonasson J, Iwarsson E, Uppal P, Vorsanova SG, Yurov YB, et al. Trisomy 21 mosaicism: we may all have a touch of Down syndrome. Cytogenet Genome Res. 2013;139(3):189-92.

23. Leon E, Zou YS, Milunsky JM. Mosaic Down syndrome in a patient with low-level mosaicism detected by microarray. Am J Med Genet A. 2010;152A(12):3154-6.

24. Ringman JM, Rao PN, Lu PH, Cederbaum S. Mosaicism for trisomy 21 in a patient with young-onset dementia: a case report and brief literature review. Arch Neurol. 2008;65(3):412-5.

25. Epstein CJ. Down Syndrome. In: Scriver CRBA, Sly WS, Valle D, editors. The metabolic and molecular bases of inherited disease. New York: McGraw-Hill; 2001. p. 1223–56.

26. Roizen NJ, Patterson D. Down's syndrome. Lancet. 2003;361(9365):1281-9.

27. Martin GM. Genetic syndromes in man with potential relevance to the pathobiology of aging. Birth Defects Orig Artic Ser. 1978;14(1):5-39.

28. Franceschi C, Garagnani P, Gensous N, Bacalini MG, Conte M, Salvioli S. Accelerated bio-cognitive aging in Down syndrome: State of the art and possible deceleration strategies. Aging Cell. 2019;18(3):e12903.

29. Horvath S, Garagnani P, Bacalini M, Pirazzini C, Salvioli S, Gentilini D, et al. Accelerated epigenetic aging in Down syndrome. Aging Cell. 2015;14(3):491-5.

30. Haydar TF, Reeves RH. Trisomy 21 and early brain development. Trends Neurosci. 2012;35(2):81-91.

31. Golden JA, Hyman BT. Development of the superior temporal neocortex is anomalous in trisomy 21. J Neuropathol Exp Neurol. 1994;53(5):513-20.

32. Lu J, Lian G, Zhou H, Esposito G, Steardo L, Delli-Bovi LC, et al. OLIG2 over-expression impairs proliferation of human Down syndrome neural progenitors. Hum Mol Genet. 2012;21(10):2330-40.

33. Letourneau A, Santoni FA, Bonilla X, Sailani MR, Gonzalez D, Kind J, et al. Domains of genome-wide gene expression dysregulation in Down's syndrome. Nature. 2014;508(7496):345-50.

34. Guidi S, Bonasoni P, Ceccarelli C, Santini D, Gualtieri F, Ciani E, et al. Neurogenesis impairment and increased cell death reduce total neuron number in the hippocampal region of fetuses with Down syndrome. Brain Pathol. 2008;18(2):180-97.

35. Coyle JT, Oster-Granite ML, Gearhart JD. The neurobiologic consequences of Down syndrome. Brain Res Bull. 1986;16(6):773-87.

36. Chapman RS, Hesketh LJ. Behavioral phenotype of individuals with Down syndrome. Ment Retard Dev Disabil Res Rev. 2000;6(2):84-95.

37. Head E, Silverman W, Patterson D, Lott IT. Aging and down syndrome. Curr Gerontol Geriatr Res. 2012;2012:412536.

38. Mori C, Spooner ET, Wisniewsk KE, Wisniewski TM, Yamaguch H, Saido TC, et al. Intraneuronal Abeta42 accumulation in Down syndrome brain. Amyloid. 2002;9(2):88-102.

39. Potter H, Granic A, Caneus J. Role of Trisomy 21 Mosaicism in Sporadic and Familial Alzheimer's Disease. Curr Alzheimer Res. 2016;13(1):7-17.

40. Wisniewski KE. Down syndrome children often have brain with maturation delay, retardation of growth, and cortical dysgenesis. Am J Med Genet Suppl. 1990;7:274-81.

41. Guihard-Costa AM, Khung S, Delbecque K, Menez F, Delezoide AL. Biometry of face and brain in fetuses with trisomy 21. Pediatr Res. 2006;59(1):33-8.

42. Pinter JD, Eliez S, Schmitt JE, Capone GT, Reiss AL. Neuroanatomy of Down's syndrome: a high-resolution MRI study. Am J Psychiatry. 2001;158(10):1659-65.

43. Pinter JD, Brown WE, Eliez S, Schmitt JE, Capone GT, Reiss AL. Amygdala and hippocampal volumes in children with Down syndrome: a high-resolution MRI study. Neurology. 2001;56(7):972-4.

44. White NS, Alkire MT, Haier RJ. A voxel-based morphometric study of nondemented adults with Down Syndrome. NeuroImage. 2003;20(1):393-403.

45. Pennington BF, Moon J, Edgin J, Stedron J, Nadel L. The neuropsychology of Down syndrome: evidence for hippocampal dysfunction. Child Dev. 2003;74(1):75-93.

46. Bahn S, Mimmack M, Ryan M, Caldwell MA, Jauniaux E, Starkey M, et al. Neuronal target genes of the neuron-restrictive silencer factor in neurospheres derived from fetuses with Down's syndrome: a gene expression study. Lancet. 2002;359(9303):310-5.

47. Esposito G, Imitola J, Lu J, De Filippis D, Scuderi C, Ganesh VS, et al. Genomic and functional profiling of human Down syndrome neural progenitors implicates S100B and aquaporin 4 in cell injury. Hum Mol Genet. 2008;17(3):440-57.

48. Contestabile A, Benfenati F, Gasparini L. Communication breaks-Down: from neurodevelopment defects to cognitive disabilities in Down syndrome. Prog Neurobiol. 2010;91(1):1-22.

49. Contestabile A, Fila T, Ceccarelli C, Bonasoni P, Bonapace L, Santini D, et al. Cell cycle alteration and decreased cell proliferation in the hippocampal dentate gyrus and in the neocortical germinal matrix of fetuses with Down syndrome and in Ts65Dn mice. Hippocampus. 2007;17(8):665-78.

50. El Hajj N, Dittrich M, Bock J, Kraus TF, Nanda I, Muller T, et al. Epigenetic dysregulation in the developing Down syndrome cortex. Epigenetics. 2016;11(8):563-78.

51. Mendioroz M, Do C, Jiang X, Liu C, Darbary HK, Lang CF, et al. Trans effects of chromosome aneuploidies on DNA methylation patterns in human Down syndrome and mouse models. Genome Biol. 2015;16:263.

52. Shaikh MN, Tejedor FJ. Mnb/Dyrk1A orchestrates a transcriptional network at the transition from self-renewing neurogenic progenitors to postmitotic neuronal precursors. J Neurogenet. 2018;32(1):37-50.

53. Hammerle B, Carnicero A, Elizalde C, Ceron J, Martinez S, Tejedor FJ. Expression patterns and subcellular localization of the Down syndrome candidate protein MNB/DYRK1A suggest a role in late neuronal differentiation. Eur J Neurosci. 2003;17(11):2277-86.

54. Hammerle B, Ulin E, Guimera J, Becker W, Guillemot F, Tejedor FJ. Transient expression of Mnb/Dyrk1a couples cell cycle exit and differentiation of neuronal precursors by inducing p27KIP1 expression and suppressing NOTCH signaling. Development. 2011;138(12):2543-54.

55. Takashima S, Mito T, Hashimoto K. Developmental Abnormalities of Dendrites of the Cerebral Cortical Neurons in Mental Retardation. Cong Anom. 1987;27:431-9.

56. Becker LE, Armstrong DL, Chan F. Dendritic atrophy in children with Down's syndrome. Ann Neurol. 1986;20(4):520-6.

57. de Haan JB, Susil B, Pritchard M, Kola I. An altered antioxidant balance occurs in Down syndrome fetal organs: implications for the "gene dosage effect" hypothesis. J Neural Transm Suppl. 2003(67):67-83.

58. Ighodaro OM. Molecular pathways associated with oxidative stress in diabetes mellitus. Biomed Pharmacother. 2018;108:656-62.

59. Wilcock DM. Neuroinflammation in the aging down syndrome brain; lessons from Alzheimer's disease. Curr Gerontol Geriatr Res. 2012;2012:170276.

60. Ermak G, Cheadle C, Becker KG, Harris CD, Davies KJ. DSCR1(Adapt78) modulates expression of SOD1. FASEB J. 2004;18(1):62-9.

61. Groner Y, Elroy-Stein O, Avraham KB, Schickler M, Knobler H, Minc-Golomb D, et al. Cell damage by excess CuZnSOD and Down's syndrome. Biomed Pharmacother. 1994;48(5-6):231-40.

62. Lott IT. Antioxidants in Down syndrome. Biochim Biophys Acta. 2012;1822(5):657-63.

63. Busciglio J, Yankner BA. Apoptosis and increased generation of reactive oxygen species in Down's syndrome neurons in vitro. Nature. 1995;378(6559):776-9.

64. Koran ME, Hohman TJ, Edwards CM, Vega JN, Pryweller JR, Slosky LE, et al. Differences in age-related effects on brain volume in Down syndrome as compared to Williams syndrome and typical development. J Neurodev Disord. 2014;6(1):8.

65. Masters CL, Simms G, Weinman NA, Multhaup G, McDonald BL, Beyreuther K. Amyloid plaque core protein in Alzheimer disease and Down syndrome. Proc Natl Acad Sci U S A. 1985;82(12):4245-9.

66. Glenner GG, Wong CW. Alzheimer's disease and Down's syndrome: sharing of a unique cerebrovascular amyloid fibril protein. Biochem Biophys Res Commun. 1984;122(3):1131-5.

67. Goldgaber D, Lerman MI, McBride OW, Saffiotti U, Gajdusek DC. Characterization and chromosomal localization of a cDNA encoding brain amyloid of Alzheimer's disease. Science. 1987;235(4791):877-80.

68. Robakis NK, Ramakrishna N, Wolfe G, Wisniewski HM. Molecular cloning and characterization of a cDNA encoding the cerebrovascular and the neuritic plaque amyloid peptides. Proc Natl Acad Sci U S A. 1987;84(12):4190-4.

69. Tanzi RE, Gusella JF, Watkins PC, Bruns GA, St George-Hyslop P, Van Keuren ML, et al. Amyloid beta protein gene: cDNA, mRNA distribution, and genetic linkage near the Alzheimer locus. Science. 1987;235(4791):880-4.

70. Korenberg JR, Pulst SM, Neve RL, West R. The Alzheimer amyloid precursor protein maps to human chromosome 21 bands q21.105-q21.05. Genomics. 1989;5(1):124-7.

71. Blanquet V, Goldgaber D, Turleau C, Creau-Goldberg N, Delabar J, Sinet PM, et al. The beta amyloid protein (AD-AP) cDNA hybridizes in normal and Alzheimer individuals near the interface of 21q21 and q22.1. Ann Genet. 1987;30(2):68-9.

72. Jenkins EC, Devine-Gage EA, Robakis NK, Yao XL, Brown WT, Houck GE, Jr., et al. Fine mapping of an Alzheimer disease-associated gene encoding beta-amyloid protein. Biochem Biophys Res Commun. 1988;151(1):1-8.

73. Rowe IF, Ridler MA, Gibberd FB. Presenile dementia associated with mosaic trisomy 21 in a patient with a Down syndrome child. Lancet. 1989;2(8656):229.

74. Schapiro MB, Kumar A, White B, Grady CL, Friedland RP, Rapoport SI. Alzheimer's Disease (AD) in Mosaic/Translocation Down's Syndrome (Ds) Without Mental Retardation. Neurology. 1989;39(3).

75. Puri BK, Zhang Z, Singh I. SPECT in adult mosaic Down's syndrome with early dementia. Clin Nucl Med. 1994;19(11):989-91.

76. Wiseman FK, Al-Janabi T, Hardy J, Karmiloff-Smith A, Nizetic D, Tybulewicz VL, et al. A genetic cause of Alzheimer disease: mechanistic insights from Down syndrome. Nat Rev Neurosci. 2015;16(9):564-74.

77. Carr J. Six weeks to 45 years: a longitudinal study of a population with Down syndrome. J Appl Res Intellect Disabil. 2012;25(5):414-22.

78. Prasher VP, Farrer MJ, Kessling AM, Fisher EM, West RJ, Barber PC, et al. Molecular mapping of Alzheimer-type dementia in Down's syndrome. Ann Neurol. 1998;43(3):380-3.

79. Doran E, Keator D, Head E, Phelan MJ, Kim R, Totoiu M, et al. Down Syndrome, Partial Trisomy 21, and Absence of Alzheimer's Disease: The Role of APP. J Alzheimers Dis. 2017;56(2):459-70.

80. Sun X, Wang Y, Qing H, Christensen MA, Liu Y, Zhou W, et al. Distinct transcriptional regulation and function of the human BACE2 and BACE1 genes. FASEB J. 2005;19(7):739-49.

81. Ahmed RR, Holler CJ, Webb RL, Li F, Beckett TL, Murphy MP. BACE1 and BACE2 enzymatic activities in Alzheimer's disease. J Neurochem. 2010;112(4):1045-53.

82. Bennett BD, Babu-Khan S, Loeloff R, Louis JC, Curran E, Citron M, et al. Expression analysis of BACE2 in brain and peripheral tissues. J Biol Chem. 2000;275(27):20647-51.

83. Holler CJ, Webb RL, Laux AL, Beckett TL, Niedowicz DM, Ahmed RR, et al. BACE2 expression increases in human neurodegenerative disease. Am J Pathol. 2012;180(1):337-50.

84. Stockley JH, Ravid R, O'Neill C. Altered beta-secretase enzyme kinetics and levels of both BACE1 and BACE2 in the Alzheimer's disease brain. FEBS Lett. 2006;580(28-29):6550-60.

85. Farzan M, Schnitzler CE, Vasilieva N, Leung D, Choe H. BACE2, a beta -secretase homolog, cleaves at the beta site and within the amyloid-beta region of the amyloid-beta precursor protein. Proc Natl Acad Sci U S A. 2000;97(17):9712-7.

86. Sun X, He G, Song W. BACE2, as a novel APP theta-secretase, is not responsible for the pathogenesis of Alzheimer's disease in Down syndrome. FASEB J. 2006;20(9):1369-76.

87. Abdul-Hay SO, Sahara T, McBride M, Kang D, Leissring MA. Identification of BACE2 as an avid ß-amyloid-degrading protease. Molecular Neurodegeneration. 2012;7(1):1-12.

88. FitzPatrick DR. Transcriptional consequences of autosomal trisomy: primary gene dosage with complex downstream effects. Trends in Genetics. 2005;21(5):249-53.

89. Prandini P, Deutsch S, Lyle R, Gagnebin M, Delucinge Vivier C, Delorenzi M, et al. Natural gene-expression variation in Down syndrome modulates the outcome of gene-dosage imbalance. Am J Hum Genet. 2007;81(2):252-63.

90. Popadin K, Peischl S, Garieri M, Sailani MR, Letourneau A, Santoni F, et al. Slightly deleterious genomic variants and transcriptome perturbations in Down syndrome embryonic selection. Genome Res. 2018;28(1):1-10.

91. Canzonetta C, Mulligan C, Deutsch S, Ruf S, O'Doherty A, Lyle R, et al. DYRK1A-dosage imbalance perturbs NRSF/REST levels, deregulating pluripotency and embryonic stem cell fate in Down syndrome. Am J Hum Genet. 2008;83(3):388-400.

92. Morris JK, Wald NJ, Watt HC. Fetal loss in Down syndrome pregnancies. Prenatal diagnosis. 1999;19(2):142-5.

93. Spencer K. What is the true fetal loss rate in pregnancies affected by trisomy 21 and how does this influence whether first trimester detection rates are superior to those in the second trimester? Prenatal diagnosis. 2001;21(9):788-9.

94. Creasy MR, Crolla JA. Prenatal mortality of trisomy 21 (Down's syndrome). Lancet. 1974;1(7856):473-4.

95. Potter H. Beyond Trisomy 21: Phenotypic Variability in People with Down Syndrome Explained by Further Chromosome Mis-segregation and Mosaic Aneuploidy. J Down Syndr Chromosom Abnorm. 2016;2(1).

96. Clarke CM, Edwards JH, Smallpeice V. 21-trisomy/normal mosaicism in an intelligent child with some mongoloid characters. Lancet. 1961;1(7185):1028-30.

97. Clarke CM, Ford CE, Edwards JH, Smallpeice V. 21 Trisomy/Normal Mosaicism in an Intelligent Child with Some Mongoloid Characters. Lancet. 1963;2(7319):1229.

98. Lyle R, Bena F, Gagos S, Gehrig C, Lopez G, Schinzel A, et al. Genotype-phenotype correlations in Down syndrome identified by array CGH in 30 cases of partial trisomy and partial monosomy chromosome 21. Eur J Hum Genet. 2009;17(4):454-66.

99. Hattori M, Fujiyama A, Taylor TD, Watanabe H, Yada T, Park HS, et al. The DNA sequence of human chromosome 21. Nature. 2000;405(6784):311.

100. Wahlsten D. Chapter 12 - Down Syndrome. In: Wahlsten D, editor. Genes, Brain Function, and Behavior: Academic Press; 2019. p. 137-47.

101. Antonarakis SE. 10 years of Genomics, chromosome 21, and Down syndrome. Genomics. 1998;51(1):1-16.

102. Pelleri MC, Cicchini E, Locatelli C, Vitale L, Caracausi M, Piovesan A, et al. Systematic reanalysis of partial trisomy 21 cases with or without Down syndrome suggests a small region on 21q22.13 as critical to the phenotype. Hum Mol Genet. 2016;25(12):2525-38.

103. Gardiner K, Costa AC. The proteins of human chromosome 21. Am J Med Genet C Semin Med Genet. 2006;142C(3):196-205.

104. McCormick MK, Schinzel A, Petersen MB, Stetten G, Driscoll DJ, Cantu ES, et al. Molecular genetic approach to the characterization of the "Down syndrome region" of chromosome 21. Genomics. 1989;5(2):325-31.

105. Arron JR, Winslow MM, Polleri A, Chang CP, Wu H, Gao X, et al. NFAT dysregulation by increased dosage of DSCR1 and DYRK1A on chromosome 21. Nature. 2006;441(7093):595-600.

106. Ronan A, Fagan K, Christie L, Conroy J, Nowak NJ, Turner G. Familial 4.3 Mb duplication of 21q22 sheds new light on the Down syndrome critical region. J Med Genet. 2007;44(7):448-51.

107. Delabar JM, Theophile D, Rahmani Z, Chettouh Z, Blouin JL, Prieur M, et al. Molecular mapping of twenty-four features of Down syndrome on chromosome 21. Eur J Hum Genet. 1993;1(2):114-24.

108. Olson LE, Richtsmeier JT, Leszl J, Reeves RH. A Chromosome 21 Critical Region Does Not Cause Specific Down Syndrome Phenotypes. Science. 2004;306(5696):687-90.

109. Olson LE, Roper RJ, Sengstaken CL, Peterson EA, Aquino V, Galdzicki Z, et al. Trisomy for the Down syndrome 'critical region' is necessary but not sufficient for brain phenotypes of trisomic mice. Human Molecular Genetics. 2007;16(7):774-82.

110. Pelleri MC, Cicchini E, Petersen MB, Tranebjaerg L, Mattina T, Magini P, et al. Partial trisomy 21 map: Ten cases further supporting the highly restricted

Down syndrome critical region (HR-DSCR) on human chromosome 21. Mol Genet Genomic Med. 2019;7(8):e797.

111. Schnabel F, Smogavec M, Funke R, Pauli S, Burfeind P, Bartels I. Down syndrome phenotype in a boy with a mosaic microduplication of chromosome 21q22. Mol Cytogenet. 2018;11:62.

112. Weisfeld-Adams JD, Tkachuk AK, Maclean KN, Meeks NL, Scott SA. A de novo 2.78-Mb duplication on chromosome 21q22.11 implicates candidate genes in the partial trisomy 21 phenotype. NPJ Genom Med. 2016;1.

113. Huret JL, Delabar JM, Marlhens F, Aurias A, Nicole A, Berthier M, et al. Down syndrome with duplication of a region of chromosome 21 containing the CuZn superoxide dismutase gene without detectable karyotypic abnormality. Hum Genet. 1987;75(3):251-7.

114. Korbel JO, Tirosh-Wagner T, Urban A, Chen X-N, Kasowski M, Dai L, et al. The genetic architecture of Down syndrome phenotypes revealed by high-resolution analysis of human segmental trisomies. Proceedings of the National Academy of Sciences. 2009;106(29):12031-6.

115. Korenberg JR, Chen XN, Schipper R, Sun Z, Gonsky R, Gerwehr S, et al. Down syndrome phenotypes: the consequences of chromosomal imbalance. Proc Natl Acad Sci U S A. 1994;91(11):4997-5001.

116. Doench JG, Fusi N, Sullender M, Hegde M, Vaimberg EW, Donovan KF, et al. Optimized sgRNA design to maximize activity and minimize off-target effects of CRISPR-Cas9. Nat Biotechnol. 2016;34(2):184-91.

117. Hsu PD, Scott DA, Weinstein JA, Ran FA, Konermann S, Agarwala V, et al. DNA targeting specificity of RNA-guided Cas9 nucleases. Nat Biotechnol. 2013;31(9):827-32.

118. Lancaster MA, Knoblich JA. Generation of cerebral organoids from human pluripotent stem cells. Nat Protoc. 2014;9(10):2329-40.

119. Brinkman EK, Chen T, Amendola M, van Steensel B. Easy quantitative assessment of genome editing by sequence trace decomposition. Nucleic Acids Res. 2014;42(22):e168.

120. Deutsch S, Choudhury U, Merla G, Howald C, Sylvan A, Antonarakis SE. Detection of aneuploidies by paralogous sequence quantification. J Med Genet. 2004;41(12):908-15.

121. Solovei I, Cremer M. 3D-FISH on cultured cells combined with immunostaining. Methods Mol Biol. 2010;659:117-26.

122. Espuny-Camacho I, Arranz AM, Fiers M, Snellinx A, Ando K, Munck S, et al. Hallmarks of Alzheimer's Disease in Stem-Cell-Derived Human Neurons Transplanted into Mouse Brain. Neuron. 2017;93(5):1066-81 e8.

123. Koonin EV, Makarova KS, Zhang F. Diversity, classification and evolution of CRISPR-Cas systems. Curr Opin Microbiol. 2017;37:67-78.

124. Kleinstiver BP, Pattanayak V, Prew MS, Tsai SQ, Nguyen NT, Zheng Z, et al. High-fidelity CRISPR-Cas9 nucleases with no detectable genome-wide off-target effects. Nature. 2016;529(7587):490-5.

125. Mali P, Yang L, Esvelt KM, Aach J, Guell M, DiCarlo JE, et al. RNA-guided human genome engineering via Cas9. Science. 2013;339(6121):823-6.

126. Dai WJ, Zhu LY, Yan ZY, Xu Y, Wang QL, Lu XJ. CRISPR-Cas9 for in vivo Gene Therapy: Promise and Hurdles. Mol Ther Nucleic Acids. 2016;5:e349.

127. Peng R, Lin G, Li J. Potential pitfalls of CRISPR/Cas9-mediated genome editing. FEBS J. 2016;283(7):1218-31.

128. Murray A, Letourneau A, Canzonetta C, Stathaki E, Gimelli S, Sloan-Bena F, et al. Brief Report: Isogenic Induced Pluripotent Stem Cell Lines From an Adult With Mosaic Down Syndrome Model Accelerated Neuronal Ageing and Neurodegeneration. STEM CELLS. 2015;33(6):2077-84.

129. Lana-Elola E, Watson-Scales S, Slender A, Gibbins D, Martineau A, Douglas C, et al. Genetic dissection of Down syndrome-associated congenital heart defects using a new mouse mapping panel. Elife. 2016;5.

130. Murray A, Letourneau A, Canzonetta C, Stathaki E, Gimelli S, Sloan-Bena F, et al. Brief report: isogenic induced pluripotent stem cell lines from an adult with mosaic down syndrome model accelerated neuronal ageing and neurodegeneration. Stem Cells. 2015;33(6):2077-84.

131. Alic I, Goh PA, Murray A, Portelius E, Gkanatsiou E, Gough G, et al. Patient-specific Alzheimer-like pathology in trisomy 21 cerebral organoids reveals BACE2 as a gene dose-sensitive AD suppressor in human brain. Mol Psychiatry. 2020.

132. Rovelet-Lecrux A, Hannequin D, Raux G, Le Meur N, Laquerriere A, Vital A, et al. APP locus duplication causes autosomal dominant early-onset Alzheimer disease with cerebral amyloid angiopathy. Nat Genet. 2006;38(1):24-6.

133. Dowjat WK, Adayev T, Kuchna I, Nowicki K, Palminiello S, Hwang YW, et al. Trisomy-driven overexpression of DYRK1A kinase in the brain of subjects with Down syndrome. Neurosci Lett. 2007;413(1):77-81.

134. Chen JY, Lin JR, Tsai FC, Meyer T. Dosage of Dyrk1a shifts cells within a p21-cyclin D1 signaling map to control the decision to enter the cell cycle. Mol Cell. 2013;52(1):87-100.

135. Park J, Song WJ, Chung KC. Function and regulation of Dyrk1A: towards understanding Down syndrome. Cell Mol Life Sci. 2009;66(20):3235-40.

136. Tejedor FJ, Hammerle B. MNB/DYRK1A as a multiple regulator of neuronal development. FEBS J. 2011;278(2):223-35.

137. Altafaj X, Dierssen M, Baamonde C, Marti E, Visa J, Guimera J, et al. Neurodevelopmental delay, motor abnormalities and cognitive deficits in transgenic mice overexpressing Dyrk1A (minibrain), a murine model of Down's syndrome. Hum Mol Genet. 2001;10(18):1915-23.

138. Courcet JB, Faivre L, Malzac P, Masurel-Paulet A, Lopez E, Callier P, et al. The DYRK1A gene is a cause of syndromic intellectual disability with severe microcephaly and epilepsy. J Med Genet. 2012;49(12):731-6.

139. Ji J, Lee H, Argiropoulos B, Dorrani N, Mann J, Martinez-Agosto JA, et al. DYRK1A haploinsufficiency causes a new recognizable syndrome with microcephaly, intellectual disability, speech impairment, and distinct facies. Eur J Hum Genet. 2015;23(11):1473-81.

140. Raveau M, Shimohata A, Amano K, Miyamoto H, Yamakawa K. DYRK1A-haploinsufficiency in mice causes autistic-like features and febrile seizures. Neurobiol Dis. 2018;110:180-91.

141. Tejedor FJ. Dyrk1a. In: Choi S, editor. Encyclopedia of Signaling Molecules. Cham: Springer International Publishing; 2018. p. 1447-57.

142. Belousov VV, Fradkov AF, Lukyanov KA, Staroverov DB, Shakhbazov KS, Terskikh AV, et al. Genetically encoded fluorescent indicator for intracellular hydrogen peroxide. Nat Methods. 2006;3(4):281-6.

143. Lyublinskaya O, Antunes F. Measuring intracellular concentration of hydrogen peroxide with the use of genetically encoded H2O2 biosensor HyPer. Redox Biol. 2019;24:101200.

144. Stemmer M, Thumberger T, Del Sol Keyer M, Wittbrodt J, Mateo JL. Correction: CCTop: An Intuitive, Flexible and Reliable CRISPR/Cas9 Target Prediction Tool. PLoS One. 2017;12(4):e0176619.

145. De Strooper B, Vassar R, Golde T. The secretases: enzymes with therapeutic potential in Alzheimer disease. Nat Rev Neurol. 2010;6(2):99-107.

146. Hung SY, Fu WM. Drug candidates in clinical trials for Alzheimer's disease. J Biomed Sci. 2017;24(1):47.

147. Pierrot N, Tyteca D, D'Auria L, Dewachter I, Gailly P, Hendrickx A, et al. Amyloid precursor protein controls cholesterol turnover needed for neuronal activity. EMBO Mol Med. 2013;5(4):608-25.

148. Dawkins E, Small DH. Insights into the physiological function of the beta-amyloid precursor protein: beyond Alzheimer's disease. J Neurochem. 2014;129(5):756-69.

149. Fong LK, Yang MM, Dos Santos Chaves R, Reyna SM, Langness VF, Woodruff G, et al. Full-length amyloid precursor protein regulates lipoprotein metabolism and amyloid-beta clearance in human astrocytes. J Biol Chem. 2018;293(29):11341-57.

150. Koike MA, Lin AJ, Pham J, Nguyen E, Yeh JJ, Rahimian R, et al. APP knockout mice experience acute mortality as the result of ischemia. PLoS One. 2012;7(8):e42665.

151. Gallagher JJ, Zhang X, Ziomek GJ, Jacobs RE, Bearer EL. Deficits in axonal transport in hippocampal-based circuitry and the visual pathway in APP knock-out animals witnessed by manganese enhanced MRI. Neuroimage. 2012;60(3):1856-66.

152. Huo Q, Chen M, He Q, Zhang J, Li B, Jin K, et al. Prefrontal Cortical GABAergic Dysfunction Contributes to Aberrant UP-State Duration in APP Knockout Mice. Cereb Cortex. 2017;27(8):4060-72.

153. Southam KA, Stennard F, Pavez C, Small DH. Knockout of Amyloid beta Protein Precursor (APP) Expression Alters Synaptogenesis, Neurite Branching and Axonal Morphology of Hippocampal Neurons. Neurochem Res. 2019;44(6):1346-55.

154. Tejedor F, Zhu XR, Kaltenbach E, Ackermann A, Baumann A, Canal I, et al. minibrain: a new protein kinase family involved in postembryonic neurogenesis in Drosophila. Neuron. 1995;14(2):287-301.

155. Arbones ML, Thomazeau A, Nakano-Kobayashi A, Hagiwara M, Delabar JM. DYRK1A and cognition: A lifelong relationship. Pharmacol Ther. 2019;194:199-221.

156. Fotaki V, Dierssen M, Alcantara S, Martinez S, Marti E, Casas C, et al. Dyrk1A haploinsufficiency affects viability and causes developmental delay and abnormal brain morphology in mice. Mol Cell Biol. 2002;22(18):6636-47.

157. Kim OH, Cho HJ, Han E, Hong TI, Ariyasiri K, Choi JH, et al. Zebrafish knockout of Down syndrome gene, DYRK1A, shows social impairments relevant to autism. Mol Autism. 2017;8:50.

158. Lui JH, Hansen DV, Kriegstein AR. Development and evolution of the human neocortex. Cell. 2011;146(1):18-36.

159. Neumann F, Gourdain S, Albac C, Dekker AD, Bui L, Dairou J, et al. DYRK1A inhibition and cognitive rescue in a Down syndrome mouse model are induced by new fluoro-DANDY derivatives. Scientific Reports. 2018;8(1):2859.

160. Pare B, Lehmann M, Beaudin M, Nordstrom U, Saikali S, Julien JP, et al. Misfolded SOD1 pathology in sporadic Amyotrophic Lateral Sclerosis. Sci Rep. 2018;8(1):14223.

161. Zinman L, Liu HN, Sato C, Wakutani Y, Marvelle AF, Moreno D, et al. A mechanism for low penetrance in an ALS family with a novel SOD1 deletion. Neurology. 2009;72(13):1153-9.

162. Gimeno A, Garcia-Gimenez JL, Audi L, Toran N, Andaluz P, Dasi F, et al. Decreased cell proliferation and higher oxidative stress in fibroblasts from Down Syndrome fetuses. Preliminary study. Biochim Biophys Acta. 2014;1842(1):116-25.

163. Sansovic I, Ivankov AM, Bobinec A, Kero M, Barisic I. Chromosomal microarray in clinical diagnosis: a study of 337 patients with congenital anomalies and developmental delays or intellectual disability. Croat Med J. 2017;58(3):231-8.

164. Belichenko NP, Belichenko PV, Kleschevnikov AM, Salehi A, Reeves RH, Mobley WC. The "Down syndrome critical region" is sufficient in the mouse model to confer behavioral, neurophysiological, and synaptic phenotypes characteristic of Down syndrome. J Neurosci. 2009;29(18):5938-48.

165. Aldridge K, Reeves RH, Olson LE, Richtsmeier JT. Differential effects of trisomy on brain shape and volume in related aneuploid mouse models. Am J Med Genet A. 2007;143A(10):1060-70.

166. Rabin KR, Whitlock JA. Malignancy in children with trisomy 21. Oncologist. 2009;14(2):164-73.

167. Lane AA, Chapuy B, Lin CY, Tivey T, Li H, Townsend EC, et al. Triplication of a 21q22 region contributes to B cell transformation through HMGN1 overexpression and loss of histone H3 Lys27 trimethylation. Nat Genet. 2014;46(6):618-23.

168. Heerema NA, Raimondi SC, Anderson JR, Biegel J, Camitta BM, Cooley LD, et al. Specific extra chromosomes occur in a modal number dependent pattern in pediatric acute lymphoblastic leukemia. Genes Chromosomes Cancer. 2007;46(7):684-93.

169. Moller RS, Kubart S, Hoeltzenbein M, Heye B, Vogel I, Hansen CP, et al. Truncation of the Down syndrome candidate gene DYRK1A in two unrelated patients with microcephaly. Am J Hum Genet. 2008;82(5):1165-70.

170. Ji J, Lee H, Argiropoulos B, Dorrani N, Mann J, Martinez-Agosto JA, et al. DYRK1A haploinsufficiency causes a new recognizable syndrome with microcephaly, intellectual disability, speech impairment, and distinct facies. European Journal of Human Genetics. 2015;23(11):1473.

171. Joo HY, Zhai L, Yang C, Nie S, Erdjument-Bromage H, Tempst P, et al. Regulation of cell cycle progression and gene expression by H2A deubiquitination. Nature. 2007;449(7165):1068-72.

172. Zhang Z, Yang H, Wang H. The histone H2A deubiquitinase USP16 interacts with HERC2 and fine-tunes cellular response to DNA damage. J Biol Chem. 2014;289(47):32883-94.

173. Adorno M, Sikandar S, Mitra SS, Kuo A, Nicolis Di Robilant B, Haro-Acosta V, et al. Usp16 contributes to somatic stem-cell defects in Down's syndrome. Nature. 2013;501(7467):380-4.

174. Kuo LJ, Yang LX. Gamma-H2AX - a novel biomarker for DNA double-strand breaks. In Vivo. 2008;22(3):305-9.

175. Guard SE, Poss ZC, Ebmeier CC, Pagratis M, Simpson H, Taatjes DJ, et al. The nuclear interactome of DYRK1A reveals a functional role in DNA damage repair. Sci Rep. 2019;9(1):6539.

176. Roewenstrunk J, Di Vona C, Chen J, Borras E, Dong C, Arato K, et al. A comprehensive proteomics-based interaction screen that links DYRK1A to RNF169 and to the DNA damage response. Sci Rep. 2019;9(1):6014.

177. Poulsen M, Lukas C, Lukas J, Bekker-Jensen S, Mailand N. Human RNF169 is a negative regulator of the ubiquitin-dependent response to DNA double-strand breaks. J Cell Biol. 2012;197(2):189-99.

178. An L, Jiang Y, Ng HH, Man EP, Chen J, Khoo US, et al. Dual-utility NLS drives RNF169-dependent DNA damage responses. Proc Natl Acad Sci U S A. 2017;114(14):E2872-E81.

179. Fradet-Turcotte A, Canny MD, Escribano-Diaz C, Orthwein A, Leung CC, Huang H, et al. 53BP1 is a reader of the DNA-damage-induced H2A Lys 15 ubiquitin mark. Nature. 2013;499(7456):50-4.

180. Wilson MD, Benlekbir S, Fradet-Turcotte A, Sherker A, Julien JP, McEwan A, et al. The structural basis of modified nucleosome recognition by 53BP1. Nature. 2016;536(7614):100-3.

181. van Bon BWM, Coe BP, de Vries BBA, Eichler EE. DYRK1A-Related Intellectual Disability Syndrome. In: Adam MP, Ardinger HH, Pagon RA, Wallace SE, Bean LJH, Stephens K, et al., editors. GeneReviews((R)). Seattle (WA)1993.

182. Barallobre MJ, Perier C, Bove J, Laguna A, Delabar JM, Vila M, et al. DYRK1A promotes dopaminergic neuron survival in the developing brain and in a mouse model of Parkinson's disease. Cell Death Dis. 2014;5:e1289.

183. Kelava I, Lancaster MA. Stem Cell Models of Human Brain Development. Cell Stem Cell. 2016;18(6):736-48.

184. Edri R, Yaffe Y, Ziller MJ, Mutukula N, Volkman R, David E, et al. Analysing human neural stem cell ontogeny by consecutive isolation of Notch active neural progenitors. Nat Commun. 2015;6:6500.

185. Elkabetz Y, Panagiotakos G, Al Shamy G, Socci ND, Tabar V, Studer L. Human ES cell-derived neural rosettes reveal a functionally distinct early neural stem cell stage. Genes Dev. 2008;22(2):152-65.

186. Iacopetti P, Michelini M, Stuckmann I, Oback B, Aaku-Saraste E, Huttner WB. Expression of the antiproliferative gene TIS21 at the onset of neurogenesis identifies single neuroepithelial cells that switch from proliferative to neuron-generating division. Proc Natl Acad Sci U S A. 1999;96(8):4639-44.

187. Yabut O, Domogauer J, D'Arcangelo G. Dyrk1A overexpression inhibits proliferation and induces premature neuronal differentiation of neural progenitor cells. J Neurosci. 2010;30(11):4004-14.

188. Sylvester PE. The hippocampus in Down's syndrome. J Ment Defic Res. 1983;27 (Pt 3):227-36.

189. Benavides-Piccione R, Dierssen M, Ballesteros-Yanez I, Martinez de Lagran M, Arbones ML, Fotaki V, et al. Alterations in the phenotype of neocortical pyramidal cells in the Dyrk1A+/- mouse. Neurobiol Dis. 2005;20(1):115-22.

190. Dierssen M, Benavides-Piccione R, Martinez-Cue C, Estivill X, Florez J, Elston GN, et al. Alterations of neocortical pyramidal cell phenotype in the Ts65Dn mouse model of Down syndrome: effects of environmental enrichment. Cereb Cortex. 2003;13(7):758-64.

191. Martinez de Lagran M, Benavides-Piccione R, Ballesteros-Yanez I, Calvo M, Morales M, Fillat C, et al. Dyrk1A influences neuronal morphogenesis through regulation of cytoskeletal dynamics in mammalian cortical neurons. Cereb Cortex. 2012;22(12):2867-77.

192. Serrano-Perez MC, Fernandez M, Neria F, Berjon-Otero M, Doncel-Perez E, Cano E, et al. NFAT transcription factors regulate survival, proliferation, migration, and differentiation of neural precursor cells. Glia. 2015;63(6):987-1004.

193. Lepagnol-Bestel AM, Zvara A, Maussion G, Quignon F, Ngimbous B, Ramoz N, et al. DYRK1A interacts with the REST/NRSF-SWI/SNF chromatin

remodelling complex to deregulate gene clusters involved in the neuronal phenotypic traits of Down syndrome. Hum Mol Genet. 2009;18(8):1405-14.

194. Fernandez-Martinez J, Vela EM, Tora-Ponsioen M, Ocana OH, Nieto MA, Galceran J. Attenuation of Notch signalling by the Down-syndrome-associated kinase DYRK1A. J Cell Sci. 2009;122(Pt 10):1574-83.

195. Rachidi M, Lopes C, Charron G, Delezoide AL, Paly E, Bloch B, et al. Spatial and temporal localization during embryonic and fetal human development of the transcription factor SIM2 in brain regions altered in Down syndrome. Int J Dev Neurosci. 2005;23(5):475-84.

196. Berto GE, Iobbi C, Camera P, Scarpa E, Iampietro C, Bianchi F, et al. The DCR protein TTC3 affects differentiation and Golgi compactness in neurons through specific actin-regulating pathways. PLoS One. 2014;9(4):e93721.

197. Wolvetang EJ, Bradfield OM, Hatzistavrou T, Crack PJ, Busciglio J, Kola I, et al. Overexpression of the chromosome 21 transcription factor Ets2 induces neuronal apoptosis. Neurobiol Dis. 2003;14(3):349-56.

198. Raveau M, Nakahari T, Asada S, Ishihara K, Amano K, Shimohata A, et al. Brain ventriculomegaly in Down syndrome mice is caused by Pcp4 dose-dependent cilia dysfunction. Hum Mol Genet. 2017;26(5):923-31.

199. Bellmaine SF, Ovchinnikov DA, Manallack DT, Cuddy CE, Elefanty AG, Stanley EG, et al. Inhibition of DYRK1A disrupts neural lineage specificationin human pluripotent stem cells. Elife. 2017;6.

200. Wisniewski KE, Dalton AJ, McLachlan C, Wen GY, Wisniewski HM. Alzheimer's disease in Down's syndrome: clinicopathologic studies. Neurology. 1985;35(7):957-61.

201. Masters CL, Multhaup G, Simms G, Pottgiesser J, Martins RN, Beyreuther K. Neuronal origin of a cerebral amyloid: neurofibrillary tangles of Alzheimer's disease contain the same protein as the amyloid of plaque cores and blood vessels. EMBO J. 1985;4(11):2757-63.

202. Maia MA, Sousa E. BACE-1 and gamma-Secretase as Therapeutic Targets for Alzheimer's Disease. Pharmaceuticals (Basel). 2019;12(1).

203. Deng Y, Wang Z, Wang R, Zhang X, Zhang S, Wu Y, et al. Amyloid-beta protein (Abeta) Glu11 is the major beta-secretase site of beta-site amyloid-beta precursor protein-cleaving enzyme 1(BACE1), and shifting the cleavage site to Abeta Asp1 contributes to Alzheimer pathogenesis. Eur J Neurosci. 2013;37(12):1962-9.

204. Qiu T, Liu Q, Chen YX, Zhao YF, Li YM. Abeta42 and Abeta40: similarities and differences. J Pept Sci. 2015;21(7):522-9.

205. Levy E, Carman MD, Fernandez-Madrid IJ, Power MD, Lieberburg I, van Duinen SG, et al. Mutation of the Alzheimer's disease amyloid gene in hereditary cerebral hemorrhage, Dutch type. Science. 1990;248(4959):1124-6.

206. Van Broeckhoven C, Haan J, Bakker E, Hardy JA, Van Hul W, Wehnert A, et al. Amyloid beta protein precursor gene and hereditary cerebral hemorrhage with amyloidosis (Dutch). Science. 1990;248(4959):1120-2.

207. Scheuner D, Eckman C, Jensen M, Song X, Citron M, Suzuki N, et al. Secreted amyloid beta-protein similar to that in the senile plaques of Alzheimer's disease is increased in vivo by the presenilin 1 and 2 and APP mutations linked to familial Alzheimer's disease. Nat Med. 1996;2(8):864-70.

208. Aizenstein HJ, Nebes RD, Saxton JA, Price JC, Mathis CA, Tsopelas ND, et al. Frequent amyloid deposition without significant cognitive impairment among the elderly. Arch Neurol. 2008;65(11):1509-17.

209. Saeed SM, Fine G. Thioflavin-T for amyloid detection. Am J Clin Pathol. 1967;47(5):588-93.

210. Schmued L, Raymick J, Tolleson W, Sarkar S, Zhang YH, Bell-Cohn A. Introducing Amylo-Glo, a novel fluorescent amyloid specific histochemical tracer especially suited for multiple labeling and large scale quantification studies. J Neurosci Methods. 2012;209(1):120-6.

211. Kitamoto T, Ogomori K, Tateishi J, Prusiner SB. Formic acid pretreatment enhances immunostaining of cerebral and systemic amyloids. Lab Invest. 1987;57(2):230-6.

212. Christensen DZ, Bayer TA, Wirths O. Formic acid is essential for immunohistochemical detection of aggregated intraneuronal Abeta peptides in mouse models of Alzheimer's disease. Brain Res. 2009;1301:116-25.

213. Mercken M, Vandermeeren M, Lubke U, Six J, Boons J, Van de Voorde A, et al. Monoclonal antibodies with selective specificity for Alzheimer Tau are directed against phosphatase-sensitive epitopes. Acta Neuropathol. 1992;84(3):265-72.

214. Goedert M, Jakes R, Vanmechelen E. Monoclonal antibody AT8 recognises tau protein phosphorylated at both serine 202 and threonine 205. Neurosci Lett. 1995;189(3):167-9.

215. Weaver CL, Espinoza M, Kress Y, Davies P. Conformational change as one of the earliest alterations of tau in Alzheimer's disease. Neurobiol Aging. 2000;21(5):719-27.

216. Gonzalez C, Armijo E, Bravo-Alegria J, Becerra-Calixto A, Mays CE, Soto C. Modeling amyloid beta and tau pathology in human cerebral organoids. Mol Psychiatry. 2018;23(12):2363-74.

217. Brouwers N, Sleegers K, Van Broeckhoven C. Molecular genetics of Alzheimer's disease: an update. Ann Med. 2008;40(8):562-83.

218. Cannavo C, Tosh J, Fisher EMC, Wiseman FK. Using mouse models to understand Alzheimer's disease mechanisms in the context of trisomy of chromosome 21. Prog Brain Res. 2020;251:181-208.

219. Cacace R, Sleegers K, Van Broeckhoven C. Molecular genetics of early-onset Alzheimer's disease revisited. Alzheimers Dement. 2016;12(6):733-48.

220. Dai MH, Zheng H, Zeng LD, Zhang Y. The genes associated with early-onset Alzheimer's disease. Oncotarget. 2018;9(19):15132-43.

221. Mullan M, Crawford F, Axelman K, Houlden H, Lilius L, Winblad B, et al. A pathogenic mutation for probable Alzheimer's disease in the APP gene at the N-terminus of beta-amyloid. Nat Genet. 1992;1(5):345-7.

222. Jonsson T, Atwal JK, Steinberg S, Snaedal J, Jonsson PV, Bjornsson S, et al. A mutation in APP protects against Alzheimer's disease and age-related cognitive decline. Nature. 2012;488(7409):96-9.

223. Moussa-Pacha NM, Abdin SM, Omar HA, Alniss H, Al-Tel TH. BACE1 inhibitors: Current status and future directions in treating Alzheimer's disease. Med Res Rev. 2020;40(1):339-84.

224. Yan R, Munzner JB, Shuck ME, Bienkowski MJ. BACE2 functions as an alternative alpha-secretase in cells. J Biol Chem. 2001;276(36):34019-27.

225. Fluhrer R, Capell A, Westmeyer G, Willem M, Hartung B, Condron MM, et al. A non-amyloidogenic function of BACE-2 in the secretory pathway. J Neurochem. 2002;81(5):1011-20.

226. Schupf N, Lee A, Park N, Dang LH, Pang D, Yale A, et al. Candidate genes for Alzheimer's disease are associated with individual differences in plasma levels of beta amyloid peptides in adults with Down syndrome. Neurobiol Aging. 2015;36(10):2907 e1-10.

227. Lee JH, Lee AJ, Dang LH, Pang D, Kisselev S, Krinsky-McHale SJ, et al. Candidate gene analysis for Alzheimer's disease in adults with Down syndrome. Neurobiol Aging. 2017;56:150-8.

228. Mok KY, Jones EL, Hanney M, Harold D, Sims R, Williams J, et al. Polymorphisms in BACE2 may affect the age of onset Alzheimer's dementia in Down syndrome. Neurobiol Aging. 2014;35(6):1513 e1-5.

229. Myllykangas L, Wavrant-De Vrieze F, Polvikoski T, Notkola IL, Sulkava R, Niinisto L, et al. Chromosome 21 BACE2 haplotype associates with Alzheimer's disease: a two-stage study. J Neurol Sci. 2005;236(1-2):17-24.

230. Huentelman M, De Both M, Jepsen W, Piras IS, Talboom JS, Willeman M, et al. Common BACE2 Polymorphisms are Associated with Altered Risk for Alzheimer's Disease and CSF Amyloid Biomarkers in APOE epsilon4 Non-Carriers. Sci Rep. 2019;9(1):9640.

231. Bateman RJ, Xiong C, Benzinger TL, Fagan AM, Goate A, Fox NC, et al. Clinical and biomarker changes in dominantly inherited Alzheimer's disease. N Engl J Med. 2012;367(9):795-804.

232. Villemagne VL, Burnham S, Bourgeat P, Brown B, Ellis KA, Salvado O, et al. Amyloid beta deposition, neurodegeneration, and cognitive decline in sporadic Alzheimer's disease: a prospective cohort study. Lancet Neurol. 2013;12(4):357-67.

233. Park J, Wetzel I, Marriott I, Dreau D, D'Avanzo C, Kim DY, et al. A 3D human triculture system modeling neurodegeneration and neuroinflammation in Alzheimer's disease. Nat Neurosci. 2018;21(7):941-51.

234. Gerakis Y, Hetz C. Brain organoids: a next step for humanized Alzheimer's disease models? Mol Psychiatry. 2019;24(4):474-8.

235. Mansour AA, Goncalves JT, Bloyd CW, Li H, Fernandes S, Quang D, et al. Erratum: An in vivo model of functional and vascularized human brain organoids. Nat Biotechnol. 2018;36(8):772.

236. Xu R, Brawner AT, Li S, Liu J, Kim H, Xue H, et al. Reversing Abnormal Neural Development by Inhibiting OLIG2 in Down Syndrome Human iPSC 2 Brain Organoids and Neuronal Mouse Chimeras. bioRxiv. 2019.

237. Blouin JL, Avramopoulos D, Pangalos C, Antonarakis SE. Normal phenotype with paternal uniparental isodisomy for chromosome 21. Am J Hum Genet. 1993;53(5):1074-8.

238. Creau-Goldberg N, Gegonne A, Delabar J, Cochet C, Cabanis MO, Stehelin D, et al. Maternal origin of a de novo balanced t(21q21q) identified by ets-2 polymorphism. Hum Genet. 1987;76(4):396-8.

239. Allach El Khattabi L, Backer S, Pinard A, Dieudonne MN, Tsatsaris V, Vaiman D, et al. A genome-wide search for new imprinted genes in the human placenta identifies DSCAM as the first imprinted gene on chromosome 21. Eur J Hum Genet. 2019;27(1):49-60.

240. Christie KA, Courtney DG, DeDionisio LA, Shern CC, De Majumdar S, Mairs LC, et al. Towards personalised allele-specific CRISPR gene editing to treat autosomal dominant disorders. Sci Rep. 2017;7(1):16174.

241. Courtney DG, Moore JE, Atkinson SD, Maurizi E, Allen EH, Pedrioli DM, et al. CRISPR/Cas9 DNA cleavage at SNP-derived PAM enables both in

vitro and in vivo KRT12 mutation-specific targeting. Gene Ther. 2016;23(1):108-12.

242. Keough KC, Lyalina S, Olvera MP, Whalen S, Conklin BR, Pollard KS. AlleleAnalyzer: a tool for personalized and allele-specific sgRNA design. Genome Biol. 2019;20(1):167.

243. Mou X, Wu Y, Cao H, Meng Q, Wang Q, Sun C, et al. Generation of disease-specific induced pluripotent stem cells from patients with different karyotypes of Down syndrome. Stem Cell Res Ther. 2012;3(2):14.

244. Yu YE, Xing Z, Do C, Pao A, Lee EJ, Krinsky-McHale S, et al. Genetic and epigenetic pathways in Down syndrome: Insights to the brain and immune system from humans and mouse models. Prog Brain Res. 2020;251:1-28.

245. Lancaster MA, Knoblich JA. Organogenesis in a dish: modeling development and disease using organoid technologies. Science. 2014;345(6194):1247125.

246. Zahs KR, Ashe KH. 'Too much good news' - are Alzheimer mouse models trying to tell us how to prevent, not cure, Alzheimer's disease? Trends Neurosci. 2010;33(8):381-9.

247. Sasaguri H, Nilsson P, Hashimoto S, Nagata K, Saito T, De Strooper B, et al. APP mouse models for Alzheimer's disease preclinical studies. EMBO J. 2017;36(17):2473-87.

248. Southan C, Hancock JM. A tale of two drug targets: the evolutionary history of BACE1 and BACE2. Front Genet. 2013;4:293.

249. Hong L, Koelsch G, Lin X, Wu S, Terzyan S, Ghosh AK, et al. Structure of the protease domain of memapsin 2 (beta-secretase) complexed with inhibitor. Science. 2000;290(5489):150-3.

250. Petrini S, Borghi R, D'Oria V, Restaldi F, Moreno S, Novelli A, et al. Aged induced pluripotent stem cell (iPSCs) as a new cellular model for studying premature aging. Aging (Albany NY). 2017;9(5):1453-69.

251. Horvath S. DNA methylation age of human tissues and cell types. Genome Biol. 2013;14(10):R115.

252. Nizetic D, Groet J. Tumorigenesis in Down's syndrome: big lessons from a small chromosome. Nat Rev Cancer. 2012;12(10):721-32.

253. Park IH, Arora N, Huo H, Maherali N, Ahfeldt T, Shimamura A, et al. Disease-specific induced pluripotent stem cells. Cell. 2008;134(5):877-86.

254. Gough G, O'Brien NL, Alic I, Goh PA, Yeap YJ, Groet J, et al. Modeling Down syndrome in cells: From stem cells to organoids. Prog Brain Res. 2020;251:55-90.

255. Hasle H. Pattern of malignant disorders in individuals with Down's syndrome. Lancet Oncol. 2001;2(7):429-36.

256. Wegiel J, Gong CX, Hwang YW. The role of DYRK1A in neurodegenerative diseases. FEBS J. 2011;278(2):236-45.

257. Okui M, Ide T, Morita K, Funakoshi E, Ito F, Ogita K, et al. High-level expression of the Mnb/Dyrk1A gene in brain and heart during rat early development. Genomics. 1999;62(2):165-71.

258. Kay LJ, Smulders-Srinivasan TK, Soundararajan M. Understanding the Multifaceted Role of Human Down Syndrome Kinase DYRK1A. Adv Protein Chem Struct Biol. 2016;105:127-71.

259. Kuhn C, Frank D, Will R, Jaschinski C, Frauen R, Katus HA, et al. DYRK1A is a novel negative regulator of cardiomyocyte hypertrophy. J Biol Chem. 2009;284(25):17320-7.

260. Lee KS, Choi M, Kwon DW, Kim D, Choi JM, Kim AK, et al. A novel de novo heterozygous DYRK1A mutation causes complete loss of DYRK1A function and developmental delay. Sci Rep. 2020;10(1):9849.

261. Cho HJ, Lee JG, Kim JH, Kim SY, Huh YH, Kim HJ, et al. Vascular defects of DYRK1A knockouts are ameliorated by modulating calcium signaling in zebrafish. Dis Model Mech. 2019;12(5).

Appendix I

Supplementary Data

Appendix I: Supplementary Data

gRNA off target analysis

The top ten off-target sites for each gRNA (BACE2 Exon 3 and DYRK1A Exon 7) that produced cell lines used further in this thesis were identified using the freely available webtool CCTOP (144). DNA from each CRISPR/Cas9-edited iPSC line was extracted as described previously and each off-target site was PCR amplified and sequenced.

For BACE2, sequences from the T21C5Δ7 iPSC line were compared with that of the parental T21C5 iPSC line. One off target site did not amplify in both cell lines and therefore could not be assessed further. This target site is however, intronic, contains four miss-matches and lies adjacent to a GAG PAM site, which makes it unlikely that it is edited. No differences were observed between edited and unedited iPSCs in the nine target sites shown below (Figure S 1).

For DYRK1A, sequences from the T21C5 *DYRK1A* KO iPSC line were compared with that of the parental T21C5 iPSC line. No differences were observed between edited and unedited iPSCs in the nine target sites shown below (Figure S 2).

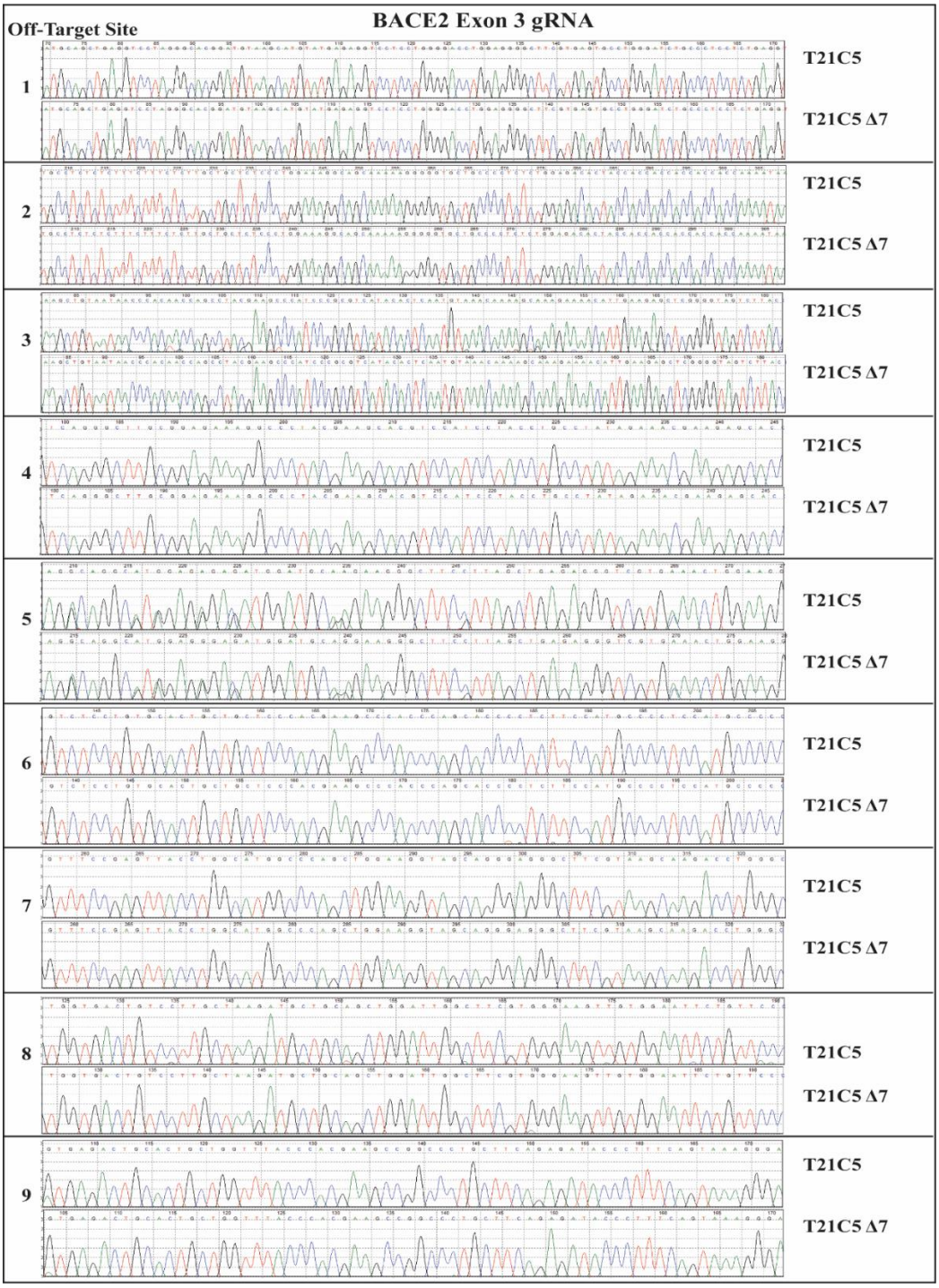

Figure S 1: Sequence traces for each of the nine BACE2 off-target sites analysed

No differences were observed in between T21C5Δ7 and parental T21C5 iPSC DNA for either site.

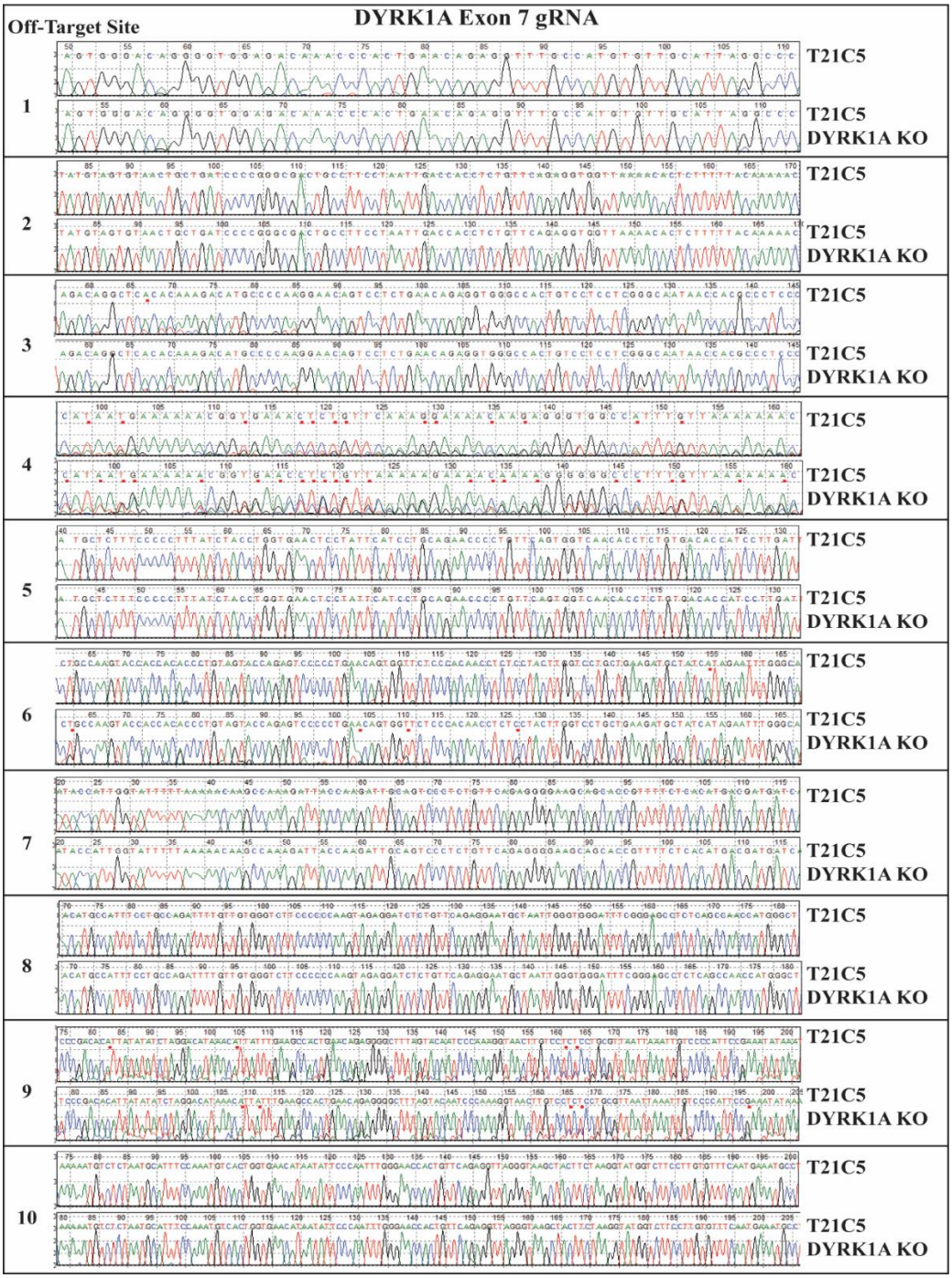

Figure S 2: Sequence traces for each of the ten DYRK1A off-target sites analysed

No differences were observed in between T21C5 DYRK1A KO and parental T21C5 iPSC DNA for either site.

Western blots for quantification of figure 52D

A total of four sample sets were run on western blot using lysates from a pool of three COs each (Figure S 3). Bands were quantified by standard densitometry and normalised to their corresponding β-actin value. β-actin-normalised samples were compared with the parental T21C5 value for each blot (n=4) and statistical significance was calculated using a Student's T-test (Figure 52D).

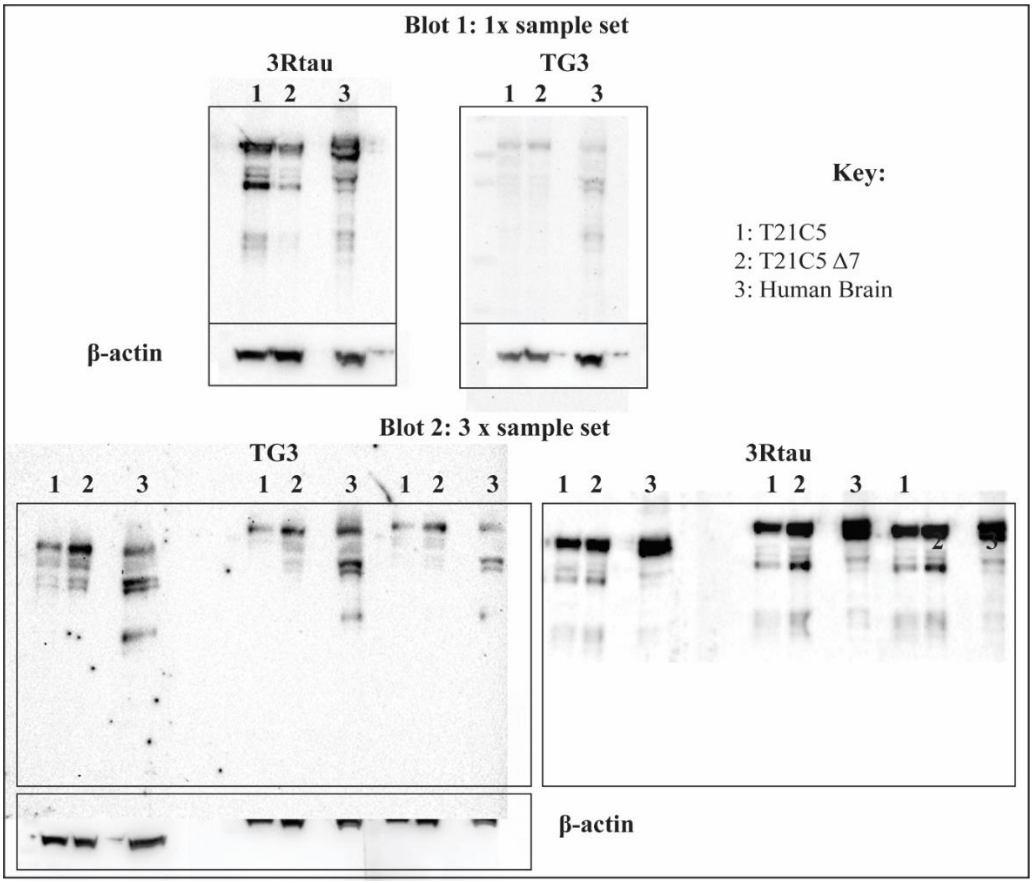

Figure S 3: Conformationally altered tau in T21C5Δ7 COs

Western blots of lysates from T21C5 and T21C5Δ7 COs at 83DIV (n=4) probed with TG3 (conformationally altered tau) and 3R-Tau (general 3 repeat tau). Lysates from human AD tissue from a 75-year-old is shown for comparison. The relative amount of pathologically conformed Tau was calculated by normalisation of the band signal intensities to the β-actin loading control.

Appendix II

Publications

Modeling Down syndrome in cells: From stem cells to organoids

Gillian Gough[a], Niamh L. O'Brien[b,c], Ivan Alic[a,d], Pollyanna A. Goh[b,c], Yee Jie Yeap[a], Jurgen Groet[b,c], Dean Nizetic[a,b,c,*], Aoife Murray[a]

[a]*Lee Kong Chian School of Medicine, Nanyang Technological University, Singapore, Singapore*
[b]*The Blizard Institute, Barts & The London School of Medicine, Queen Mary University of London, London, United Kingdom*
[c]*LonDownS Consortium, London, United Kingdom*
[d]*Department of Anatomy, Histology and Embryology, Faculty of Veterinary Medicine, University of Zagreb, Zagreb, Croatia*
**Corresponding author: Tel.: +44-7976-553679, e-mail address: d.nizetic@qmul.ac.uk*

Abstract

Down Syndrome (DS) is a complex chromosomal disorder, with neurological issues, featuring among the symptoms. Primary neuronal cells and tissues are extremely useful, but limited both in supply and experimental manipulability. To better understand the cellular, molecular and pathological mechanisms involved in DS neurodevelopment and neurodegeneration, a range of different cellular models have been developed over the years including human: mouse hybrid cells, transchromosomic mouse embryonic stem cells (ESCs) and human ESC and induced pluripotent stem cells derived from different sources. All of these model systems have provided useful information in the study of DS. Furthermore, different technologies to genetically modify or correct trisomy of either single genes or the whole chromosome have been developed using these cellular models. New techniques and protocols to allow better modeling of cellular mechanisms and disease processes are being developed and the use of cerebral organoids offers great promise for future research into the neural phenotypes seen in DS.

Keywords

iPSC, Organoids, Transchromosomic, Down syndrome, Trisomy 21, Mosaic, CRISPR/Cas9

Abbreviations

aCGH	array-comparative genomic hybridization
AD	Alzheimer's disease

Progress in Brain Research, ISSN 0079-6123, https://doi.org/10.1016/bs.pbr.2019.10.003

AF	amniotic fluid
APP	amyloid precursor protein
Aβ	amyloid-β
CCCP	carbonyl cyanide *m*-chlorophenylhydrazone
Col VI	collagen VI
CRISPR	clustered regularly interspaced short palindromic repeats
D21	disomy 21
DCF	2,7-dichlorofluorescein
DS	Down syndrome
DSCR	Down syndrome critical region
dupAPP	duplication of APP
EGCG	epigallocatechin gallate
fAD	familial Alzheimer's disease
gRNA	guide RNA
(h)ESC	(human) embryonic stem cell
(h)iPSC	(human) induced pluripotent stem cell
HSA21	human chromosome 21
MGE	medial ganglion eminence
MMP	mitochondrial membrane potential
MMU10/16/17	mouse chromosome 10/16/17
NPC	neural progenitor cell
PSC	pluripotent stem cell
PSEN1	presenilin 1
ROS	reactive oxygen species
SSEA4	stage-specific embryonic antigen4
T21	trisomy 21
TKNEO	thymidine kinase, neomycin resistance fusion gene
Tra	Tumor-related antigen

1 Introduction

Many cells and cell lines have been used to study various aspects of Down Syndrome (DS), including neurological, hematopoietic and cardiac pathology/phenotypes. This chapter will focus on the cellular models of DS that have been used for neurological studies, and in particular on human cellular models. DS is a complex syndrome with both neurodevelopmental and neurodegenerative aspects. In fact, trisomy 21 (T21) is the leading genetic cause for both intellectual disability and Alzheimer's disease (AD) (Coyle et al., 1986).

T21 causes multiple structural and functional derangements of neural systems throughout all stages of life, examples of which are given below, and which clearly impact overall neurodevelopment in DS. At a fetal stage, a number of differences in the developing T21 brain can already be detected including smaller brain hemispheres, a significantly reduced cerebellum (Guihard-Costa et al., 2006), increased cell death and a reduction in the number of hippocampal neurons (Guidi et al., 2008).

Later in life, severe hippocampal dysfunction, (as a major component of learning and cognitive impairment) (Pennington et al., 2003) and decreased hippocampal and cerebellar volumes can be observed (Aylward et al., 1999; Pinter et al., 2001).

The mechanisms linking T21 with all these defects are only partially understood. Indirect effects through global transcriptome perturbance, in particular T21-driven gene expression dysregulation domains (GEDDs) (Letourneau et al., 2014), open a whole new set of mechanistic questions. Direct effects of some chromosome 21 genes have been seen, for example, the role of *DYRK1A* on synaptic plasticity (Ahn et al., 2006). However, the gene/mechanisms causing impaired response to Shh are only partially explained by the action of DYRK1A (Schneider et al., 2015). *DYRK1A* is an extremely dose-sensitive gene and is implicated in level-regulating feedback loops with NRSF/REST (Canzonetta et al., 2008; Lu et al., 2011), NFAT (Arron et al., 2006), and TP53 (Park et al., 2010; Zhang et al., 2011), its mutations or truncations cause microcephaly (Ji et al., 2015), and duplication of the minimal chromosomal region including *DYRK1A* caused mild learning disability, short stature and brachycephaly, but normal head circumference (Ronan et al., 2007) (demonstrating that chromosome 21 genes other than *DYRK1A* are also critical for brain and head size determination).

The two major pathological hallmarks of AD; extracellular Amyloid-β (Aβ) plaques and intracellular neurofibrillary tangles are present in virtually all adults with DS over the age of 40 and intracellular Aβ accumulation has even been reported in individuals with DS as young as 15 years old (Head et al., 2012; Mori et al., 2002). The early incidence of AD-like neuropathology in DS is linked to triplication of the amyloid precursor protein (APP) gene on human chromosome 21 (HSA21) (Doran et al., 2017; Prasher et al., 1998). Thus, T21 is the most commonly known cause of obligatory development of the neuropathological hallmarks of AD (Nizetic et al., 2015). In non-DS individuals, the prevalence of AD rises exponentially after the age of 65 (Kocahan and Dogan, 2017). In some families, however, non-DS individuals with a rare genetic micro-duplication of APP (dupAPP) display familial early onset AD (Cabrejo et al., 2006; Rovelet-Lecrux et al., 2006; Sleegers et al., 2006). All individuals with dupAPP will develop AD by 60 years old, with the median onset age of clinical dementia being 41–51 years (Wiseman et al., 2015).

Somewhat paradoxically, despite also having three copies of APP, approximately 30% of people with DS only begin displaying symptoms of dementia at age 50–60 and some never during their lifetime (Wiseman et al., 2015). In addition to the pathological hallmarks of AD, people with DS display an altered free radical metabolism and mitochondrial dysfunction, which may further increase Aβ peptide production and the formation of Aβ plaques (Head et al., 2012; Perluigi and Butterfield, 2012; Wilcock, 2012).

A body of work using primary cells and tissues from patients with DS exists, and has been used in combination with studies in stem cells models to increase our understanding of the cellular and molecular mechanisms which are disrupted in DS. We briefly summarize some key points from this work, before describing in detail the human stem cell and organoid models more recently used to model various aspects of DS.

2 Primary human cells and tissues

Primary fetal DS neurons showed neurodegenerative changes after only 7 days in culture, which were not observed in normal controls (Busciglio and Yankner, 1995). This phenotype appeared specific to neurons as astrocyte viability was not impaired. Morphological features of the degenerating neurons (DNA fragmentation, chromatin condensation, membrane blebbing) suggested the cell death was caused by apoptosis, as opposed to necrosis. Treatment with a range of antioxidants improved the viability of DS neurons but had little effect on normal cultures, suggesting that reactive oxygen species (ROS) were responsible for the degeneration of DS neurons. Indeed, increased 2,7-dichlorofluorescein (DCF) fluorescence in DS neurons confirmed an increase in ROS in DS neurons compared to normal controls (Busciglio and Yankner, 1995). Later, it was demonstrated that altered metabolism of APP is associated with mitochondrial dysfunction in DS in primary human cortical cultures (Busciglio et al., 2002). Comparison of DS astrocytes to age-matched normal controls showed an increase in APP levels and the C-terminal C99 fragment (the product of β-secretase cleavage), along with intracellular accumulation of Aβ42 in DS cells. To confirm the mitochondrial defects, astrocyte cultures were labeled with a fluorescent probe, JC1, which allows assessment of mitochondrial activity. This confirmed that DS astrocytes show reduced mitochondrial membrane potential (MMP) compared to normal astrocytes. Normal astrocytes treated with carbonyl cyanide *m*-chlorophenylhydrazone (CCCP), an uncoupler of oxidative phosphorylation in mitochondria, also showed significantly reduced MMP (Busciglio et al., 2002).

A gene expression study comparing DS fetal cortical neuronal precursor cells (NPCs) to control NPCs identified selective repression of *SCG10* and other genes regulated by the transcription factor NRSF/REST, including *L1CAM*, *synapsin* and *β4-tubulin* (Bahn et al., 2002). All of these down-regulated genes play a role in neuronal outgrowth and plasticity. Notably, *NRSF*/*REST* itself was also downregulated. Differentiation of neurospheres from DS compared to control cells highlighted several abnormalities in the DS cultures including a reduction in neurogenesis, reduced neurite length and misshapen neurites with excessive side-branching (Bahn et al., 2002). Further studies compared the transcriptome of the human adult brain between seven DS individuals and eight normal controls. As expected, a large number of genes on HSA21 were upregulated, accompanied by widespread transcriptional disruption across the genome (Lockstone et al., 2007). This is in contrast to a previous study in DS human fetal brain that suggested few transcriptional changes occurred outside of HSA21 (Mao et al., 2005). Genome-wide transcriptional alterations in DS were confirmed in a more recent and larger study, in which tissues from 15 DS brains were compared to 15 age-matched euploid controls, spanning a range from fetal to adult tissues (Olmos-Serrano et al., 2016). In particular this study reported dysregulation of genes involved in oligodendrocyte differentiation and myelination, providing insight into the molecular mechanisms of developmental defects observed in DS.

3 Stem cell models of DS

The ideal cells to study the full effect of a supernumerary HSA21 are primary human cells and tissues from individuals with DS. However, as the supply of such samples is limited, a range of other systems have been explored. In order to tease apart the roles of various genes on HSA21, it is important to be able to manipulate the cells in different ways, which is not possible in primary cells or tissues. The neurodevelopmental aspects of DS are also difficult to study in primary cells or post-mortem tissues.

While beneficial, the utility of primary neuronal cells and tissues are somewhat limited and cannot be experimentally manipulated to the same degree as stem cell models. Multiple stem cell models of DS have been developed, ranging from transchromosomic mouse embryonic stem cells (ESCs) expressing human HSA21, human ESCs and human induced pluripotent stem cells (iPSCs) derived from various fetal and adult sources. Combined with various differentiation protocols and experimental manipulation, these models provide a platform to study cell types and cellular and molecular mechanisms which are not possible with donated primary material.

3.1 Transchromosomic mouse embryonic stem cells

The syntenic regions of HSA21 are spread across three mouse chromosomes (MMU10, MMU16 and MMU17). The topic of mouse and animal models are the subjects of other chapters in this book, and here we will only discuss the use of mouse-human hybrid cells and mouse transchromosomic cells, both of which express HSA21 as an extra chromosome in the context of a normal mouse genome.

In order to study the effect of the full complement of HSA21 genes in a trisomic context, a mouse-human hybrid cell line was generated. The WA17 cell line contains two–three copies of HSA21, and was derived from a fusion of mouse A9 fibroblasts and human WI-38 fibroblasts (Raziuddin et al., 1984). Using these transchromosomic cells, it was possible to demonstrate that mouse fibroblasts expressing HSA21 (WA17) suffered from aberrant adhesion, migration and proliferation (Delom et al., 2009). WA17 cells also showed increased adherence to collagen VI (Col VI), reduced migration in a wound scratch assay and reduced proliferation rate compared to the control (A9) cells on either fibronectin or Col VI matrices (Delom et al., 2009). These cellular phenotypes of aberrant migration, adhesion and proliferation are linked to the pathogenesis of congenital heart defects, often seen in DS.

Moving on from the transchromosomic fibroblast system, a transchromosomic mouse ESC system was developed (Hernandez et al., 1999). The transchromosomic mouse ESCs (47-1) contain a freely segregating HSA21 in addition to the complete mouse genome. A point of caution with this transchromosomic cell system is that the cells were created with the use of irradiation, which introduced some genomic rearrangements (Gribble et al., 2013). However, as will be discussed, this model has been extremely useful in teasing apart the role of individual HSA21 genes and their

contribution to different DS phenotypes. Moreover, the results obtained from experiments using these cells have been validated in other cellular models and primary human tissues. Transchromosomic ESCs were also used to generate mouse models, but here we will focus on the work pertaining to the cellular system and comparison of the transchromosomic (47-1) to the parental ESCs (D3). Work from our lab showed that addition of HSA21 to the mouse ESCs suppressed the acquisition of neural fate in a teratoma model (Mensah et al., 2007). 47-1 or D3 ESCs were injected into opposite flanks of recipient mice and allowed to form teratomas for 30 days. When the resultant teratomas were analyzed, 47-1 showed a threefold lower percentage of neuroectodermal tissue, as well as reduced mRNA expression of both the neural marker *β3-tubulin* and the glial marker *Gfap*.

Later, using the same cellular system, it was demonstrated that *DYRK1A* dosage imbalance perturbs NRSF/REST levels, and results in deregulation of pluripotency and stem cell fate in DS (Canzonetta et al., 2008). In agreement with the work by Bahn et al. in DS fetal brain cells, downregulation of *Nrsf/Rest* was also detected in the transchromosomic mouse ESCs 47-1, compared to control D3 ESCs. Taking advantage of the unique feature offered by the 47-1 model, it was possible to selectively silence a single copy of *DYRK1A* by using human allele specific RNAi oligonucleotides targeted to the 3′ UTR which differs between mouse and human. This allowed reduction of the dose of *DYRK1A* while keeping all other HSA21 genes in a trisomic dose. Selectively silencing *DYRK1A* in the 47-1 cells effectively corrected the expression of *Nrsf/Rest*, returning it to the range of expression detected in D3 cells. *Nrsf/Rest* expression was also altered in response to treatment with the selective DYRK1A-kinase specific inhibitor, epigallocatechin gallate (EGCG) (Canzonetta et al., 2008). Similar to the fetal brain studies, when trisomic ESCs (47-1) were induced to differentiate, they showed a significant reduction in neurogenesis and abnormal neurite branching compared to the D3 control cells (Bahn et al., 2002; Canzonetta et al., 2008). The interaction between DYRK1A and NRSF/REST, and the existence of a transcriptional feedback loop between the two, has since been validated in other studies (Lepagnol-Bestel et al., 2009; Lu et al., 2011). Selective silencing of human specific alleles in the trisomic 47-1 context also identified the overdose of *RUNX1* as a key contributor to the disturbance of early hematopoiesis in DS (De Vita et al., 2010). This role of *RUNX1*, along with *ETS2* and *ERG*, in the expansion of early hematopoietic progenitors was later confirmed in a human iPSC-based model (Banno et al., 2016), as well as mouse models with fine-tunable alterations of the *RUNX1* gene dose (Lie et al., 2018).

Quantitative proteomics analysis identified proteomic differences that are present between the undifferentiated 47-1 and control D3 ESCs. Such differences already at an ESC state could influence the differentiation of these cells further downstream (Wang et al., 2009). Results from the 47-1/D3 experiments were replicated in the transchromosomic fibroblast system WA17/A9, in tissues from the adult Tc1 mice (mice containing an almost complete HSA21) (O'doherty et al., 2005) and in human fetal kidney lysates. In line with other proteomic studies in DS samples, the authors also detected an effect of altered *NRSF/REST* gene dosage in control of protein

expression in 47-1 cells, with a higher than expected number of transcriptomically altered proteins containing a REST binding motif within 50 kb of the transcriptional start site (Bahn et al., 2002; Wang et al., 2009).

3.2 DS Embryonic and fetal derived cells

Both ESCs and iPSCs are extremely useful cellular systems to study DS. iPSCs facilitate the study of patient specific cells, and both ESCs and iPSCs allow the opportunity to study the developmental aspects of DS in greater depth. While discussing the use of ESCs it is important to note that all ESC lines used in research are subject to rigorous ethical and consent practices. It has previously been reported that only a fraction of T21 embryos will survive to term, with many undergoing spontaneous abortion in utero, with estimates ranging from 31% to 75% (Creasy and Crolla, 1974; Morris et al., 1999; Spencer, 2001). Hence, complex genetic and epigenetic modifications allowing for full term gestation may not be present in some hESC-derived cell lines (Park et al., 2008a). Studying ESCs, derived from early blastocysts may allow access to cells/genetic permutations that would not survive to term, and therefore offer the chance to study key components of development of DS embryos.

3.2.1 Embryonic stem cells (ESCs)

A series of aneuploidy human ESCs, including three different T21 lines, were established (Biancotti et al., 2010) and along with two further T21 ES lines all five were used in a study to identify the molecular and cellular pathways involved in neural differentiation (Halevy et al., 2016). Gene expression arrays comparing T21 ESC-derived neural progenitor cells (NPCs) to normal controls, revealed an enrichment of the RUNX1 binding site in the promoter regions of upregulated genes in the T21 NPCs. Subsequent deletion of *RUNX1* by CRISPR/Cas9 gene editing resulted in down-regulation of a number of genes compared to their isogeneic, non-targeted controls, and 70% of those down-regulated genes were found to be putative RUNX1 targets. Furthermore, ablation of *RUNX1* corrected the phenotype of increased apoptosis in the T21-NPCs (Halevy et al., 2016). These results indicate an important role for RUNX1 in developing human peripheral and central nervous system.

Human T21 ESC lines Genea053 (Dumevska et al., 2016a) and Genea021 (Dumevska et al., 2016b) were both derived from surplus assisted reproductive technology (ART) blastocysts. In addition, two disomic sibling lines are available Genea021 (Dumevska et al., 2016b). To date, only characterization of these ES lines have been published, and no disease modeling or differentiation has been reported.

3.2.2 Fetal neural stem cells

The importance of studying the correct cell type for any given aspect of disease modeling was highlighted when expression of BACE2 was examined in patient derived cells. Following initial results in studies with primary DS fibroblasts (which showed only an increase in secreted BACE2 but no increase in intracellular protein), fetal brain-derived stem cells were shown to express increased levels of intracellular

BACE2 compared to controls accompanied by an increase in the amount of secreted BACE2 detected in the cell culture medium (Barbiero et al., 2003).

Human DS fetal NPCs have also been generated from gestational age 8 to 18 week cortex (Bahn et al., 2002), 13 and 18 week cortex (Bhattacharyya et al., 2009), and from 19 to 21 week frontal cortex (Esposito et al., 2008). Collectively, these studies identified gene expression differences in DS NPCs resulting in decreased neurogenesis and increased gliogenesis. Quantitative PCR showed repression of a number of Nrsf-REST regulated genes in DS NPCs, along with altered neurite morphology in differentiated neurons (Bahn et al., 2002). Comparison on age-matched DS and euploid controls, showed that DS neurospheres were smaller than the euploid controls and that the reduced growth of neurospheres coincided with reduced neurogenesis (Bhattacharyya et al., 2009). Furthermore, gene expression arrays showed transcriptional dysregulation of a number of genes involved in neural progenitor development, cell death and division. An important finding of this report is that NPCs derived from 13 week T21 fetal cortex were almost indistinguishable from controls at early timepoints. When neurospheres were expanded for less than 6 weeks before plating for neural differentiation, no significant differences were observed in the number of neurons formed. However, if allowed to expand for over 10 weeks before plating for neurons, the number of neurons produced was significantly reduced in DS cultures (Bhattacharyya et al., 2009). This mirrors the normal cortical development in early gestation of a DS fetus, with defects only appearing later in gestation. The aim of the study by Esposito and colleagues was to identify potential aberrant pathways and examine the neuropathological mechanisms that may give rise to DS. Microarray profiling of the NPCs showed upregulation of a number of genes, both on HSA21 itself and other chromosomes. In keeping with the reported gliogenic shift in DS, a slight increase in GFAP expression was observed in the DS-NPCs. Immunostaining confirmed an increase in other glial related proteins including vimentin and O4, along with a decrease in neural progenitor (Nestin) and neuronal (MAP2) markers. Network analysis of the dysregulated genes highlighted genes involved in cell death and oxidative stress. Further investigation examined the role of upregulation of S100B and APP in activation of stress responses and the increase in ROS. In turn, this was accompanied by an upregulation of AQP4 in the DS-NPCs, which they suggest may serve to mitigate cell damage and death due to the induction of ROS (Esposito et al., 2008).

3.2.3 Fetal iPSCs

ESCs or fetal derived stem cells are of limited supply as they require surplus embryos from IVF or consent to isolate cells after termination of a pregnancy. Another approach to obtain cells from the fetal stage of development is the isolation of mid-trimester amniotic fluid (AF) stem cells from women already undergoing prenatal diagnosis. This approach was used to generate AF-iPSCs from trisomy 21 and control fetuses (Pipino et al., 2014). AF-iPSCs could be successfully differentiated toward hematopoietic and neural lineages, both important cell types to study, in the context of modeling different aspects of DS. This study stopped short of examining

any differences in the AF-iPSC-derived differentiated cells, only stating differentiation of these cells was possible and it could be feasible to use them for future in-depth studies (Pipino et al., 2014). Others also generated AF-iPSCs from T21 and normal cells and then proceeded to differentiate them into neural progenitor cell and neurons (Lu et al., 2013). T21 iPS-NPCs showed an increase in APP and a decrease in MeCP2, a protein essential for neuronal maturation, by both qPCR and Western blot. An increase in the five HSA21 miRNAs in T21 compared to D21 iPS-NPCs was also detected. Among these miR-155 and miR802 are known to inhibit expression of MeCP2, which in turn plays a further role in control of downstream genes involved in neurogenesis. Finally, when further differentiating the NPCs into neurons, a decrease in neuronal differentiation efficiency of T21 NPCs compared to the controls was detected, suggesting developmental defects during neurogenesis (Lu et al., 2013).

3.3 Human iPSCs (from somatic cells of living donors)

Even though it is sometimes possible to harvest consented primary cells directly from patients, the ability to perform studies on individuals with DS or their tissues is limited by the fact that relevant phenotypes occur in cells and tissues that are not readily accessible, such as the central nervous system. In addition, the use of primary cells for research is often limited by low cell numbers, culture induced cellular changes and senescence. As an alternative to primary cells, human embryonic stem cells (hESC) offer great potential for high-throughput disease modeling due to their ability to self-renew. Their use in research is, however, limited by ethical reasons.

Owing to the work of Takahashi and Yamanaka, patient derived induced pluripotent stem cells (iPSCs) can be created by overexpressing four pluripotency-related transcription factors in somatic cells (Takahashi and Yamanaka, 2006; Takahashi et al., 2007). Four transcription factors: OCT4, SOX2, KLF4 and c-MYC (OSKM) were narrowed down from a pool of 24 transcription factors that were identified as candidate genes for both inducing pluripotency and maintaining embryonic stem cell identity (Takahashi and Yamanaka, 2006; Takahashi et al., 2007). This initial work on adult fibroblasts was followed up and the same four factors were used to generate iPSCs from human fetal, neonatal and adult primary cells (Park et al., 2008b). Generation of iPSCs from adult human fibroblasts was also achieved using a different cocktail of four transcription factors, namely, OCT4, SOX2, NANOG and LIN28 (Yu et al., 2007).

The generation of iPSCs from patients with complex multigene conditions such as DS could lead to a better understanding of the associations between genes on chromosome 21 and the underlying molecular mechanisms that are responsible for T21-related conditions such as accelerated cellular aging, cognitive decline, Alzheimer's Disease-like dementia and cancer. iPSCs provide useful tools for disease modeling, tissue engineering, drug testing and cellular based therapies with a low risk of immune rejection. In addition, in vitro cellular phenotypes in

patient-derived iPSCs can be assessed alongside the patient's medical history, allowing researchers to gain a more comprehensive understanding of the phenotypes associated with T21 (Park et al., 2008a).

3.3.1 iPSC morphology and phenotype

Following OSKM overexpression in somatic cells, the resulting iPSCs display the morphological phenotypes of ESCs, such as a round shape, large nucleoli, and scant cytoplasm (Takahashi and Yamanaka, 2006). iPSCs are also comparable to embryonic stem cells in their ability to self-renew or differentiate into cells of all three germ layers (Takahashi and Yamanaka, 2006). The generation of iPSCs can be validated by the positive expression of markers such as: Nanog, stage specific embryonic antigen-4 (SSEA-4), tumor-related antigen (Tra)-1-60, Tra-1-81 and the transcription factor Oct4, which is involved in the maintenance of pluripotency as well as the ability of iPSCs to self-renew (Shi and Jin, 2010; Takahashi et al., 2007). Additional characterization can be performed by alkaline phosphatase staining, which is a marker of undifferentiated cells.

3.3.2 Reprogramming of somatic cells from patients with DS

A full list of all published DS-iPSCs can be found in Table 1. Features of some of these lines, and the methods used to generate them are discussed below, and further in the text we discuss key results obtained from neuronal disease modeling with these iPSCS.

The first DS-iPSCs were reprogrammed from the fibroblasts of two male patients with trisomy 21 by retrovirus mediated overexpression of OSKM (Park et al., 2008a). The resulting iPSCs have been used to model DS phenotypes with regards to myeloid leukemia, neurogenesis and Alzheimer's disease-related pathologies (Jiang et al., 2013; Maclean et al., 2012; Shi et al., 2012b). Lentiviral vectors have been used to create iPSC lines from dermal fibroblasts of two male patients with different karyotypes of DS (Mou et al., 2012). The first patient, aged 3 years, presented with translocation DS, while the second, aged 4 years presented with T21 (Mou et al., 2012). One benefit of using a lentiviral vector as opposed to a retroviral vector is that lentiviruses can infect both dividing and non-dividing cells whereas retroviruses only infect dividing cells. This feature of lentiviruses is thought to improve reprogramming efficiency. The resulting DS-iPSCs maintained the genetic characteristics of the patient somatic cells, further increasing the potential use of DS-iPSCs for disease modeling (Mou et al., 2012).

Given that both retroviral and lentiviral vectors can integrate into the genome of the infected cells, the iPSCs generated by these methods often suffer from numerous artificially induced genomic DNA rearrangements (Hussein et al., 2011) and their subsequent use is limited to a research setting and their safety for use in a clinical setting cannot be confirmed (Schlaeger et al., 2015). For this reason, reprogramming somatic cells using non-integrating methods such as episomal vectors or Sendai virus have become increasingly popular. Episomal reprogramming makes use of plasmids containing Epstein-Barr virus-derived sequences to prolong the expression of reprogramming factors. This allows them to be extra-chromosomally replicated in

Table 1 DS-iPSC lines.

Reference	Cell source	Reprogramming method	iPSC feature	Phenotypes investigated
Park et al. (2008a,b)	DS1 and DS1 fibroblasts from two male patients with T21 aged 1 year and 1 month, respectively	Retrovirus expressing OSKM pseudotyped in VSVg	Two iPSC lines with full trisomy 21	Hematopoiesis (Maclean et al., 2012), neurogenesis and Alzheimer's disease-related pathology (Shi et al., 2012a,b,c; Jiang et al., 2013)
Mou et al. (2012)	Fibroblasts from two male patients Patient 1: age 3 with translocation DS Patient 2: age 4 with T21	Lentiviral vectors overexpressing OSKM	iPSC1: 46,XY,-21,+t (21q21q) iPSC2: full trisomy 21	
Chou et al. (2012)	Fibroblasts from four patients with T21	Retroviruses expressing OSKM individually or by a single polycistronic lentivirus encoding OSKM regulated by a doxycycline-inducible promoter	All four iPSC lines displayed full trisomy 21	Onset of human hematopoiesis and abnormalities in erythropoiesis
Briggs et al. (2013)	Fibroblasts from a male patient with DS	Episomal reprogramming using plasmids consisting of Oct4, Sox2, Nanog, Lin28, c-Myc, KLF4 and SV40LT.	Full trisomy 21	Neural lineage potency, differentiation kinetics, proliferation and axon extension. Gliogenic shift. Oxidative stress.
Chen et al. (2014)	Fibroblasts from two male and one female patient with DS	Maloney murine leukemia-based retroviral vectors for each reprogramming factor	Full trisomy 21	Gene expression profiles, oxidative stress and synaptogenic molecules in T21 astroglia
Lu et al. (2013)	Second trimester amniotic fluid stem cells	Lentiviral vectors overexpressing OSKM	Full trisomy 21	Neurogenesis impairment The role of ginseng on secreted Aβ40 and hyperphosphorylated Tau levels in iPSC-derived neurons (Chang et al., 2015)

Continued

Table 1 DS-iPSC lines.—Cont'd

Reference	Cell source	Reprogramming method	iPSC feature	Phenotypes investigated
Pipino et al. (2014)	Second trimester amniotic fluid stem cells	Cre-lox-inducible polycistronic lentiviral vector overexpressing OSKM	46, XX,der(14;21)(q10;q10),+21	Neural and hematopoietic lineage differentiation
iPSCs with isogenic controls				
Maclean et al. (2012)	Fibroblasts from adult with DS	Originally reprogrammed via retrovirus (Park et al., 2008a,b)	Production of euploid isogenic iPSCs via culture-induced spontaneous loss of HSA21	Gene expression profiling and hematopoiesis
Weick et al. (2013)	Fibroblasts from two male patients with T21 Patient 1: age 1 year, fibroblasts in culture developed low level mosaicism Patient 2: age 1 month	Patient 1: fibroblasts reprogrammed via retrovirus Patient 2: fibroblasts reprogrammed via Sendai Virus	Two T21 iPSC lines with Full trisomy 21, one of which has an isogenic control	Gene expression changes, susceptibility to oxidative stress, neurogenesis and synaptic activity
Hibaoui et al. (2014)	Fetal skin fibroblasts from monozygotic twins discordant for T21	Cre-lox-inducible polycistronic lentiviral vector overexpressing OSKM	Two iPSC lines were generated from a twin with T21 and a twin with a normal karyotype	Transcriptome analysis, neurogenesis, the effect of DYRK1A on neural development
Murray et al. (2015)	Fibroblasts from a young adult diagnosed with mosaic DS	Sendai Virus overexpressing OSKM	Three euploid and three trisomy 21 iPSC lines from an individual with constitutional mosaicism	T21-related cellular differences in differentiation, aging, neurodegeneration, mitochondrial abnormalities, DNA double-strand breaks in neurons
Real et al. (2018)	Fibroblasts from T21 donor	Sendai Virus (Cytotune 2.0)	iPSC lines with full trisomy 21, and one isogenic clone via culture-induced spontaneous loss of HSA21	Neuronal development and synapse formation and function during engraftment of hiPSC-derived neurons into mouse brain

Reference	Cell source	Reprogramming method	Gene editing/isogenic model creation	Phenotypes reported
Genetically modified iPSCs				
Li et al. (2012)	Fibroblasts from a patient with DS	Reprogrammed via lentivirus carrying Lin28, NANOG, SOX2 and OCT4	TKNEO transgene insertion into HSA21 via Adenovirus. TKNEO induced spontaneous loss of HSA21	
Jiang et al. (2013)	Fibroblasts from adult with DS reprogrammed by Park et al. (2008a,b)	Originally reprogrammed via lentivirus (Park et al., 2008a,b)	Insertion of XIST via ZFN to silence the additional copy of HSA21	Neural proliferation and neural rosette formation
Ovchinnikov et al. (2018)	Fibroblasts from a male patient with DS reprogrammed by Briggs et al. (2013)	Originally reprogrammed via episomal reprogramming by Briggs et al. (2013)	CRISPR/Cas9 to inactivate a single copy of APP	Transcriptome analysis, levels of secreted Aβ42, Aβ42/Aβ40 ratio and tau phosphorylation in cortical neuron cultures

dividing cells and subsequently removed from the cells by culturing them in the absence of drug selection (Yu et al., 2009). In addition to OSKM, the episomal reprogramming method includes the transcription factors Nanog, Lin28 and SV40LT to improve efficiency and reduce the possible toxic effects of high-level c-Myc expression (Yu et al., 2009).

Episomal reprogramming was used to generate unrelated WT and DS-iPSCs from control and patient fibroblasts (Briggs et al., 2013). The resulting DS-iPSCs and unrelated controls were differentiated into cells of neural lineage with a similar lineage potency, differentiation kinetics, proliferation and axon extension during early neurogenesis. In addition, the DS-iPSC derived neural cultures were able to successfully recapitulate differences in glial cell representation seen in fetal and adult DS brains (Briggs et al., 2013).

Integration-free reprogramming by the temperature-sensitive Sendai virus (SeV) has also been used to generate iPSCs from patient fibroblasts (Murray et al., 2015; Weick et al., 2013). The use of Sendai virus is an attractive method for iPSCs reprogramming due to its ability to produce large amounts of protein without entering the nucleus of the infected cell, its relatively high reprogramming efficiency and the fact that it can be easily removed from infected cells (Fusaki et al., 2009). Additionally, the temperature-sensitive mutation prevents SeV from being able to proliferate at standard culture temperatures (Seki et al., 2010).

Using SeV overexpressing OSKM DS-iPSCs were created from two patients with T21 and further demonstrated that T21 iPSCs and T21-iPSC-derived neurons display characteristic developmental defects that are consistent with the cognitive deficits seen in individuals with DS (Weick et al., 2013). In addition to two T21-iPSC lines, one euploid isogenic control was generated due to the presence of low level mosaicism in one batch of patient fibroblasts.

In the same way, we generated a panel of isogenic disomic (D21)- and T21-iPSCs from an adult patient with constitutional mosaicism (Murray et al., 2015). This first instance of isogenic non-integrationally reprogrammed DS-iPSCs showed that T21-iPSCs were able to successfully reproduce the known T21-related cellular differences in differentiation, aging, neurodegeneration, abnormalities in mitochondrial size and number as well as increases in DNA double-strand breaks in neurons (Murray et al., 2015).

While primary dermal fibroblasts are the most commonly reprogrammed cell type, other cell sources, such as blood and amniotic fluid have been used to generate iPSCs (Fig. 1) (Aasen et al., 2008; Anchan et al., 2011; Loh et al., 2009). At least two reports detail the generation of T21-iPSCs from second trimester amniotic fluid cells using lentiviral vectors overexpressing OSKM (Lu et al., 2013; Pipino et al., 2014). Amniotic fluid cells are an attractive source of cells for reprogramming due to the ease with which they can be obtained in routine amniocentesis or a caesarian delivery, the ease with which they can be reprogrammed because of their similar transcriptional and epigenetic states to other early embryonic cell types and their lower number of accumulated DNA damage commonly found in older cell types (Anchan et al., 2011; Galende et al., 2010).

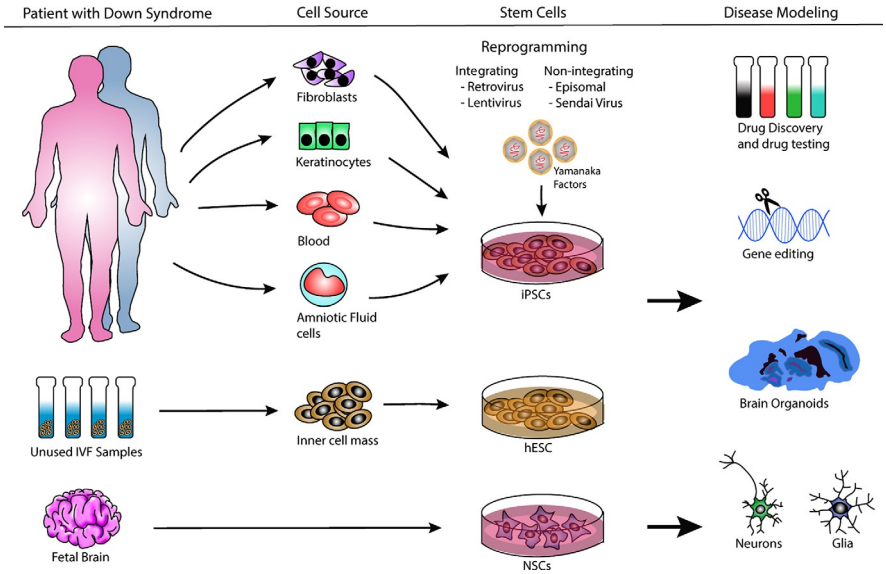

FIG. 1

An outline of the typical steps required to reprogram somatic cells to iPSCs followed by differentiation of the iPSCs into cells and tissues of neural origin.

The first T21 amniotic fluid-derived iPSCs were differentiated into NPCs and subsequently neurons to study neurogenesis impairment in DS (Lu et al., 2013). The T21-iPSC-derived NPCs generated fewer neurons and expressed elevated levels of APP consistent with previous reports in T21-iPSC-derived neurons and DS brains (Becker et al., 1991; Head and Lott, 2004; Shi et al., 2012b).

Since lentiviral vectors integrate into the genome of the infected cells, a modified Cre-excisable polycistronic lentiviral vector was used to reprogram second trimester amniotic fluid cells (Pipino et al., 2014). The presence of a loxP site within the vector makes it possible for most of the integrated gene to be excised by Cre-mediated excision (Soldner et al., 2009). Traces of the integrated transcription factors do, however, remain in the genome of the reprogrammed iPSCs, which could increase the risk of insertional mutations and may therefore be a concern for translational studies. In addition to neurological characteristics, the hematopoietic potential of amniotic fluid derived iPSCs was investigated by this group (Pipino et al., 2014).

3.3.3 Isogenic iPSCs

T21 models with euploid isogenic controls are invaluable to DS research because many phenotypic features of DS result from complex interactions between multiple genes. iPSCs with isogenic controls reduce the need for multiple studies that account for genetic and epigenetic variation. Thus, they are important research tools for understanding the underlying molecular mechanisms of specific DS phenotypes.

Using previously characterized T21-iPSCs (Park et al., 2008a), a group of researchers studying the effects of T21 on hematopoiesis generated isogenic euploid iPSCs as a result of culture induced spontaneous loss of the extra copy of chromosome 21 (Maclean et al., 2012). Another isogenic set of D21 and T21 iPSCs was generated in a similar manner though culture or reprogramming induced chromosome loss (Real et al., 2018). An alternative, naturally occurring source of isogenic euploid and T21-iPSCs are those generated from individuals who are mosaic for T21. Mosaicism is the rarest variant of DS, occurring in 2%–4% of DS cases (Brigida and Siniscalco, 2016). As mentioned previously, we and others have generated isogenic iPSCs via mosaicism (Murray et al., 2015; Weick et al., 2013).

Though it is a very rare occurrence, iPSCs have been generated from the fibroblasts of monozygotic twins discordant for T21 using the Cre-lox-inducible polycistronic lentiviral vector overexpressing OSKM (Hibaoui et al., 2014). However, a caveat of these iPSCs is that they suffer from additional chromosomal rearrangements and copy number changes greater than the number of genes on HSA21. Following evaluation of the multilineage potential of the iPSCs via transplantation into immunodeficient SCID mice, DS pathogenesis in neural progenitor cells (NPSs) and neurons were investigated. In particular, the role of DYRK1A in DS neurogenesis was investigated via DYRK1A inhibition using EGCG or short hairpin RNA (shRNA) knockdown (Hibaoui et al., 2014).

The potential for copy number variants and insertion mutagenesis as a result of culture induced stress or the reprogramming process highlights the importance of high-resolution genomic analysis of iPSCs used for disease modeling. Of the T21-iPSCs created thus far, only three groups have confirmed the isogenic nature of the resulting iPSCs by a genome-wide high-resolution array-comparative genomic hybridization (aCGH) analysis (Hibaoui et al., 2014; Murray et al., 2015; Real et al., 2018). Thus, the presence of artificial copy-number rearrangements cannot be ruled out in other DS-iPSC lines. Isogenic cellular models generated though gene editing to silence the third copy of chromosome 21 or with the use of CRISPR/Cas9 technology to correct individual genes will be discussed in the next section.

3.4 iPSC-derived DS neuronal cultures

With the development of iPSCs it became possible to generate patient specific neuronal cultures. Numerous DS iPSC lines were generated by different labs (Table 1) along with different methods to induce neuronal differentiation. This allowed multiple aspects of neuronal differentiation and function to be examined.

3.4.1 2D neuronal cultures

A dual SMAD inhibition protocol using Noggin and SB431542 was developed for the 2D neural conversion of hPSCs (Chambers et al., 2009). This improved upon previous methods which required stromal feeder cells or initial embryoid body formation. A 2D monolayer approach was chosen in an effort to establish an even distribution and homogenous differentiation of the cells. Following neural induction,

neuronal subtype patterning into dopaminergic or mortoneurons could be obtained by inclusion of different growth factors and cytokines in the culture media. The dual SMAD inhibition approach was then applied for directed differentiation of hPSCs to excitatory glutamatergic cortical neurons (Shi et al., 2012a,c). This protocol recapitulated the temporal development of the six layers of neurons seen in the human cortex. Comparison of PSC-derived cortical neurons generated from a collection of normal and T21 hESC and iPSCs (hESC (H9), DS-hESC (SC-321), hiPSCs (BBHX and CR) and DS iPSC (DS1-iPS4)) demonstrated that the DS neurons developed a range of AD pathologies in culture (Shi et al., 2012b). No difference in the total number of neurons nor the proportion of upper layer neurons was observed in the DS neurons compared to the control. A significant increase in the amount of secreted Aβ40 was detected in the DS neurons from an early point in differentiation. Later, both Aβ40 and Aβ42 could be detected at increased levels. Short term treatment of the neurons with a gamma secretase inhibitor (DAPT) reduced the production of Aβ peptides, while longer term treatment reduced them to undetectable levels (Shi et al., 2012b). Following on from this, aged neuronal cultures from the DS-iPSC developed intra and extra- cellular amyloid aggregates that could be detected by immunostaining with an Aβ42 specific antibody. To address the Tau pathology that accompanies amyloid aggregation in AD, phosphorylated Tau was detected in the DS-derived neuronal cultures, and this Tau was mislocalized in foci compared to the diffuse localization in control neurons. Particularly intriguing to note is that the DS-iPSC line used in this study was generated from fibroblasts obtained from a 13 month old infant (Park et al., 2008a), and indeed the DS-hESC was obtained from an embryo, highlighting that cells from embryos or young infants can be used to model aspects of an aging, neurodegenerative disorder.

Comparable efficiency and timing of neural conversion between DS and control neurons was reported, but at later points, DS cultures showed a twofold bias toward glial lineages (Briggs et al., 2013). However, they used a different neural differentiation protocol, based on the formation of free floating neurospheres. Additionally this work demonstrated that DS neural cultures are more sensitive to oxidative stress induced by H_2O_2 treatment, as measured by increased apoptotic cells by TUNEL staining. Pharmacological treatment with the antioxidant *N*-acetylcysteine rescued this phenotype, providing a proof of concept for testing corrective treatments for DS using iPSCs (Briggs et al., 2013).

Following another method for neural differentiation of iPSCs consisting of various stages of suspension and adherent culture, deficits in human trisomy 21 iPSCs and neurons were investigated (Weick et al., 2013). In contrast to AD phenotypes, they aimed to uncover deficits in iPSC-derived neurons that would explain the intellectual disability observed in DS. Of note in this study is that iPSCs were generated from a fibroblasts showing low level T21 mosaicism and so were able to isolate an isogenic D21 clone along with two T21 iPSC clones. Again, consistent with other work, (Briggs et al., 2013; Shi et al., 2012b; Weick et al., 2013) no difference in the early cortical neural progenitors or initial neuronal differentiation was observed between the T21 and control cells (Weick et al., 2013). Large gene expression

changes and oxidative stress vulnerability were detected in the T21 neurons (Weick et al., 2013). While previous reports observed no difference in the density of synapses, this cellular model highlighted a deficiency in the ability of DS neurons to form functional synapses. Although the basic physiological results such as cell size, resting membrane potential and action potential amplitude showed no difference, the T21 iPSC-derived neurons showed a reduction in spontaneous postsynaptic currents and frequency compared with the controls. This was accompanied by a decrease in the number of synapsin positive punctae on T21 neurites (Weick et al., 2013).

A unique set of iPSCs were successfully generated from fetal fibroblasts of monozygotic twins, discordant for trisomy 21 (Hibaoui et al., 2014). Differential gene expression analysis again showed a genome wide alterations in gene expression profiles between the normal and T21 twin iPSC line, with a significant enrichment of T21 downregulated genes involved in nervous system and brain development and neurogenesis. During characterization of the iPSCs teratoma formation assays highlighted a difference between the normal and T21 twin iPSCs, with the T21 cells forming multiple cysts and undifferentiated mesenchyme, and a lack of ectoderm germ structures (Hibaoui et al., 2014). Despite this lack of ectoderm formation in teratomas, in vitro both the normal and T21 lines could be induced to form neural progenitors and neurons. However, when assessed by qPCR, the T21 NPCs showed reduced expression of the neuroepithelial marker *NES* and neural markers *TUBB3*, *MAP2* and *FOXA2* compared to the normal control, along with increased expression of astroglial markers, *GFAP, S100B* and *VIM*. This echoes the results observed in fetal neural progenitors seen by Esposito et al. (2008), as well as the transchromosomic model (Canzonetta et al., 2008). The defective neurogenesis was accompanied by both a proliferation deficit (reduction of Ki67 positive cells) and increased apoptosis (increased caspase-3 activity). Consistent with the results seen in NPCs, when the cells were further differentiated to mature neurons, the T21 cells showed a reduction in β3-TUBULIN and MAP2, and an increase in GFAP, S100B, VIMENTIN, OLIG1 and OLIG1 compared to the control. In the β3-TUBULIN positive neurons that did form, T21 cells showed a decrease in the number of neurite branches and neurite length. Furthermore, synaptic impairment, a reduction in glutamatergic neurons and an increase in *GAD67* (GABAergic neuron marker) were all observed in T21 neurons. To investigate the role of DYRK1A in neurogenesis, the ability of the selective DYRK1A inhibitor EGCG to correct the neurogenesis phenotypes observed in their T21 cell system was tested. Treatment with EGCG, or knockdown of DYRK1A by shRNA in the T21 iPSCs promoted NPC proliferation, reduced apoptosis and overall led to an improved expression of β3-TUBULIN and MAP2 in differentiated neurons (Hibaoui et al., 2014). This corroborates previous results in human fetal brain cells and transchromosomic mouse ESC-derived neurons (Bahn et al., 2002; Canzonetta et al., 2008).

Following the directed differentiation protocol developed by (Shi et al., 2012c) isogenic D21 and T21 neurons were compared and showed a significant increase in amyloid production (Murray et al., 2015). This was accompanied by mitochondrial abnormalities (increased size and number) and an increase in DNA damage.

Whether the mitochondrial phenotype is due to mitochondrial fragmentation or an attempt by the cells to compensate for a hypofunctional mitochondria remains to be tested. The T21 NPCs also showed a retarded proliferation compared to the isogenic D21 controls, similar to the result observed by Hibaoui et al. (2014), however, in this case, the reduced proliferation was not accompanied by any significant increase in cell death (Murray et al., 2015).

Studies from fetal brain tissue and mouse models point to an impairment in interneuron development in DS. To study the development of cortical interneurons in DS euploid and T21 iPSCs and normal hESCs were assessed for the production, proliferation and migration of medial ganglion eminence (MGE) progenitors (Huo et al., 2018). A range of defects were observed in DS GABAergic interneurons in vitro and in vivo, including altered subtypes, reduced soma size, branches and neurite length. In order to assess differentiation and development of the neurons in a more natural environment, GABAergic progenitors were transplanted into the medial septum of SCID mouse brains and analyzed 6 months after transplantation. Here a significant reduction in migration and axonal projections of the human T21 neurons to the mouse hippocampus and olfactory bulb were detected (Huo et al., 2018).

Neurons derived from iPSCs from patients with different genetic forms of familial AD showed differences in APP processing. In particular, PSEN1 and APP V717I mutant neurons exhibited a relative increase in Aβ42 compared to Aβ40 at day 80, whereas T21 and dupAPP did not (Moore et al., 2015). Only neurons with genetic alteration of APP (APP717F, dupAPP and T21) showed an increase in tau protein levels, but not any of the neurons with Tau mutations themselves (Moore et al., 2015). Having confirmed that either β-secretase or γ-secretase inhibitor treatment dramatically reduced the amount of extracellular Aβ, it was next demonstrated that inhibition of β-secretase reduced intracellular tau, while inhibition of γ-secretase increased the levels of tau. Intriguingly alternation of APP processing using the gamma secretase modulator E2012, had a different effect on tau depending on the nature of the AD-related mutation. In fact E2012 treatment had the most pronounced effects on APP processing and Tau protein levels in T21 neurons, indicating a difference in how some T21 neurons may be affected by AD treatments (Moore et al., 2015).

T21 iPSC-derived neuronal cultures were used in a primary phenotypic screen for modulators of APP processing, with an aim to identify compounds that permit the initial β-secretase cleavage, but then modulate the further processing of the C-terminal AP. Such compound(s) would shift the production of Aβ away from the longer more toxic species (Aβ42), instead generating shorter species, but without affecting the total Aβ production or the γ-secretase cleavage of other substrates (Brownjohn et al., 2017). The initial screen involved testing the effect of a panel of drugs on Aβ38, Aβ40 and Aβ42 secretion from T21 iPSC-derived neurons, with an aim of identifying compounds that increased the ratio of Aβ38:Aβ42 and Aβ40:Aβ42, indicating an overall reduction in Aβ42 production. A number of drugs belonging to the avermectin family were identified, and in particular selamectin was shown to have the most potent effect and was subsequently tested on iPSC-derived neurons with other early onset AD mutations; dupAPP, APP V717I, PSEN1 M146I,

and a healthy control. The same effect of selametcin was observed in all the disease lines tested, but not in the healthy control (Brownjohn et al., 2017). Avermectins seem to phenocopy to effect of gamma secretase modulators such as E2012 on APP processing, but avermectins act in a gamma secretase independent manner. This is important to consider because gamma secretase has a range of targets in the cell, and this treatment would allow the modulation of APP processing without inhibiting the action of gamma secretase on other targets. This screening study highlights the utility of disease specific, iPSC-derived cells in phenotypic screens for drug discovery (Brownjohn et al., 2017).

Human iPSC-derived neurons in the early stages of differentiation were transplanted into the somatosensory cortex of adult mice to allow studies of human neuron dynamics in vivo (Real et al., 2018). The human neurons successfully engrafted in the mouse brain, proliferated, developed and differentiated as expected. Mature grafts organized into a vascularized, complex cytoarchitecture containing neurons and glia, composed of cells from both the human transplanted cells and the host mouse brain. This elegant system allowed the authors to monitor human neuronal development in the physiological microenvironment provided by the mouse brain. Of particular advantage is that this system provides vasculature, missing in other iPSC-derived neuronal differentiation systems. Moreover, when DS iPSC-derived neurons were used, an overproduction of astroglia was detected in the grafts compared to controls, recapitulating the human pathology (Dossi et al., 2018). In addition, an increase in dendritic spine density and spine stability was detected in T21 grafted neurons compared to controls, but a decrease in both burst and global activity (Real et al., 2018)

3.4.2 Organoids

The human brain is a complex organ containing multiple cell and tissue types that interact with one another through intricate pathways. More often than not neuropathological conditions are the result of complex interactions between these cell types. While differentiation of human iPSCs into neurons in 2D culture has contributed significantly to our understanding of the pathogenesis associated with neurodegenerative diseases, these systems are only able to model a single brain region without fully capturing the complex interactions between different cell types. DS rodent models are useful tools for modeling development and pathogenesis of T21-associated neurological disorders, features such as brain structure, neuronal density, dendrite morphology and overall brain development greatly differs between rodents and humans (Benavides-Piccione et al., 2002; Watase and Zoghbi, 2003).

A number of cerebral spheroid or organoid protocols have recently been developed to allow for better modeling of the complexities of neural structure and function and providing a more realistic 3D environment for cells to develop and mature (Amiri et al., 2018; Eiraku et al., 2008; Lancaster and Knoblich, 2014; Lancaster et al., 2013; Pasca et al., 2015; Song et al., 2019; Velasco et al., 2019). Human cerebral or "whole-brain" organoids derived from human pluripotent stem cells (hPSCs) were used to successfully model brain development and microcephaly

(Lancaster et al., 2013). These in vitro 3D representations of the developing human brain, exhibit a variety of region-specific identities, including those found in the hindbrain, midbrain and forebrain regions. This process relies solely on precisely timed manipulation of cell culture conditions in combination with the intrinsic ability of PSCs to self-organize and differentiate into the cells of various cortical layers in the developing human brain (Lancaster et al., 2013; Sutcliffe and Lancaster, 2017). The resulting cerebral organoids were able to recapitulate the typical organization of the developing human brain from ventricle-like cavities and a surrounding ventricular zone organization ($PAX6^+$ apical radial glial cells and $\beta3\text{-}TUBULIN^+$ neurons at the basal surface) to distinct inner and outer sub-ventricular zones. As such, cerebral organoids offer a degree of complexity and three-dimensional spatial cues that cells may require to better recapitulate and model neuronal development and disease pathology.

Further to cerebral organoids, other groups have developed protocols using various combinations of inducive signals to "purify" human brain organoids so that they represent a particular brain region. Forebrain organoids, which appeared around the same time as cerebral organoids result from the inhibition of TGFβ and WNT during the first 18 days of culture thus, promoting telencephalic differentiation (Kadoshima et al., 2013). Through long term culture of hESC-derived cortical neuroepithelium, this group was able to show the development of a multilayered structure encompassing three distinct neuronal zones (subplate, cortical plate and Cajal-Retzius cell zone) and progenitor zones (ventricular, subventricular and intermediate zones) at a development speed roughly comparable to that of the developing fetal brain.

Midbrain organoids were later developed and shown to consist of three distinct layers: the proliferative ventral zone (consisting of $MASH1^+$ and $OTX2^+$ neural progenitors), the intermediate zone (also consisting of midbrain progenitors as well as migrating immature dopaminergic neurons) and the mantle zone (comprising mature dopaminergic neurons) (Jo et al., 2016). The dopaminergic neurons found in these organoids were not only electrically active, but also functionally mature and able to produce dopamine. In addition to iPSCs, these organoids can also be produced from neural stem cells, highlighting the potential use of fate restricted neural stem cells in 3D culture (Monzel et al., 2017). Though many protocols exist for the differentiation of stem cells into oligodendrocytes, the process is often time consuming with low efficiency (Douvaras and Fossati, 2015). These midbrain organoids, however, were able to achieve a high level of oligodendrocyte differentiation as well as neurite myelination complete with nodes of Ranvier. The use of these midbrain organoids therefore have the potential to shed light on defects in oligodendrocyte differentiation and myelination commonly seen in the brains of individuals and the Ts65Dn mouse model of DS (Olmos-Serrano et al., 2016; Wisniewski and Schmidt-Sidor, 1989), although this work remains to be done.

Ventral forebrain organoids were developed from DS and control hiPSCs. After 5 weeks of culture the DS organoids were shown to overproduce OLIG2+ neural progenitors, and at 8 weeks showed an overproduction of GABAergic interneurons

(Xu et al., 2019). These results are discordant to the findings by Huo et al. (2018) who showed a reduction in the number of GABAergic neurons produced by DS iPSC-derived neurons compared to controls, using a 2D differentiation protocol. These discrepancies may arise from the different protocols used (i.e., organoid vs 2D culture). However, both studies highlight an imbalance in neuronal subtype development in DS. Early ventral forebrain organoids were dissociated into single cells and injected into the ventral forebrain of P0 mice to allow the neurons engraft and develop further. At 6 months post-injection, the mice transplanted with DS-derived cells also showed an overproduction of GABAergic neurons and an impairment in recognition memory. Inhibition of OLIG2 expression rescued this GABAergic imbalance in both the organoids and the chimeric mice (Xu et al., 2019).

Though most studies have focused on pathologies in early neurogenesis, such as microcephaly or ZIKA virus exposure (Kadoshima et al., 2013; Lancaster et al., 2013; Qian et al., 2016), the interest in using 3D organoids to model age-related conditions such as AD and Parkinson's disease is rising (Gonzalez et al., 2018; Monzel et al., 2017; Raja et al., 2016). DS fetal brains also show abnormal development and it will be interesting to see if the organoids can model aspects of this in a similar way to microcephaly. Peer-reviewed reports on DS organoids do not yet exist, but presentations at conferences indicate that this work is well underway and results can be expected soon.

One of the major limitations to modeling AD in 2D neuronal cultures is the diffusion of extracellular Aβ aggregates into the media, resulting in dilution of these aggregates through media changes (Raja et al., 2016). 3D brain organoids combat this limitation by providing environment sufficient for Aβ aggregation (Gonzalez et al., 2018; Raja et al., 2016). Using iPSCs derived from patients with fAD (dup APP) or presenilin1 mutations, self-organizing 3D human neural tissue structures were generated that were able to recapitulate some of the features of AD such as amyloid aggregation, hyperphosphorylation of Tau and endosomal abnormalities (Raja et al., 2016). In addition to disease modeling, brain organoids could be useful tools for drug discovery and testing. It was also shown that treatment of the patient-derived organoids with β- and γ-secretase inhibitors improved AD pathology by reducing Aβ aggregates and levels of hyperphosphorylated tau.

A more recent study using iPSCs derived from patients with fAD and a single iPSC line from a DS fibroblast sample showed that cerebral organoids can spontaneously develop the pathological signs of AD, such as amyloid plaques and elements of Tau pathology (Gonzalez et al., 2018). Although just from a single patient each with AD or DS, the results are encouraging as they demonstrate the use of organoids not just for neurodevelopmental studies, but also for neurodegenerative studies. As DS consists of both neurodevelopmental and neurodegenerative aspects, organoids may open a new avenue to investigate different cellular phenotypes in DS.

Though brain organoids have great potential to allow researchers to understand neuronal pathologies, organoids are limited by the fact that they are not vascularized, do not develop microglia and have synaptic activity. Due to the lack of vascularization, deeper tissues tend to die as a result of a lack of oxygen and nutrient supply. Therefore, when

differentiation iPSCs to neurons it is important to consider the experimental question and which differentiation protocol may offer the best platform to study that question, whether it is 2D culture, organoids or mouse transplantation systems.

4 Correcting T21 gene dose

Different methods have been tried to genetically correct the gene dose of trisomy 21 by either eliminating the entire chromosome, or by selectively mutating specific genes. A distinction is made here between pharmacologically inhibiting a gene product and in actually correcting the gene dose itself. The approaches to achieve this have been varied and include XIST-mediated (Jiang et al., 2013) or TKNEO-mediated silencing of the trisomic chromosome in iPSCs (Li et al., 2012) and ZSCAN-induced elimination of the extra chromosome (Amano et al., 2015). These approaches all achieve complete chromosomal dose correction. Alternatively, others have taken a candidate gene(s) approach and selectively deleted or copy number reduced the gene dose using CRISPR/Cas9 mediated gene manipulation.

4.1 Genetic modification and correction of trisomy 21 phenotypes

DS has a wide range of phenotypic features that vary among individuals. Such large variation could result from differences in the expression profile of genes on HSA21 (Prandini et al., 2007); and the effects of T21 on the gene expression profile of the rest of the genome (Canzonetta et al., 2008; Fitzpatrick, 2005; Letourneau et al., 2014). HSA21 was first mapped in 1999 with the goal of understanding how genes on chromosome 21 contribute to specific phenotypes seen in individuals with DS (Wang et al., 1999). Other approaches to identifying the associations between genotype and phenotype include mapping of partial trisomies, which made it possible to attribute most features of DS to a specific region on chromosome 21 (DS Critical Region (DSCR)) (Korbel et al., 2009; Lyle et al., 2009), comparisons of gene expression and transcriptome profiles between euploid and T21 cells and tissues (Bahn et al., 2002; Briggs et al., 2013; Mao et al., 2005; Wang et al., 2009), trisomy correction to create isogenic cellular models or CRISPR/Cas9 correction of a single HSA21 gene for the purpose of understanding the individual genes contribution to a specific feature of DS. As already discussed, the transchromosomic mouse ESC model (47-1/D3), also facilitated the correction of individual genes from trisomy to disomy, by selectively targeting human specific 3′UTR sequences with and RNAi based approach (Canzonetta et al., 2008; De Vita et al., 2010). Methods that have been used for genetic modification and correction of trisomy 21 are summarized in Fig. 2.

4.1.1 XIST silencing

The group of Jeanne Lawrence commandeered the naturally occurring cellular mechanism of dealing with an additional chromosome. Male and female mammals have a gene copy number difference due to the presence of two X-chromosomes in females.

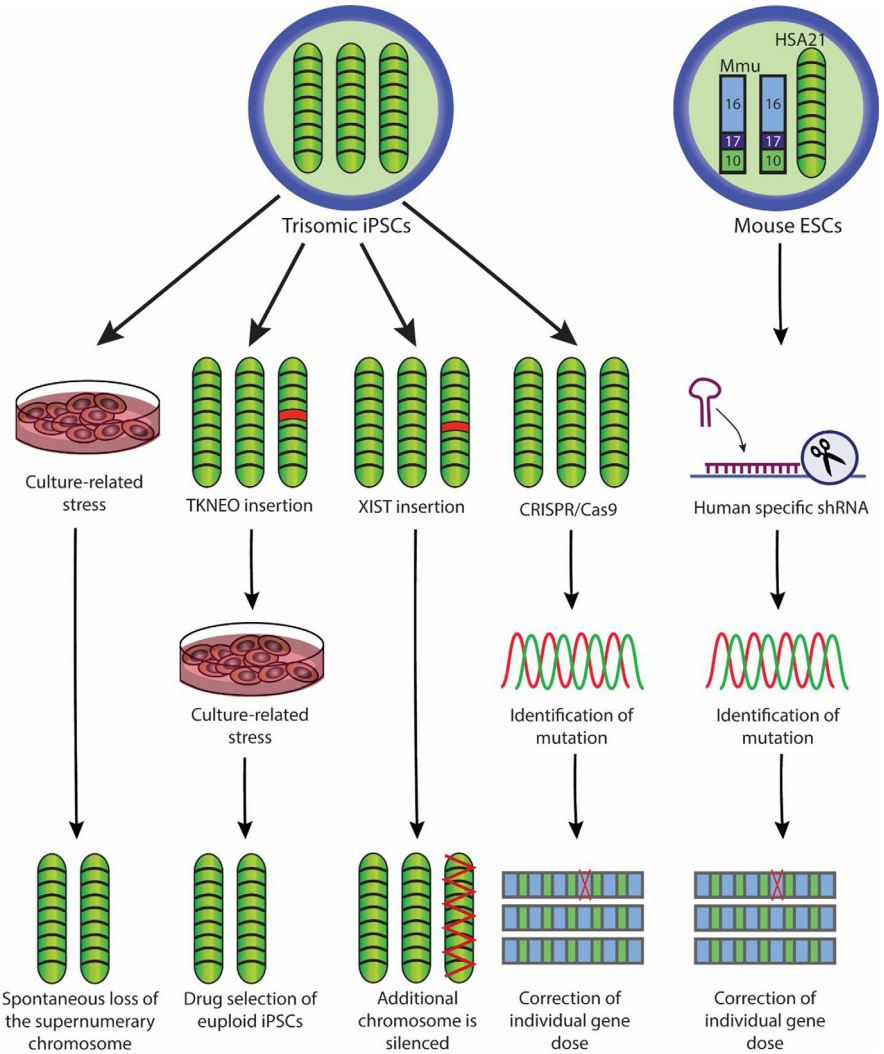

FIG. 2

An outline of the different approaches that have been used to either fully or partially restore gene dose from trisomy to disomy.

Cells compensate for this by selectively silencing one copy of the X-chromosome in females by coating the additional chromosome with a large non-coding RNA, *XIST*, which is exclusively transcribed from the inactivated chromosome (Brown et al., 1992). They hypothesized that the same mechanism could be used to silence the trisomic chromosome 21, if the chromosome could be manipulated to express the *XIST* RNA. Addition of *XIST* into intron 1 of the *DYRK1A* locus in DS-iPSCs

was achieved using zinc finger-mediated targeting (Jiang et al., 2013). To add a further level of control, the XIST transgene was placed under the control of a doxycycline inducible promoter. Remarkably the strategy was successful, the iPSCs retained their pluripotency and the silenced XIST coated chromosome formed a condensed Barr body as seen with X-chromosome inactivation. Having effectively reduced the gene dose of chromosome 21 back to disomic levels, it was shown that trisomy correction also improved neural induction efficiency, highlighting an example of how this method can be used to study the mechanisms underlying DS neurodevelopment. Indeed the strategy also provides a simple isogenic control T21:D21 control for comparison, i.e., by treating cells with doxycycline or not.

4.1.2 TKNEO-mediated silencing

An alternative approach to silence the whole chromosome was also developed (Li et al., 2012). They inserted a *TKNEO* fusion transgene encoding both thymidine kinase and neomycin resistance, into the *APP* locus on one copy of chromosome 21, using viral delivery and homologous recombination. The *TKNEO* transgene allowed for a positive–negative selection of correctly targeted iPSCs. Initial selection was carried out by culture in G418 to select cells with neomycin resistance. Following this cells were cultured for three passages without G418 to allow chromosome loss to take place and then subsequently treated with ganciclovir to select against thymidine kinase expression as cells expressing thymidine kinase phosphorylate gancilovir and convert it to a toxic drug. Therefore only cells that had lost the *TKNEO* expression could survive the treatment. Follow-up analysis demonstrated that the most common way for cells to lose the transgene expression was through loss of the entire chromosome, although cases of *TKNEO* coding mutations, *TKNEO* transgene deletion and *TKNEO* transgene silencing were all observed.

4.1.3 ZSCAN4 mediated

Another method of trisomy correction, not relying on genetic engineering, has also been reported. Using non-immortalized primary human fibroblast cells from four different individuals with DS, trisomy could be at least partially corrected in cultured cells by treatment with ZSCAN4 (Amano et al., 2015). *Zscan4* had previously been identified as a gene that is expressed specifically in the 2-cell stage of mouse preimplantation embryos (Falco et al., 2007), and it has been shown to be required for genome stability in mouse ESCs (Zalzman et al., 2010). While ZSCAN4 treatment did not fully correct trisomy to disomy in the DS fibroblasts, it reduced the number of trisomic cells. After 6 weeks of treatment up to 41% of cells showed a normal karyotype (Amano et al., 2015). This loss of the trisomic chromosome was not just a culture-induced artifact, as mock-treated cells showed no increase in disomic cells over the course of treatment. Other approaches to correct trisomy in cells involve the use of significant genetic engineering. This approach with synthetic protein appears to be a footprint-free method and it is intriguing to think about how such a treatment could be developed for therapy in the future.

4.1.4 Clustered regularly interspaced short palindromic repeats (CRISPR)/Cas9

CRISPR and its associated endonuclease 9 (CRISPR-Cas9) is a ribonucleoprotein complex that forms part of the bacterial and archaeal adaptive immune response (Mojica et al., 2005; Pourcel et al., 2005). This programmable form of immunity can be adapted to target any sequence leading to its first use as an RNA-guided genome editing tool in eukaryotic cells (Cong et al., 2013). Once in the cell nucleus, the guide RNA (gRNA) directs SpCas9 to the target site by Watson-Crick base-pairing, where it binds to and cleaves the double stranded DNA (Dai et al., 2016; Mali et al., 2013; Peng et al., 2016).

To identify the contribution of the supernumerary copy of APP to the severity and presentation of Alzheimer-like pathogenesis in DS, CRISPR/Cas9 gene editing techniques were employed to delete a single copy of APP exon 3 from T21-iPSCs (Ovchinnikov et al., 2018). Six isogenic iPSC lines (two with T21, one DS $APP^{+/+/-}$, and three euploid iPSC lines) were differentiated into cortical neurons with comparable differentiation trajectories in 90 days of culture. Transcriptome analysis of the cortical neuronal cultures revealed that the supernumerary copy of APP influences the expression of genes on HSA21, particularly those expressed between days 45 and 65 of neuronal culture. DS $APP^{+/+/-}$ iPSC-derived cortical neurons displayed a "normalized" expression of APP protein levels as well as a "normalized" Aβ42/Aβ40 ratio as compared to the DS $APP^{+/+/+}$ iPSC-derived cortical neurons. However, neuronal sensitivity to hydrogen peroxide, which has previously been linked to increased Aβ42 levels (Manterola et al., 2013), was not affected by APP correction in DS $APP^{+/+/-}$ or APP overexpression in hESCs at days 45 and 90 of culture. Similarly, tau phosphorylation was unaffected by APP normalization as confirmed by immunofluorescence detection of hyperphosphorylated tau in both the cell bodies and axons of day 120 neurons (Ovchinnikov et al., 2018).

Acknowledgments

The Nizetic lab is supported by: The Wellcome Trust "LonDownS Consortium" Strategic Funding Award (098330/Z/12/Z) (UK), the Singapore National Medical Research Council (NMRC/CIRG/1438/2015), Singapore Ministry of Education Academic Research Fund Tier 2 grants (2015-T2-1-023 & 2015-T2-2-119) and AM was awarded a William Harvey Academy Fellowship, co-funded by the People Programme (Marie Curie Actions) of the European Union's Seventh Framework Programme (FP7/2007-2013) under REA grant agreement n° 608765.

References

Aasen, T., Raya, A., Barrero, M.J., Garreta, E., Consiglio, A., Gonzalez, F., Vassena, R., Bilic, J., Pekarik, V., Tiscornia, G., Edel, M., Boue, S., Izpisua Belmonte, J.C., 2008. Efficient and rapid generation of induced pluripotent stem cells from human keratinocytes. Nat. Biotechnol. 26, 1276–1284.

Ahn, K.J., Jeong, H.K., Choi, H.S., Ryoo, S.R., Kim, Y.J., Goo, J.S., Choi, S.Y., Han, J.S., Ha, I., Song, W.J., 2006. DYRK1A BAC transgenic mice show altered synaptic plasticity with learning and memory defects. Neurobiol. Dis. 22, 463–472.

Amano, T., Jeffries, E., Amano, M., Ko, A.C., Yu, H., Ko, M.S., 2015. Correction of Down syndrome and Edwards syndrome aneuploidies in human cell cultures. DNA Res. 22, 331–342.

Amiri, A., Coppola, G., Scuderi, S., Wu, F., Roychowdhury, T., Liu, F., Pochareddy, S., Shin, Y., Safi, A., Song, L., Zhu, Y., Sousa, A.M.M., Psych, E.C., Gerstein, M., Crawford, G.E., Sestan, N., Abyzov, A., Vaccarino, F.M., 2018. Transcriptome and epigenome landscape of human cortical development modeled in organoids. Science, 362 (6420). 1–9.

Anchan, R.M., Quaas, P., Gerami-Naini, B., Bartake, H., Griffin, A., Zhou, Y., Day, D., Eaton, J.L., George, L.L., Naber, C., Turbe-Doan, A., Park, P.J., Hornstein, M.D., Maas, R.L., 2011. Amniocytes can serve a dual function as a source of IPS cells and feeder layers. Hum. Mol. Genet. 20, 962–974.

Arron, J.R., Winslow, M.M., Polleri, A., Chang, C.P., Wu, H., Gao, X., Neilson, J.R., Chen, L., Heit, J.J., Kim, S.K., Yamasaki, N., Miyakawa, T., Francke, U., Graef, I.A., Crabtree, G.R., 2006. NFAT dysregulation by increased dosage of DSCR1 and DYRK1A on chromosome 21. Nature 441, 595–600.

Aylward, E.H., Li, Q., Honeycutt, N.A., Warren, A.C., Pulsifer, M.B., Barta, P.E., Chan, M.D., Smith, P.D., Jerram, M., Pearlson, G.D., 1999. MRI volumes of the hippocampus and amygdala in adults with Down's syndrome with and without dementia. Am. J. Psychiatry 156, 564–568.

Bahn, S., Mimmack, M., Ryan, M., Caldwell, M.A., Jauniaux, E., Starkey, M., Svendsen, C.N., Emson, P., 2002. Neuronal target genes of the neuron-restrictive silencer factor in neurospheres derived from fetuses with Down's syndrome: a gene expression study. Lancet 359, 310–315.

Banno, K., Omori, S., Hirata, K., Nawa, N., Nakagawa, N., Nishimura, K., Ohtaka, M., Nakanishi, M., Sakuma, T., Yamamoto, T., Toki, T., Ito, E., Yamamoto, T., Kokubu, C., Takeda, J., Taniguchi, H., Arahori, H., Wada, K., Kitabatake, Y., Ozono, K., 2016. Systematic cellular disease models reveal synergistic interaction of trisomy 21 and GATA1 mutations in hematopoietic abnormalities. Cell Rep. 15, 1228–1241.

Barbiero, L., Benussi, L., Ghidoni, R., Alberici, A., Russo, C., Schettini, G., Pagano, S.F., Parati, E.A., Mazzoli, F., Nicosia, F., Signorini, S., Feudatari, E., Binetti, G., 2003. BACE-2 is overexpressed in Down's syndrome. Exp. Neurol. 182, 335–345.

Becker, L., Mito, T., Takashima, S., Onodera, K., 1991. Growth and development of the brain in Down syndrome. Prog. Clin. Biol. Res. 373, 133–152.

Benavides-Piccione, R., Ballesteros-Yanez, I., Defelipe, J., Yuste, R., 2002. Cortical area and species differences in dendritic spine morphology. J. Neurocytol. 31, 337–346.

Bhattacharyya, A., McMillan, E., Chen, S.I., Wallace, K., Svendsen, C.N., 2009. A critical period in cortical interneuron neurogenesis in Down syndrome revealed by human neural progenitor cells. Dev. Neurosci. 31, 497–510.

Biancotti, J.C., Narwani, K., Buehler, N., Mandefro, B., Golan-Lev, T., Yanuka, O., Clark, A., Hill, D., Benvenisty, N., Lavon, N., 2010. Human embryonic stem cells as models for aneuploid chromosomal syndromes. Stem Cells 28, 1530–1540.

Briggs, J.A., Sun, J., Shepherd, J., Ovchinnikov, D.A., Chung, T.L., Nayler, S.P., Kao, L.P., Morrow, C.A., Thakar, N.Y., Soo, S.Y., Peura, T., Grimmond, S., Wolvetang, E.J., 2013. Integration-free induced pluripotent stem cells model genetic and neural developmental features of Down syndrome etiology. Stem Cells 31, 467–478.

Brigida, A.L., Siniscalco, D., 2016. Induced pluripotent stem cells as a cellular model for studying Down syndrome. J. Stem Cells Regen. Med. 12, 54–60.

Brown, C.J., Hendrich, B.D., Rupert, J.L., Lafreniere, R.G., Xing, Y., Lawrence, J., Willard, H.F., 1992. The human XIST gene: analysis of a 17 kb inactive X-specific RNA that contains conserved repeats and is highly localized within the nucleus. Cell 71, 527–542.

Brownjohn, P.W., Smith, J., Portelius, E., Serneels, L., Kvartsberg, H., De Strooper, B., Blennow, K., Zetterberg, H., Livesey, F.J., 2017. Phenotypic screening identifies modulators of amyloid precursor protein processing in human stem cell models of Alzheimer's disease. Stem Cell Rep. 8, 870–882.

Busciglio, J., Yankner, B.A., 1995. Apoptosis and increased generation of reactive oxygen species in Down's syndrome neurons in vitro. Nature 378, 776–779.

Busciglio, J., Pelsman, A., Wong, C., Pigino, G., Yuan, M., Mori, H., Yankner, B.A., 2002. Altered metabolism of the amyloid beta precursor protein is associated with mitochondrial dysfunction in Down's syndrome. Neuron 33, 677–688.

Cabrejo, L., Guyant-Marechal, L., Laquerriere, A., Vercelletto, M., De La Fourniere, F., Thomas-Anterion, C., Verny, C., Letournel, F., Pasquier, F., Vital, A., Checler, F., Frebourg, T., Campion, D., Hannequin, D., 2006. Phenotype associated with APP duplication in five families. Brain 129, 2966–2976.

Canzonetta, C., Mulligan, C., Deutsch, S., Ruf, S., O'doherty, A., Lyle, R., Borel, C., Lin-Marq, N., Delom, F., Groet, J., Schnappauf, F., De Vita, S., Averill, S., Priestley, J.V., Martin, J.E., Shipley, J., Denyer, G., Epstein, C.J., Fillat, C., Estivill, X., Tybulewicz, V.L., Fisher, E.M., Antonarakis, S.E., Nizetic, D., 2008. DYRK1A-dosage imbalance perturbs NRSF/REST levels, deregulating pluripotency and embryonic stem cell fate in Down syndrome. Am. J. Hum. Genet. 83, 388–400.

Chambers, S.M., Fasano, C.A., Papapetrou, E.P., Tomishima, M., Sadelain, M., Studer, L., 2009. Highly efficient neural conversion of human ES and iPS cells by dual inhibition of SMAD signaling. Nat. Biotechnol. 27, 275–280.

Chang, C.Y., Chen, S.M., Lu, H.E., Lai, S.M., Lai, P.S., Shen, P.W., Chen, P.Y., Shen, C.I., Harn, H.J., Lin, S.Z., Hwang, S.M., Su, H.L., 2015. N-butylidenephthalide attenuates Alzheimer's disease-like cytopathy in Down syndrome induced pluripotent stem cell-derived neurons. Sci. Rep. 5, 8744.

Chen, C., Jiang, P., Xue, H., Peterson, S.E., Tran, H.T., McCann, A.E., Parast, M.M., Li, S., Pleasure, D.E., Laurent, L.C., Loring, J.F., Liu, Y., Deng, W., 2014. Role of astroglia in Down's syndrome revealed by patient-derived human-induced pluripotent stem cells. Nat. Commun. 5, 4430.

Chou, S.T., Byrska-Bishop, M., Tober, J.M., Yao, Y., Vandorn, D., Opalinska, J.B., Mills, J.A., Choi, J.K., Speck, N.A., Gadue, P., Hardison, R.C., Nemiroff, R.L., French, D.L., Weiss, M.J., 2012. Trisomy 21-associated defects in human primitive hematopoiesis revealed through induced pluripotent stem cells. Proc. Natl. Acad. Sci. U. S. A. 109, 17573–17578.

Cong, L., Ran, F.A., Cox, D., Lin, S., Barretto, R., Habib, N., Hsu, P.D., Wu, X., Jiang, W., Marraffini, L.A., Zhang, F., 2013. Multiplex genome engineering using CRISPR/Cas systems. Science 339, 819–823.

Coyle, J.T., Oster-Granite, M.L., Gearhart, J.D., 1986. The neurobiologic consequences of Down syndrome. Brain Res. Bull. 16, 773–787.

Creasy, M.R., Crolla, J.A., 1974. Prenatal mortality of trisomy 21 (Down's syndrome). Lancet 1, 473–474.

Dai, W.J., Zhu, L.Y., Yan, Z.Y., Xu, Y., Wang, Q.L., Lu, X.J., 2016. CRISPR-Cas9 for in vivo gene therapy: promise and hurdles. Mol. Ther. Nucleic Acids 5, e349.

De Vita, S., Canzonetta, C., Mulligan, C., Delom, F., Groet, J., Baldo, C., Vanes, L., Dagna-Bricarelli, F., Hoischen, A., Veltman, J., Fisher, E.M., Tybulewicz, V.L., Nizetic, D., 2010. Trisomic dose of several chromosome 21 genes perturbs haematopoietic stem and progenitor cell differentiation in Down's syndrome. Oncogene 29, 6102–6114.

Delom, F., Burt, E., Hoischen, A., Veltman, J., Groet, J., Cotter, F.E., Nizetic, D., 2009. Transchromosomic cell model of Down syndrome shows aberrant migration, adhesion and proteome response to extracellular matrix. Proteome Sci. 7, 31.

Doran, E., Keator, D., Head, E., Phelan, M.J., Kim, R., Totoiu, M., Barrio, J.R., Small, G.W., Potkin, S.G., Lott, I.T., 2017. Down syndrome, partial trisomy 21, and absence of Alzheimer's disease: the role of APP. J. Alzheimers Dis. 56, 459–470.

Dossi, E., Vasile, F., Rouach, N., 2018. Human astrocytes in the diseased brain. Brain Res. Bull. 136, 139–156.

Douvaras, P., Fossati, V., 2015. Generation and isolation of oligodendrocyte progenitor cells from human pluripotent stem cells. Nat. Protoc. 10, 1143–1154.

Dumevska, B., Mckernan, R., Goel, D., Schmidt, U., 2016a. Derivation of trisomy 21 affected human embryonic stem cell line Genea053. Stem Cell Res. 16, 500–502.

Dumevska, B., Bosman, A., Mckernan, R., Main, H., Schmidt, U., Peura, T., 2016b. Derivation of trisomy 21 affected human embryonic stem cell line Genea021. Stem Cell Res. 16, 401–404.

Eiraku, M., Watanabe, K., Matsuo-Takasaki, M., Kawada, M., Yonemura, S., Matsumura, M., Wataya, T., Nishiyama, A., Muguruma, K., Sasai, Y., 2008. Self-organized formation of polarized cortical tissues from ESCs and its active manipulation by extrinsic signals. Cell Stem Cell 3, 519–532.

Esposito, G., Imitola, J., Lu, J., De Filippis, D., Scuderi, C., Ganesh, V.S., Folkerth, R., Hecht, J., Shin, S., Iuvone, T., Chesnut, J., Steardo, L., Sheen, V., 2008. Genomic and functional profiling of human Down syndrome neural progenitors implicates S100B and aquaporin 4 in cell injury. Hum. Mol. Genet. 17, 440–457.

Falco, G., Lee, S.L., Stanghellini, I., Bassey, U.C., Hamatani, T., Ko, M.S., 2007. Zscan4: a novel gene expressed exclusively in late 2-cell embryos and embryonic stem cells. Dev. Biol. 307, 539–550.

Fitzpatrick, D.R., 2005. Transcriptional consequences of autosomal trisomy: primary gene dosage with complex downstream effects. Trends Genet. 21, 249–253.

Fusaki, N., Ban, H., Nishiyama, A., Saeki, K., Hasegawa, M., 2009. Efficient induction of transgene-free human pluripotent stem cells using a vector based on Sendai virus, an RNA virus that does not integrate into the host genome. Proc. Jpn. Acad. Ser. B Phys. Biol. Sci. 85, 348–362.

Galende, E., Karakikes, I., Edelmann, L., Desnick, R.J., Kerenyi, T., Khoueiry, G., Lafferty, J., McGinn, J.T., Brodman, M., Fuster, V., Hajjar, R.J., Polgar, K., 2010. Amniotic fluid cells are more efficiently reprogrammed to pluripotency than adult cells. Cell. Reprogram. 12, 117–125.

Gonzalez, C., Armijo, E., Bravo-Alegria, J., Becerra-Calixto, A., Mays, C.E., Soto, C., 2018. Modeling amyloid beta and tau pathology in human cerebral organoids. Mol. Psychiatry 23, 2363–2374.

Gribble, S.M., Wiseman, F.K., Clayton, S., Prigmore, E., Langley, E., Yang, F., Maguire, S., Fu, B., Rajan, D., Sheppard, O., Scott, C., Hauser, H., Stephens, P.J., Stebbings, L.A., Ng, B.L., Fitzgerald, T., Quail, M.A., Banerjee, R., Rothkamm, K., Tybulewicz, V.L., Fisher, E.M., Carter, N.P., 2013. Massively parallel sequencing reveals the complex structure of an irradiated human chromosome on a mouse background in the Tc1 model of Down syndrome. PLoS One 8, e60482.

Guidi, S., Bonasoni, P., Ceccarelli, C., Santini, D., Gualtieri, F., Ciani, E., Bartesaghi, R., 2008. Neurogenesis impairment and increased cell death reduce total neuron number in the hippocampal region of fetuses with Down syndrome. Brain Pathol. 18, 180–197.

Guihard-Costa, A.M., Khung, S., Delbecque, K., Menez, F., Delezoide, A.L., 2006. Biometry of face and brain in fetuses with trisomy 21. Pediatr. Res. 59, 33–38.

Halevy, T., Biancotti, J.C., Yanuka, O., Golan-Lev, T., Benvenisty, N., 2016. Molecular characterization of Down syndrome embryonic stem cells reveals a role for RUNX1 in neural differentiation. Stem Cell Rep. 7, 777–786.

Head, E., Lott, I.T., 2004. Down syndrome and beta-amyloid deposition. Curr. Opin. Neurol. 17, 95–100.

Head, E., Powell, D., Gold, B.T., Schmitt, F.A., 2012. Alzheimer's disease in down syndrome. Eur. J. Neurodegener. Dis. 1, 353–364.

Hernandez, D., Mee, P.J., Martin, J.E., Tybulewicz, V.L., Fisher, E.M., 1999. Transchromosomal mouse embryonic stem cell lines and chimeric mice that contain freely segregating segments of human chromosome 21. Hum. Mol. Genet. 8, 923–933.

Hibaoui, Y., Grad, I., Letourneau, A., Sailani, M.R., Dahoun, S., Santoni, F.A., Gimelli, S., Guipponi, M., Pelte, M.F., Bena, F., Antonarakis, S.E., Feki, A., 2014. Modelling and rescuing neurodevelopmental defect of Down syndrome using induced pluripotent stem cells from monozygotic twins discordant for trisomy 21. EMBO Mol. Med. 6, 259–277.

Huo, H.Q., Qu, Z.Y., Yuan, F., Ma, L., Yao, L., Xu, M., Hu, Y., Ji, J., Bhattacharyya, A., Zhang, S.C., Liu, Y., 2018. Modeling Down syndrome with patient iPSCs reveals cellular and migration deficits of GABAergic neurons. Stem Cell Rep. 10, 1251–1266.

Hussein, S.M., Batada, N.N., Vuoristo, S., Ching, R.W., Autio, R., Narva, E., Ng, S., Sourour, M., Hamalainen, R., Olsson, C., Lundin, K., Mikkola, M., Trokovic, R., Peitz, M., Brustle, O., Bazett-Jones, D.P., Alitalo, K., Lahesmaa, R., Nagy, A., Otonkoski, T., 2011. Copy number variation and selection during reprogramming to pluripotency. Nature 471, 58–62.

Ji, J., Lee, H., Argiropoulos, B., Dorrani, N., Mann, J., Martinez-Agosto, J.A., Gomez-Ospina, N., Gallant, N., Bernstein, J.A., Hudgins, L., Slattery, L., Isidor, B., Le Caignec, C., David, A., Obersztyn, E., Wisniowiecka-Kowalnik, B., Fox, M., Deignan, J.L., Vilain, E., Hendricks, E., Horton Harr, M., Noon, S.E., Jackson, J.R., Wilkens, A., Mirzaa, G., Salamon, N., Abramson, J., Zackai, E.H., Krantz, I., Innes, A.M., Nelson, S.F., Grody, W.W., Quintero-Rivera, F., 2015. DYRK1A haploinsufficiency causes a new recognizable syndrome with microcephaly, intellectual disability, speech impairment, and distinct facies. Eur. J. Hum. Genet. 23, 1473–1481.

Jiang, J., Jing, Y., Cost, G.J., Chiang, J.C., Kolpa, H.J., Cotton, A.M., Carone, D.M., Carone, B.R., Shivak, D.A., Guschin, D.Y., Pearl, J.R., Rebar, E.J., Byron, M., Gregory, P.D., Brown, C.J., Urnov, F.D., Hall, L.L., Lawrence, J.B., 2013. Translating dosage compensation to trisomy 21. Nature 500, 296–300.

Jo, J., Xiao, Y., Sun, A.X., Cukuroglu, E., Tran, H.D., Goke, J., Tan, Z.Y., Saw, T.Y., Tan, C.P., Lokman, H., Lee, Y., Kim, D., Ko, H.S., Kim, S.O., Park, J.H., Cho, N.J., Hyde, T.M., Kleinman, J.E., Shin, J.H., Weinberger, D.R., Tan, E.K., Je, H.S., Ng, H.H., 2016. Midbrain-like organoids from human pluripotent stem cells contain functional dopaminergic and neuromelanin-producing neurons. Cell Stem Cell 19, 248–257.

Kadoshima, T., Sakaguchi, H., Nakano, T., Soen, M., Ando, S., Eiraku, M., Sasai, Y., 2013. Self-organization of axial polarity, inside-out layer pattern, and species-specific progenitor dynamics in human ES cell-derived neocortex. Proc. Natl. Acad. Sci. U. S. A. 110, 20284–20289.

Kocahan, S., Dogan, Z., 2017. Mechanisms of Alzheimer's disease pathogenesis and prevention: the brain, neural pathology, N-methyl-D-aspartate receptors, tau protein and other risk factors. Clin. Psychopharmacol. Neurosci. 15, 1–8.

Korbel, J.O., Tirosh-Wagner, T., Urban, A.E., Chen, X.N., Kasowski, M., Dai, L., Grubert, F., Erdman, C., Gao, M.C., Lange, K., Sobel, E.M., Barlow, G.M., Aylsworth, A.S., Carpenter, N.J., Clark, R.D., Cohen, M.Y., Doran, E., Falik-Zaccai, T., Lewin, S.O., Lott, I.T., McGillivray, B.C., Moeschler, J.B., Pettenati, M.J., Pueschel, S.M., Rao, K.W., Shaffer, L.G., Shohat, M., Van Riper, A.J., Warburton, D., Weissman, S., Gerstein, M.B., Snyder, M., Korenberg, J.R., 2009. The genetic architecture of Down syndrome phenotypes revealed by high-resolution analysis of human segmental trisomies. Proc. Natl. Acad. Sci. U. S. A. 106, 12031–12036.

Lancaster, M.A., Knoblich, J.A., 2014. Organogenesis in a dish: modeling development and disease using organoid technologies. Science 345, 1247125.

Lancaster, M.A., Renner, M., Martin, C.A., Wenzel, D., Bicknell, L.S., Hurles, M.E., Homfray, T., Penninger, J.M., Jackson, A.P., Knoblich, J.A., 2013. Cerebral organoids model human brain development and microcephaly. Nature 501, 373–379.

Lepagnol-Bestel, A.M., Zvara, A., Maussion, G., Quignon, F., Ngimbous, B., Ramoz, N., Imbeaud, S., Loe-Mie, Y., Benihoud, K., Agier, N., Salin, P.A., Cardona, A., Khung-Savatovsky, S., Kallunki, P., Delabar, J.M., Puskas, L.G., Delacroix, H., Aggerbeck, L., Delezoide, A.L., Delattre, O., Gorwood, P., Moalic, J.M., Simonneau, M., 2009. DYRK1A interacts with the REST/NRSF-SWI/SNF chromatin remodelling complex to deregulate gene clusters involved in the neuronal phenotypic traits of Down syndrome. Hum. Mol. Genet. 18, 1405–1414.

Letourneau, A., Santoni, F.A., Bonilla, X., Sailani, M.R., Gonzalez, D., Kind, J., Chevalier, C., Thurman, R., Sandstrom, R.S., Hibaoui, Y., Garieri, M., Popadin, K., Falconnet, E., Gagnebin, M., Gehrig, C., Vannier, A., Guipponi, M., Farinelli, L., Robyr, D., Migliavacca, E., Borel, C., Deutsch, S., Feki, A., Stamatoyannopoulos, J.A., Herault, Y., Van Steensel, B., Guigo, R., Antonarakis, S.E., 2014. Domains of genome-wide gene expression dysregulation in Down's syndrome. Nature 508, 345–350.

Li, L.B., Chang, K.H., Wang, P.R., Hirata, R.K., Papayannopoulou, T., Russell, D.W., 2012. Trisomy correction in Down syndrome induced pluripotent stem cells. Cell Stem Cell 11, 615–619.

Lie, A.L.M., Marinopoulou, E., Lilly, A.J., Challinor, M., Patel, R., Lancrin, C., Kouskoff, V., Lacaud, G., 2018. Regulation of RUNX1 dosage is crucial for efficient blood formation from hemogenic endothelium. Development, 145 (5). 1–14.

Lockstone, H.E., Harris, L.W., Swatton, J.E., Wayland, M.T., Holland, A.J., Bahn, S., 2007. Gene expression profiling in the adult Down syndrome brain. Genomics 90, 647–660.

Loh, Y.H., Agarwal, S., Park, I.H., Urbach, A., Huo, H., Heffner, G.C., Kim, K., Miller, J.D., Ng, K., Daley, G.Q., 2009. Generation of induced pluripotent stem cells from human blood. Blood 113, 5476–5479.

Lu, M., Zheng, L., Han, B., Wang, L., Wang, P., Liu, H., Sun, X., 2011. REST regulates DYRK1A transcription in a negative feedback loop. J. Biol. Chem. 286, 10755–10763.

Lu, H.E., Yang, Y.C., Chen, S.M., Su, H.L., Huang, P.C., Tsai, M.S., Wang, T.H., Tseng, C.P., Hwang, S.M., 2013. Modeling neurogenesis impairment in Down syndrome with induced pluripotent stem cells from Trisomy 21 amniotic fluid cells. Exp. Cell Res. 319, 498–505.

Lyle, R., Bena, F., Gagos, S., Gehrig, C., Lopez, G., Schinzel, A., Lespinasse, J., Bottani, A., Dahoun, S., Taine, L., Doco-Fenzy, M., Cornillet-Lefebvre, P., Pelet, A., Lyonnet, S., Toutain, A., Colleaux, L., Horst, J., Kennerknecht, I., Wakamatsu, N., Descartes, M., Franklin, J.C., Florentin-Arar, L., Kitsiou, S., Ait Yahya-Graison, E., Costantine, M.,

Sinet, P.M., Delabar, J.M., Antonarakis, S.E., 2009. Genotype-phenotype correlations in Down syndrome identified by array CGH in 30 cases of partial trisomy and partial monosomy chromosome 21. Eur. J. Hum. Genet. 17, 454–466.

Maclean, G.A., Menne, T.F., Guo, G., Sanchez, D.J., Park, I.H., Daley, G.Q., Orkin, S.H., 2012. Altered hematopoiesis in trisomy 21 as revealed through in vitro differentiation of isogenic human pluripotent cells. Proc. Natl. Acad. Sci. U. S. A. 109, 17567–17572.

Mali, P., Yang, L., Esvelt, K.M., Aach, J., Guell, M., Dicarlo, J.E., Norville, J.E., Church, G.M., 2013. RNA-guided human genome engineering via Cas9. Science 339, 823–826.

Manterola, L., Hernando-Rodriguez, M., Ruiz, A., Apraiz, A., Arrizabalaga, O., Vellon, L., Alberdi, E., Cavaliere, F., Lacerda, H.M., Jimenez, S., Parada, L.A., Matute, C., Zugaza, J.L., 2013. 1-42 Beta-amyloid peptide requires PDK1/nPKC/Rac 1 pathway to induce neuronal death. Transl. Psychiatry 3, e219.

Mao, R., Wang, X., Spitznagel Jr., E.L., Frelin, L.P., Ting, J.C., Ding, H., Kim, J.W., Ruczinski, I., Downey, T.J., Pevsner, J., 2005. Primary and secondary transcriptional effects in the developing human Down syndrome brain and heart. Genome Biol. 6, R107.

Mensah, A., Mulligan, C., Linehan, J., Ruf, S., O'doherty, A., Grygalewicz, B., Shipley, J., Groet, J., Tybulewicz, V., Fisher, E., Brandner, S., Nizetic, D., 2007. An additional human chromosome 21 causes suppression of neural fate of pluripotent mouse embryonic stem cells in a teratoma model. BMC Dev. Biol. 7, 131.

Mojica, F.J., Diez-Villasenor, C., Garcia-Martinez, J., Soria, E., 2005. Intervening sequences of regularly spaced prokaryotic repeats derive from foreign genetic elements. J. Mol. Evol. 60, 174–182.

Monzel, A.S., Smits, L.M., Hemmer, K., Hachi, S., Moreno, E.L., Van Wuellen, T., Jarazo, J., Walter, J., Bruggemann, I., Boussaad, I., Berger, E., Fleming, R.M.T., Bolognin, S., Schwamborn, J.C., 2017. Derivation of human midbrain-specific organoids from neuroepithelial stem cells. Stem Cell Rep. 8, 1144–1154.

Moore, S., Evans, L.D., Andersson, T., Portelius, E., Smith, J., Dias, T.B., Saurat, N., Mcglade, A., Kirwan, P., Blennow, K., Hardy, J., Zetterberg, H., Livesey, F.J., 2015. APP metabolism regulates tau proteostasis in human cerebral cortex neurons. Cell Rep. 11, 689–696.

Mori, C., Spooner, E.T., Wisniewsk, K.E., Wisniewski, T.M., Yamaguch, H., Saido, T.C., Tolan, D.R., Selkoe, D.J., Lemere, C.A., 2002. Intraneuronal Abeta42 accumulation in Down syndrome brain. Amyloid 9, 88–102.

Morris, J.K., Wald, N.J., Watt, H.C., 1999. Fetal loss in Down syndrome pregnancies. Prenat. Diagn. 19, 142–145.

Mou, X., Wu, Y., Cao, H., Meng, Q., Wang, Q., Sun, C., Hu, S., Ma, Y., Zhang, H., 2012. Generation of disease-specific induced pluripotent stem cells from patients with different karyotypes of Down syndrome. Stem Cell Res. Ther. 3, 14.

Murray, A., Letourneau, A., Canzonetta, C., Stathaki, E., Gimelli, S., Sloan-Bena, F., Abrehart, R., Goh, P., Lim, S., Baldo, C., Dagna-Bricarelli, F., Hannan, S., Mortensen, M., Ballard, D., Syndercombe Court, D., Fusaki, N., Hasegawa, M., Smart, T.G., Bishop, C., Antonarakis, S.E., Groet, J., Nizetic, D., 2015. Brief report: isogenic induced pluripotent stem cell lines from an adult with mosaic Down syndrome model accelerated neuronal ageing and neurodegeneration. Stem Cells 33, 2077–2084.

Nizetic, D., Chen, C.L., Hong, W., Koo, E.H., 2015. Inter-dependent mechanisms behind cognitive dysfunction, vascular biology and Alzheimer's dementia in down syndrome: multifaceted roles of APP. Front. Behav. Neurosci. 9, 299.

O'doherty, A., Ruf, S., Mulligan, C., Hildreth, V., Errington, M.L., Cooke, S., Sesay, A., Modino, S., Vanes, L., Hernandez, D., Linehan, J.M., Sharpe, P.T., Brandner, S.,

Bliss, T.V., Henderson, D.J., Nizetic, D., Tybulewicz, V.L., Fisher, E.M., 2005. An aneuploid mouse strain carrying human chromosome 21 with Down syndrome phenotypes. Science 309, 2033–2037.

Olmos-Serrano, J.L., Kang, H.J., Tyler, W.A., Silbereis, J.C., Cheng, F., Zhu, Y., Pletikos, M., Jankovic-Rapan, L., Cramer, N.P., Galdzicki, Z., Goodliffe, J., Peters, A., Sethares, C., Delalle, I., Golden, J.A., Haydar, T.F., Sestan, N., 2016. Down syndrome developmental brain transcriptome reveals defective oligodendrocyte differentiation and myelination. Neuron 89, 1208–1222.

Ovchinnikov, D.A., Korn, O., Virshup, I., Wells, C.A., Wolvetang, E.J., 2018. The impact of APP on Alzheimer-like pathogenesis and gene expression in Down syndrome iPSC-derived neurons. Stem Cell Rep. 11, 32–42.

Park, I.H., Arora, N., Huo, H., Maherali, N., Ahfeldt, T., Shimamura, A., Lensch, M.W., Cowan, C., Hochedlinger, K., Daley, G.Q., 2008a. Disease-specific induced pluripotent stem cells. Cell 134, 877–886.

Park, I.H., Zhao, R., West, J.A., Yabuuchi, A., Huo, H., Ince, T.A., Lerou, P.H., Lensch, M.W., Daley, G.Q., 2008b. Reprogramming of human somatic cells to pluripotency with defined factors. Nature 451, 141–146.

Park, J., Oh, Y., Yoo, L., Jung, M.S., Song, W.J., Lee, S.H., Seo, H., Chung, K.C., 2010. Dyrk1A phosphorylates p53 and inhibits proliferation of embryonic neuronal cells. J. Biol. Chem. 285, 31895–31906.

Pasca, A.M., Sloan, S.A., Clarke, L.E., Tian, Y., Makinson, C.D., Huber, N., Kim, C.H., Park, J.Y., O'rourke, N.A., Nguyen, K.D., Smith, S.J., Huguenard, J.R., Geschwind, D.H., Barres, B.A., Pasca, S.P., 2015. Functional cortical neurons and astrocytes from human pluripotent stem cells in 3D culture. Nat. Methods 12, 671–678.

Peng, R., Lin, G., Li, J., 2016. Potential pitfalls of CRISPR/Cas9-mediated genome editing. FEBS J. 283, 1218–1231.

Pennington, B.F., Moon, J., Edgin, J., Stedron, J., Nadel, L., 2003. The neuropsychology of Down syndrome: evidence for hippocampal dysfunction. Child Dev. 74, 75–93.

Perluigi, M., Butterfield, D.A., 2012. Oxidative stress and down syndrome: a route toward Alzheimer-like dementia. Curr. Gerontol. Geriatr. Res. 2012, 724904.

Pinter, J.D., Eliez, S., Schmitt, J.E., Capone, G.T., Reiss, A.L., 2001. Neuroanatomy of Down's syndrome: a high-resolution MRI study. Am. J. Psychiatry 158, 1659–1665.

Pipino, C., Mukherjee, S., David, A.L., Blundell, M.P., Shaw, S.W., Sung, P., Shangaris, P., Waters, J.J., Ellershaw, D., Cavazzana, M., Mostoslavsky, G., Pandolfi, A., Pierro, A., Guillot, P.V., Thrasher, A.J., De Coppi, P., 2014. Trisomy 21 mid-trimester amniotic fluid induced pluripotent stem cells maintain genetic signatures during reprogramming: implications for disease modeling and cryobanking. Cell. Reprogram. 16, 331–344.

Pourcel, C., Salvignol, G., Vergnaud, G., 2005. CRISPR elements in Yersinia pestis acquire new repeats by preferential uptake of bacteriophage DNA, and provide additional tools for evolutionary studies. Microbiology 151, 653–663.

Prandini, P., Deutsch, S., Lyle, R., Gagnebin, M., Delucinge Vivier, C., Delorenzi, M., Gehrig, C., Descombes, P., Sherman, S., Dagna Bricarelli, F., Baldo, C., Novelli, A., Dallapiccola, B., Antonarakis, S.E., 2007. Natural gene-expression variation in Down syndrome modulates the outcome of gene-dosage imbalance. Am. J. Hum. Genet. 81, 252–263.

Prasher, V.P., Farrer, M.J., Kessling, A.M., Fisher, E.M., West, R.J., Barber, P.C., Butler, A.C., 1998. Molecular mapping of Alzheimer-type dementia in Down's syndrome. Ann. Neurol. 43, 380–383.

Qian, X., Nguyen, H.N., Song, M.M., Hadiono, C., Ogden, S.C., Hammack, C., Yao, B., Hamersky, G.R., Jacob, F., Zhong, C., Yoon, K.J., Jeang, W., Lin, L., Li, Y.,

Thakor, J., Berg, D.A., Zhang, C., Kang, E., Chickering, M., Nauen, D., Ho, C.Y., Wen, Z., Christian, K.M., Shi, P.Y., Maher, B.J., Wu, H., Jin, P., Tang, H., Song, H., Ming, G.L., 2016. Brain-region-specific organoids using mini-bioreactors for modeling ZIKV exposure. Cell 165, 1238–1254.

Raja, W.K., Mungenast, A.E., Lin, Y.T., Ko, T., Abdurrob, F., Seo, J., Tsai, L.H., 2016. Self-organizing 3D human neural tissue derived from induced pluripotent stem cells recapitulate Alzheimer's disease phenotypes. PLoS One 11, e0161969.

Raziuddin, A., Sarkar, F.H., Dutkowski, R., Shulman, L., Ruddle, F.H., Gupta, S.L., 1984. Receptors for human alpha and beta interferon but not for gamma interferon are specified by human chromosome 21. Proc. Natl. Acad. Sci. U. S. A. 81, 5504–5508.

Real, R., Peter, M., Trabalza, A., Khan, S., Smith, M.A., Dopp, J., Barnes, S.J., Momoh, A., Strano, A., Volpi, E., Knott, G., Livesey, F.J., De Paola, V., 2018. In vivo modeling of human neuron dynamics and Down syndrome. Science, 362 (6416). 1–9.

Ronan, A., Fagan, K., Christie, L., Conroy, J., Nowak, N.J., Turner, G., 2007. Familial 4.3 Mb duplication of 21q22 sheds new light on the Down syndrome critical region. J. Med. Genet. 44, 448–451.

Rovelet-Lecrux, A., Hannequin, D., Raux, G., Le Meur, N., Laquerriere, A., Vital, A., Dumanchin, C., Feuillette, S., Brice, A., Vercelletto, M., Dubas, F., Frebourg, T., Campion, D., 2006. APP locus duplication causes autosomal dominant early-onset Alzheimer disease with cerebral amyloid angiopathy. Nat. Genet. 38, 24–26.

Schlaeger, T.M., Daheron, L., Brickler, T.R., Entwisle, S., Chan, K., Cianci, A., Devine, A., Ettenger, A., Fitzgerald, K., Godfrey, M., Gupta, D., McPherson, J., Malwadkar, P., Gupta, M., Bell, B., Doi, A., Jung, N., Li, X., Lynes, M.S., Brookes, E., Cherry, A.B., Demirbas, D., Tsankov, A.M., Zon, L.I., Rubin, L.L., Feinberg, A.P., Meissner, A., Cowan, C.A., Daley, G.Q., 2015. A comparison of non-integrating reprogramming methods. Nat. Biotechnol. 33, 58–63.

Schneider, P., Bayo-Fina, J.M., Singh, R., Kumar Dhanyamraju, P., Holz, P., Baier, A., Fendrich, V., Ramaswamy, A., Baumeister, S., Martinez, E.D., Lauth, M., 2015. Identification of a novel actin-dependent signal transducing module allows for the targeted degradation of GLI1. Nat. Commun. 6, 8023.

Seki, T., Yuasa, S., Oda, M., Egashira, T., Yae, K., Kusumoto, D., Nakata, H., Tohyama, S., Hashimoto, H., Kodaira, M., Okada, Y., Seimiya, H., Fusaki, N., Hasegawa, M., Fukuda, K., 2010. Generation of induced pluripotent stem cells from human terminally differentiated circulating T cells. Cell Stem Cell 7, 11–14.

Shi, G., Jin, Y., 2010. Role of Oct4 in maintaining and regaining stem cell pluripotency. Stem Cell Res. Ther. 1, 39.

Shi, Y., Kirwan, P., Smith, J., Robinson, H.P., Livesey, F.J., 2012a. Human cerebral cortex development from pluripotent stem cells to functional excitatory synapses. Nat. Neurosci. 15, 477–486. S1.

Shi, Y., Kirwan, P., Smith, J., Maclean, G., Orkin, S.H., Livesey, F.J., 2012b. A human stem cell model of early Alzheimer's disease pathology in Down syndrome. Sci. Transl. Med. 4, 124ra29.

Shi, Y., Kirwan, P., Livesey, F.J., 2012c. Directed differentiation of human pluripotent stem cells to cerebral cortex neurons and neural networks. Nat. Protoc. 7, 1836–1846.

Sleegers, K., Brouwers, N., Gijselinck, I., Theuns, J., Goossens, D., Wauters, J., Del-Favero, J., Cruts, M., Van Duijn, C.M., Van Broeckhoven, C., 2006. APP duplication is sufficient to cause early onset Alzheimer's dementia with cerebral amyloid angiopathy. Brain 129, 2977–2983.

Soldner, F., Hockemeyer, D., Beard, C., Gao, Q., Bell, G.W., Cook, E.G., Hargus, G., Blak, A., Cooper, O., Mitalipova, M., Isacson, O., Jaenisch, R., 2009. Parkinson's disease patient-derived induced pluripotent stem cells free of viral reprogramming factors. Cell 136, 964–977.

Song, L., Yuan, X., Jones, Z., Griffin, K., Zhou, Y., Ma, T., Li, Y., 2019. Assembly of human stem cell-derived cortical spheroids and vascular spheroids to model 3-D brain-like tissues. Sci. Rep. 9, 5977.

Spencer, K., 2001. What is the true fetal loss rate in pregnancies affected by trisomy 21 and how does this influence whether first trimester detection rates are superior to those in the second trimester? Prenat. Diagn. 21, 788–789.

Sutcliffe, M., Lancaster, M.A., 2017. A simple method of generating 3D brain organoids using standard laboratory equipment. Methods Mol. Biol. 1576, 1–12.

Takahashi, K., Yamanaka, S., 2006. Induction of pluripotent stem cells from mouse embryonic and adult fibroblast cultures by defined factors. Cell 126, 663–676.

Takahashi, K., Tanabe, K., Ohnuki, M., Narita, M., Ichisaka, T., Tomoda, K., Yamanaka, S., 2007. Induction of pluripotent stem cells from adult human fibroblasts by defined factors. Cell 131, 861–872.

Velasco, S., Kedaigle, A.J., Simmons, S.K., Nash, A., Rocha, M., Quadrato, G., Paulsen, B., Nguyen, L., Adiconis, X., Regev, A., Levin, J.Z., Arlotta, P., 2019. Individual brain organoids reproducibly form cell diversity of the human cerebral cortex. Nature 570, 523–527.

Wang, S.Y., Cruts, M., Del-Favero, J., Zhang, Y., Tissir, F., Potier, M.C., Patterson, D., Nizetic, D., Bosch, A., Chen, H., Bennett, L., Estivill, X., Kessling, A., Antonarakis, S.E., Van Broeckhoven, C., 1999. A high-resolution physical map of human chromosome 21p using yeast artificial chromosomes. Genome Res. 9, 1059–1073.

Wang, Y., Mulligan, C., Denyer, G., Delom, F., Dagna-Bricarelli, F., Tybulewicz, V.L., Fisher, E.M., Griffiths, W.J., Nizetic, D., Groet, J., 2009. Quantitative proteomics characterization of a mouse embryonic stem cell model of Down syndrome. Mol. Cell. Proteomics 8, 585–595.

Watase, K., Zoghbi, H.Y., 2003. Modelling brain diseases in mice: the challenges of design and analysis. Nat. Rev. Genet. 4, 296–307.

Weick, J.P., Held, D.L., Bonadurer 3rd, G.F., Doers, M.E., Liu, Y., Maguire, C., Clark, A., Knackert, J.A., Molinarolo, K., Musser, M., Yao, L., Yin, Y., Lu, J., Zhang, X., Zhang, S.C., Bhattacharyya, A., 2013. Deficits in human trisomy 21 iPSCs and neurons. Proc. Natl. Acad. Sci. U. S. A. 110, 9962–9967.

Wilcock, D.M., 2012. Neuroinflammation in the aging Down syndrome brain; lessons from Alzheimer's disease. Curr. Gerontol. Geriatr. Res. 2012, 170276.

Wiseman, F.K., Al-Janabi, T., Hardy, J., Karmiloff-Smith, A., Nizetic, D., Tybulewicz, V.L., Fisher, E.M., Strydom, A., 2015. A genetic cause of Alzheimer disease: mechanistic insights from Down syndrome. Nat. Rev. Neurosci. 16, 564–574.

Wisniewski, K.E., Schmidt-Sidor, B., 1989. Postnatal delay of myelin formation in brains from Down syndrome infants and children. Clin. Neuropathol. 8, 55–62.

Xu, R., Brawner, A.T., Li, S., Liu, J.J., Kim, H., Xue, H., Pang, Z.P., Kim, W.Y., Hart, R.P., Liu, Y., Jiang, P., 2019. OLIG2 drives abnormal neurodevelopmental phenotypes in human iPSC-based organoid and chimeric mouse models of Down syndrome. Cell Stem Cell 24, 908–926 e8.

Yu, J., Vodyanik, M.A., Smuga-Otto, K., Antosiewicz-Bourget, J., Frane, J.L., Tian, S., Nie, J., Jonsdottir, G.A., Ruotti, V., Stewart, R., Slukvin, I.I., Thomson, J.A., 2007. Induced pluripotent stem cell lines derived from human somatic cells. Science 318, 1917–1920.

Yu, J., Hu, K., Smuga-Otto, K., Tian, S., Stewart, R., Slukvin, I.I., Thomson, J.A., 2009. Human induced pluripotent stem cells free of vector and transgene sequences. Science 324, 797–801.

Zalzman, M., Falco, G., Sharova, L.V., Nishiyama, A., Thomas, M., Lee, S.L., Stagg, C.A., Hoang, H.G., Yang, H.T., Indig, F.E., Wersto, R.P., Ko, M.S., 2010. Zscan4 regulates telomere elongation and genomic stability in ES cells. Nature 464, 858–863.

Zhang, Y., Liao, J.M., Zeng, S.X., Lu, H., 2011. p53 downregulates Down syndrome-associated DYRK1A through miR-1246. EMBO Rep. 12, 811–817.

Molecular Psychiatry
https://doi.org/10.1038/s41380-020-0806-5

ARTICLE

Patient-specific Alzheimer-like pathology in trisomy 21 cerebral organoids reveals BACE2 as a gene dose-sensitive AD suppressor in human brain

Ivan Alić[1,2,3] · Pollyanna A. Goh[2,4] · Aoife Murray[1] · Erik Portelius[5] · Eleni Gkanatsiou[5] · Gillian Gough[1] · Kin Y. Mok[4,6] · David Koschut[1] · Reinhard Brunmeir[1] · Yee Jie Yeap[1] · Niamh L. O'Brien[2,4] · Jürgen Groet[2,4] · Xiaowei Shao[1] · Steven Havlicek[7] · N. Ray Dunn[1,8] · Hlin Kvartsberg[5] · Gunnar Brinkmalm[5] · Rosalyn Hithersay[4,9,10] · Carla Startin[4,9] · Sarah Hamburg[4,9] · Margaret Phillips[11] · Konstantin Pervushin[11] · Mark Turmaine[12] · David Wallon[13] · Anne Rovelet-Lecrux[13] · Hilkka Soininen[14] · Emanuela Volpi[15] · Joanne E. Martin[2] · Jia Nee Foo[1,7] · David L. Becker[1] · Agueda Rostagno[16] · Jorge Ghiso[16] · Željka Krsnik[17] · Goran Šimić[17] · Ivica Kostović[17] · Dinko Mitrečić[17] · LonDownS Consortium[4] · Paul T. Francis[18] · Kaj Blennow[5] · Andre Strydom[4,9,10] · John Hardy[4,6] · Henrik Zetterberg[5,6] · Dean Nižetić[1,2,4]

Received: 29 January 2020 / Revised: 18 May 2020 / Accepted: 29 May 2020

Abstract

A population of more than six million people worldwide at high risk of Alzheimer's disease (AD) are those with Down Syndrome (DS, caused by trisomy 21 (T21)), 70% of whom develop dementia during lifetime, caused by an extra copy of β-amyloid-(Aβ)-precursor-protein gene. We report AD-like pathology in cerebral organoids grown in vitro from non-invasively sampled strands of hair from 71% of DS donors. The pathology consisted of extracellular diffuse and fibrillar Aβ deposits, hyperphosphorylated/pathologically conformed Tau, and premature neuronal loss. Presence/absence of AD-like pathology was donor-specific (reproducible between individual organoids/iPSC lines/experiments). Pathology could be triggered in pathology-negative T21 organoids by CRISPR/Cas9-mediated elimination of the third copy of chromosome 21 gene *BACE2*, but prevented by combined chemical β and γ-secretase inhibition. We found that T21 organoids secrete increased proportions of Aβ-preventing (Aβ1–19) and Aβ-degradation products (Aβ1–20 and Aβ1–34). We show these profiles mirror in cerebrospinal fluid of people with DS. We demonstrate that this protective mechanism is mediated by *BACE2*-trisomy and cross-inhibited by clinically trialled BACE1 inhibitors. Combined, our data prove the physiological role of *BACE2* as a dose-sensitive AD-suppressor gene, potentially explaining the dementia delay in ~30% of people with DS. We also show that DS cerebral organoids could be explored as pre-morbid AD-risk population detector and a system for hypothesis-free drug screens as well as identification of natural suppressor genes for neurodegenerative diseases.

Introduction

Production [1–3], and degradation [4] of β-amyloid peptides (Aβ) are among the central processes in the pathogenesis of Alzheimer's disease (AD). The canonical Aβ peptide is produced after sequential cleavage of the β-amyloid precursor-protein (APP) by β-secretase and γ-secretase, generating a peptide that most often begins 99 amino acids (aa) from the C-terminus of APP with Asp1 and contains the next 37–42 aa of the APP sequence, generating a range of peptides (Aβ1–37, 38, 39, 40, and 42). The longer of these peptides can be detected in toxic amyloid aggregates in the brain, associated with AD and other neurodegenerative disorders [5]. As *APP* gene is located on human

These authors contributed equally (ordered alphabetically): Aoife Murray, Erik Portelius, Ivan Alić, Pollyanna A. Goh

These authors jointly supervised this work: John Hardy, Henrik Zetterberg, Dean Nižetić

A full list of LonDownS Consortium members and their affiliations appear below the acknowledgements section.

Supplementary information The online version of this article (https://doi.org/10.1038/s41380-020-0806-5) contains supplementary material, which is available to authorized users.

✉ Dean Nižetić
d.nizetic@qmul.ac.uk

Extended author information available on the last page of the article

Published online: 10 July 2020

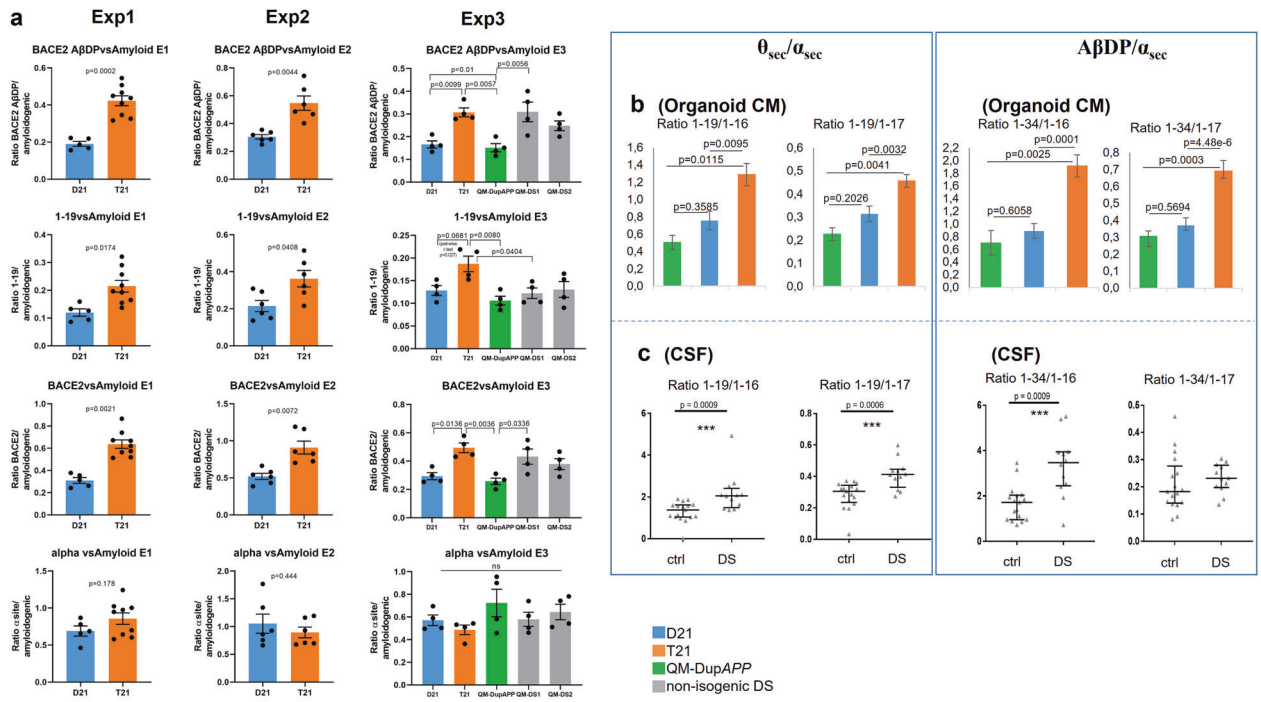

Fig. 1 Aβ peptide profiles secreted by trisomy 21 cerebral organoids. a Using Aβ IP-MS spectra from organoid (see Supplementary Figs. 1, 2, 4) conditioned media (CM), ratios were calculated of areas under the peak between the non-amyloidogenic and amyloidogenic peptides within a single mass-spectrogram. IP-MS spectra were produced for three timepoints (four timepoints in exp3) for each iPSC-derived organoid line, in each of three independent experiments (each experiment starting at the point of undifferentiated iPSC). The team performing the IP-MS analysis was blinded to the genotypes in all experiments. BACE2-AβDP (clearance) products = [1–20 & 1–34], total BACE2 = [1–19 & 1–20 & 1–34], amyloidogenic peptides = [1–38 & 1–39 & 1–40 & 1–42], α-site products = [1–16 & 1–17]. Exp1 and Exp2 *p* values: Holm–Bonferroni sequential corrections ($\alpha = 0.05$) of two-tailed student *t* test comparisons. Exp3: Holm-corrected *p* values after one-way ANOVA. Error bars: standard error. Combined data for the isogenic iPSC lines for all three experiments passed the Holm–Bonferroni correction ($\alpha = 0.05$) of sequential two-tailed student *t* test comparisons of each peptide ratio shown in Fig. 1a (available on request). T21 and D21: isogenic iPCS derived from a single mosaic individual with DS published previously (Murray A et al. 2015), QM-DS1 and QM-DS2: unrelated DS iPSC, DupAPP: FEOAD iPSC. **b** All three experiments in Fig. 1a were combined to calculate the ratios of BACE2-related non-amyloidogenic peptides (1–19 or 1–34) to BACE2-unrelated non-amyloidogenic peptides (1–16 or 1–17) in organoid CM. Holm-corrected *p* values after one-way ANOVA are shown. Error bars: standard error. **c** Same ratios as in part 'a' were calculated on IP-MS spectra obtained from cerebrospinal fluid samples of people with DS ($n = 17$) and age-matched normal controls ($n = 12$). Data are presented as mean ±1SD.

chromosome 21, people with Down Syndrome (DS, caused by trisomy 21 (T21)) are born with one extra copy of this gene, which increases their risk of developing AD. Non-DS (euploid) people inheriting triplication of the *APP* gene alone (Dup*APP*) develop AD symptoms by age 60 with 100% penetrance. Paradoxically, only ~70% of people with DS develop clinical dementia by age 60, suggesting the presence of other unknown chromosome 21-located genes that modulate the age of dementia onset [6, 7]. A number of secretases participate in the physiological cleavage of APP [1, 8], generating various peptides involved in neuronal pathology. BACE1 is the main β-secretase in the brain [9], whereas the expression and function of its homologue BACE2 (encoded by a chromosome 21 gene) remain less clear [10, 11]. At least three different activities of BACE2 were recorded with regards to APP processing: as an auxiliary β-secretase (pro-amyloidogenic), as a θ-secretase (degrading the β-CTF and preventing the formation of Aβ), and as Aβ-degrading protease (AβDP) (degrading synthetic Aβ-peptides at extremely acidic pH). It remains unclear which of these activities reflect the role of BACE2 in AD. The potential activity of BACE2 as an anti-amyloidogenic θ-secretase can be predicted from studies on a variety of transfected cell lines that overexpress *APP*, and artificially manipulate the dose of BACE2 [12–15]. These studies uncovered that BACE2 can cleave the product of β-secretase (APP β-CTF) between aa19 and aa20, generating a 1–19 fragment [13–15], thereby potentially preventing the formation of amyloidogenic Aβ, and degrading the β-CTF that has been implicated in neuronal toxicity, and impairment of several neuronal functions, such as axonal transport and autophagy [16]. When offered synthetic Aβ40/42 peptides in solution, purified BACE2 protein can rapidly degrade them by cutting after aa20 and aa34, to generate the 1–20 and 1–34 peptide products, but only at very acidic pH (3.5–4). In this reaction, BACE2 is 150-fold more efficient

than BACE1, which is also capable of this cleavage, upon conditions of increased enzyme concentration/time [12, 14]. Neither of these two putative anti-amyloidogenic actions of BACE2 (the θ-secretase activity, generating aa1–19, or the Aβ-degrading protease activity (AβDP or Aβ clearance) generating aa1–20 and aa1–34), have yet been demonstrated to be the functional role of BACE2 under physiologically fluctuating gene doses in vivo in the human brain. A naturally occurring form of gene overdose for both *APP* and *BACE2* is DS, caused by the trisomy of human chromosome 21 (T21) that harbours both *APP* and *BACE2* genes. As increased levels of soluble Aβ were observed already in foetal brains in DS [17], we examined cerebral organoids grown from induced pluripotent stem cells (iPSC) generated by non-integrational reprogramming of primary cells donated by people with DS, including an isogenic DS (T21) iPSC model [18], as a platform to analyse the T21-specific effects on APP proteolytic processing.

Results

Trisomy 21 (but not Dup*APP*) skews the ratios of Aβ non-amyloidogenic peptides

We compared organoids from isogenic iPSC clones, derived from the same individual with DS, mosaic for T21 and normal disomy 21 (D21) cells [18]. Cerebral organoids were derived following a published protocol [19], and shown to contain neurons expressing markers of all six layers of the human cortex (Supplementary Fig. 1) and no significant difference in the proportions of neurons and astrocytes between the D21 and T21 organoids (Supplementary Fig. 2). The integrity and copy number of the iPSC lines were validated at the point of starting the organoid differentiation, for chromosome 21 (Supplementary Fig. 3), and the whole genome (available on request). T21/D21 status was further verified by interphase Fluorescence In Situ Hybridization (FISH) on mature organoid slices, (Supplementary Fig. 4a). The C-terminal region of APP can be processed by the sequential action of different proteases to produce a range of protein fragments and peptide species, including Aβ (Supplementary Fig. 5). Aβ peptide profiles were analysed from organoid-conditioned media (CM) whereby each CM sample was taken from a 6 cm dish culturing a pool of 12–16 organoids derived from one iPSC clone, in total: $n = 15$ CM samples for Exp1 (three trisomic isogenic clones, two disomic isogenic clones, three timepoints each), $n = 12$ CM samples for Exp2 (two trisomic isogenic clones, two disomic isogenic clones, three timepoints each) and $n = 20$ CM samples for Exp3 (one trisomic isogenic clone, one disomic isogenic clone, one DupAPP clone, one line each for two different unrelated DS individuals, four timepoints each). CM was collected at timepoints between days 100–137 of culturing and analysed using immunoprecipitation in combination with mass spectrometry (IP-MS) [20]. Please see "Methods" and "Supplementary Data" sections for more detailed explanations, and statistical controls used for individual iPSC line-to-line comparisons (Fig. 1a). Relative ratios were calculated of areas under the peak between the peptides of interest within a single mass spectrum (raw data example in Supplementary Fig. 6d), therefore unaffected by the variability in the total cell mass between wells growing organoids. The proportions of non-amyloidogenic peptides with the signature of BACE2 cleavage products, both as a putative θ-secretase (as reflected by the Aβ1–19 product) and putative AβDP or Aβ-clearance products (Aβ1–20 & 1–34), or combined, (relative to the sum of Aβ amyloidogenic peptides (Aβ1–38 & 1–39 & 1–40 & 1–42)) were approximately doubled in CM from T21 organoids, compared with isogenic normal controls, and reached levels of >80% of the amyloidogenic peptide levels (Fig. 1a). This result was fully reproduced in three independent experiments, each starting from undifferentiated iPSCs (three vertical columns of graphs in Fig. 1a). In experiment 3, more recently generated iPSC lines from different individuals were introduced; from a euploid patient with FEOAD caused by Dup*APP* [21], and from two unrelated people with DS (Supplementary Figs. 1–3). The 1–34 & 1–20/amyloidogenic ratios were not significantly different between D21 and Dup*APP* lines, suggesting the third copy of the *APP* gene alone did not cause any change in this ratio. Ratios of 1–34 & 1–20/amyloidogenic peptides and combined BACE2-products/amyloidogenics were significantly increased in T21 clones (combining all three T21 individuals) compared with D21 or Dup*APP* lines (Fig. 1a). The ratio of 1–19/amyloidogenics was significantly higher in T21 clones from the isogenic model, compared with its disomic isogenic control, and compared with Dup*APP*, but it was unchanged in the other two unrelated DS iPSC lines (see also Supplementary Information for a more-detailed explanation). As the proportions of BACE2-unrelated α-site cleavage products (1–16, 1–17) were not different between T21 and isogenic D21 organoids (in any of the three experiments) (Fig. 1a), it can be predicted that the increased presence of 1–19, 1–20, and 1–34 peptides in T21 contributes towards an overall increase in soluble peptides that are non-amyloidogenic. The validity of this prediction was tested by an independent biochemical method (ELISA), by measuring the Aβ-peptide concentrations within the isogenic T21:D21 organoid CM comparison, which showed an increase in absolute concentrations caused by T21 for each Aβ 1–38, 1–40, and 1–42, with no difference in the Aβ 1–42/1–40 ratio between T21 and isogenic D21 clones, mirroring the readout in the absolute levels of IP-MS peaks (Supplementary Fig. 6).

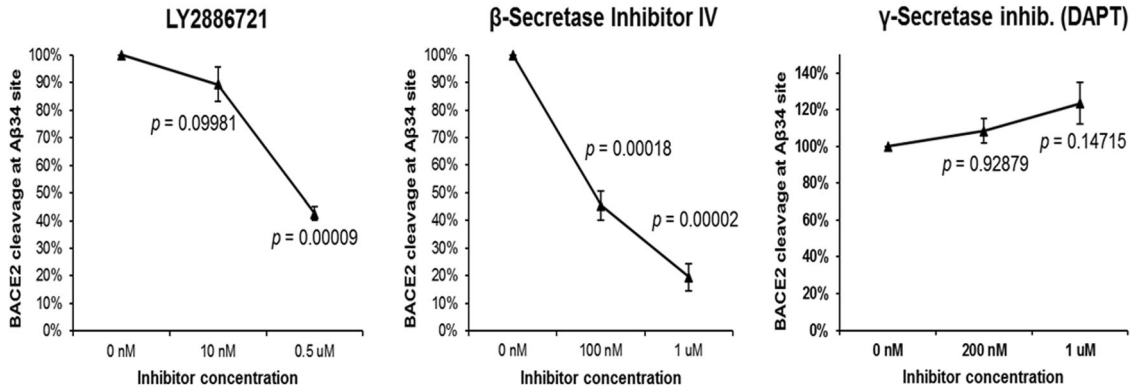

Fig. 2 FRET-based assay for BACE2 cleavage. A newly custom designed FRET reagent (spanning the Aβ34 site) was digested at pH=3.5 by the human BACE2 in presence or absence of the stated inhibitors for 2 h. Enzyme activity was defined by measuring the fluorescence increase before and after the incubation. Blank-subtracted fluorescence units were normalized to the control digest and a one-way ANOVA was performed. *P* values were calculated with a post hoc Bonferroni multiple comparison (only pairs relative to the untreated control simultaneously compared). Error bars: standard error. $n = 3$ replicates per inhibitor per concentration.

Analysis of IP-MS area under peak (used in Fig. 1 to calculate relative ratios) showed a near linear correlation when plotted against absolute peptide concentrations measured by ELISA, for each Aβ 1–38, 1–40, and 1–42 (Supplementary Fig. 6), validating our relative ratio calculations by an independent biochemical method.

To estimate the contribution of BACE2 towards the anti-amyloidogenic pathway relative to other anti-amyloidogenic cleavages at the α-site, we calculated the peptide ratios of 1–19/1–16 or 1–17 (θ secretase/α secretase products) and 1–34/1–16 or 1–17 (BACE2-AβDP/α secretase products). We observed that T21 organoids produce statistically highly significant increases in all four of these ratios, relative to isogenic D21, or non-isogenic Dup*APP* organoids (Fig. 1b). Therefore, we conclude that T21 causes these effects in our organoid system. The D21 ratios were not significantly different to Dup*APP*, suggesting that the third copy of genes other than *APP* causes these effects. These peptide profiling data strongly favour the hypothesis of a genetic dose-sensitive anti-amyloidogenic action of BACE2.

Non-amyloidogenic Aβ peptide ratios mirror between T21 organoids and DS-CSF

In order to assess if the peptide ratio differences from Fig. 1b have any relevance in vivo, we analysed the Aβ-peptide profiles immunoprecipitated from human cerebrospinal fluid (CSF). We have previously produced IP-MS data on CSF from people with DS and age-matched controls [22]. We repeated the calculations shown for organoids in Fig. 1b, on IP-MS results from CSF samples from DS ($n = 17$) and age-matched euploid people ($n = 12$). All four relative ratio calculations showed an increase in peptide ratios in CSF from people with DS, compared with age-matched euploid controls, of which three comparisons were statistically highly significant (Fig. 1c). This suggests that in DS brains, the third copy of *BACE2* skews the anti-amyloidogenic processing significantly towards BACE2-cleavages, relative to other anti-amyloidogenic enzymes cleaving at the α-site. Importantly, these CSF results validate the in vivo relevance of the peptide ratios obtained using CM from iPSC-derived cerebral organoids (comparison of Fig. 1b and Fig. 1c).

Aβ-degrading activity of BACE2 is cross-inhibited by clinically trialed BACE1 inhibitors

Chemical inhibition of BACE1 remains an attractive therapeutic strategy for AD. As BACE2 is a homologous protein, most inhibitors tested in clinical trials also cross-inhibit the (pro-amyloidogenic) β-secretase activity of BACE2, which has been proven as the cause of several unwanted side-effects, such as skin pigmentation changes. As our data suggest that the opposite, Aβ-degrading, activity of BACE2 has an important role, we designed a new FRET-based in vitro assay, in which efficient AβDP-cutting after Aβ aa34 by BACE2 at pH=3.5 could be measured (Fig. 2), whereas zero activity by BACE1 was detectable under same conditions (Supplementary Information). We demonstrated that at least two BACE1 inhibitor compounds (of which one recently used in clinical trials) inhibit the AβDP (Aβ-clearance) activity of BACE2 in a dose-dependent manner (Fig. 2). This has, to our knowledge, so far not been shown, and could provide an additional explanation for the failure of some BACE1 inhibitor clinical trials, and should be taken in consideration when testing new inhibitors.

AβDP product (Aβx-34) colocalises with BACE2 in human brain and organoid neurons

As in vitro experiments showed that BACE2 can very efficiently cleave the Aβ34 site in the FRET peptide (Fig. 2)

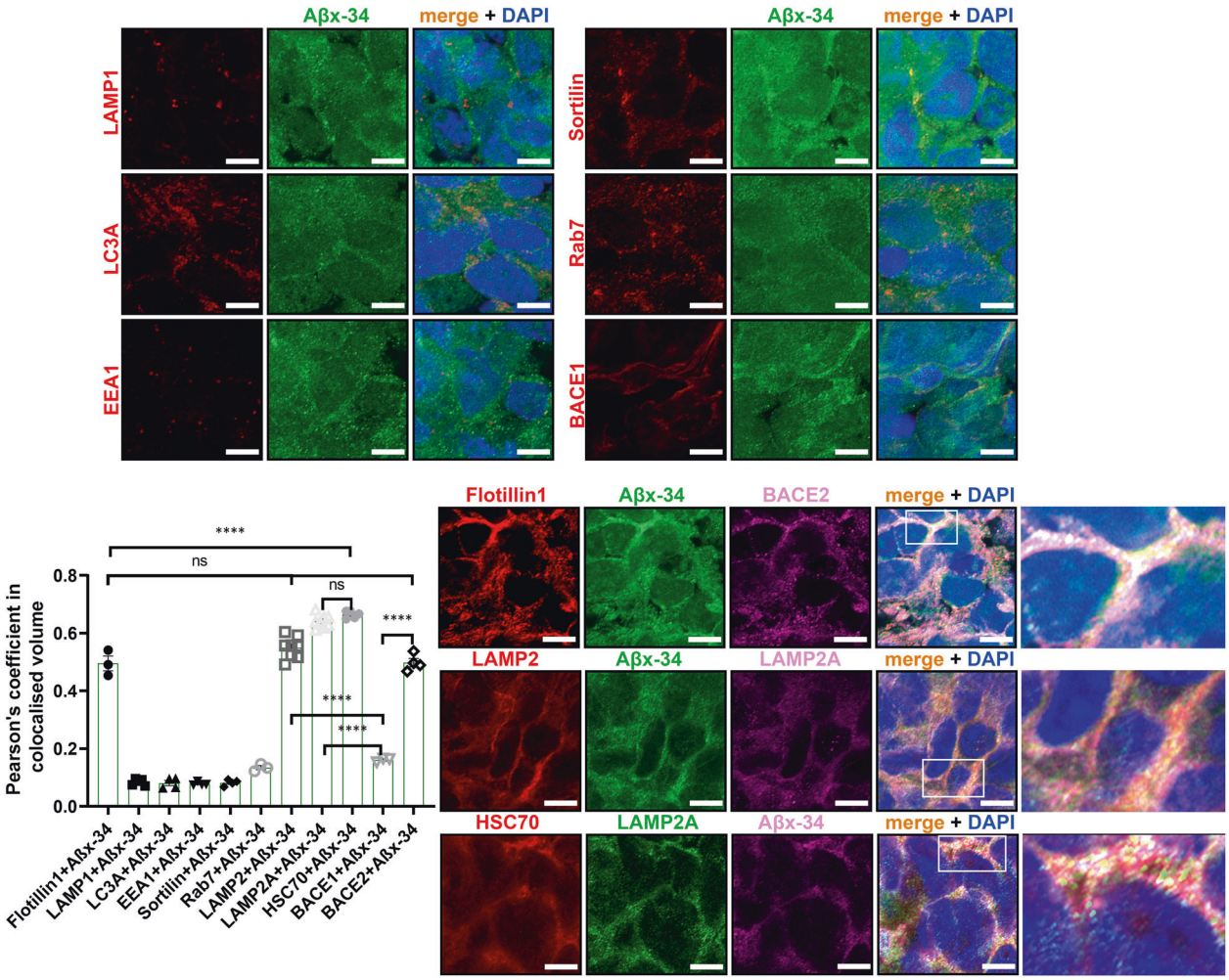

Fig. 3 Subcellular compartment localisation of Aβ degradation product Aβx-34 in hiPSC-derived cerebral organoid sections. Pairwise Pearson's coefficient of colocalisation for a pair of co-stained antibodies: Aβx-34, and a specific marker for the subcellular vesicle compartment: lipid rafts (Flotillin1), lysosomes (LAMP1), macro-autophagosomes (LC3A), early endosomes (EEA1), macro-autophagosome-lysosome fusion/exosomes (Sortilin), late endosomes (Rab7), specific sub-sets of lysosomes (LAMP2, LAMP2A) and CMA-chaperone (HSC70). In the final two columns of the histogram, the Pearson's colocalisation level was shown between Aβx-34 and BACE1 or BACE2, respectively (repeated in more detail in Supplementary Fig. 7). Greater than 95% of cells in all of these images were MAP2+ neurons (not shown). Representative images of the organoid stainings from which the coefficients were calculated are shown in the panels. Last column in the bottom right panel is the zoomed-in inset from the previous column. Images were captured using AiryScan Zeiss confocal microscopy, and single 0.16 µm slices are shown (from 20 µm full z-stack analysed). Error bars: standard error, *p* values: after standard one-way ANOVA using post hoc Bonferroni multiple comparison calculation. Scale bar: 5 µm.

and synthetic Aβ1–40 peptide in solution at an acidic pH [12], we sought to visualize if the presence of the substrate (Aβ1–40), enzyme (BACE2), and one of the products of this reaction (Aβ1–34) can be detected in our organoids, in a subcellular compartment known to be acidic. First, by immunofluorescence (IF) using pan-anti-Aβ (4G8), anti-BACE2, or neo-epitope-specific antibodies against Aβx-40 and Aβx-34 [23], we detected significantly higher signals (normalized to pan-neuronal marker) in T21 organoid neurons, compared with isogenic D21 ones (Supplementary Fig. 4b–d). Pearson's coefficient showed a high level of colocalisation (>0.55) of both the main substrate (Aβx-40) and its putative degradation product (Aβx-34) with BACE2 in neurons of cerebral organoids, in LAMP2+ compartment (known to be a subset of lyzosomes, therefore low pH vesicles) (Fig. 3 & Supplementary Fig. 7). In comparison, the Pearson's coefficient for BACE1 with Aβx-34 was only 0.16 (Fig. 3 & Supplementary Fig. 7), and its pattern of subcellular localization was different to BACE2 (high colocalization with Rab7 and Sortilin, much lower with LAMP2). Using IF on human brain sections, a similar highly significant difference was observed (Fig. 4a, b): Aβx-34 colocalised with BACE2 (0.52 (±0.034 SEM)) as opposed to BACE1 (0.01 (±0.021 SEM)). The colocalised signal of Aβx-34 and BACE2 was seen in three categories of objects (Fig. 4), in all analysed samples: four individual

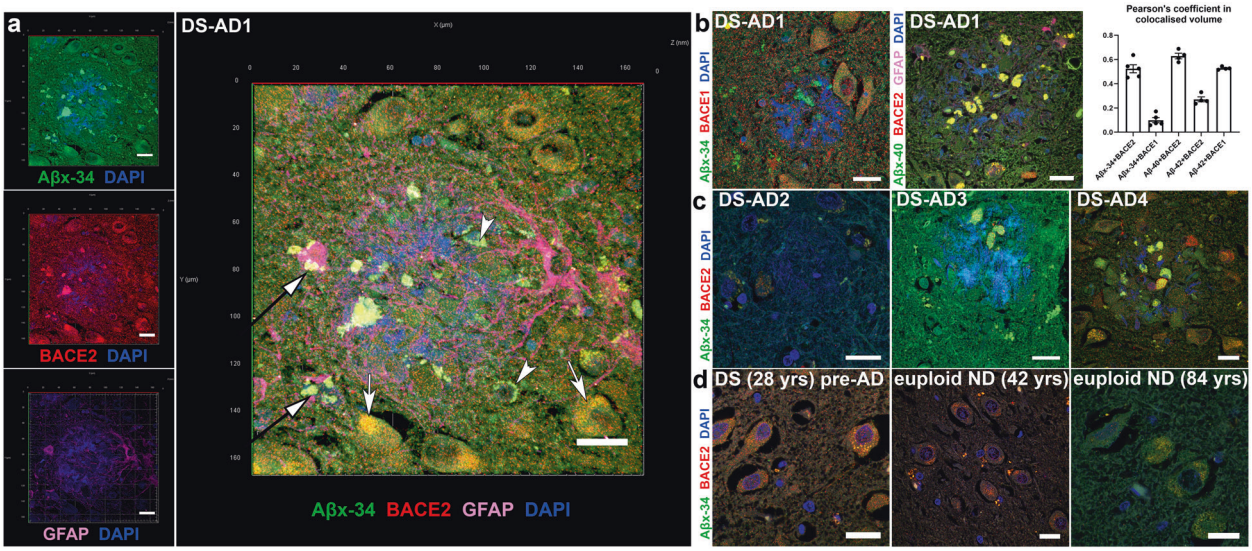

Fig. 4 Localisation of AβDP degradation products and Aβ peptides with BACE2 in hippocampal sections of the human post-mortem brain. a Immunofluorescence analysis of the brain of DS-AD-1 co-stained for Aβx-34, BACE2, and GFAP. A typical near-circular neuritic plaque is shown (in which DAPI faintly stains the fibrillar amyloid deposits). Arrows indicate three categories of objects in which the colocalisation of BACE2 and the AβDP product Aβx-34 is observed. White arrows: intraneuronal fine-vesicular pattern; white arrowheads: large intraneuronal spherical granules (lipofuscin); black arrows with white arrowheads: amorphous extracellular aggregates. See Methods and Supplementary Fig. 8 for experiments controlling the extent of lipofuscin autofluorescence effects. **b** DS-AD1 brain co-stained for Aβx-34 and BACE1, or Aβx-40, BACE2 and GFAP, and Pearson's coefficient of colocalisation for proteins stained in parts 'a' and 'b', with the addition of the staining for Aβx-42 neo-epitope (not shown). Error bars: SEM. **c** Same IF staining combinations as in part 'a' (except for GFAP) were used in three additional brain samples: DS-AD-2, 3, and 4. **d** Brain sample co-stained for BACE2 and Aβx-34 of a 28 yrs old person with Down syndrome without dementia, and euploid non-demented (ND) controls aged 42 and 84. Scale bar: 20 µm.

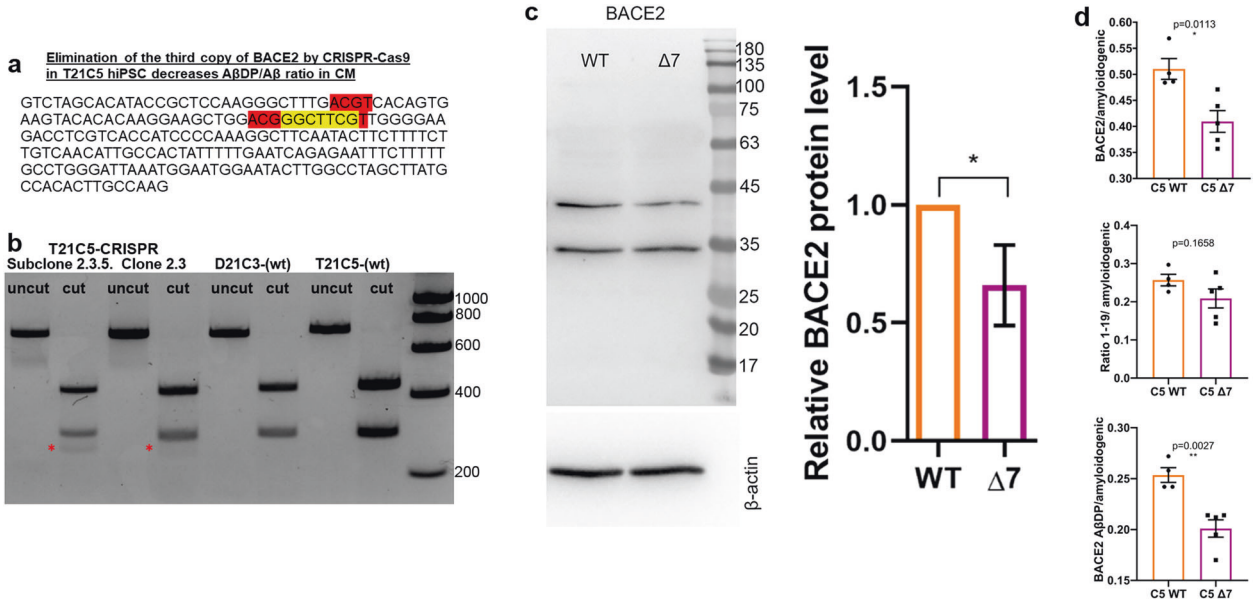

Fig. 5 CRISPR/SpCas9-HF1-mediated reduction of BACE2 copy number from three to two in the T21C5 hiPSC line. a *BACE2* exon3 sequence with 7 bp deletion (yellow) provoked by the CRISPR/SpCas9-HF1 is shown. Red: restriction endonuclease HpyCH4IV sites (a de novo HpyCH4IV site is generated by the 7 bp deletion). b agarose gel electrophoresis of the 733 bp PCR product containing the targeted site before (uncut) and after digestion with HpyCH4IV (cut), for the initial clone 2.5, and its colony-purified sub-clone 2.3.5 (renamed further below as "Δ7"). The 294 bp fragment in 2.3.5 is reduced to 65% of the wt value (normalized to the 439 bp band), and a de novo 255 bp fragment appears in CRISPR-targeted line (red asterisk). **c** Western blot stained with anti-BACE2 antibody of the lysates of the iPSC line Δ7 compared with the wt T21C5 iPSC line. Quantification of the total actin-normalised BACE2 signal showed a significant reduction in Δ7 compared with T21 unedited line. Error bars: standard error, *p* value: student's *t* test. **d** BACE2-AβDP/amyloidogenic peptides ratio after IP-MS analysis of CM produced by the 48DIV organoids derived from the iPSC line Δ7 compared with the T21C5wt control were significantly decreased. Error bars: standard error, *p* values: two-tailed *t* test comparison.

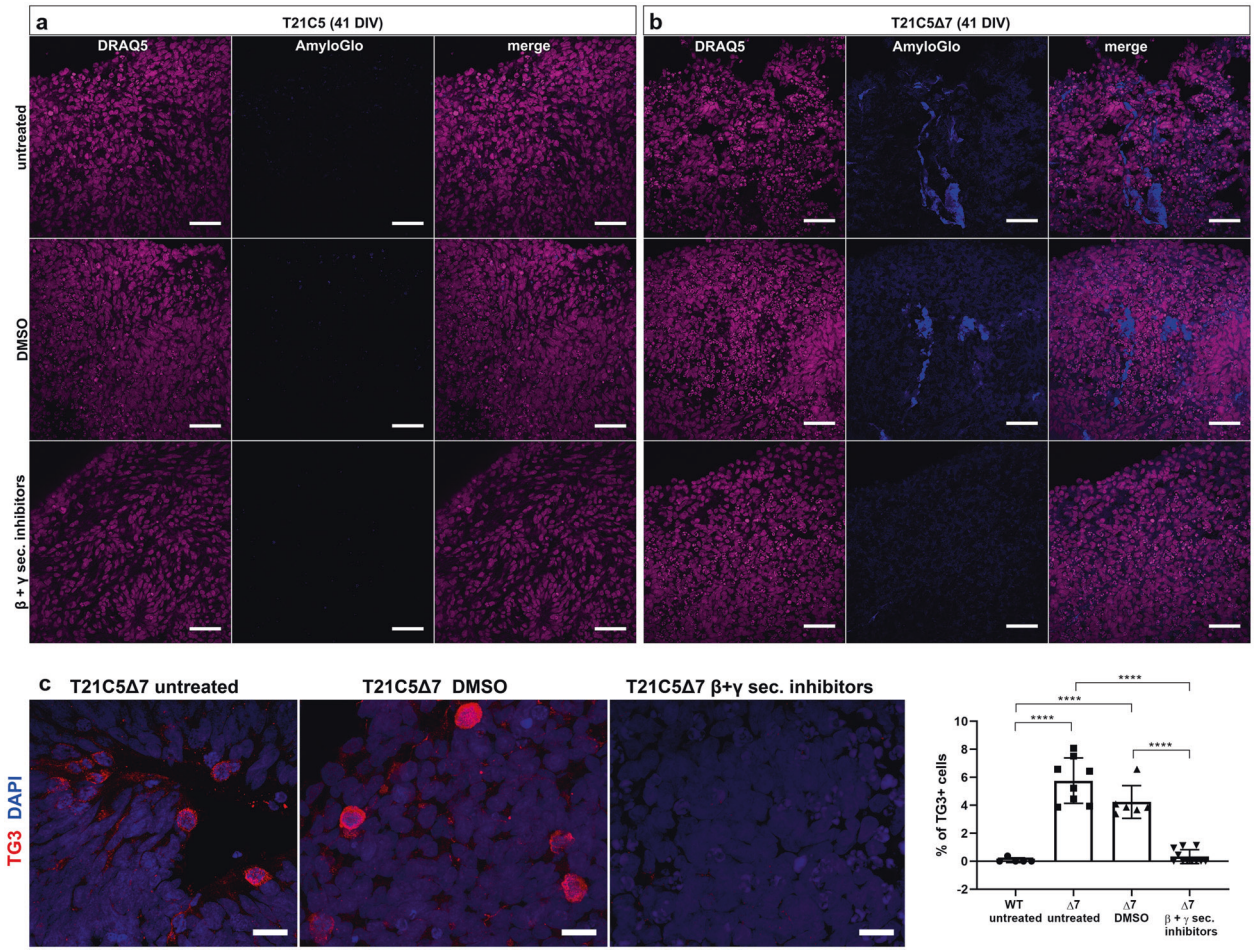

Fig. 6 CRISPR/SpCas9-HF1-mediated reduction of BACE2 copy number from three to two in the T21C5 hiPSC line provoked early AD-like pathology in organoids. a–c Early AD-like pathology was provoked in 41DIV T21C5Δ7 organoids, but was not detected in T21C5 parental organoids. **a–b** Treatment of the T21C5Δ7 with combined βI-IV (β-sectretase inhibitor) and compound E (γ-secretase inhibitor) from 20 to 41DIV completely prevented the formation of extracellular amyloid deposits. Staining with amyloid specific dye (AmyloGlo) and nuclear dye (DRAQ5). Scale bar 50 µm. **c** β- and γ-secretase inhibitor treatment highly significantly reduced the presence of TG3+ (pathologically conformed Tau) cells in T21C5Δ7 organoids compared with untreated T21C5Δ7 organoids. Scale bar: 20 µm. Error bars: SD, $****p < 0.0001$. Only statistically significant differences are shown.

DS-AD brains (Fig. 4a–c), five euploid sporadic AD subjects (example in Supplementary Fig. 8a, for complete list of brain samples see Supplementary Table 1) and (in the fine vesicle compartment only) in five non-demented control euploid subjects' neurons (age 42–84), as well as DS brain from a 28 yr old with no plaques or dementia, (examples in Fig. 4d, for complete list of brain samples see Supplementary Table 1). Lambda scanning and Sudan black B stainings were independently used to subtract the autofluorescence of lipofuscin granules (Supplementary Fig. 8f, g). This has proven that the fine-vesicular pattern and large amorphous extracellular aggregates are not autofluorescent lipofuscin granules, but real colocalisations of BACE2 and Aβx-34 (Supplementary Fig. 8). Colocalised signals of Aβx-34 and BACE2 were particularly strong in areas surrounding neuritic plaques (Fig. 4a–c).

As AβDP cleavage by BACE2 is efficient only at low pH, we sought to analyse in more detail the BACE2 and Aβx-34 colocalisation in highly acidic cellular compartments. For this reason, we co-stained lysosome markers LAMP1 or LAMP2 with Aβx-34. In addition, macro-autophagic vacuoles containing Aβ were shown to accumulate in AD distended neurites [24], which is why we also stained with the macro-autophagosome marker LC3A. As we further found that Aβx-34 did not colocalise with LAMP1 or LC3A, but colocalised strongly with LAMP2 (Fig. 3, Supplementary Fig. 7 and Supplementary Information), we tested colocalisation with the components of an alternative autophagy pathway: chaperone-mediated autophagy (CMA), and found a very high level of colocalisation (Fig. 3).

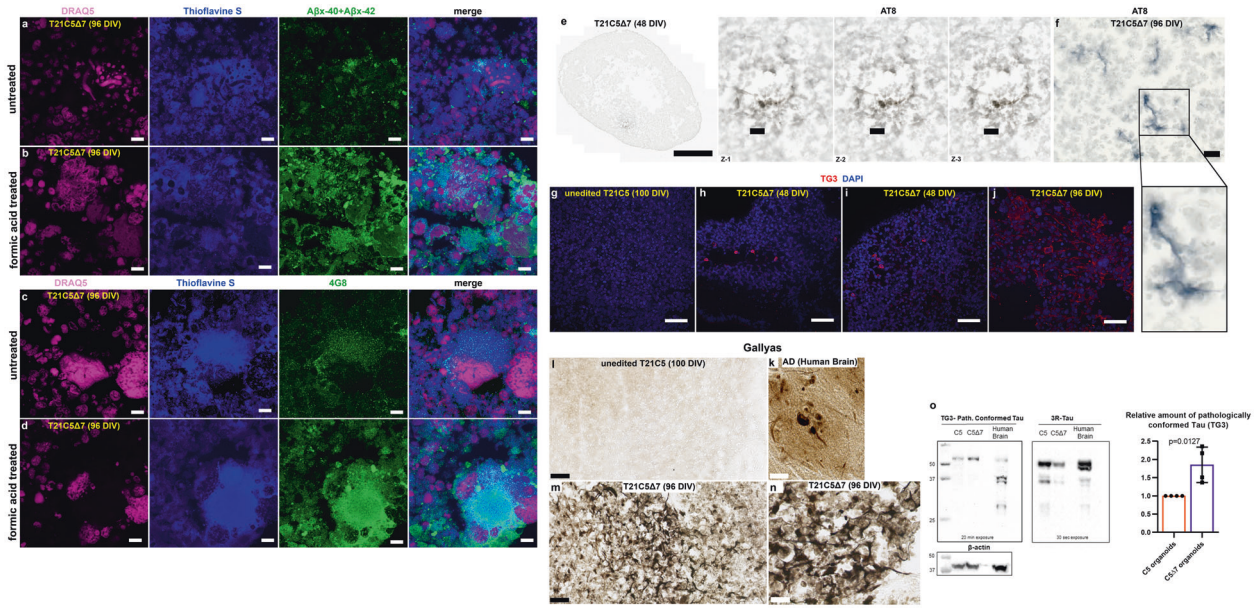

Fig. 7 Amyloid and Tau pathology are shown with six different methods in T21C5Δ7 organoids that have BACE2 copy number reduced from three to two by CRISPR/Cas9. a–d The signal of amyloid specific antibodies Aβx-40 + Aβx-42 (**a**, **b**), or 4G8 (**c**, **d**) colocalising with Thioflavine S in T21C5Δ7 (96DIV) organoids was drastically increased upon treatment with 87% Formic acid for 10 minutes at RT, proving it contains the insoluble extracellular β-amyloid deposits. Scale bar: 10 µm. **e** AT8 (hyperphosphorylated Tau) positive neurites within plaque-like structure in 48DIV organoids. Left: the whole organoid slice, scale bar: 500 µm. Right: zoom in on the plaque-like structure from 'e', in the three individual z-slices (interval between slices, 1 µm; scale bar: 20 µm). **f** AT8 (hyperphosphorylated Tau) positive neurites in 96DIV organoids. Scale bar: 10 µm. **g–j** TG3 (conformationally altered Tau) staining of unedited control T21C5 (100DIV) **g**, CRISPR-edited T21C5Δ7 (48DIV) with TG3-positive neurons in 48DIV organoids **h**, **i**, and CRISPR-edited T21C5Δ7 (96DIV) showing many TG3+ neurons with diffuse staining of extracellularized mal-conformed Tau aggregates **j**. Scale bar: 50 µm. **k–n** Gallyas staining of human AD brain **k**, unedited control T21C5 (100DIV) **l**, CRISPR-edited T21C5Δ7 (96DIV) **m**, **n** shows negative staining in parental unedited organoid **l** and very strong signal in neurons and plaque-like associated neurites within T21C5Δ7 organoid **m**, **n**. Scale bars: 50 µm **l**, **m** and 20 µm **n** and 5 µm **k**. **o** Representative western blot of T21C5 and T21C5Δ7 organoid lysates stained using antibodies against pathologically conformationally altered Tau (TG3) or general 3 repeat (3 R) Tau. β-actin was used as a loading control. Human brain tissue of a 75 year old is shown for comparison. Comparison of the average values ($n = 4$) for CRISPR-edited T21C5Δ7 showed a highly significant relative increase in TG3 compared with unedited ($n = 4$) T21C5 organoids, as indicated in the graph, $p = 0.0127$.

Trisomy of *BACE2* skews non-amyloidogenic Aβ peptide ratios and suppresses AD-like pathology in organoids

Using CRISPR/SpCas9-HF1, we eliminated a single copy of *BACE2* in the trisomic iPSC clone C5 (T21C5Δ7, a Δ7 bp in *BACE2* exon3, knocking out one of three copies of the gene), while maintaining the trisomy of the rest of chromosome 21 (Fig. 5a–c, Supplementary Fig. 9, Supplementary Information). Total actin-normalised BACE2 signal showed a 27–34% reduction in Δ7 compared with T21 unedited clone, and no significant difference compared with D21 control (Fig. 5c, Supplementary Fig. 10). Total protein level of APP in Δ7 remained at trisomic levels, significantly increased compared with the disomic control (Supplementary Fig. 10). The CRISPR-edited iPSCs formed cerebral organoids expressing markers of all six neuronal layers by 48 days in vitro (DIV) (Supplementary Fig. 9c). The CRISPR correction of *BACE2* gene dose from three to two, resulted in a significant decrease in levels of putative BACE2-AβDP (Aβ-clearance) products (1–20 & 1–34), as well as total BACE2-related non-amyloidogenic peptides (1–19 & 1–20 & 1–34), relative to amyloidogenic peptides (Fig. 5d). This pinpoints the triplication of *BACE2* as a likely cause of specific anti-amyloidogenic T21 effects we observed in Fig. 1a. Furthermore, we used two different dyes to detect any presence of amyloid deposits (the traditional Thioflavine S, and a newer, more sensitive dye AmyloGlo [25]) in organoid sections. Remarkably, elimination of the third *BACE2* copy caused the T21 organoids (that had not shown any overt amyloid deposits at 100DIV, see T21C5 in Supplementary Fig. 11, top row) to develop extremely early AD-plaque-like deposits (AmyloGlo+ and Thioflavine S+) in the cortical part of the organoid by 48DIV (Supplementary Fig. 11, middle row), that progressed aggressively and became much stronger and denser by 96 DIV, accompanied by massive cell death (Supplementary Fig. 11, bottom row, Supplementary Fig. 12).

In order to prove that extracellular deposits staining positively with amyloid dyes really are related to

Table 1 List of participant donors of cells for iPSC-organoid generation and reproducibility of AD-like pathology (by histological analysis).

Participant	DS	Age at sample collection	Sex	Dementia status	APOE	Donated primary material	Number of iPSC clones generated	Number of clones used for organoid generation	Number of organoids with AD-like-pathology/total number of histologically analysed organoids
QM-DS1	Yes	40	F	Diagnosed at 40, symptoms at 37	3,3	Hair strands	3	2	9/9 (two iPSC clones analysed)
QM-DS2	Yes	67	M	Diagnosed at 63	3,3	Hair strands	5	1	12/12
QM-DS3	Yes	38	M	Diagnosed at 37	3,4	Hair strands	1	1	7/7
QM-DS4	Yes	64	M	Diagnosed at 62 (brother and sister have AD)	3,3	Hair strands	3	2	6/6 (two iPSC clones analysed)
QM-DS5	Yes	60	M	Diagnosed at 62	3,3	Hair strands	3	2	6/6 (two iPSC clones analysed)
QM-DS6	Yes	31	F	No dementia at 37	3,4	Hair strands	8	2	0/6 (two iPSC clones analysed)
QM-Dup*APP*	No	64	M	FEOAD, no DS	3,3	Blood sample	2	2	5/5 (two iPSC clones analysed)
D21C3 (isogenic) D21C9 (isogenic) D21C7 (isogenic)	D21 normal karyotype from DS mosaic	16	F	Unknown	3,4	Skin biopsy	3	3	0/10 (three iPSC clones analysed)
T21C6 (isogenic) T21C13 (isogenic) T21C5 (isogenic)	T21 karyotype from DS mosaic						3	3	0/23 (three iPSC clones analysed)
T21C5Δ7 (isogenic CRISPR BACE2)	T21 karyotype from DS mosaic (disomy BACE2 by CRISPR)						1	1	18/18
T21C5Δ7 (isogenic CRISPR BACE2) + DMSO									3/3
T21C5Δ7 (isogenic CRISPR BACE2)+ β and γ sec inhibitors									0/4

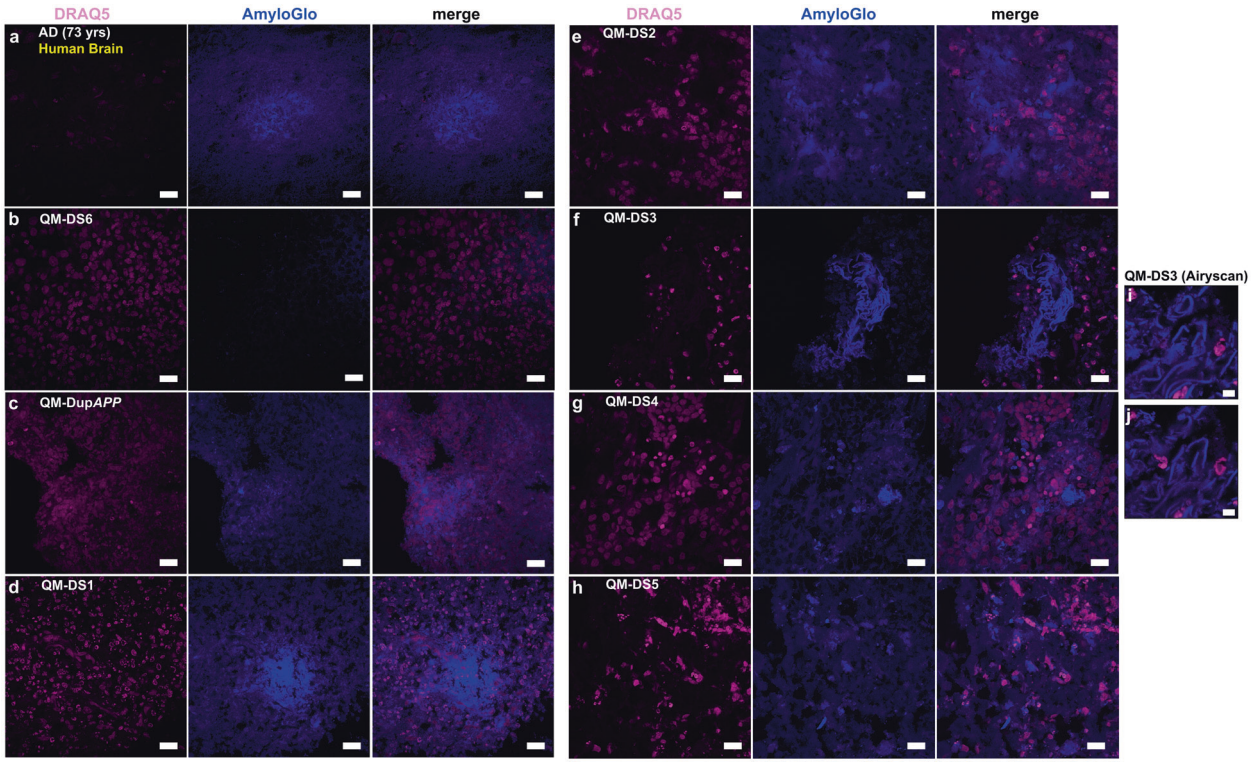

Fig. 8 Amyloid-like pathology, staining with AmyloGlo, is shown in different lines of organoids and Human AD Brain served as positive control. a Human AD Brain (73 yrs) shows amyloid plaques in the Entorhinal cortex. **b** QM-DS6 (DIV100) shows no AD pathology. **c–h** QM-DupAPP and QM-DS1, 2, 3, 4, 5 show AmyloGlo-positive aggregates, similar to human brain. Scale bar: 20 µm. **i**, **j** Airyscan analysis of QM-DS3 showing super-resolution images of AmyloGlo-positive material with fibrillar-like appearance. Scale bar: 5 µm.

hyperproduction of Aβ amyloidogenic peptides, we cultured T21C5Δ7 organoids in media containing high concentrations of β and γ secretase inhibitors. Early T21C5 and T21C5Δ7 organoids were treated with a combination of β-secretase inhibitor IV and compound E (γ secretase inhibitor XII) (Supplementary Table 2) from 20DIV to 41DIV (Fig. 6). Amyloid-like deposits were readily detected with AmyloGlo in the untreated and vehicle only treated T21C5Δ7 organoids (Fig. 6b), but were completely absent from T21C5Δ7 organoids treated with β and γ secretase inhibitors (Fig. 6b, bottom row). Inhibitor treatment also significantly reduced the number of neurons expressing pathologically conformed Tau (TG3-positive cells) in the T21C5Δ7 compared with untreated controls (Fig. 6c). No AmyloGlo-positive aggregates or TG3-positive cells were detected in T21C5 organoids under any treatment conditions at DIV41 (Fig. 6a, c) and were also absent in the same organoids at DIV100 (Fig. 7g, l, Supplementary Fig. 11). Also, no obvious deleterious effects of the inhibitors, or vehicle control, could be seen in early unedited T21C5 organoids.

Further histo-pathological verification showed that elimination of one copy of *BACE2*-triggered progressive accumulation of extracellular deposits that co-stain with Thioflavine S and antibodies against Aβ, both 4G8 and neo-epitope specific Aβx-40 & Aβx-42. The antibody signal intensity in colocalisations with Thioflavine S drastically increased upon pre-treatment with 87% formic acid (Fig. 7a–d), proving that the deposits contain insoluble Aβ material. This is further corroborated by the isolation of fibrillary material from the detergent-insoluble fraction of the CRISPR-edited organoid. When viewed by transmission electron microscopy (TEM) the filaments found exhibited a straight morphology of <10 nm diameter (Supplementary Fig. 13a), closely resembling fibrils grown in vitro from synthetic Aβ1–40 peptide (Supplementary Fig. 13c). Furthermore, neuritic plaque-like features were detected by IHC co-staining with Gallyas in CRISPR-edited organoids (Fig. 7m, n), but not their unedited T21 control (Fig. 7l). Human brain from an AD patient is shown for comparison stained with Gallyas (Fig. 7k). Tau pathology was also observed by IHC using the hyperphosphorylated Tau antibody AT8 (Fig. 7e, f), and by IF for conformationally altered Tau (TG3, Fig. 7g–j). The relative increase in the amount of conformationally altered (pathological) Tau in CRISPR-edited organoids T21C5Δ7, compared with

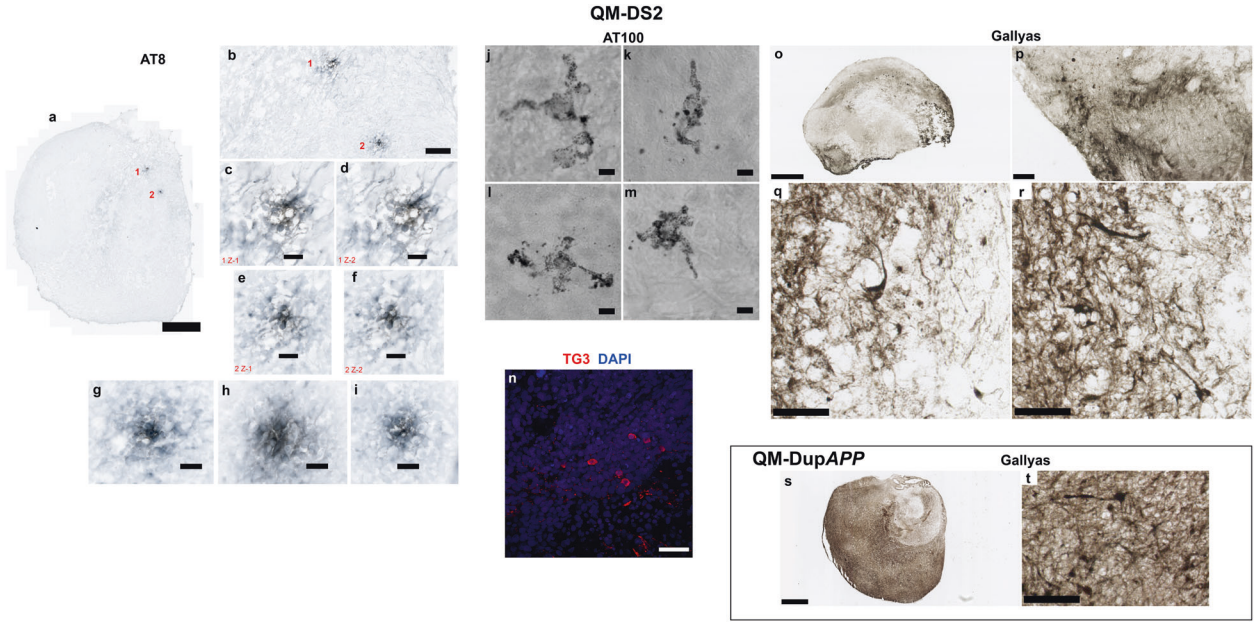

Fig. 9 Tau pathology, staining with Gallyas, and with three different antibodies (hyperphosphorylated, conformationally altered, and filamentous Tau) in QM-DupAPP (100DIV) and QM-DS2 (100DIV) organoids. a Scan of whole QM-DS2 organoid section shows two hyperphosphorylated Tau foci (neuritic plaque-like structures). Scale bar: 500 µm. **b** Zoom in on the same foci. Scale bar: 100 µm. **c**, **d** AT8-positive neurites in the pathological structure number 1 in two individual z-slices. Scale bar: 20 µm. **e**, **f** AT8-positive neurites in the pathological structure number 2 in two individual z-slices. Scale bar: 20 µm. **g–i** AT8-positive neurites in further three pathological foci found at a different depth, from the same organoid (not shown at lower magnification). Scale bar: 20 µm. **j–m** AT100 (filamentous Tau) positive neurons in the cortical layer of QM-DS2 organoid, partly showing "ballooned neuron" pathology. Scale bar: 5 µm. **n** TG3 (conformationally altered Tau) positive cells in the cortical layer of QM-DS2 organoid. Scale bar: 50 µm. **o** Scan of whole QM-DS2 organoid section stained with Gallyas. Scale bar: 500 µm**. p–r** zoom in on the parts of the same organoid shows strongly Gallyas-positive individual neurons. Scale bar: 50 µm **p** 20 µm **q**, **r**. **s** Scan of whole QM-DupAPP organoid section stained with Gallyas. Scale bar: 500 µm. **t** Zoom in on the same organoid shows equally strong individual neurons as in QM-DS2 organoid. Scale bar: 50 µm.

unedited T21 control organoids, was also independently confirmed by immunoblotting using TG3 antibody. As shown in Fig. 7o, the protein material isolated from T21C5Δ7 organoids produced significantly more TG3 signal than unedited controls, albeit having a weaker signal with the general 3R-Tau antibody (consistent with the observed neuronal loss, Supplementary Fig. 12).

AD-like pathology develops reproducibly in unedited cerebral organoids from 71% of DS donors, and it is donor-specific

Our data in Figs. 5–7 show that severing the *BACE2* dose by a third, using CRISPR/Cas9, might tip the balance against the anti-amyloidogenic activity, and provoke AD-like pathology. Our data in Fig. 1 suggest that anti-amyloidogenic activity of BACE2 is gene dose dependent, and its level varies between individuals, and it has been previously reported that SNP allelic differences in *BACE2* gene correlate with age of dementia onset in DS [26]. We therefore hypothesized that organoids grown from some people with DS may develop AD-like pathology without any CRISPR-Cas9 intervention. We then tested this hypothesis using iPSC lines from six different individuals with DS, and one Dup*APP* patient (Table 1). We detected amyloid-like aggregates (both diffuse and compact in appearance) in 5/7 unedited iPSC-derived organoids from people with DS, and one with Dup*APP* (Fig. 8). The two donors whose iPSC-organoids did not show pathology are (i) the T21 iPSC from our isogenic model (whose clinical status is unknown) and (ii) QM-DS6, a donor who remains free from dementia symptoms at age 37 (Table 1). Organoids from another five DS donors, and one Dup*APP* patient, (all diagnosed with clinical dementia) all showed presence of diffuse and compact amyloid-like deposits (Fig. 8) as well as presence of neuritic plaque-like features (focal hyperphosphorylated tau (AT8+), conformationally altered tau (TG3+), and filamentous Tau (AT100+)) within neuropil neurites within plaque-like circular foci (Fig. 9a–n). This was corroborated by Gallyas intraneuronal positivity (Fig. 9o–t). Similarly as for T21C5Δ7, we were able to isolate fibrillary material from the detergent-insoluble fraction of QM-Dup*APP* organoid (Supplementary Fig. 13b), that on TEM resembled fibrils grown in vitro from synthetic Aβ1–40 peptide (Supplementary Fig. 13c). Most importantly: tested individual organoids from one

donor (from multiple iPSC clones and multiple independent experiments) either all did (Dup*APP*, QM-DS1-5), or all did not (isogenic T21, QM-DS6) show AD-like pathology (Table 1), proving the pathology is donor dependent. This open possibilities of developing assays for pre-therapy risk-stratification and individualized drug–response quantitation. In order to further test the hypothesis that decreasing the level of BACE2 may provoke some AD-like pathology in organoids, we artificially decreased the level of BACE2 using shRNA, in the QM-DS6 patient's iPSCs, that did not show AD-like pathology. The shRNA succeeded in decreasing the BACE2 protein level by only 28%, (Supplementary Fig. 14a) similar to the CRISPR correction of three to two copies shown in Fig. 5. This intervention indeed provoked early (46DIV) presence of AmyloGlo+ aggregates, and a significant increase in TG3+ neurons (showing pathologically conformed Tau), (Supplementary Fig. 14b,c). Therefore, we conclude that correction of the trisomic over-expression of BACE2 in two different and independent individuals with DS (one using CRISPR, one using shRNA) both provoked a similar early AD-like pathology.

Discussion

Several human brain studies show detectable expression and β-secretase activity of BACE2, though at much lower levels than that of BACE1 [27–30]. Chemical inhibition of β-secretase activity is an attractive therapeutic approach aimed at reducing the production of Aβ [31–33]. Complete knockout of *Bace1* abolished all β-secretase activity in mouse neurons, while leaving some degree of β-secretase activity in astrocytes [34]. This activity was abolished by the complete knockout of both *Bace1* and *Bace2*, leading to a hypothesis that a BACE2-driven β-secretase activity in astrocytes may contribute to accelerate the Aβ-production and AD pathology in DS [34]. In human brain, the β-secretase activity of BACE1 correlated positively with the amount of Aβ, whereas the β-secretase activity of BACE2 did not [27]. On the other hand, SNPs at the *BACE2* locus (and not *BACE1*) correlate with the age of onset of dementia in people with DS [26], as well as sporadic LOAD in euploid people in the Finnish population [35], and a recent report showed that a de novo intronic deletion within one allele of *BACE2* caused EOAD in a 50-year-old euploid person [36].

All of the above data implicate that a single allele alteration in the genetic dose of *BACE2* is capable of affecting the risk of AD dementia, but do not resolve the question whether BACE2 per se acts predominantly as an accelerator, or a suppressor of AD pathology. The answer to this question requires clarification, as most chemical inhibitors used in clinical trials have dual activity against BACE1 and BACE2 [32, 37].

The increased ratios of 1–20 & 1–34 (BACE2-AβDP) to the amyloidogenic and α-site products are among our most consistent and robust observations in T21 organoid CM and DS-CSF (Fig. 1b, c). The 1–34 generating cleavage can only occur after the cuts by both β- and γ-secretases have released Aβ, because the hidden transmembrane site between aa34 and aa35 is inaccessible to any proteolytic enzymes until the soluble Aβ (1–37 to 1–42) molecules are released from the membrane [12, 13]. Therefore, the Aβ1-34 species can only be a product of an AβDP activity (a catabolic degradation or clearance of an already made Aβ1–37 to 1–42 peptides). Besides BACE2, the only enzymes with potential to cleave the peptide bond Leu34–Met35 are BACE1 [12, 14], and extracellular matrix (ECM) metalloproteinases (MMP2 and MMP9) [38], since no other Aβ-degrading enzymes (neither IDE, nor NEP, nor ECE) are known to cleave at this site [39]. BACE1 action is unlikely to cause the increased ratios we observe, as BACE1 can only generate this cut in solution at very high enzyme concentration and after prolonged incubation [12].

To further corroborate this point, we designed a novel FRET-assay and established the conditions in which BACE2 can efficiently cleave at Aβ34 site (Fig. 2) in 2 hours, conditions under which BACE1 activity at the Aβ34 site was undetectable (Supplementary Information). We also demonstrated that two BACE1 inhibitors (β-Secretase Inhibitor IV—CAS 797035-11-1 (Calbiochem, originally a Merck compound)), and LY2886721 (Eli Lilly compound recently used in clinical trials) both inhibit the AβDP activity of BACE2 in vitro, whereas the γ–secretase inhibitor (DAPT) had no effect.

This suggests that the AβDP activity (cutting the peptide bond Leu34–Met35) has a different enzymatic preference, conditions, and pH, as compared with the classical β-secretase cleavage that both BACE1 and BACE2 are capable of. As FRET assays cleaving this classical (before Asp1) site are generally used to measure the BACE1 inhibitors' selectivity for BACE1 or BACE2, our data suggest that the degree of selectivity for any given inhibitor calculated this way, does not necessarily reflect whether the same selectivity would apply for their cross-inhibition of the Leu34–Met35 site cleavage (AβDP) activity. Interestingly, the presence of the Aβx-34 degradation product, both alone [23] and colocalising with BACE2 (Fig. 4) show elevated levels in cells and extracellular aggregates immediately surrounding neuritic plaques, suggesting BACE2 degradation of not only newly produced Aβ, but also of Aβ that is released and re-deposited (from and to) existing deposits. A recent report on widespread somatic changes in individual neurons suggests an additional mechanism for the production of toxic Aβ species, including products that do not

require secretase cleavage [40], underscoring the importance of efficient Aβ degrading mechanisms that protect from AD, such as the one exerted by BACE2 that we describe here.

A recent mouse model has shown that introducing a third dose of chromosome 21 to a mouse that several hundred fold overexpresses Aβ40 and 42 worsens the amyloid plaque load, and this correlates with an unexpected decrease in the Aβ40/42 ratio [41]. This unfavourable ratio effect (the cause of which is unknown) is expected to worsen the plaque load and AD pathology, and a mere 1.5× increase of *Bace2* dose in this mouse model has no chance in protecting the mouse against a >100× overload of Aβ. In another mouse model, where transgenic *BACE2* was artificially over-expressed together with transgenic wt*APP*, it actually decreased Aβ40 and 42 to the wt mouse control levels, and the presence of *BACE2* transgene reversed behavioural pathologies seen in Tg*APP* mouse [42].

This indicates that a balance of doses of *APP* and *BACE2* affects levels of soluble Aβ40 and 42, and their oligomerization and aggregation as a consequence. Our results in Figs. 5–7 further corroborate that a significant disturbance of this balance by a reduction in *BACE2* copy number is sufficient to cause an early AD-like pathology in T21 cerebral organoids. We did not see any amyloid plaque-like structures at >100DIV organoids from three independent T21 iPSC clones (or normal disomic clones) of our isogenic system (Supplementary Figs. 1, 2, 4, 7, 11, 15, Figs. 3, 7, 8). Surprisingly, CRISPR/Cas9 elimination of the third copy of *BACE2* in the same T21 clone caused widespread AmyloGlo+ deposits at 41DIV, and widespread neuritic plaque-like structures with profound neuron loss (Supplementary Figs. 11, 12) and Tau pathology at 96DIV (Figs. 6, 7). Our data in Fig. 1 suggest that anti-amyloidogenic activity of BACE2 is gene dose dependent, and its level varies between individuals, with SNP allelic differences in *BACE2* correlating with age of dementia onset [26]. We therefore hypothesized that organoids grown from some people with DS may develop AD-like pathology without any CRISPR-Cas9 intervention. Diffuse amyloid plaque-like appearance with Tau pathology was recently reported in 110 days old cerebral organoids from only a single clone of a single DS-hiPSC line [43] so far. We subsequently analysed iPSC-derived organoids at approximately the same cell culture age from a total of seven different individuals with DS and one with Dup*APP*. We found flagrant AD-like pathological changes in 5/7 DS tested (71%), as well as the one Dup*APP*. Very interestingly, when this assessment was repeated in independent experiments, and when individual organoids from a single experiment were compared, it was a black/white picture: either they all had AD-like pathology, or none did, driven solely by the genotype of the donor (Table 1). Our data, though not conclusive, are illustrative of the stratifying potential of this technology. For example, the cerebral organoids from individual QM-DS3 showed the worst AD-like pathology with fibrillary amyloid deposits (Fig. 8f, i, j, Table 1), and this individual was diagnosed with dementia at age 37. In contrast, organoids from individual QM-DS6 showed no pathology (Fig. 8b, Table 1), and this individual was also dementia free at age 37. This opens up possibilities for finding correlations with clinical parameters, for which a much larger number of individuals would have to be tested. Concordantly with our hypothesis, when QM-DS6 iPSCs had their BACE2 level lowered by 28% using an shRNA construct, this provoked early amyloid and Tau pathology in otherwise pathology-negative organoids (Supplementary Fig. 14).

To confirm that the AmyloGlo deposits were in fact aggregated β-amyloid containing material, early organoids were treated with a combination of β-secretase inhibitor IV (βI-IV) and gamma secretase inhibitor XII (Compound E) (Fig. 6a, b). The combination of these inhibitors should prevent any production of Aβ, and therefore eliminate AmyloGlo positivity. After treatment for 21 days, the inhibitor treatment did indeed prevent the formation of plaque-like deposits within T21C5Δ7 organoids, confirming that such deposits are comprised of β-amyloid. The same treatment conditions also significantly reduced the number of TG3-positive cells in T21C5Δ7 organoids (Fig. 6c), highlighting the ability to modulate both amyloid and tau pathology in the cerebral organoid system. This also demonstrates the feasibility of using this AD-like organoid pathology in future hypothesis-free drug screens for chemical compounds that may prevent/inhibit amyloid production or aggregation.

In view of our results, it becomes inviting to hypothesize that triplication of *BACE2* may be the cause of the delayed onset of dementia in 30% of people with DS compared with Dup*APP* [7], and (because of the predicted abundance of BACE2 mRNA in endothelial cells) also the cause of a significantly lower degree of cerebral amyloid angiopathy (CAA) in the brains of people with DS compared with those of Dup*APP* [44]. Our organoid system is not informative in this regard, as we could not detect any endothelial cells in our organoids (not shown). This, however, is also an advantage, as it allows uncovering the mechanisms that are specific to neurons in the absence of endothelial or blood cell-derived tissue components.

In neurons, a recent report also found that an increased *APP* dose may act (through an unknown mechanism) as a transcriptional repressor of several chromosome 21 genes, including *BACE2* [45]. This observation needs further verification and mechanistic explanation, but if true, it would imply that the protective effect of the third copy of *BACE2* in DS that we observe is actually quenched by the third copy of *APP*, which opens up possibilities of

chemically intervening to inhibit this transcriptional repression and potentially unleash a much greater degree of BACE2 protection. An integration of the two observations (the one in [45] and the one in our report) suggests this could be exploited as an additional new protective/therapeutic strategy for AD in general.

We found, surprisingly, an equally high or higher level of colocalisation of Aβx-34 with LAMP2A, as with the general LAMP2 (Fig. 3). The high level of colocalisation with LAMP2A and absence of colocalisation with either LC3A or LAMP1 (Fig. 3) suggest that AβDP activity of BACE2 that generates Aβ34 is not related to classical lysosomal degradation or macroautophagy, but rather could be related to a CMA-like process [46, 47]. The only published study that linked CMA with APP processing [48] found a motif that satisfies the criteria for a CMA-recognition KFERQ motif at the very C-terminus of APP (KFFEQ), and this paper demonstrated that C99 (β-CTF) can bind HSC70. However, paradoxically, when this motif is deleted from the β-CTF, the binding to HSC70 is not abolished, but rather increased, suggesting the presence of another, alternative CMA-recognition motif within the β-CTF peptide [48]. The association of the AβDP x-34 product with LAMP2A/CMA compartment is a provocative new observation that requires further studies.

In conclusion, we found that relative levels of specific non-amyloidogenic and AβDP (Aβ-clearance) products are higher in T21 organoids and DS-CSF, and they respond to the dose of *BACE2* (and not *APP*). We also demonstrated that BACE2-AβDP activity generating one of these products can be cross-inhibited in solution by recently clinically tested BACE1 inhibitors. All components of the AβDP degradation reaction (hitherto only demonstrated in solution in vitro): the main substrate (Aβx-40), the enzyme (BACE2), and its putative degradation product (Aβx-34), we found highly colocalised in discrete intracellular vesicles in human brain neurons, (and not astrocytes), suggesting that at least some of the AβDP activity generating Aβx-34 takes place intra-neuronally and physiologically during lifetime, before the onset of AD pathology, in both normal and DS brains. Furthermore, we directly demonstrated that the trisomic level of *BACE2* protected T21-hiPSC organoids from early AD-like amyloid plaque pathology, therefore proving the physiological role of BACE2 as an AD-suppressor gene. The BACE2's θ-secretase anti-amyloidogenic cleavage and the AβDP degradation actions could both be contributing to an overall AD-suppressive effect. Regardless of the contribution of each of these modes of action, our combined data suggest that increasing the action of BACE2 could be exploited as a therapeutic/protective strategy to delay the onset of AD, whereas cross-inhibition of BACE2-AβDP activity by BACE1 inhibitors would have the unwanted worsening effects on disease progression. We also show that cerebral organoids from genome-unedited iPSCs could be explored as a system for pre-morbid detection of high-risk population for AD, as well as for identification of natural dose-sensitive AD-suppressor genes.

Methods

Human subjects—clinical assessment

Human subjects were participants in the "The London Down Syndrome Consortium (LonDownS): an integrated study of cognition and risk for AD in Down Syndrome" inter-disciplinary study, enrolled after informed consent, as per ethical approval 13/WA/0194, IRAS project ID:120344 see http://www.ucl.ac.uk/london-down-syndrome-consortium). Dementia diagnostic status was obtained via carer report and medical records, based on assessment by the individual's own clinician. To confirm diagnoses, we collected detailed data on dementia symptoms from the Cambridge Examination for Mental Disorders of Older People with Down's Syndrome and Others with Intellectual Disabilities (CAMDEX), a clinical tool used for diagnosing dementia in individuals with DS. This was independently reviewed by two psychiatrists. One iPSC line (QM-DS1) was established from an individual 40 year old who was diagnosed with dementia aged 40. Consensus ratings agreed that this individual showed signs of dementia and died 2 years later following significant decline. AD was noted as the cause of death. Another line came from an individual (QM-DS2) who was diagnosed with dementia aged 63. The sample was taken at age 67 and at this time point, consensus was that the individual presented with signs indicative of possible dementia. This individual was still alive for follow up 2 years later, with a confirmed diagnosis of AD-dementia and AD-related seizures developed at age 68. The third line came from an individual diagnosed with dementia at age 37 (QM-DS3). Another line came from the individual QM-DS6, who donated hair at age 31, and remains dementia free after follow up at age 37. The age, sex, ApoE genotype, and dementia status of all other individuals are detailed in Table 1.

Primary hair follicle keratinocyte sampling

Upon specific informed consent, three to six individual strands of hair were non-invasively plucked from the scalp hair of donor subjects, and placed in transport medium (DMEM (Sigma D5546), 2 mM glutamine (Sigma G7513), 1x Pen/Strep (Sigma, P4333), 10% foetal calf serum). Upon arrival to the laboratory, hair follicles were placed in collagen coated T25 flasks in KGM2 medium (Lonza

CC-3107) and incubated at 37 °C, 5% CO_2. Primary keratinocyte cultures were split after reaching 35–50% confluency using 0.05% Trypsin/0.02% EDTA.

Reprogramming of primary keratinocytes

Primary keratinocyte cultures were expanded to 70% confluency, electroporated with plasmids encoding reprogramming factors in episomal vectors (non-integrational reprogramming), and transferred to 0.1% gelatin coated wells (six-well plate), pre-seeded with mitotically disabled mouse embryonic fibroblast (MEF) feeder cells. Specifically, trypsinised 700,000 keratinocytes were washed once with sterile PBS and electroporated using the Nucleofector 4D (Lonza, X-module apparatus, kit V4XP-3024, programme DS138, following manufacturer's instructions) with 3 µg of the episomal plasmid mix (equimolar mixture of plasmids obtained from Addgene: pCE-hOct3/4, pCE-hSK, pCE-hUL, pCE-mp53DD and pCXB-EBNA1). After electroporation, cells were transferred from the cuvette to KGM2 medium (Lonza CC-3103 and CC-4125). Solution was gently mixed and transferred to the six-well plate with feeders. On day 2 (48 hours after electroporation) medium was removed and replaced with fresh KGM2 medium. On the day 4, the medium was switched to standard human embryonic stem cell (hESC) medium (high glucose DMEM with 20% Knockout Serum Replacement, non-essential amino acids, Glutamax+penstrep (Life Technologies), 2-mercaptoethanol (100 µM) with 10–20 ng/mL of FGF2). From day 10 onwards, MEF-CM supplemented with 10–20 ng/mL of FGF2 was used. By day 20, iPSC colonies were observed. After day 30, large iPSC colonies were mechanically picked, and expanded using ReLeSR and hESC medium plus ROCK inhibitor (Y-27632, Stem Cell Technologies). The iPSC lines were generated in this way from six unrelated people with DS (QM-DS1, QM-DS2, QM-DS3, QM-DS4, QM-DS5, and QM-DS6, respectively, detailed in Table 1). The iPSCs from a 64-year-old euploid patient with FEOAD caused by Dup*APP* [21] (QM-Dup*APP*) were generated from peripheral blood mononuclear cells, using the same non-integrational episomal reprogramming vectors as above, and a modified protocol. Specifically, 10^6 PBMCs were electroporated with 3 µg of episomal plasmids (equimolar) using program EO-115 and solution p3 on the Amaxa 4D nucleofector. Electroporated PBMCs were transferred into one well of a six-well plate seeded with MEFs in PBMC recovery medium (RPMI supplemented with 200 µM 1-thioglycerol (Sigma M6145), 1 µM Dexamethasone (Sigma D1756), 2 U/ml Erythropoietin (R&D Systems 287-TC-500), 100 µg/ml Holotransferrin (R&D Systems 2914-HT), 40 ng/ml IGF-1 (Peprotech 100-11), 10 ng/ml IL-3 (Peprotech 200-03), 100 ng/ml SCF (Peprotech 300-07). After 2 days, 2 ml of PBMC recovery medium was added to transfected cells. After another 2 days, PBMC recovery medium was replaced every second day with hESC medium supplemented with 10 ng/ml FGF2. Visible iPSC colonies were mechanically picked and expanded as per the keratinocyte reprogramming protocol. The iPSCs for the isogenic DS model included isogenic clones derived from an individual with DS mosaic for T21 were described by us previously [18]: D21C3, D21C7, D21C9 and T21C5, T21C6, T21C13. These were generated by non-integrationally reprogramming primary skin fibroblasts from a person with mosaic DS, using Sendai virus delivered standard Yamanaka OKSM factors. The total number of iPSC clones generated per patient is listed in Table 1. iPSCs were maintained on Geltrex coated plates and cultured in E8 medium (Life Technologies) supplemented with penicillin/streptomycin. Passaging was carried out using ReLESR and 10 µM ROCK inhibitor was included in culture media for 24 hours after passaging.

Cerebral organoids

Cerebral organoids were generated following a published protocol [19] with the following changes. iPSC lines were first transitioned into feeder free conditions using either mTESR1 or E8 media with geltrex. To form embryoid bodies (EBs), hiPSCs were washed once with PBS, then incubated with Gentle Cell Dissociation Solution (Stemcell Technologies) for 4 mins. This solution was then removed and accutase added and incubated for a further 4 mins. mTESR1/E8 medium at double the volume of accutase was added to the cells and a single cell suspension generated by titurating. Cells were centrifuged to remove accutase and then resuspended in hESC medium supplemented with 4 ng/ml FGF2 and 50micromolar ROCK inhibitor. In all, 9000 cells were used to form a single EB in each well using a V-shaped ultra low attachment 96 well plate (Corning). Specifically, iPSCs were allowed to form EBs in suspension by culturing for 6 days in hESC medium with low FGF, in non-adherent culture dishes. After 5–7 days, EBs were transferred into a 24 well ultra low attachment plate for neural induction. Neural induction was achieved by culturing for further 5–7 days in DMEM-F12 supplemented with 1% of each: N_2, GlutaMAX, and MEM-NEAA, plus 1 µg/ml heparin. Neurally induced EBs showing neuroectodermal "clearing" in brightlight microscopy were embedded in matrigel droplets, and transferred to 6 cm dishes containing organoid differentiation medium-A, (for 4–5 days), followed by organoid differentiation medium+A [19]. Organoid maturation was carried out with 12–16 organoids per 6 cm dish on an orbital shaker at 37 °C, 5% CO_2. Aliquots of CM were collected from mature organoids (100–137 days old from day of EB formation),

3–4 days after feeding (to allow time for cells to secrete products into the culture media). Three completely independent experiments were carried out each time starting from undifferentiated iPSC stage, and CM was collected at 3–4 timepoints in each experiment. CM was immediately frozen and stored at −80 °C.

For inhibitor treatment, organoids were treated from 20DIV (6 days after embedding in matrigel) to 41DIV. βI-IV and Compound E were added freshly to the media before use at final concentrations of 2.5 μM and 6 nM, respectively. Media was replaced every 3–4 days during treatment. DMSO of the same volume was used as a vehicle only control.

IP-MS

CM from organoids was analysed by IP-MS, using a previously described method [20]. The team performing the MS was blinded to the genotypes in all experiments. In exp1, all three independent trisomic clones (T21C6, T21C5, and T21C13) were compared with two independent disomic clones (D21C3 and D21C7), whereas in exp2, two independent trisomic clones (T21C6 and T21C13) were compared with two independent disomic clones (D21C7 and D21C9).

In exp3, a T21C6 clone was compared with the isogenic D21C9 clone, and to hiPSC lines from three unrelated individuals: a Dup*APP* FEOAD patient (QM-Dup*APP*), and two unrelated adult people with DS (QM-DS1 and QM-DS2).

In all three experiments, IP-MS results for all iPSC lines that were used in a particular experiment are shown. IP-MS results were used to calculate the relative ratios of peptides and these ratios were taken as data points for the statistical comparisons.

IP-MS spectra were also obtained from the CSF samples of people with DS and age-matched normal controls. Peak ratios calculated as described above. The cohorts, methods, and spectra behind these data were previously described [22].

FISH

FISH on organoid cryosections was performed as described [49]. In brief, slides were rinsed in PBS, rehydrated in 10 mM sodium citrate buffer and incubated in the same buffer at 80 °C for 20 min. Slides were cooled down and incubated in 2× saline sodium citrate (SSC) for 5 min and in 50% formamide in 2× SSC for 1 h. After incubation slides were covered with previously prepared hybridization chamber and incubated with 10 μL of XA 13/18/21 (D-5607-100-TC, MetaSystems Probes) Probe, protected from the light, at 45°C for 2 h, at 80 °C for 5 min and for 2 days at 37 °C in the water bath. Slides were rinsed with 2× SSC at 37 °C (3 × 15 min) and with 0.12× SSC at 60 °C (2 × 5 min) on the shaker, equilibrated in 2× SSC at 37 °C for 2 min, counterstained with 4′,6-diamidino-2-phenylindole (DAPI) for 10 min and covered with Dako Fluorescent Mounting Medium. Fluorescence was captured on Zeiss LSM800 inverted confocal microscope with Airyscan using ×63 oil-immersed objective. Image analysis was performed using IMARIS ×64-v9.1.2. Software (BITPLANE, An Oxford Instruments Co., Zurich, Switzerland). The spots specific for chromosome 21 were labelled in the red spectrum, whereas the spots specific for chromosome 13 were labelled in the green spectrum. More than 500 nuclei from eight different Z-stacks were evaluated for each clone. Based on the observed number of fluorescent hybridization signals, nuclei were assigned to four different categories, namely "one signal", "two signals" "three signals" and ">three signals". Damaged nuclei or overlapped nuclei with other nuclei were not included in scoring.

Immunostaining of organoids

Cerebral organoids derived from iPSCs and grown for indicated number of DIV were fixed in 4% paraformaldehyde (PFA), cryoprotected in 30% sucrose/PBS solution and embedded in OCT. Twenty micron thick sections were cut and mounted on Superfrost Plus slides (Fisher Scientific) for immunostaining.

For immunofluorescent staining, permeabilisation, and blocking was carried out in 3% donkey serum with 0.2% TritonX-100 in PBS for 1 h at room temperature (RT). Primary antibodies (Supplementary Table 3) were diluted in 1% donkey serum with 0.2% TritonX-100 in PBS and incubated overnight at 4 °C. Following washes with PBS, secondary antibodies (Supplementary Table 4) were diluted in 1% donkey serum with 0.2% TritonX-100 in PBS and incubated for 2 h at RT. Following washes with PBS, sections were counterstained with DAPI or DRAQ5 (Supplementary Table 2) for 10 min at RT, washed again and mounted with DAKO fluorescent mounting medium. As negative controls for all antibodies, secondary antibody only controls were carried out (Supplementary Fig. 15).

Western blot

For western blots, whole-cell lysates of iPSCs (Fig. 5c, Supplementary Fig. 14a) or organoids (Fig. 7o) were separated in a 10% acrylamide gel by SDS-PAGE and transferred to a nitrocellulose membrane according to the manufacturers protocols (Bio-Rad). Following a 60 min incubation in 5% non-fat milk in TBS-T the membrane was incubated with primary and secondary antibodies (Supplementary Tables 3, 4). Quantification was carried

out using ImageJ software, strictly using the same membranes re-stained using the antibodies shown. For the protein of interest (BACE2 or TG3), the signal was adjusted to corresponding β-actin loading control for all samples. Such adjusted values for unedited/untargeted cells ($n = 4$) were set to 1, and used to calculate the fold change for edited/targeted ($n = 4$) replicates, and the resulting fold change values for pairs run on the same gel were averaged and analysed by student's *t* test. Membrane stripping between stainings was carried out using Thermo-Fisher stripping solution, following manufacturer's instructions.

AmyloGlo and Thioflavine S staining

For AmyloGlo staining, OCT embedded slices were rinsed with PBS, and incubated in 70% ethanol for 5 min at RT, followed by washing with milli Q water for 2 min at RT. Slices were then incubated with AmyloGlo solution for 10 min in the dark at RT, followed by washing in 0.9% saline solution for 5 min at RT, and counterstaining with DRAQ5 for 10 min at RT. Thioflavine S staining was performed as described [50]. OCT embedded slices were rinsed with PBS and incubated with Thioflavine S solution for 10 min in the dark at RT, differentiated in 80% ethanol and counterstained with DRAQ5 for 10 min at RT, rinsed with PBS and mounted with DAKO fluorescent mounting medium.

Formic acid pre-treatment

To increase signal of insoluble β-amyloid material T21C5Δ7 (96DIV) organoid slices were treated with 87% Formic acid for 10 min at RT. After 10 min formic acid was rinsed three times with PBS and samples were immunostained as described above.

Human brain samples

PFA-fixed, paraffin-embedded human anonymized postmortem brain samples were obtained from the Brain Bank of the Croatian Institute for Brain Research (CIBR), Institute of Pathology of The Royal London Hospital (IP-RLH) and the South West Dementia Brain Bank (UK) (Supplementary Table 1). Slices were cut at 5–10 µm thickness, and stained using primary antibodies, secondary fluorophore-coupled anti-Ig antibodies and their respective dilutions (Supplementary Tables 3, 4).

Immunohistochemistry and immunofluorescence on human brain tissue

PFA-fixed, paraffin-embedded 5–10 µm thick slides were de-paraffinised by incubation in xylene, rehydrated in a graded series of ethanol and rinsed in PBS for 10 min. For antigen retrieval, the slides were steamed in 0.01 M citrate buffer, pH 6.0 at 100 °C for 30 min, cooled and rinsed 3 × 10 min in PBS. On slides used for IHC, endogenous peroxidases were quenched with 0.025% hydrogen peroxide for 30 min at RT and rinsed 3 × 10 min in PBS. Double immunohistochemical staining was performed "Polink DS-MR-Hu A2 Kit for Immunohistochemistry Staining" (GBI Labs, DS202A-18). In brief, Polymer-HRP and AP Double staining kit distinctly labels two different antigens in human tissue, using mouse (GBI-Permanent Red) and rabbit (DAB-brown) antibodies. Single IHC was performed "VECTASTAIN ABC HRP Kit". For immunofluorescence, following antigen retrieval, slides were incubated in blocking/permeabilisation solution (0.2% Triton X-100 in PBS + 3% donkey serum) for 1 h at RT. The slides were incubated over night at 4 °C with primary antibodies (Supplementary Table 3) in solution (0.2% Triton X-100 in PBS + 1% donkey serum). Next day primary antibodies were rinsed 3 × 5 min in PBS and incubated for 2 h with secondary antibodies (Supplementary Table 4) in 0.2% Triton X-100 in PBS at RT and rinsed 3 × 5 min in PBS. Nuclei were counterstained with DAPI for 10 min, rinsed 3 × 5 min in PBS and mounted with Dako Fluorescent Mounting Medium. In order to distinguish the contribution of lipofuscin autofluorescence to the colocalised signals, specificity of primary antibodies (Aβx-34 and BACE2) has been validated using three different methods: Sudan black B staining (Supplementary Fig. 8a), pre-incubation with BACE2 specific immunogenic peptide (Supplementary Fig. 8b–e) and Lambda (λ) scan function on confocal microscope (Supplementary Fig. 8f, g). Three different samples (DS-AD1, DS (28 yrs) pre-AD and euploid sporadic AD (73 yrs) after IHC were stained with 0.1% Sudan black B in 70% ethanol for 20 min at RT and analysed on confocal microscope with Airyscan. Sample DS-AD1 was stained with antibodies solution, 12 h pre-absorbed with BACE2 specific immunogenic peptide, and analysed on confocal microscope and slide scanner. Lambda scan records a series of individual images within a defined wavelength range (in our case from 630 nm to end of spectrum) and each image was detected at a specific emission wavelength, at 10 nm intervals. For lambda scan analysis, samples were stained with one primary antibody and labelled with far-red secondary antibody (647). As negative control, we used secondary antibody (647) alone and, as additional negative control, one sample was counterstained with DAPI only, without secondary antibody. As we used a far-red (647) antibody, we analysed expression from 630 nm to the end of spectrum at 10 nm intervals. Aβx-34 and BACE2 antibodies showed specific peaks, significantly over and above the autofluorescent signal, in all three specific ROI indicated in Fig. 4 and Supplementary Fig. 8

(intraneuronal fine-vesicles, large intraneuronal spherical granules and extracellular aggregates). DAPI and secondary antibody alone show peaks only at background level. Samples were analysed by: LSM800 Inverted Confocal Microscope with Airyscan (ZEISS), LSM800 Upright Confocal Microscope (ZEISS), LEICA DM6000 CFS, and Axioscan.Z1 Slide Scanner (ZEISS). As negative controls for all antibodies, secondary antibody only controls were carried out (Supplementary Fig. 8h).

Gallyas staining

For Gallyas staining samples were depariffinised and/or rinsed in PBS, then treated with Ammonium-Silver Nitrate (0.1 g NH_4NO_3, 0.1 g $AgNO_3$, 0.3 mL 4% NaOH) solution for 30 min protected from the light, rinsed with 0.5% acetic acid (3 × 3 min) and placed in developer solution for 5–30 min. Developer solution was made from three stock solutions: 25 ml of Solution A (50 g Na_2CO_3 + 1000 mL distilled water), 7.5 ml of Solution B (2 g NH_4NO_3 + 2 g $AgNO_3$ + 10 g Tungstosalicic acid hydrate + 1000 mL distilled water) and 17.5 ml of Solution C (2 g NH_4NO_3 + 2 g $AgNO_3$ + 10 g Tungstosalicic acid hydrate + 7.3 ml 37% formaldehyde solution +1000 mL distilled water). After developer solution samples were rinsed in water and placed in destaining solution (30 g K_2CO_3 + 55 g EDTA-Na_2 + 25 g $FeCl_3$ + 120 g $Na_2S_2O_3$ + 20 g KBr +1000 mL distilled water). Finally, samples were rinsed two times in 0.5% acetic acid. After staining samples were rinsed in water, dehydrated in a graded series of ethanol, cleared in Histo-Clear and mounted with Histomount mounting medium. Samples were scanned by NanoZoomer 2.0RS (HAMAMATSU).

Image analysis

Immunofluorescent stains of 20 µm thick slices are shown as maximal projections captured on Zeiss LSM800 upright confocal microscope using ×63 oil-immersed objective. Image analysis was performed using IMARIS x64-v9.3.1. Software (BITPLANE, An Oxford Instruments Co., Zurich, Switzerland). Quantification was performed blinded to the genotype, on five independent images representing three individual organoids per genotype, and containing 3000–4000 cells per image. Only images within the "cortical" part of the organoid were considered for analysis. For quantification of protein/peptide markers, total fluorescence intensity of positive signals for each wavelength for a given antibody was normalised to the total fluorescence intensity for MAP2 as a pan-neuronal marker.

For colocalisation calculations: image analysis was performed using IMARIS software. Pairwise Pearson's coefficient of colocalised volume for a pair of co-stained antibodies with contrasting fluorescence wavelengths was automatically calculated by the IMARIS software on 3–8 images from three independent organoids, per any given antibody combination, using a maximal projection through the entire z-stack.

A new FRET-assay for the detection of AβDP activity generating Aβ1-34

We designed and synthesized a new FRET-based peptide containing the fluorophore at one end and the quencher at the other end, and spanning the Aβ34 site in its middle. The exact peptide design is under discussion for intellectual property protection. The FRET (BACE2 R&D Systems, not based on amyloid sequence) control peptide (10 µM) (not shown) or the newly designed FRET Aβ34 site peptide (10 µM) were digested at 37 °C by human BACE2 (R&D systems, 1 ng/µL) in presence or absence of the stated inhibitors for 2 h. Three replicates per inhibitor per concentration were used. Enzyme activity was defined by measuring the fluorescence increase before and after the incubation. After blank-subtracted fluorescence units were normalized to the control digest, one-way analysis of variance (ANOVA) was performed. *P* values were calculated with a post hoc Bonferroni correction for multiple comparisons (only pairs relative to the untreated control were simultaneously compared). Error bars represent standard error.

Statistical analysis

Initial analysis was carried out using Microsoft Excel to calculate two-tailed student *t* tests. Additional Holm–Bonferroni correction was carried out using the Excel macro from ref. [51]. For all multiple comparison analysis, ANOVA and Holm–Bonferroni calculations were performed at http://astatsa.com/OneWay_Anova_with_TukeyHSD/, or using GraphPad Prism 8.4.1 software.

SNP arrays

iPSC lines genome integrity: genomic DNA was isolated from iPSCs using standard column kits. DNA of all iPSC lines shown in the manuscript were re-analysed at the similar passage used for the derivation of organoids using SNP arrays Illumina OmniExpress v1.1 chips and analysis performed in Genome Studio 2.0 software. Following CRISPR editing, T21C5Δ7 was assessed by SNP array and no genomic alternations were detected compared with the parental C5 iPSC clone. See the raw data from this for chromosome 21 array, the rest are not shown for the lack of space, data available on request). The genome integrity of the isogenic iPSC clones was previously published [18] (but was repeated here as described above). No additional

rearrangements owing to re-programming or passaging were observed.

The cohort of people with DS has been described in recent reports [52, 53]. In brief, participants donated DNA samples and had detailed cognitive and clinical assessments to determine dementia status [54]. Age of dementia diagnosis was established and shown in Table 1. Genotyping was done in the UCL Genomics Centre using Human OmniExpressExome v1.2,v1.3,v1.4 beadchips. SNP clustering and genotyping, was undertaken using GenomeStudio (Illumina, San Diego, CA, USA). Manual reclustering for Chr 21 SNPs was done using GenomeStudio module v1.9.4 polyploidy-genotyping (http://res.illumina.com/documents/products/technotes/technote_genomestudio_polyploid_genotyping.pdf).

Quantitative paralogous amplification-pyrosequencing

Quantitative paralogous amplification-pyrosequencing was carried out based on the published method [55]. This method takes advantage of the existence of identical sequences on chromosome 21 and one other autosome, allowing amplification of both loci with a single primer pair. Paralogous sequence mismatches in amplified products from chromosome 21 (GABPA and ITSN) can be quantified relative to their paralogous regions on chromosome 7 and 5, respectively. As such, trisomic cells show a 60:40 ratio for the paralogous sequence, whereas disomic cells produce a 50:50 ratio. Primers used for amplification and pyrosequencing are listed in Supplementary Table 5. Pyrosequencing was performed on the Pyromark Q48 machine (Qiagen) following standard procedures.

CRISPR/SpCas9-HF1 editing of the *BACE2* locus

The guide-RNA (gRNA) targeting *BACE2* Exon 3 was cloned into a vector containing the high fidelity SpCas9-HF1 [56] and blasticidin S resistance gene. The complete plasmid was delivered via Lipofectamine3000 to a trisomic iPSC clone T21C5 (full official name NIZEDSM1iT21-C5), which was described and characterized in a previous report [18]. Untransfected iPSCs were removed by treatment with blasticidin (2 µg/ml for 48 h). Individual colonies were picked and further sub cloned by limiting dilution to achieve clonal cell lines. DNA was purified from individual clones, PCR amplified and sequenced by Sanger Sequencing. Sequences were analysed in Mutation Surveyor (V3.1.0) and "Tracking InDels by dEcomposition (TIDE)" (TIDE V 2.0.1, Desktop Genetics). TIDE analysis of the CRISPR-targeted clone 2.3.5 DNA sequence gave a score of 65% of the wt read remaining (not shown). The quality of the gRNA was assessed using two different prediction software platforms: CCTop online software [57], and the MIT online platform (http://crispr.mit.edu/). The same two software platforms were used to predict the off-target sites. Neither platform found any off-targets with 0, 1, or 2 mismatches. The top 10 CCTop-predicted sites were PCR amplified in both Δ7 and WT clones, then sequenced by Sanger Sequencing to rule out off-target events. No differences in the sequence were found.

shRNA targeting of BACE2 in iPSCs

One day after plating, small colonies of feeder free iPSCs were transduced with lentiviral shRNA particles targeting BACE2 (sc-29776) or a non-targeting control (sc-108080). Lentiviral particles were obtained from Santa Cruz Biotechnology Inc. The lentiviral particles for BACE2 contain three different shRNAs targeting human BACE2. In total, 5000 infectious units (IFU) of virus were added per 12-well, and incubated overnight. The following day, viral media was removed and replaced with fresh media. Four days after transduction, stably transduced cells were selected by treatment with 0.5 µg/ml puromycin for 14 days, passaging as required. Following this, iPSCs were maintained in 0.3 µg/ml puromycin. Knockdown of BACE2 was confirmed by western blot (Supplementary Fig. 14a).

Protein isolation from cortical organoids

Organoids were collected at specified durations in culture (expressed as DIV) and washed twice with ice-cold PBS. The samples were resuspended in ice-cold NP-40 Buffer (150 mM NaCl, 1% NP-40, 50 mM Tris pH8) containing EDTA free protease inhibitors (complete cocktail, Roche) and lysed using a 1 ml tissue homogenizer (Fisher). Each sample was centrifuged at 10,000 rpm for 10 minutes at 4 °C and the homogenates were stored at −80 °C. Protein concentration was determined using the bicinchoninic acid method (Pierce).

Detection of fibrillary material from organoids by transmission electron microscopy (TEM)

Organoids were lysed following the same procedure for protein extraction, however, samples were initially spun at 20,000 × *g* for 20 minutes at 4 °C. Following the first centrifugation, supernatants were removed and kept on ice. The remaining cell pellets were resuspended in 5× weight/volume buffer (10 mM Tris-HCL pH7.5, 0.8 M NaCl, and 10% sucrose) [58] containing proteases inhibitor and spun at 20,000 × *g* for 20 minutes at 4 °C. An equal volume of supernatant 1 was added to the supernatant from the second centrifugation step. 1% *N*-lauroysarcosinate (weight/volume) was added and the samples were rocked at RT for

1 hour. The samples were ultra-centrifuged at 100,000 × *g* for 1 hour at 4 °C. The supernatant was decanted and the sarkosyl-insoluble pellet was resuspended in ice-cold PBS prior to imaging. The samples were deposited on to glow-discharged 400 mesh formvar/carbon film-coated copper grids, negatively stained with a 2% aqueous (w/v) uranyl acetate solution and then immediately analysed at 100 kV using a JEOL TEM1010 equipped with a Gatan Orius camera.

TEM analysis of synthetic Aβ1–40 fibrils in vitro

Synthetic Aβ peptide powder (China peptides) was treated with 1,1,1,3,3,3-hexafluoro-2-propanol and lyophilized. The peptide was then dissolved in 20 µL of 100 mM NaOH and then diluted with buffer. A 50 µM stock of this monomeric Aβ peptide was grown at 37 °C shaking at 180 rpm for 48–60 hours before recording the TEM images. In all, 4 µL of extract was added to a 15 nm thick, lacey carbon on 300 mesh grid (glow-discharged) for 2 minutes followed by negative staining with 2% uranyl acetate for 1 minute and then air dried. The grids were then viewed under FEI T12, 120 kV Transmission electron microscope equipped with a 4 K CCD camera (FEI) at ×30,000 magnification under low-dose conditions.

Data availability

All data that support the findings described in this study are available within the manuscript and the related supplementary information, and from the corresponding authors upon reasonable request.

Acknowledgements DN's work was funded by the Singapore National Medical Research Council (NMRC/CIRG/1438/2015), Singapore Ministry of Education Academic Research Fund Tier 2 grants (2015-T2-1-023 & 2015-T2-2-119), The Wellcome Trust Collaborative Award in Science 217199/Z/19/Z, and by the "Research Cooperability" Programme of the Croatian Science Foundation PZS-2019-02-4277 and EU-JPND-"Heroes" and "CoEN" Consortia. DN, JH, and AS all received funding as part of The Wellcome Trust "LonDownS Consortium" Strategic Funding Award (098330/Z/12/Z) (UK), and JH received funding from the Dementia Research Institute, an anonymous foundation and the Dolby foundation. HZ is a Wallenberg Academy Fellow supported by grants from the Swedish Research Council, the European Research Council, Swedish State Support for Clinical Research (ALFGBG-720931) the UK Dementia Research Institute at UCL. KB holds the Torsten Söderberg Professorship in Medicine at the Royal Swedish Academy of Sciences, and is supported by the Swedish Research Council (#2017-00915), the Swedish Alzheimer Foundation (#AF-742881), Hjärnfonden, Sweden (#FO2017-0243), and the Swedish State Support for Clinical Research (#ALFGBG-715986). AM was awarded a William Harvey Academy Fellowship, co-funded by the People Programme (Marie Curie Actions) of the European Union's Seventh Framework Programme (FP7/2007-2013) under REA grant agreement no. 608765. JNF received a fellowship from the Singapore National Research Foundation (NRF-NRFF2016-03). ARL received funding from the Fondation pour la Recherche Médicale (FRM). JGh and AR are supported by the BrightFocus Foundation (A2015275S), and NIH grant AG059695. The work of ŽK, GŠ, IK, and DM research was co-financed by the Scientific Centre of Excellence for Basic, Clinical and Translational Neuroscience (project "Experimental and clinical research of hypoxic-ischemic damage in perinatal and adult brain"; GA KK01.1.1.01.0007 funded by the European Union through the European Regional Development Fund). ŽK is also supported by the Adris Foundation. GŠ is also supported by the Croatian Science Foundation (HRZZ IP-2019-04-3584). DM is supported by the Croatian Science Foundation (IP-2016-06-9451). The South West Dementia Brain Bank is jointly funded by Alzheimer's Research UK and Alzheimer's Society, and is supported by BRACE (Bristol Research into Alzheimer's and Care of the Elderly) and the Medical Research Council, UK. All unique materials will be made available for academic and non-commercial research purposes. We acknowledge Balakrishnan Kannan in the LKC imaging facility for his assistance. The authors thank Géraldine Joly-Hélas, Pascal Chambon, Željka Punčec, Ana Bosak, and Danica Budinščak for technical help, Marie Loh and Jacqueline Tai for the use of pyrosequencer, Moses Tandiono for help with SNP array experiments, Selina Wray for some antibodies, and Anna Barron and Madeline Lancaster for advice. We are grateful to Maria Grazia Spillantini for advice, critical comments, and AT100 antibody.

LonDownS Consortium Andre Strydom[19,20], Elizabeth Fisher[21], Frances Wiseman[21], Dean Nizetic[22,23], John Hardy[24,25], Victor Tybulewicz[26,27], Annette Karmiloff-Smith[28]

[19]Department of Forensic and Neurodevelopmental Sciences, Institute of Psychiatry, Psychology and Neuroscience, King's College London, London, UK; [20]Division of Psychiatry, University College London, London, UK; [21]Department of Neurodegenerative Disease, UCL Institute of Neurology, London, UK; [22]Blizard Institute, Barts and the London School of Medicine, Queen Mary University of London, London, UK; [23]Lee Kong Chian School of Medicine, Nanyang Technological University, Singapore, Singapore; [24]Reta Lila Weston Institute, Institute of Neurology, University College London, London, London, UK; [25]UK Dementia Research Institute, University College London, London, UK; [27]Francis Crick Institute, London, UK; [26]Department of Medicine, Imperial College, London, UK; [28]Birkbeck University, London, UK

Author contributions IA, PAG, AM, EP, JH, HZ, and DN contributed to the concept and design, the acquisition, analysis and interpretation, and drafting of manuscript. AS, DK, JGr, SHav, NRD, and KB contributed to the concept and design and to acquisition and analysis and interpretation. YJY, GB, RH, CS, SHam, DW, ARL, HK, JEM, AR, JGh, ŽK, GŠ, and LC contributed to acquisition of data. GG, KYM, RB, NLO, MP, KP, MT, DLB, and DM contributed to acquisition, analysis, and interpretation of data. EG, XS, HS, and JNF contributed to acquisition and analysis of data. EV contributed to analysis and interpretation. IK and PTF contributed to the concept and design and the acquisition of data.

Compliance with ethical standards

Conflict of interest HZ has served at scientific advisory boards for CogRx, Roche Diagnostics, Samumed, and Wave and is a co-founder of Brain Biomarker Solutions in Gothenburg AB, a GU Ventures-based platform company at the University of Gothenburg (all unrelated to the submitted work). JEM chairs the MNDA Research Advisory Board and is a director of Biomoti, a cancer drug-delivery company.

References

1. De Strooper B, Vassar R, Golde T. The secretases: enzymes with therapeutic potential in Alzheimer disease. Nat Rev Neurol. 2010;6:99–107.
2. Hardy J, Selkoe DJ. The amyloid hypothesis of Alzheimer's disease: progress and problems on the road to therapeutics. Science. 2002;297:353–6.
3. Masters CL, Simms G, Weinman NA, Multhaup G, McDonald BL, Beyreuther K. Amyloid plaque core protein in Alzheimer disease and Down syndrome. Proc Natl Acad Sci USA. 1985;4245–9.
4. Mawuenyega KG, Sigurdson W, Ovod V, Munsell L, Kasten T, Morris JC, et al. Decreased clearance of CNS beta-amyloid in Alzheimer's disease. Science. 2010;330:1774.
5. Scheltens P, Blennow K, Breteler MM, de Strooper B, Frisoni GB, Salloway S, et al. Alzheimer's disease. Lancet. 2016;388:505–17.
6. Hithersay R, Startin CM, Hamburg S, Mok KY, Hardy J, Fisher EMC, et al. Association of Dementia With Mortality Among Adults With Down Syndrome Older Than 35 Years. *JAMA Neurol*. 2018;76:52–160.
7. Wiseman FK, Al-Janabi T, Hardy J, Karmiloff-Smith A, Nizetic D, Tybulewicz VL, et al. A genetic cause of Alzheimer disease: mechanistic insights from Down syndrome. Nat Rev Neurosci. 2015;16:564–74.
8. Willem M, Tahirovic S, Busche MA, Ovsepian SV, Chafai M, Kootar S, et al. eta-Secretase processing of APP inhibits neuronal activity in the hippocampus. Nature. 2015;526:443–7.
9. Vassar R, Bennett BD, Babu-Khan S, Kahn S, Mendiaz EA, Denis P, et al. Beta-secretase cleavage of Alzheimer's amyloid precursor protein by the transmembrane aspartic protease BACE. Science. 1999;286:735–41.
10. Vassar R, Kuhn PH, Haass C, Kennedy ME, Rajendran L, Wong PC, et al. Function, therapeutic potential and cell biology of BACE proteases: current status and future prospects. J Neurochem. 2014;130:4–28.
11. Yan R. Physiological Functions of the beta-Site Amyloid Precursor Protein Cleaving Enzyme 1 and 2. *Front Mol Neurosci* 2017;10:97 (2017).
12. Abdul-Hay SO, Sahara T, McBride M, Kang D, Leissring MA. Identification of BACE2 as an avid ss-amyloid-degrading protease. Mol Neurodegener. 2012;7:46.
13. Fluhrer R, Capell A, Westmeyer G, Willem M, Hartung B, Condron MM, et al. A non-amyloidogenic function of BACE-2 in the secretory pathway. J Neurochem. 2002;81:1011–20.
14. Shi XP, Tugusheva K, Bruce JE, Lucka A, Wu GX, Chen-Dodson E, et al. Beta-secretase cleavage at amino acid residue 34 in the amyloid beta peptide is dependent upon gamma-secretase activity. J Biol Chem. 2003;278:21286–94.
15. Sun X, He G, Song W. BACE2, as a novel APP theta-secretase, is not responsible for the pathogenesis of Alzheimer's disease in Down syndrome. FASEB J. 2006;20:1369–76.
16. Salehi A, Delcroix JD, Belichenko PV, Zhan K, Wu C, Valletta JS, et al. Increased App expression in a mouse model of Down's syndrome disrupts NGF transport and causes cholinergic neuron degeneration. Neuron. 2006;51:29–42.
17. Teller JK, Russo C, DeBusk LM, Angelini G, Zaccheo D, Dagna-Bricarelli F, et al. Presence of soluble amyloid beta-peptide precedes amyloid plaque formation in Down's syndrome. Nature medicine. 1996;2:93–5.
18. Murray A, Letourneau A, Canzonetta C, Stathaki E, Gimelli S, Sloan-Bena F, et al. Isogenic Induced Pluripotent Stem Cell Lines from an Adult with Mosaic Down Syndrome Model Accelerated neuronal Ageing and Neurodegeneration. Stem Cell. 2015;33:77–84.
19. Lancaster MA, Knoblich JA. Generation of cerebral organoids from human pluripotent stem cells. Nature protocols. 2014;9:2329–40.
20. Portelius E, Tran AJ, Andreasson U, Persson R, Brinkmalm G, Zetterberg H, et al. Characterization of amyloid beta peptides in cerebrospinal fluid by an automated immunoprecipitation procedure followed by mass spectrometry. J Proteome Res. 2007;6:4433–9.
21. Rovelet-Lecrux A, Hannequin D, Raux G, Le Meur N, Laquerriere A, Vital A, et al. APP locus duplication causes autosomal dominant early-onset Alzheimer disease with cerebral amyloid angiopathy. Nature genetics. 2006;38:24–6.
22. Portelius E, Holtta M, Soininen H, Bjerke M, Zetterberg H, Westerlund A, et al. Altered cerebrospinal fluid levels of amyloid beta and amyloid precursor-like protein 1 peptides in Down's syndrome. Neuromolecular Med. 2014;16:510–6.
23. Cabrera E, Mathews P, Mezhericher E, Beach TG, Deng J, Neubert TA, et al. Abeta truncated species: Implications for brain clearance mechanisms and amyloid plaque deposition. Biochim Biophys Acta. 2018;1864:208–25.
24. Yu WH, Cuervo AM, Kumar A, Peterhoff CM, Schmidt SD, Lee JH, et al. Macroautophagy–a novel Beta-amyloid peptide-generating pathway activated in Alzheimer's disease. J Cell Biol. 2005;171:87–98.
25. Schmued L, Raymick J, Tolleson W, Sarkar S, Zhang YH, Bell-Cohn A. Introducing Amylo-Glo, a novel fluorescent amyloid specific histochemical tracer especially suited for multiple labeling and large scale quantification studies. J Neurosci Methods. 2012;209:120–6.
26. Mok KY, Jones EL, Hanney M, Harold D, Sims R, Williams J, et al. Polymorphisms in BACE2 may affect the age of onset Alzheimer's dementia in Down syndrome. Neurobiol Aging. 2014;35:1513 e1511–1515.
27. Ahmed RR, Holler CJ, Webb RL, Li F, Beckett TL, Murphy MP. BACE1 and BACE2 enzymatic activities in Alzheimer's disease. J Neurochem. 2010;112:1045–53.
28. Bennett BD, Babu-Khan S, Loeloff R, Louis JC, Curran E, Citron M, et al. Expression analysis of BACE2 in brain and peripheral tissues. J Biol Chem. 2000;275:20647–51.
29. Holler CJ, Webb RL, Laux AL, Beckett TL, Niedowicz DM, Ahmed RR, et al. BACE2 expression increases in human neurodegenerative disease. Am J Pathol. 2012;180:337–50.
30. Stockley JH, Ravid R, O'Neill C. Altered beta-secretase enzyme kinetics and levels of both BACE1 and BACE2 in the Alzheimer's disease brain. FEBS Lett. 2006;580:6550–60.
31. Dobrowolska Zakaria JA, Vassar RJ. A promising, novel, and unique BACE1 inhibitor emerges in the quest to prevent Alzheimer's disease. EMBO Mol Med. 2018;10:e9717.
32. Neumann U, Ufer M, Jacobson LH, Rouzade-Dominguez ML, Huledal G, Kolly C, et al. The BACE-1 inhibitor CNP520 for prevention trials in Alzheimer's disease. EMBO Mol Med. 2018;10:pii:e9316.

33. Vassar R. BACE1 inhibitor drugs in clinical trials for Alzheimer's disease. Alzheimers Res Ther. 2014;6:89.
34. Dominguez D, Tournoy J, Hartmann D, Huth T, Cryns K, Deforce S, et al. Phenotypic and biochemical analyses of BACE1- and BACE2-deficient mice. J Biol Chem. 2005;280:30797–806.
35. Myllykangas L, Wavrant-De Vrieze F, Polvikoski T, Notkola IL, Sulkava R, Niinisto L, et al. Chromosome 21 BACE2 haplotype associates with Alzheimer's disease: a two-stage study. J Neurol Sci. 2005;236:17–24.
36. Rovelet-Lecrux A, Charbonnier C, Wallon D, Nicolas G, Seaman MN, Pottier C, et al. De novo deleterious genetic variations target a biological network centered on Abeta peptide in early-onset Alzheimer disease. Mol Psychiatry. 2015;20:1046–56.
37. Evin G. Future Therapeutics in Alzheimer's Disease: Development Status of BACE Inhibitors. BioDrugs. 2016;30:173–94.
38. Hernandez-Guillamon M, Mawhirt S, Blais S, Montaner J, Neubert TA, Rostagno A, et al. Sequential Amyloid-beta Degradation by the Matrix Metalloproteases MMP-2 and MMP-9. J Biol Chem. 2015;290:15078–91.
39. Saido T, Leissring MA. Proteolytic degradation of amyloid beta-protein. Cold Spring Harb Perspect Med. 2012;2:a006379.
40. Lee MH, Siddoway B, Kaeser GE, Segota I, Rivera R, Romanow WJ, et al. Somatic APP gene recombination in Alzheimer's disease and normal neurons. Nature. 2018;563:39–45.
41. Wiseman FK, Pulford LJ, Barkus C, Liao F, Portelius E, Webb R, et al. Trisomy of human chromosome 21 enhances amyloid-beta deposition independently of an extra copy of APP. Brain. 2018.
42. Azkona G, Levannon D, Groner Y, Dierssen M. In vivo effects of APP are not exacerbated by BACE2 co-overexpression: behavioural characterization of a double transgenic mouse model. Amino Acids. 2010;39:1571–80.
43. Gonzalez C, Armijo E, Bravo-Alegria J, Becerra-Calixto A, Mays CE, Soto C. Modeling amyloid beta and tau pathology in human cerebral organoids. Mol Psychiatry. 2018;23:2363–74.
44. Mann DMA, Davidson YS, Robinson AC, Allen N, Hashimoto T, Richardson A, et al. Patterns and severity of vascular amyloid in Alzheimer's disease associated with duplications and missense mutations in APP gene, Down syndrome and sporadic Alzheimer's disease. Acta Neuropathol. 2018;136:569–87.
45. Ovchinnikov DA, Korn O, Virshup I, Wells CA, Wolvetang EJ. The Impact of APP on Alzheimer-like Pathogenesis and Gene Expression in Down Syndrome iPSC-Derived Neurons. Stem Cell Reports. 2018;11:32–42.
46. Cuervo AM, Dice JF. Unique properties of lamp2a compared to other lamp2 isoforms. J Cell Sci. 2000;113:4441–50.
47. Kaushik S, Cuervo AM. The coming of age of chaperone-mediated autophagy. Nat Rev Mol Cell Biol. 2018;19:365–81.
48. Park JS, Kim DH, Yoon SY. Regulation of amyloid precursor protein processing by its KFERQ motif. BMB Rep. 2016;49:337–42.
49. Solovei I, Cremer M. 3D-FISH on cultured cells combined with immunostaining. Methods Mol Biol. 2010;659:117–26.
50. Espuny-Camacho I, Arranz AM, Fiers M, Snellinx A, Ando K, Munck S, et al. Hallmarks of Alzheimer's Disease in Stem-Cell-Derived Human Neurons Transplanted into Mouse Brain. Neuron. 2017;93:1066–81 e1068.
51. Gaetano J. Holm-Bonferroni sequential correction: An EXCEL calculator (1.2) [Microsoft Excel workbook]. 2013; https://doi.org/10.13140/RG.2.1.3920.0481.
52. Startin CM, Hamburg S, Hithersay R, Al-Janabi T, Mok KY, Hardy J, et al. Cognitive markers of preclinical and prodromal Alzheimer's disease in Down syndrome. Alzheimers Dement. 2019;15:245–57.
53. Strydom A, Heslegrave A, Startin CM, Mok KY, Hardy J, Groet J, et al. Neurofilament light as a blood biomarker for neurodegeneration in Down syndrome. Alzheimers Res Ther. 2018;10:39.
54. Startin CM, Hamburg S, Hithersay R, Davies A, Rodger E, Aggarwal N, et al. The LonDownS adult cognitive assessment to study cognitive abilities and decline in Down syndrome. Wellcome Open Res. 2016;1:11.
55. Deutsch S, Choudhury U, Merla G, Howald C, Sylvan A, Antonarakis SE. Detection of aneuploidies by paralogous sequence quantification. J Med Genet. 2004;41:908–15.
56. Kleinstiver BP, Pattanayak V, Prew MS, Tsai SQ, Nguyen NT, Zheng Z, et al. High-fidelity CRISPR-Cas9 nucleases with no detectable genome-wide off-target effects. Nature. 2016;529:490–5.
57. Stemmer M, Thumberger T, Del Sol Keyer M, Wittbrodt J, Mateo JL. CCTop: An Intuitive, Flexible and Reliable CRISPR/Cas9 Target Prediction Tool. PloS ONE. 2015;10:e0124633.
58. Goedert M, Spillantini MG, Cairns NJ, Crowther RA. Tau proteins of Alzheimer paired helical filaments: abnormal phosphorylation of all six brain isoforms. Neuron. 1992;8:159–68.

Affiliations

Ivan Alić[1,2,3] · Pollyanna A. Goh[2,4] · Aoife Murray[1] · Erik Portelius[5] · Eleni Gkanatsiou[5] · Gillian Gough[1] · Kin Y. Mok[4,6] · David Koschut[1] · Reinhard Brunmeir[1] · Yee Jie Yeap[1] · Niamh L. O'Brien[2,4] · Jürgen Groet[2,4] · Xiaowei Shao[1] · Steven Havlicek[7] · N. Ray Dunn[1,8] · Hlin Kvartsberg[5] · Gunnar Brinkmalm[5] · Rosalyn Hithersay[4,9,10] · Carla Startin[4,9] · Sarah Hamburg[4,9] · Margaret Phillips[11] · Konstantin Pervushin[11] · Mark Turmaine[12] · David Wallon[13] · Anne Rovelet-Lecrux[13] · Hilkka Soininen[14] · Emanuela Volpi[15] · Joanne E. Martin[2] · Jia Nee Foo[1,7] · David L. Becker[1] · Agueda Rostagno[16] · Jorge Ghiso[16] · Željka Krsnik[17] · Goran Šimić[17] · Ivica Kostović[17] · Dinko Mitrečić[17] · LonDownS Consortium[4] · Paul T. Francis[18] · Kaj Blennow[5] · Andre Strydom[4,9,10] · John Hardy[4,6] · Henrik Zetterberg[5,6] · Dean Nižetić[1,2,4]

[1] Lee Kong Chian School of Medicine, Nanyang Technological University, Singapore 308232, Singapore

[2] The Blizard Institute, Barts & The London School of Medicine, Queen Mary University of London, London E1 2AT, UK

[3] Department of Anatomy, Histology and Embryology, Faculty of Veterinary Medicine, University of Zagreb, 10000 Zagreb, Croatia

[4] LonDownS Consortium, London, UK

[5] Department of Psychiatry and Neurochemistry, Institute of Neuroscience and Physiology, The Sahlgrenska Academy at the University of Gothenburg, Gothenburg S-405 30, Sweden

[6] Dementia Research Institute & Reta Lila Weston Institute, Institute of Neurology, University College London, London WC1N 3BG, UK

[7] Genome Institute of Singapore, Agency for Science, Technology and Research (A*STAR), Singapore 138672, Singapore

[8] Institute of Medical Biology, Agency for Science, Technology and Research (A*STAR), Singapore 138648, Singapore

[9] Division of Psychiatry, University College London, London WC1E 6BT, UK

[10] Department of Forensic and Neurodevelopmental Sciences, Institute of Psychiatry, Psychology & Neuroscience, King's College London, London SE5 8AF, UK

[11] School of Biological Sciences, Nanyang Technological University, Singapore 639798, Singapore

[12] Division of Biosciences, University College London, Gower Street, London WC1E 6BT, UK

[13] Normandie Univ, UNIROUEN, Inserm U1245 and Rouen University Hospital, Department of Neurology and CNR-MAJ, F 76000, Normandy Center for Genomic and Personalized Medicine, Rouen, France

[14] University of Eastern Finland, Institute of Clinical Medicine/ Neurology, Kuopio FI-70211, Finland

[15] School of Life Sciences, University of Westminster, London W1W 6UW, UK

[16] Department of Pathology & Department of Psychiatry, New York University School of Medicine, New York, NY 10016, USA

[17] Croatian Institute for Brain Research, School of Medicine, University of Zagreb, 10000 Zagreb, Croatia

[18] Wolfson Centre for Age-Related Diseases, King's College London, London SE1 1UL, UK

Supplementary Figures

Supplementary Fig. 1. Cerebral organoids express cortical neuronal layer-specific and astrocyte markers. Representative images of isogenic D21 (**a-c**), isogenic T21 (**d-f**), and non-isogenic QM-DS1 (T21) (**g-i**), QM-DS2 (T21) **(j-l**) and QM-DupAPP (**m-o**) organoids are shown, confirming expression of TBR1 (layer IV), CTIP2 (layer V), FOXG1 (layers II and III), BRN2 (layer VI), REELIN (layer I), SATB2 (layer III), GFAP (astrocytes) and 3R-Tau (neurons). Final image in each row is a merge of individual antibodies in that row. Scale bar: 100μm.

Supplementary Fig. 2. Comparison of the proportions of neurons and astrocytes to total cells in cerebral organoids. Isogenic D21 and T21 cerebral organoids, as well as organoids from DupAPP, QM-DS1 and QM-DS2 iPSCs generated mostly neurons and a small proportion of astrocytes, with none or minor differences in the proportion of astrocytes or neurons between the lines. Quantification was performed on 8 representative (Z-stack) figures each from three individual organoids per genotype. Neurons are labelled with MAP2 and astrocytes with GFAP, each marker was normalized to DAPI. Image analysis was performed using IMARIS software. Error bars: standard error. Scale bar: 20 μm.

Supplementary Fig. 3. SNP arrays confirmed trisomy of chromosome 21 in all the iPSC lines used in this study, or in the case of QM-DupAPP, the partial duplication of a 580kbp segment of chromosome 21. The duplicated region in QM-DupAPP is also shown in a magnified image. Representative images of QM-DS1 and QM-DS2 confirm the expression of pluripotency markers (SSEA-4, Oct4 and Tra 1-60), scale bar: 300μm, and Alkaline Phosphatase activity, scale bar: 100μm.

Supplementary Fig. 4. Quantitative comparison of 100DIV isogenic T21 and D21 organoid "cortical" regions by FISH and I.F. a For Fluorescence In Situ Hybridisation (FISH), organoid slices were processed and probed with a MetaSystems Probes for chromosome 21 (red) and chromosome 13 (green). Quantification was performed automatically using IMARIS software (nuclei were scored for 1, 2, 3 or >3 spots n>500 nuclei for each line). Scale bar: 3μm. **b** APP-4G8 antibody (green), BACE2 (red), MAP2 (magenta), DAPI (blue). Scale bar: 10μm. **c** Aβx-34

neo-epitope specific antibody (green), BACE2 (red), MAP2 (magenta), DAPI (blue). Scale bar: 10μm. **d** Quantification was performed blinded to the genotype, on 5 independent images representing three individual organoids per genotype, and containing 3,000-4,000 cells per image. Only images within the "cortical" part of the organoid were considered for the analysis. Graphs show total fluorescence intensity of positive signals for each wavelength for a given antibody, normalised by the total fluorescence intensity of MAP2 as a pan-neuronal marker. Additional staining (not shown) was analysed for Aβx-40 neo-epitope specific antibody. Image analysis was performed using IMARIS software. Error bars: standard error, and p-values: calculated after Holm-Bonferroni correction (α=0.05) of sequential two-tailed student t-test comparisons.

Supplementary Fig. 5. Simplified schematic representation of APP695 from amino acid 500 to the C-terminal. The amino acid cleavage site for each secretase is noted in parentheses, and for sites in Aβ the respective peptide position is also noted. Secretases for each cleavage site are η: MT5-MMP, δ: AEP, β: BACE1, α: ADAM10, θ: BACE2, γ: gamma secretase complex. In addition to it's role as a θ-secretase, in which C99 is cleaved to preclude Aβ formation, in this report we highlight the role of BACE2 to act on Aβ as substrate, as an Aβ-degrading protease (AβDP).

Supplementary Fig. 6. Conditioned media from isogenic D21 and T21 organoids was compared by IP-MS and ELISA. a IP-MS showed that all amyloid peptide species were increased in T21 compared to D21 samples. **b** Despite the increase in peptides from T21 organoids, no significant change in ratio of Aβ40:Aβ42 was detected by ELISA **c** The increase in peptide concentrations for Aβ38, Aβ40 and Aβ42 in T21 organoid CM was confirmed by MSD ELISA. **d** representative Aβ IP-MS spectra of organoid CM (*co-IP-ed unknown non-β-amyloid peptide). **e** Areas under the peak (used as a readout in all IP-MS experiments) show near linear correlation with ELISA-measured levels of Aβ peptides.

Supplementary Fig. 7. Aβx-34 colocalises with BACE2 much more than with BACE1 in T21 cerebral organoids. a Pairwise Pearson's coefficient of colocalised volume for a pair of co-stained antibodies: Aβx-34 in all combinations, either BACE1 or BACE2 as a second antibody, and a marker of the sub-cellular vesicle compartment (shown at the bottom of each 3-columns histogram) as a third antibody. Error bars: standard error, and p-values: standard one-way ANOVA using post-hoc Bonferroni correction for multiple comparisons calculation. Representative individual z-slice images for the calculations performed in a are shown in **b** and c. b BACE1 (green), **c** BACE2 (green), with either Aβx-34, Sortilin or LAMP2 (red) and DAPI (blue). Scale bar: 10μm.

Supplementary Fig. 8. Validation and controls for immunohistochemistry. a Sudan black B was used to confirm the specificity of the Aβx-34 and BACE2 antibodies in human brain sections, and to eliminate lipofuscin autofluorescence. Three different human brain samples were used: DS-AD1, DS (28 yrs) pre-AD and euploid sporadic AD (73 yrs). Both antibodies show the same pattern of expression and colocalisation after Sudan black B staining (white arrows: intraneuronal fine-vesicular pattern and black arrows with white arrowhead: amorphous extra-cellular aggregates) except for a loss of the large intraneuronal spherical granules (white arrowheads, Fig. 3), which are likely lipofuscin. Scale bar: 5μm. **b** and **c** Chromogenic, immunohistochemical analysis of the human brain sections of DS-AD1, stained using polymer-HRP/AP double-staining kit. **b** The primary antibody against BACE2 was labelled with DAB (brown) and primary antibody against Aβx-34 neo-epitope was labelled with GBI-permanent-red (red); **b(i)** is a zoomed-in inset of the rectangle in B. c same as b, but both antibodies were pre-absorbed for 12 hours, and incubated overnight, with the excess of immunogenic peptide for the BACE2 antibody; **c(i)** is a zoomed-in inset of the rectangle in c. d and e: BACE2 antibody specificity control for immunofluorescence on T21 organoids (100DIV). Scale bar: 10μm. **d** Immunofluorescent staining with Aβx-34 and BACE2, **e** same as **b** and **d**, but both antibodies were pre-absorbed for 12 hours, and incubated overnight, with the excess of immunogenic peptide for the BACE2 antibody. The specificity for the neo-epitope specific antibody against Aβx-34 was extensively proven in a previous report (Cabrera et al., 2018). **f** and **g** In order to distinguish the contribution of lipofuscin auto-fluorescence to the colocalised signals, specificity of primary antibodies (Aβx-34 and BACE2) has been validated using Lambda (λ) scan function on confocal microscope (see Methods). **f** Aβx-34 shows specific peak in different ROI and uniform pattern on the three different human brain samples: DS-AD1 (59 yrs), DS (28

yrs) pre-AD and DS (8 months). As negative control of staining, DAPI and secondary antibody alone were used. **g** BACE2 also shows specific peak in different ROI and uniform pattern in human brain. **h** secondary antibody alone control. Scale bar: 20μm.

Supplementary Fig. 9. Validation of the genome integrity of CRISPR-edited iPSCs by SNP array and paralogous amplification quantitative pyrosequencing, and that CRISPR-edited cerebral organoids express cortical neuronal layer-specific markers.

a Following CRISPR editing, C5Δ7 iPSC line was assessed by SNP array and no genomic alternations were detected compared to the parental C5 iPSC line. B-allele frequency and LogR ratio plots comparing these two lines are shown for chromosome 21. Data for the whole genome available on request. **b** To further confirm retention of trisomy after BACE2 CRISPR editing, selected other genes on chromosome 21 were validated as trisomic using quantitative paralogous amplification/pyrosequencing method. GABPA and ITSN allele number were quantified relative to paralogous sequence mismatches on other chromosomes. GABPA and ITSN both show approximate 60:40 ratios for trisomic cells, and 50:50 ratios for disomic cells as expected. Quantified nucleotides are shown on the pyrogram in shaded grey boxes and the relative values for the corresponding peaks are shown. **c** Representative images of T21C5Δ7 organoids at DIV48 are shown, confirming expression of REELIN (layer I), BRN2 (layer VI), TBR1 (layer IV), FOXG1 (layers II and III), CTIP2 (layer V), SATB2 (layer III) and pan-neuronal makers MAP2 and 3R-Tau. Final image in each row is a merge of individual antibodies in that row. Scale bar: 50μm.

Supplementary Fig. 10. CRISPR/SpCas9-HF1-mediated reduction of BACE2 copy number from 3 to 2 in the T21C5 hiPSC line, reduced BACE2 protein expression to disomic levels, but does not alter the level of APP protein. Western blot stained with anti-BACE2 antibody or anti-APP antibody of the lysates of the iPSC line Δ7 compared to the wt T21C5, and D21C3 iPSC lines. Quantification of the total actin-normalised BACE2 signal showed a 27% reduction in Δ7 compared to T21 unedited line, and no significant difference compared to D21 control. Quantification of the total actin-normalised APP signal showed no significant difference between Δ7 and

unedited T21 line, whereas they both had significantly higher APP protein levels compared to the disomic control line. Error bars: standard error, p-values after standard one way ANOVA and Tukey's multiple comparisons test.

Supplementary Fig. 11. Staining of extracellular β-amyloid deposits in organoids with two different methods. **a** Early AD-like pathology was provoked in the Δ7 organoids. Staining with amyloid specific dye (AmyloGlo) and nuclear dye (DRAQ5). Top row: wt unedited control T21C5 (100DIV), Middle row: T21C5Δ7 (48DIV) and bottom row: T21C5Δ7 (96DIV); amyloid deposits are seen in Δ7 after 48DIV, but not its parental clone, at same organoid age. **b** Staining with Thioflavine S shows the same plaque-like pathology observed using AmyloGlo in the Δ7 after 48DIV. Scale bar: 20μm.

Supplementary Fig. 12. Cell death and neuronal loss in CRISPR-edited T21C5Δ7 organoids. Quantification was performed on 8 representative (Z-stack) figures from three individual organoid per genotype. Number of DAPI+ nuclei are shown in the volume of 10 000 μm^3. Graph show decreased number of nuclei in CRISPR-edited T21C5Δ7 (DIV48) organoids compared to parental T21C5 organoids and significantly decreased number of nuclei in 96DIV organoids ($p<0.0001$). Significantly decreased number of nuclei were observed between DIV48 and DIV96 in CRISPR-edited T21C5Δ7 ($p<0.001$). Error bars: standard error, and p-values after standard one-way ANOVA and Tukey's multiple comparison test.

Supplementary Fig. 13. Electron micrographs of negatively stained filaments isolated from insoluble fraction of the AD-like pathology containing organoid lysates. a, b representative straight filaments found in the lysates from the organoids T21C5Δ7 and QM-DupAPP, respectively. **c** Aβ1-40 synthetic peptide fibrils grown in vitro. Scale bars: a, c: 20nm, b: 40nm.

Supplementary Fig. 14. shRNA-mediated knockdown of BACE2 in QM-DS6 reduced protein expression in iPSCs and provoked AD-like pathology. a Stable iPSCs lines were generated expressing shRNA against BACE2 or a control scrambled (SCR) shRNA. Reduction of BACE2 expression compared to the scrambled control was confirmed by Western blotting, n=4, p=0.04, Student's t-test. **b-d** Cerebral organoids were generated from stable shRNA-expressing iPSCs and analysed after 46DIV. **b** the reduction in BACE2 expression resulted in the appearance of AD-like pathology (AmyloGlo deposits), scale bar: 50µm. **c-d** BACE2 shRNA also resulted in a significant increase in the number of neurons expressing conformationally altered Tau (TG3+). Scale bar: 20µm. Three different organoids and a minimum of 10 images per condition were used for analysis, p=0.0025, two-tailed Student's t-test. Error bars: standard error.

Supplementary Fig. 15. Secondary antibody alone controls for organoid immunostaining. DAPI staining confirms the presence of cells, but no unspecific signal from secondary antibodies. Scale bar: 20µm.

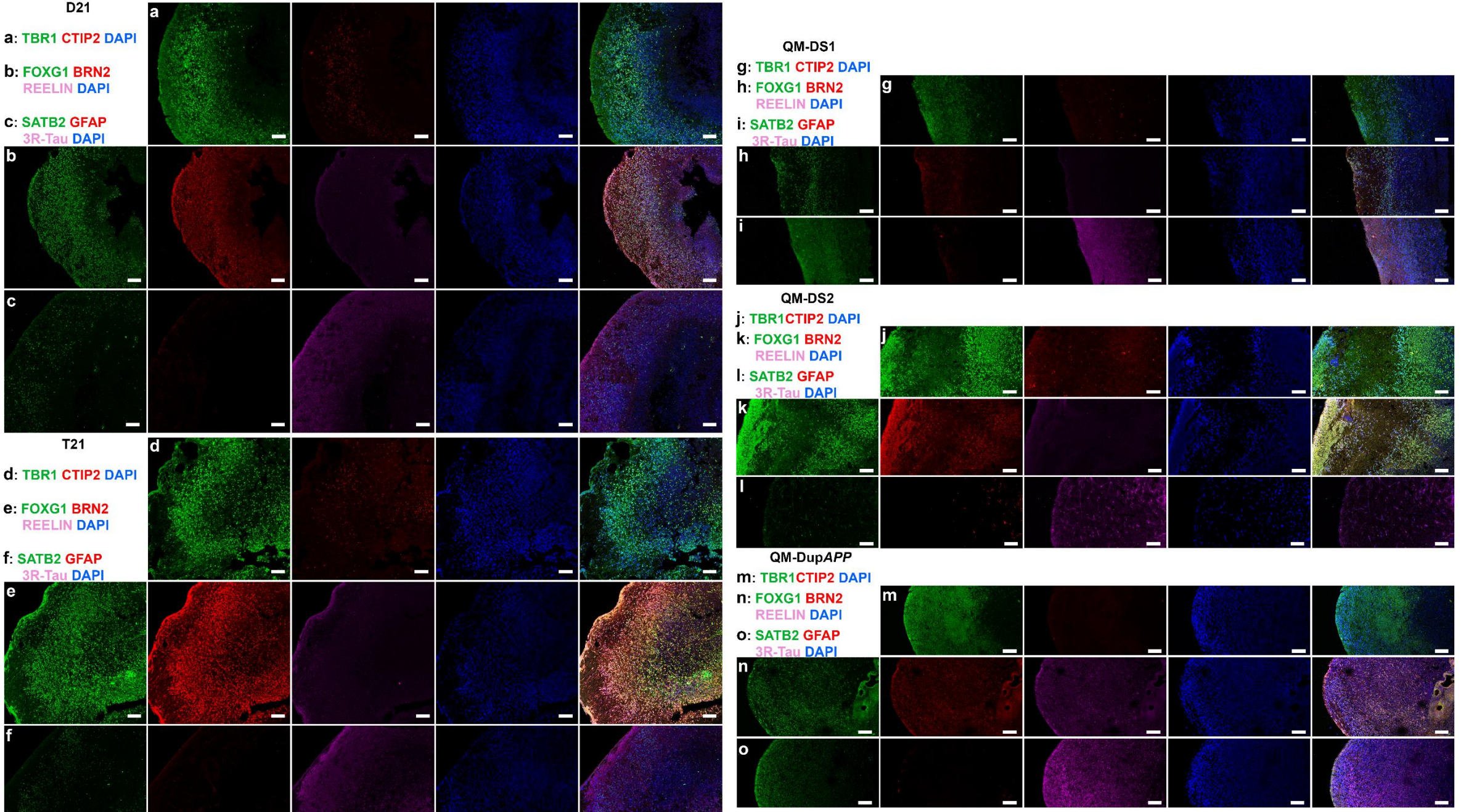

Supplementary Figure 1

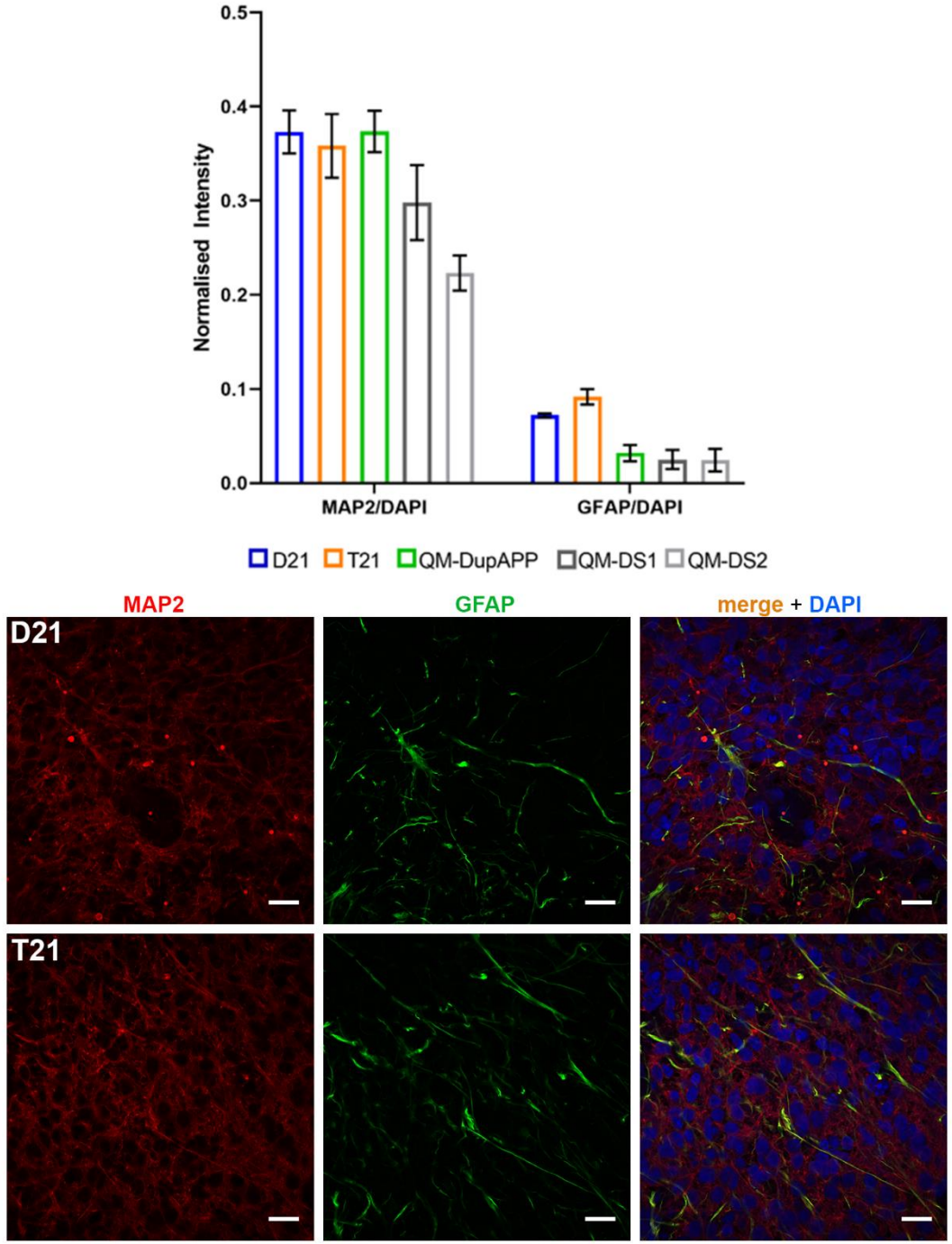

Supplementary Figure 2

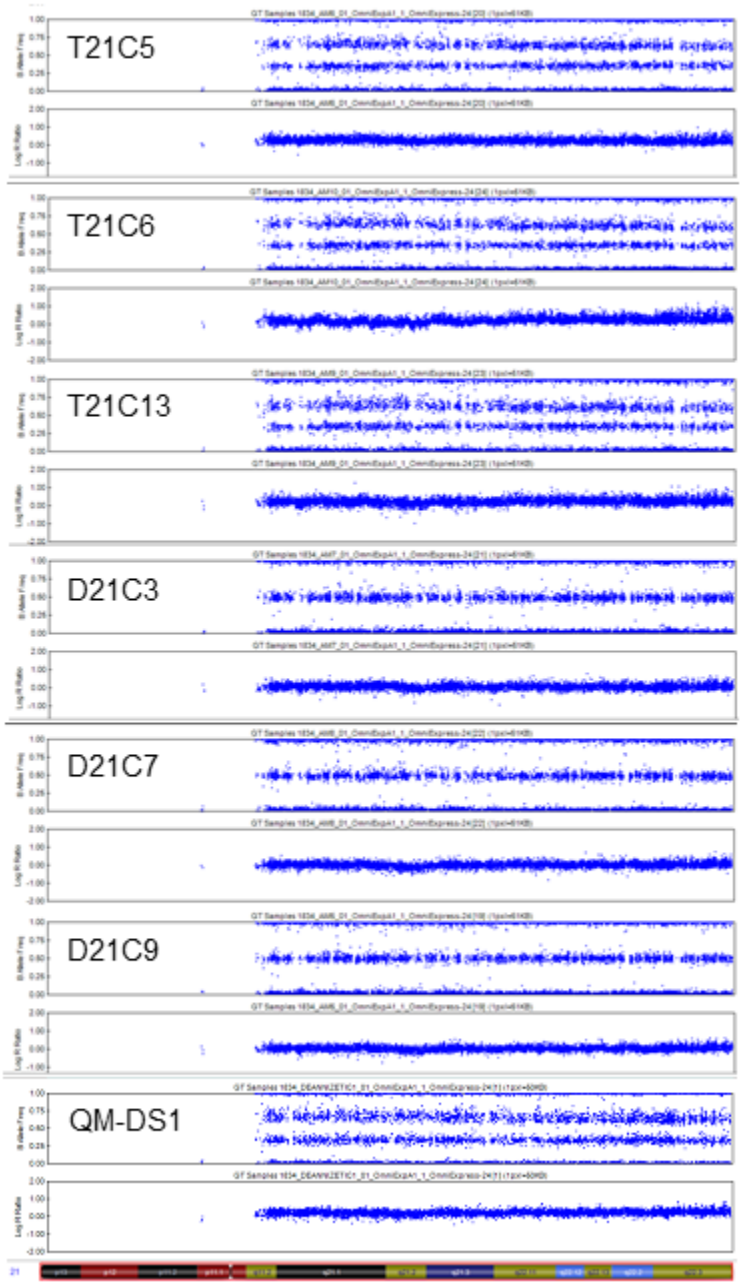

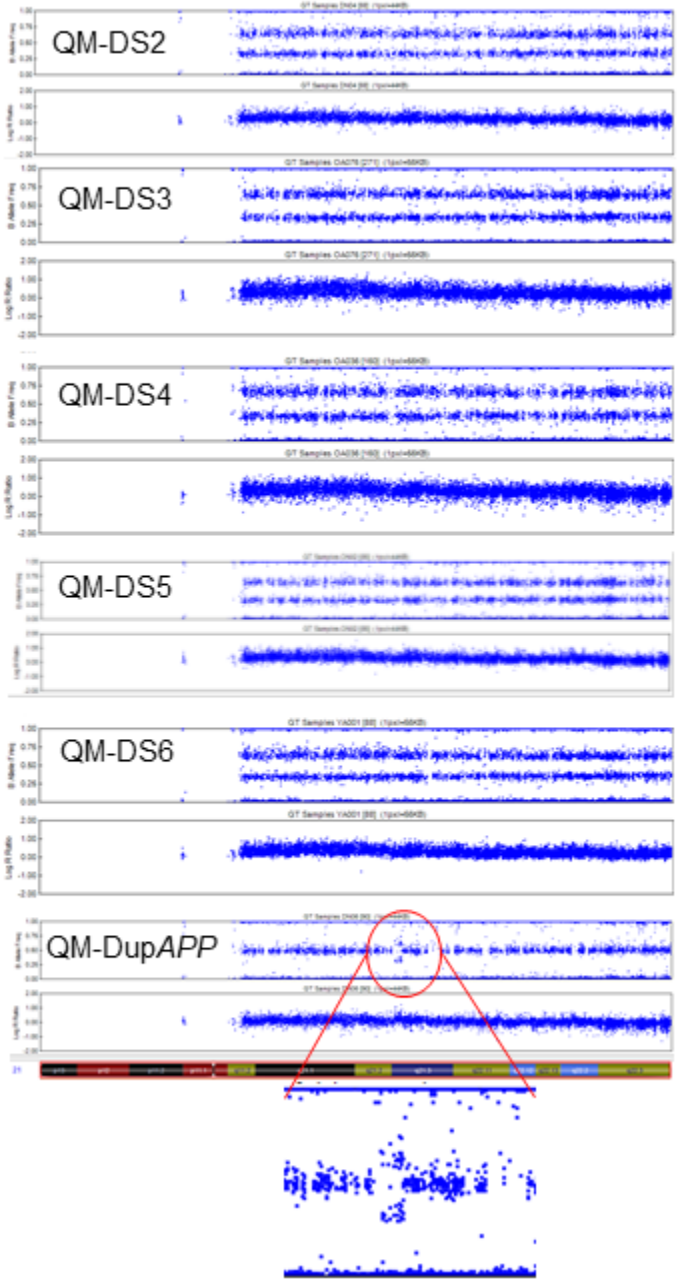

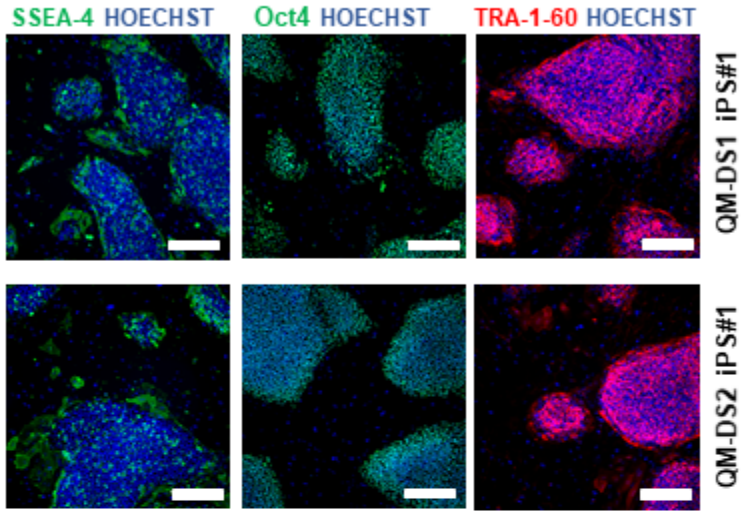

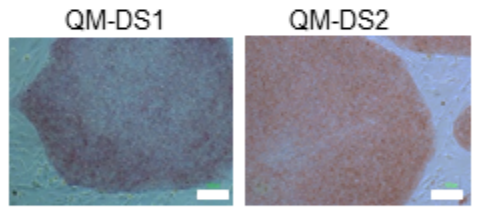

Alkaline phosphatase

Supplementary Figure 3

Supplementary Figure 4

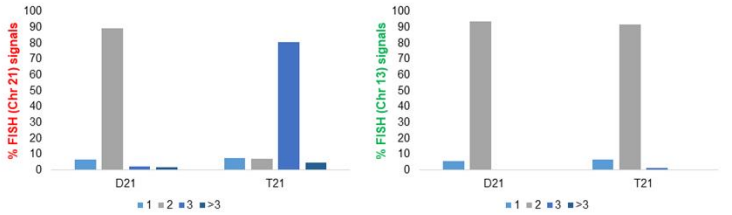

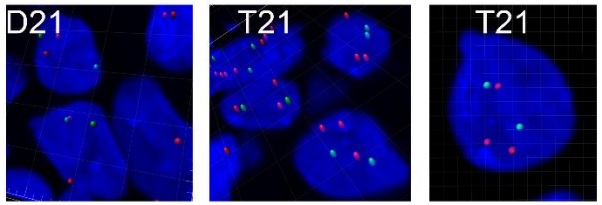

FISH probes
Chr 21
Chr 13

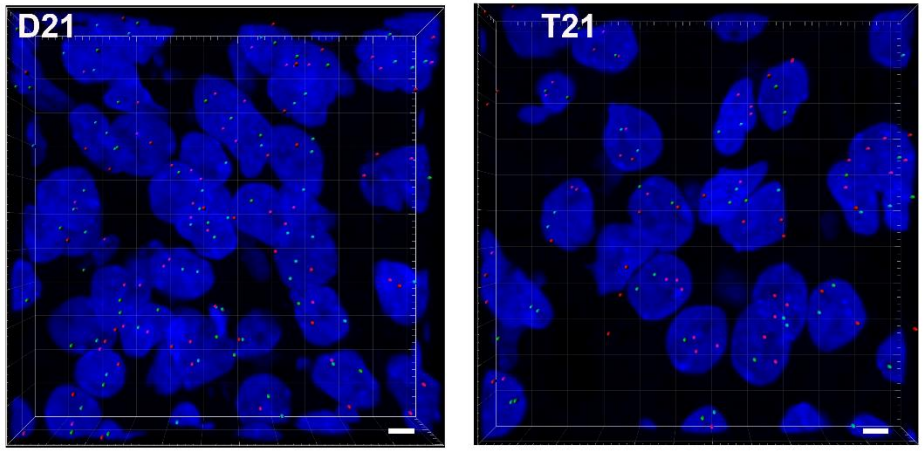

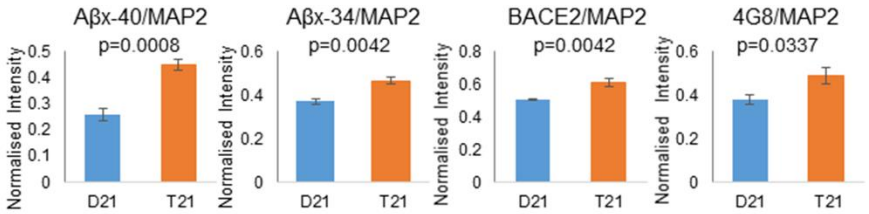

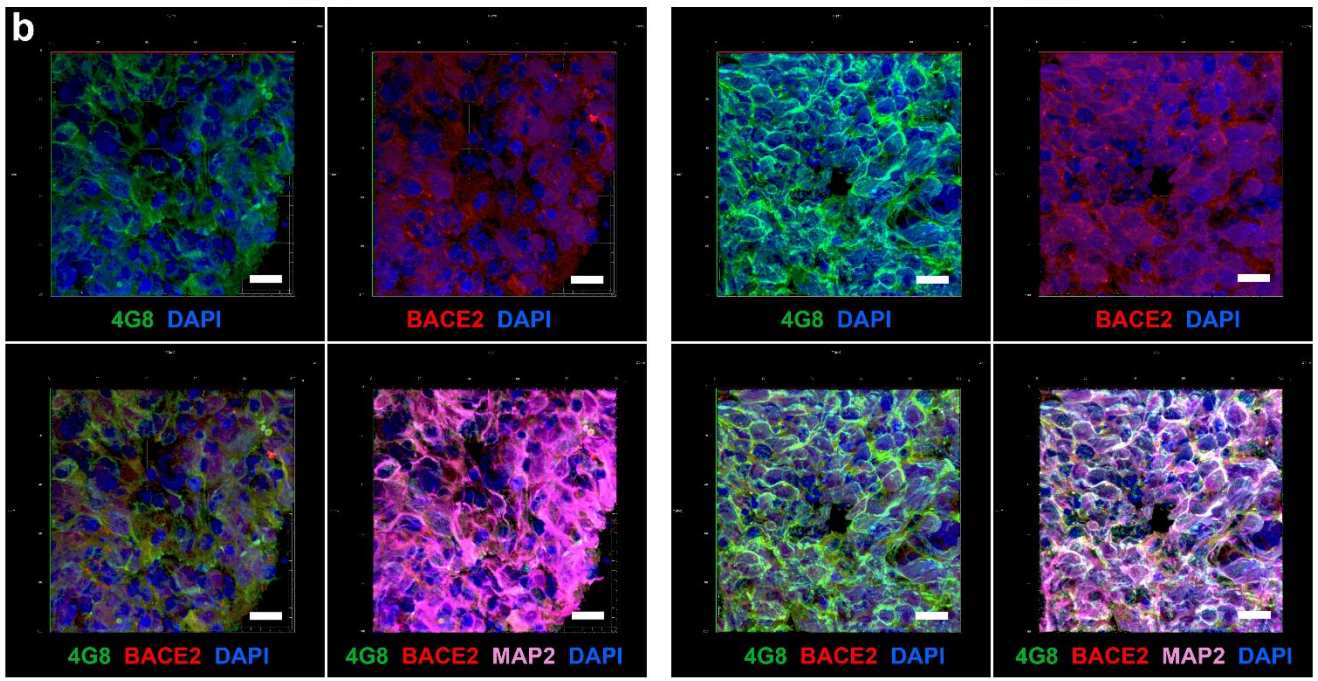

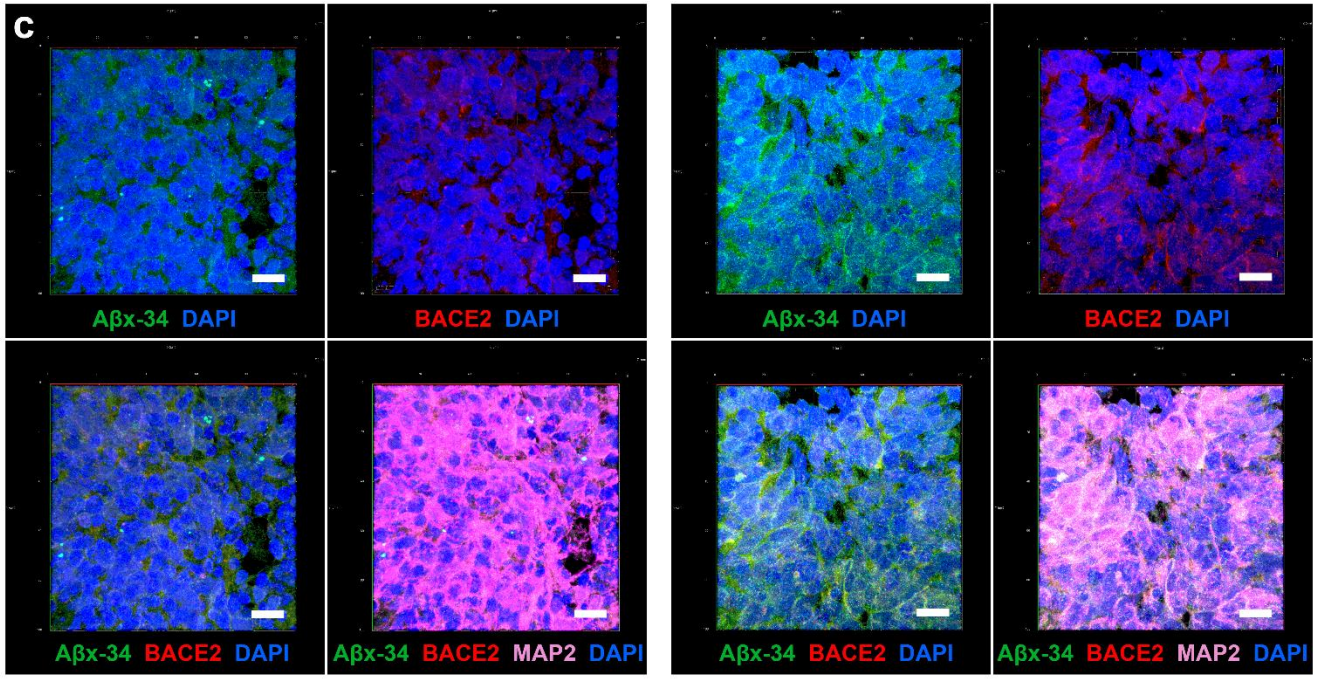

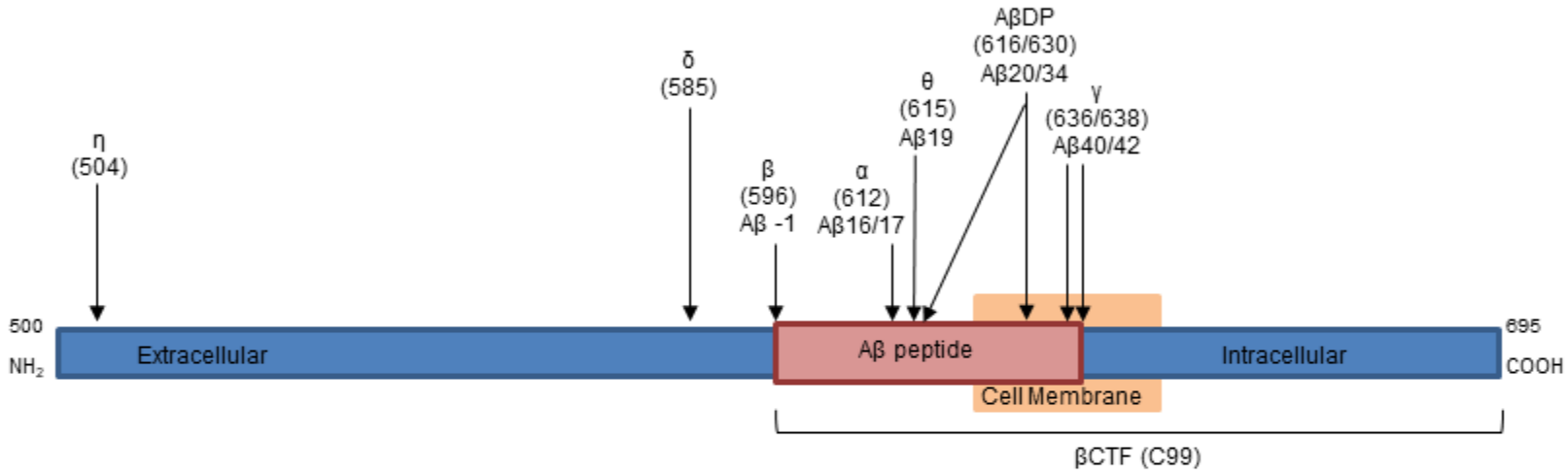

Supplementary Figure 5

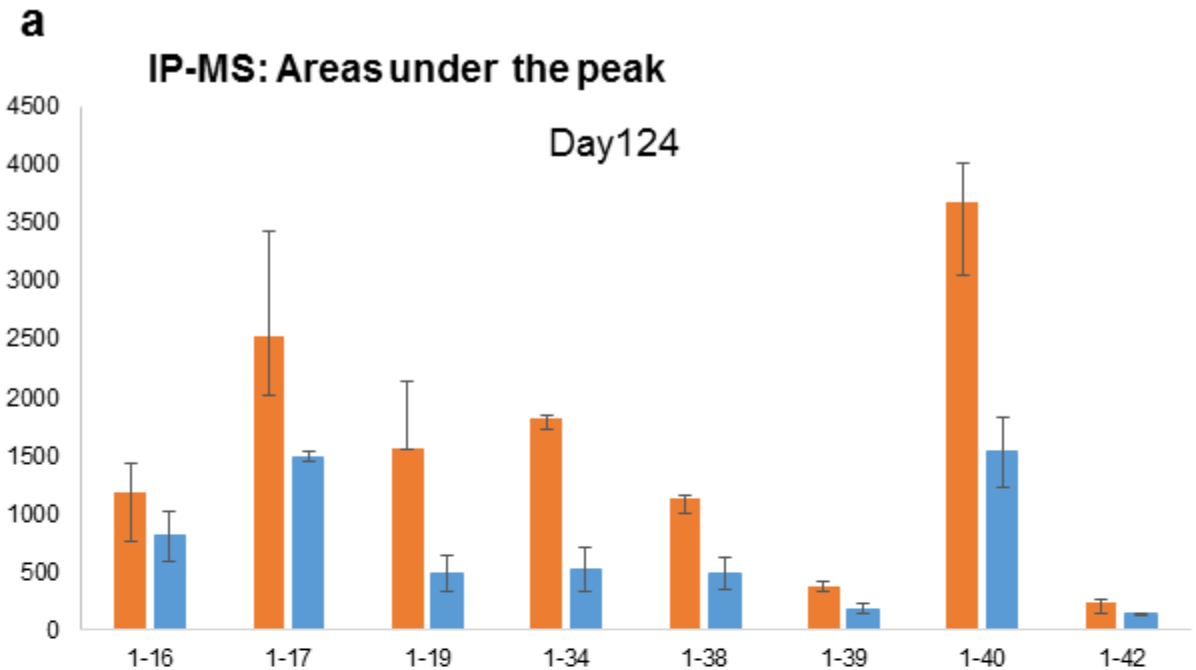

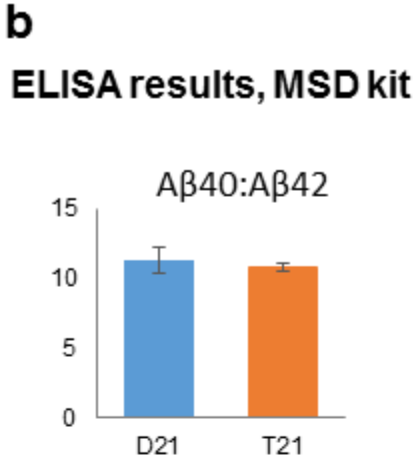

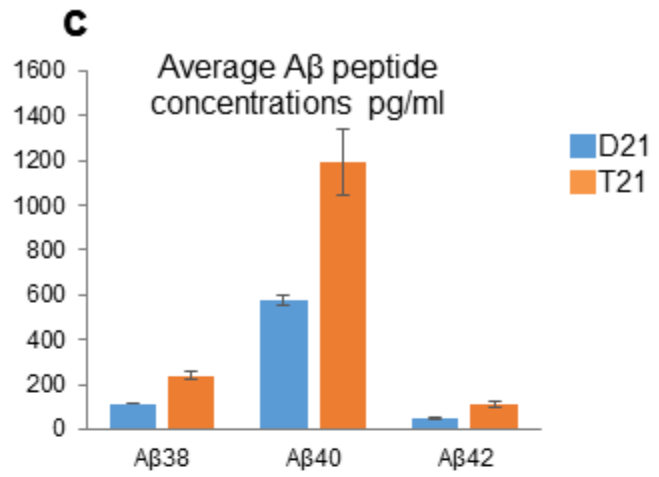

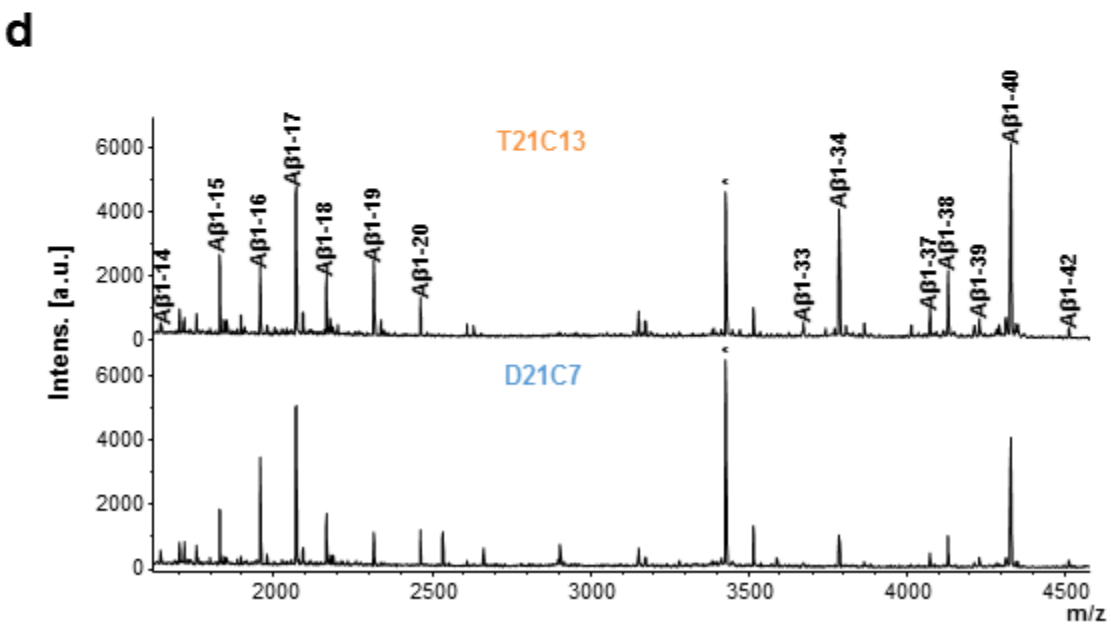

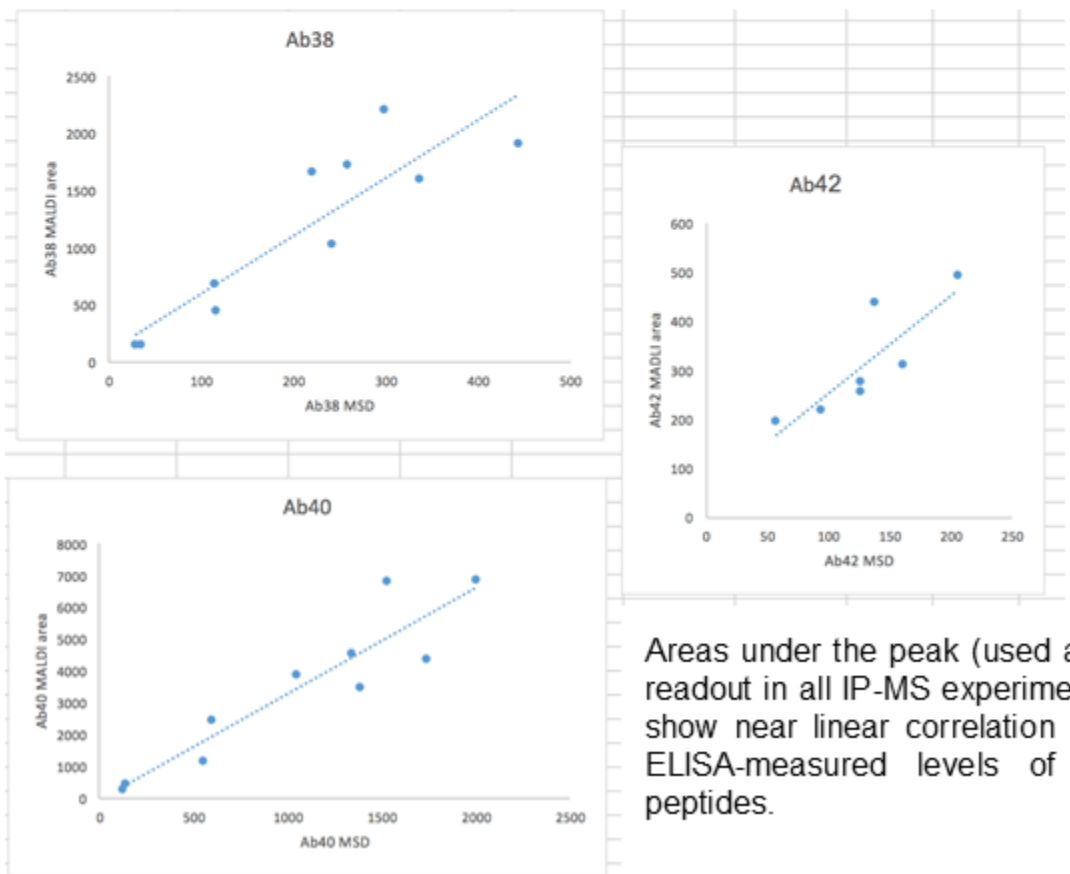

Areas under the peak (used as a readout in all IP-MS experiments) show near linear correlation with ELISA-measured levels of Aβ peptides.

Supplementary Figure 6

Supplementary Figure 7

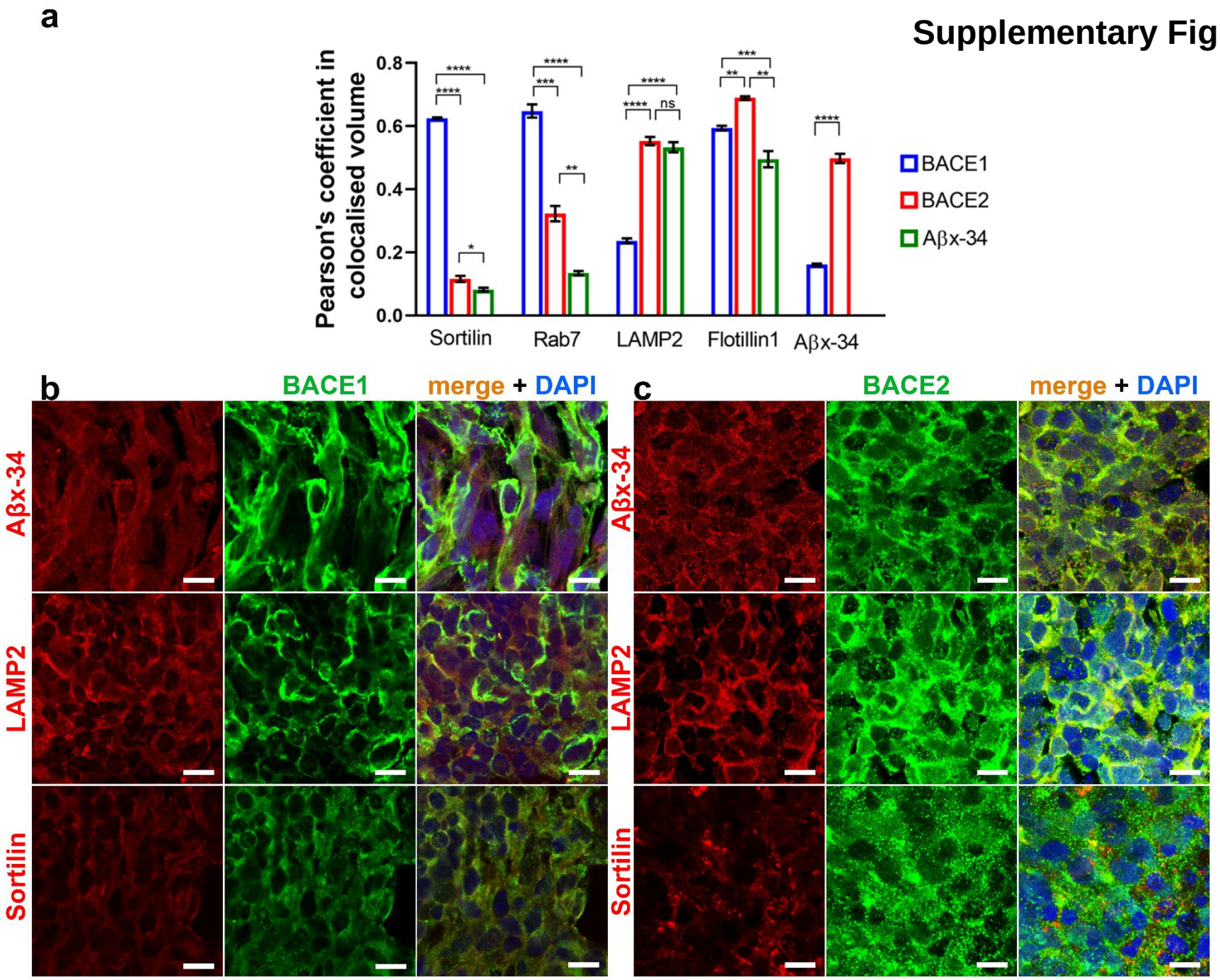

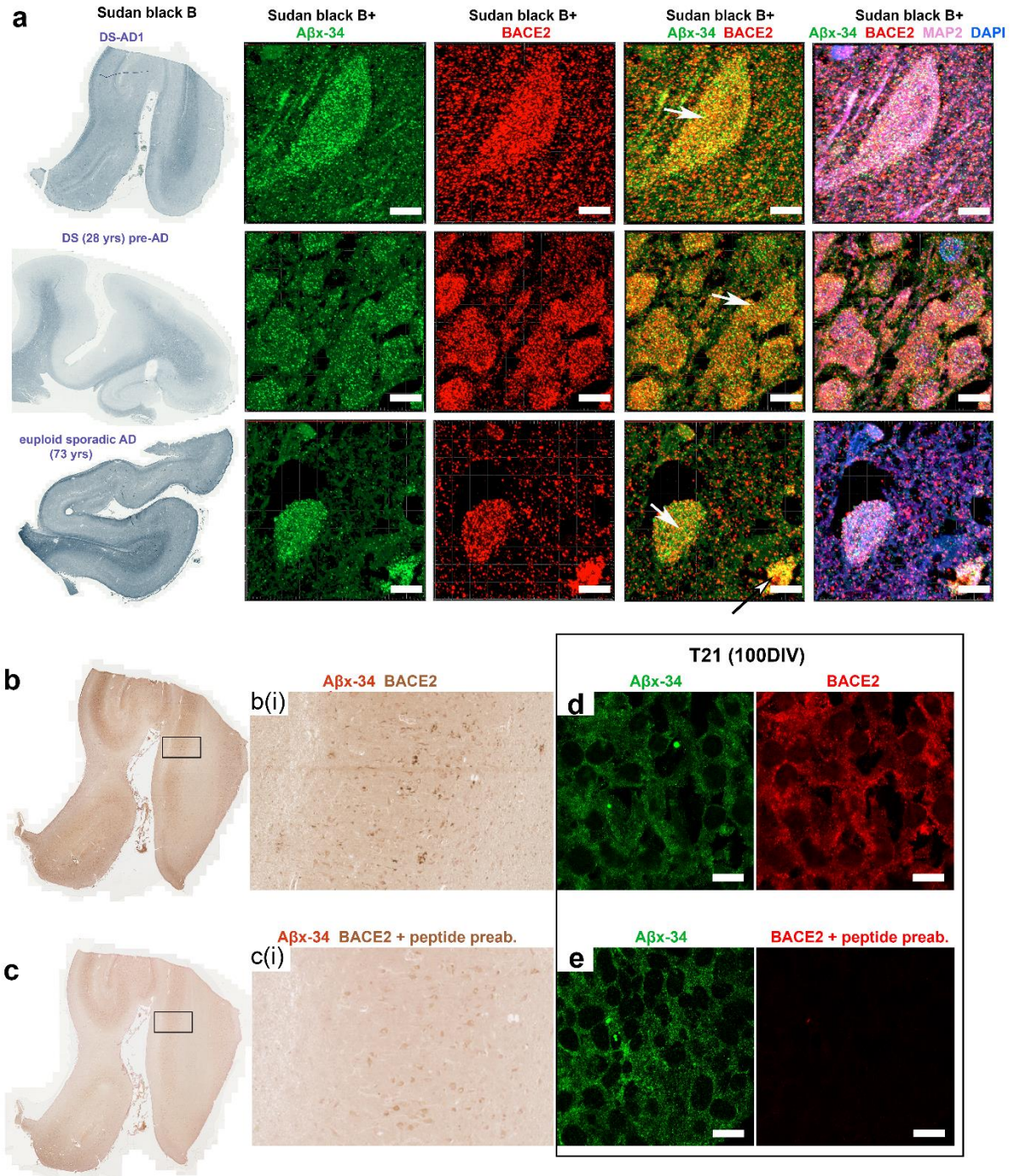

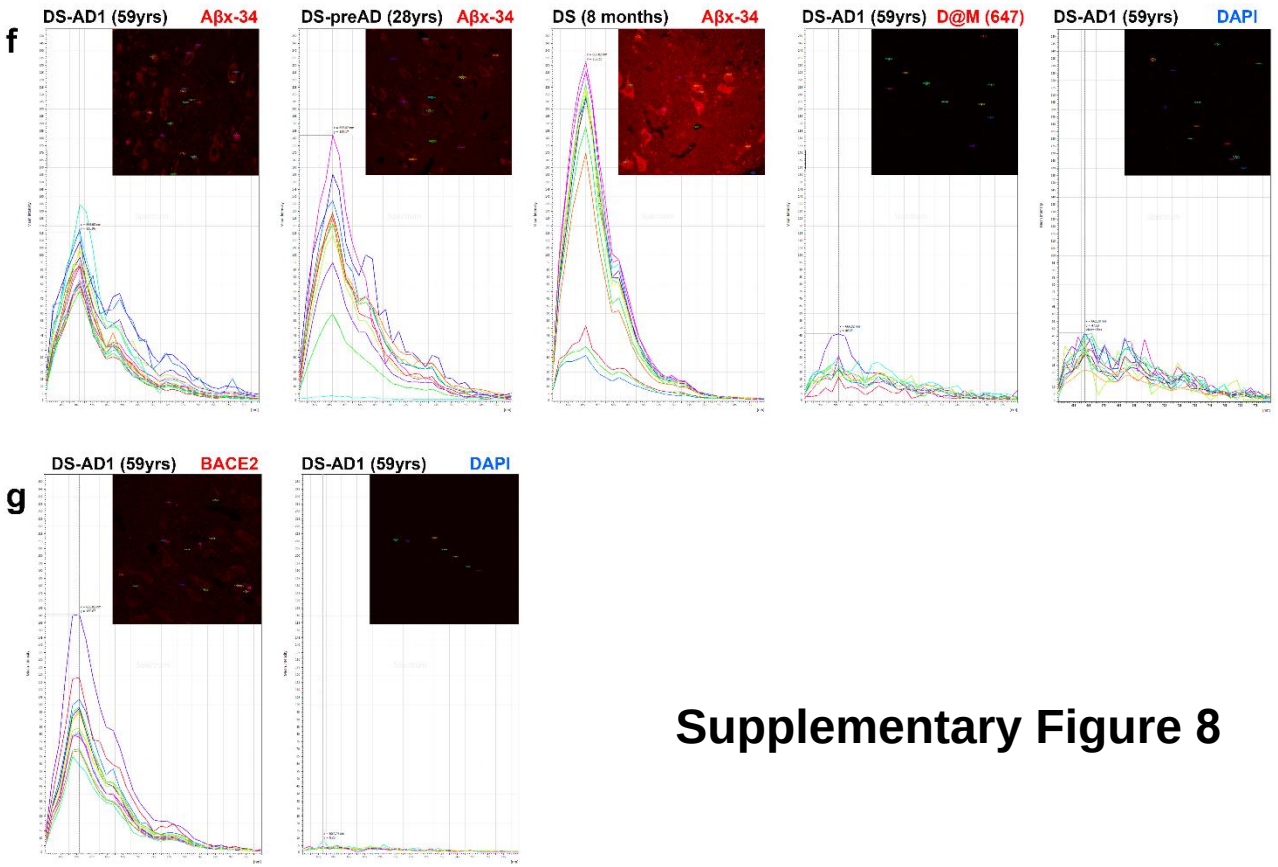

Supplementary Figure 8

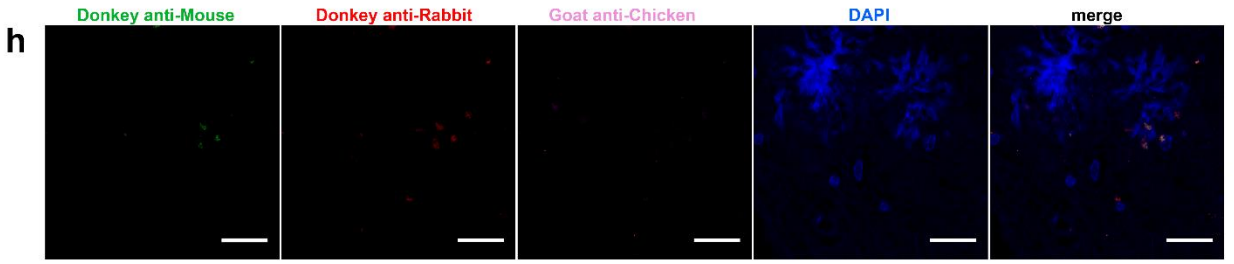

Supplementary Figure 9

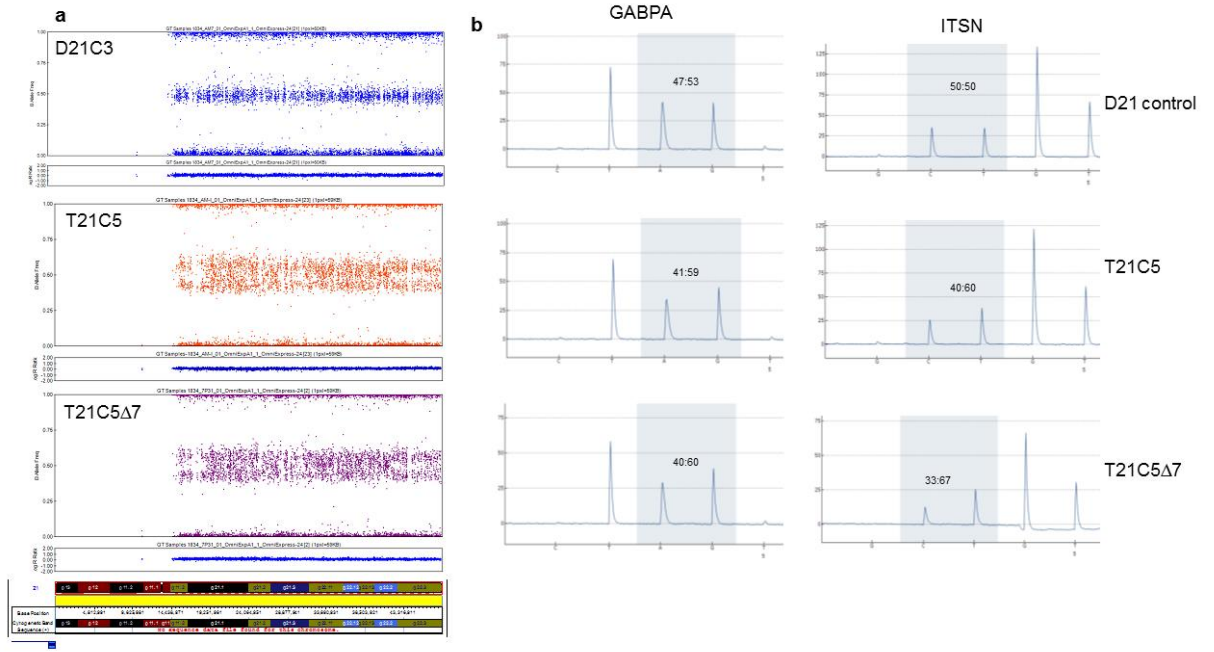

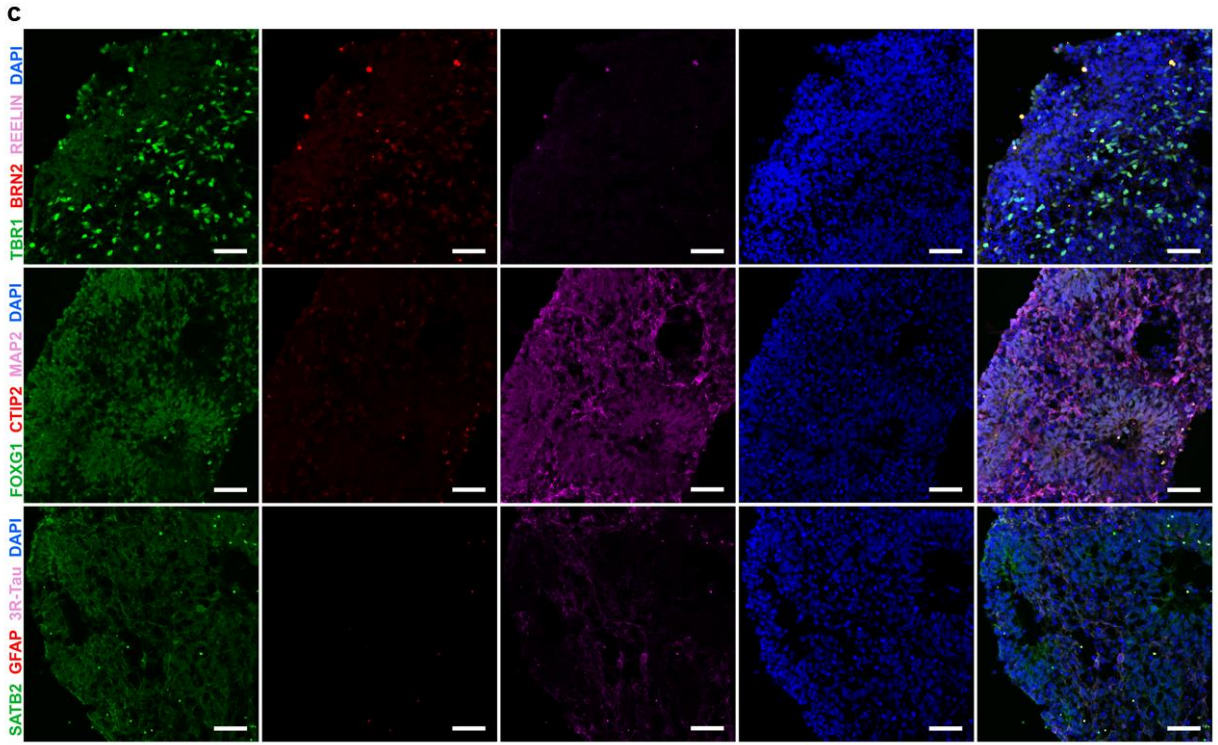

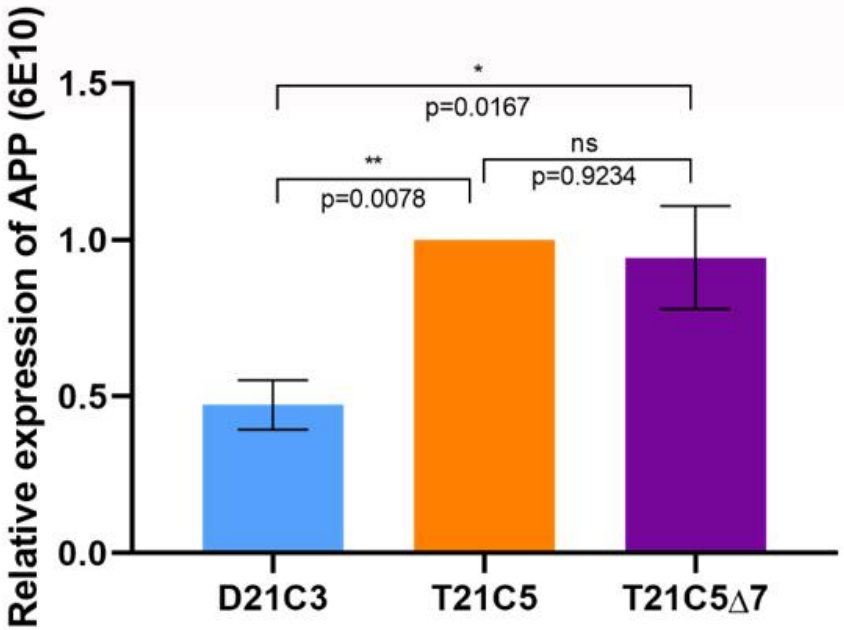

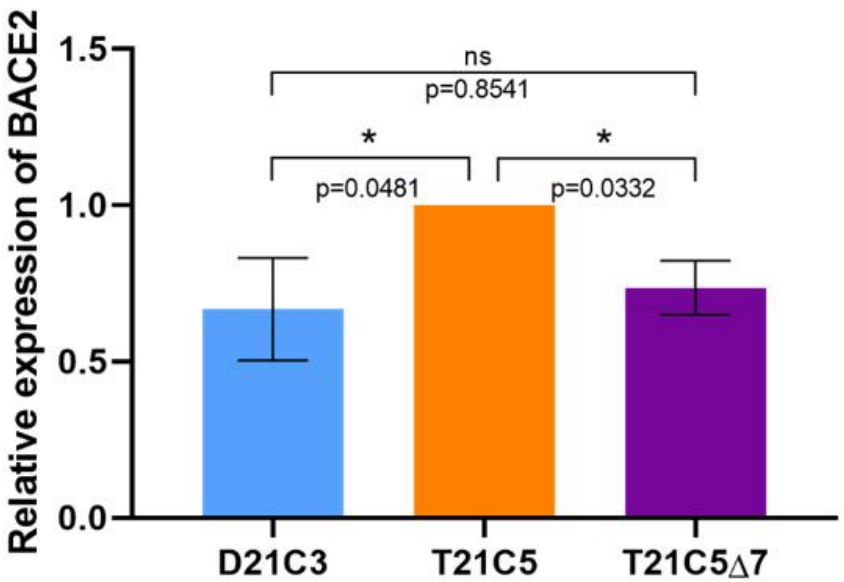

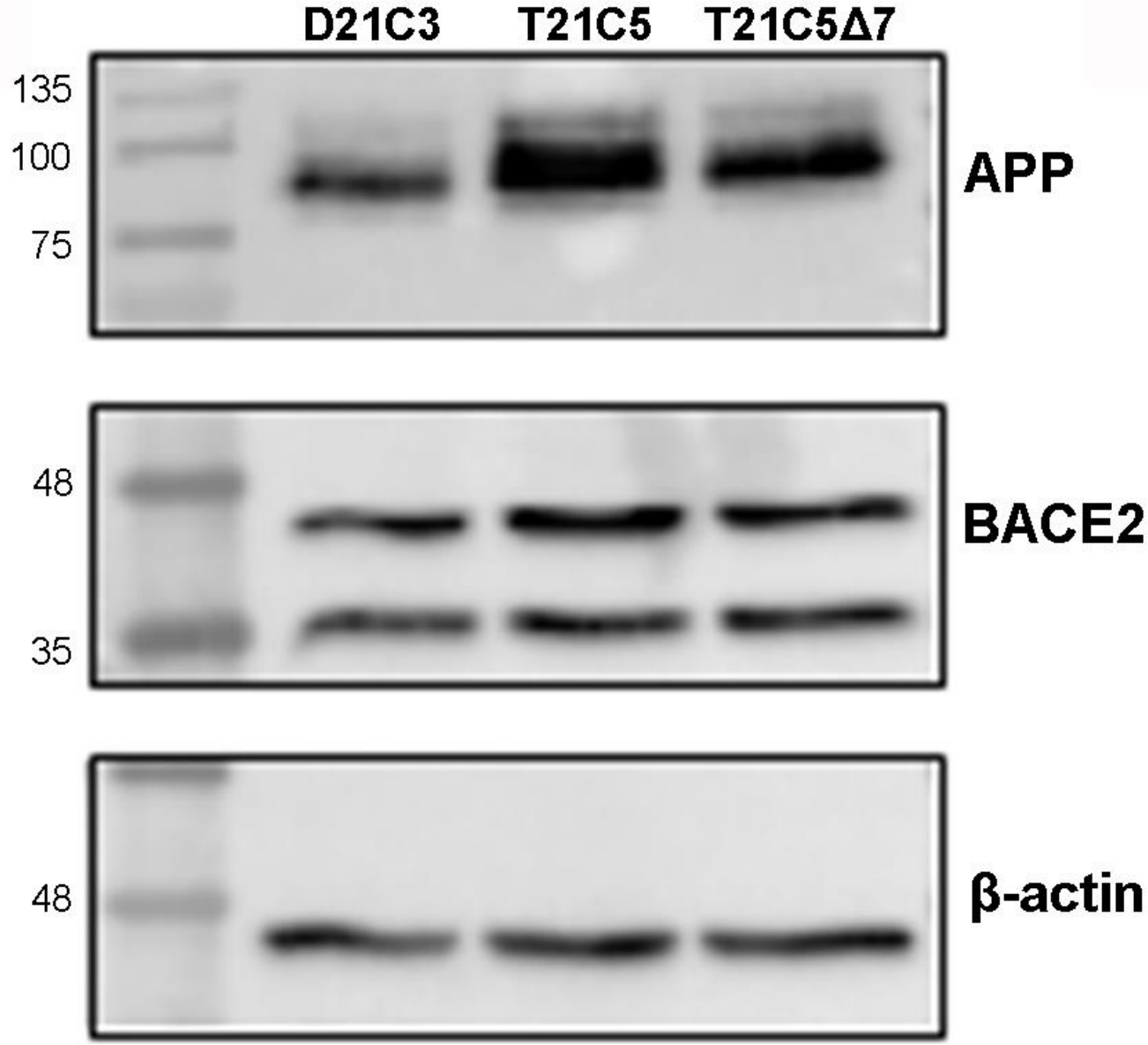

Supplementary Figure 10

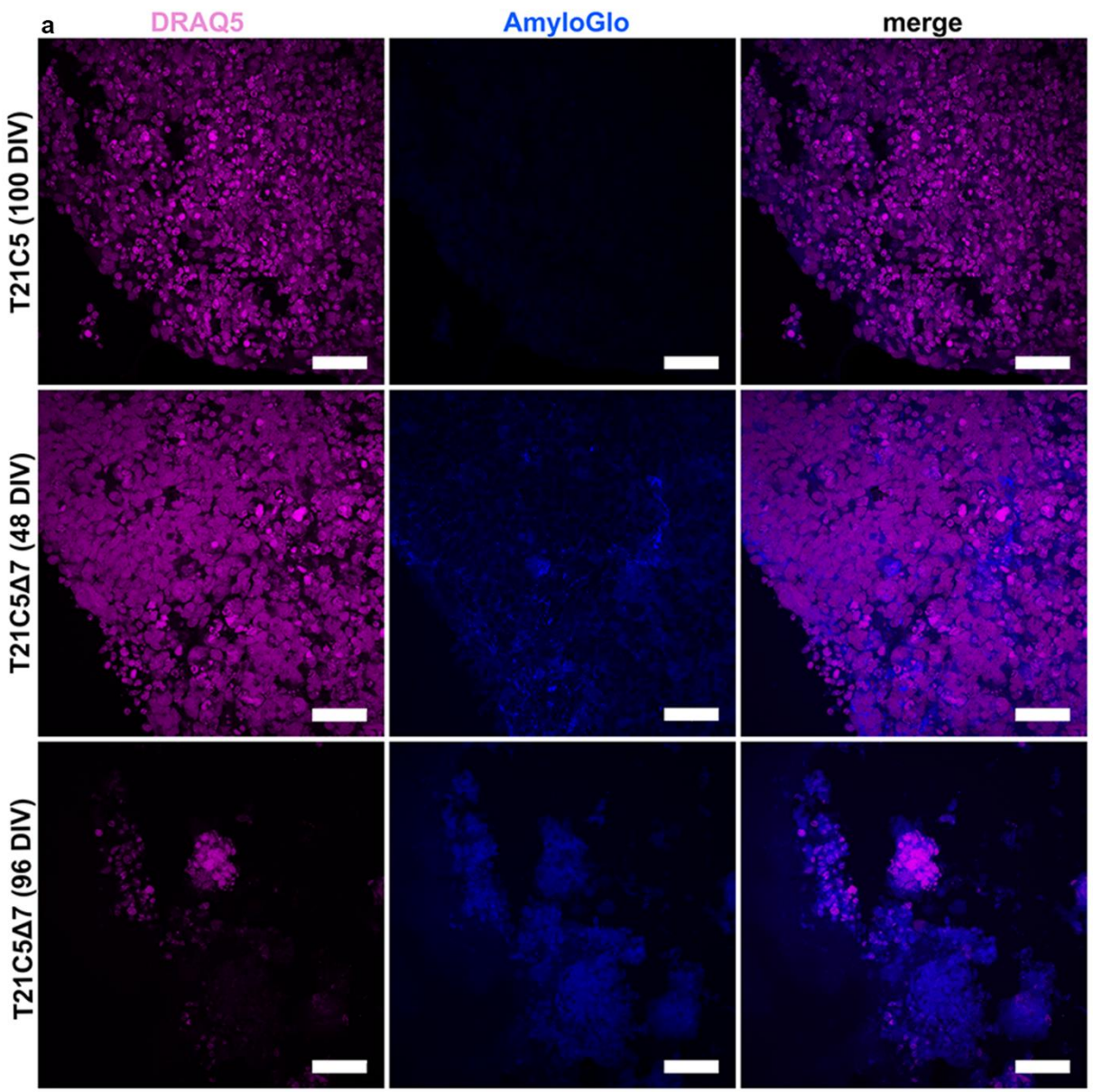

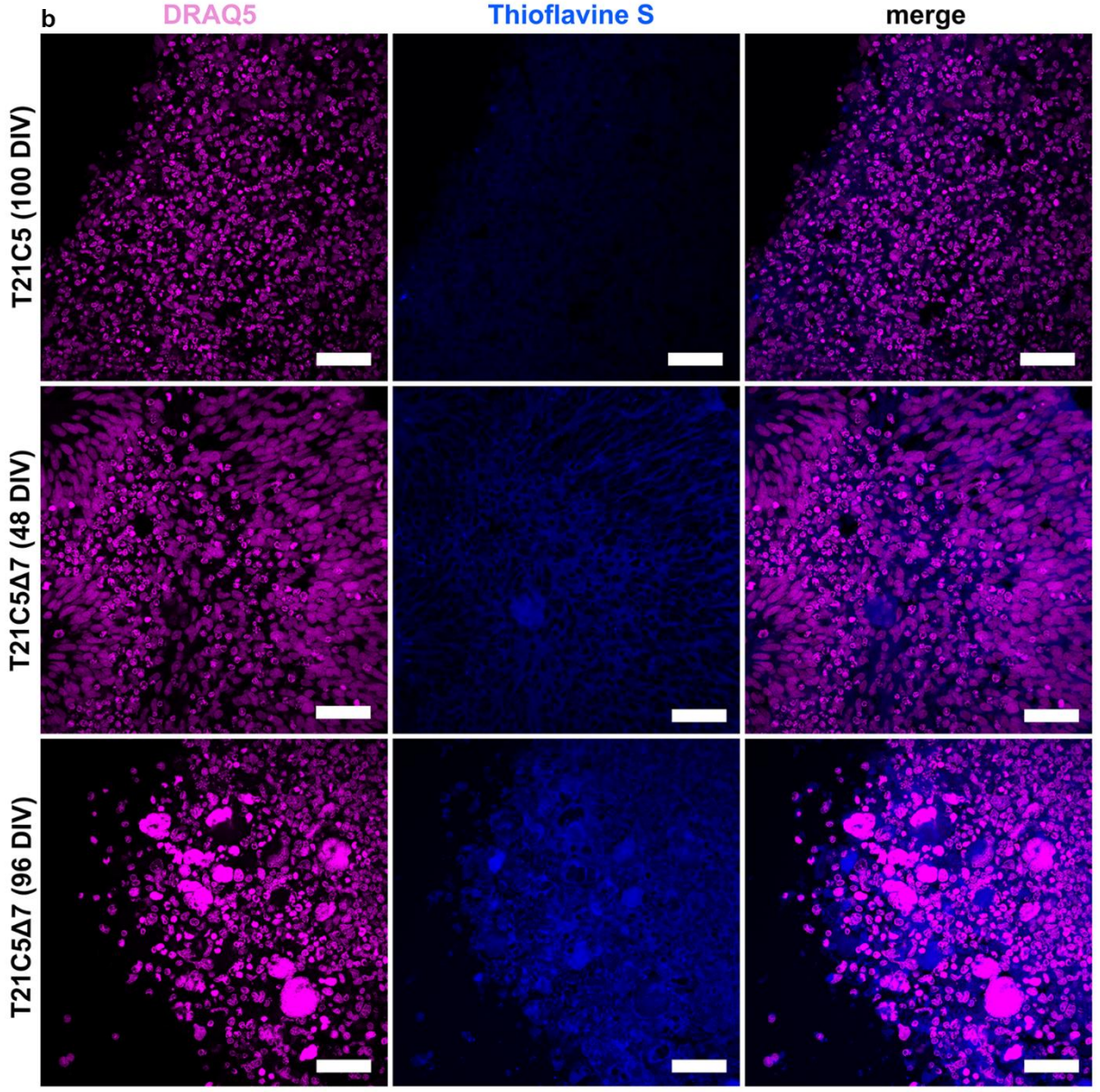

Supplementary Figure 11

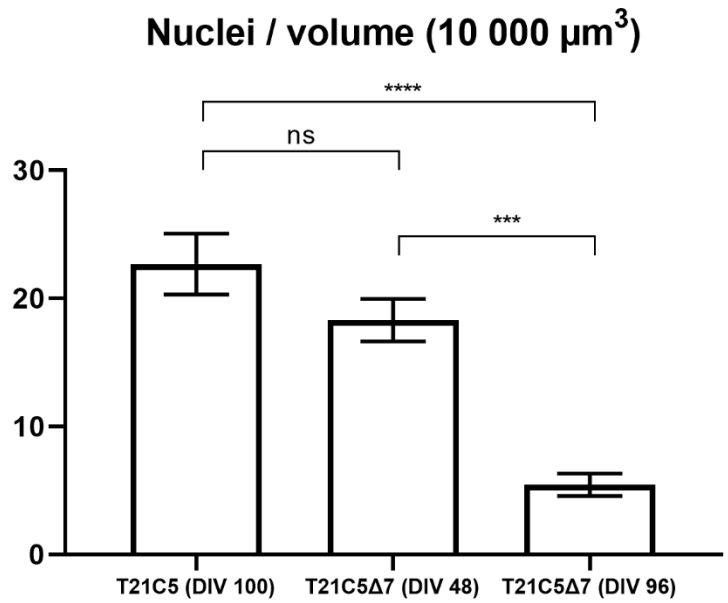

Supplementary Figure 12

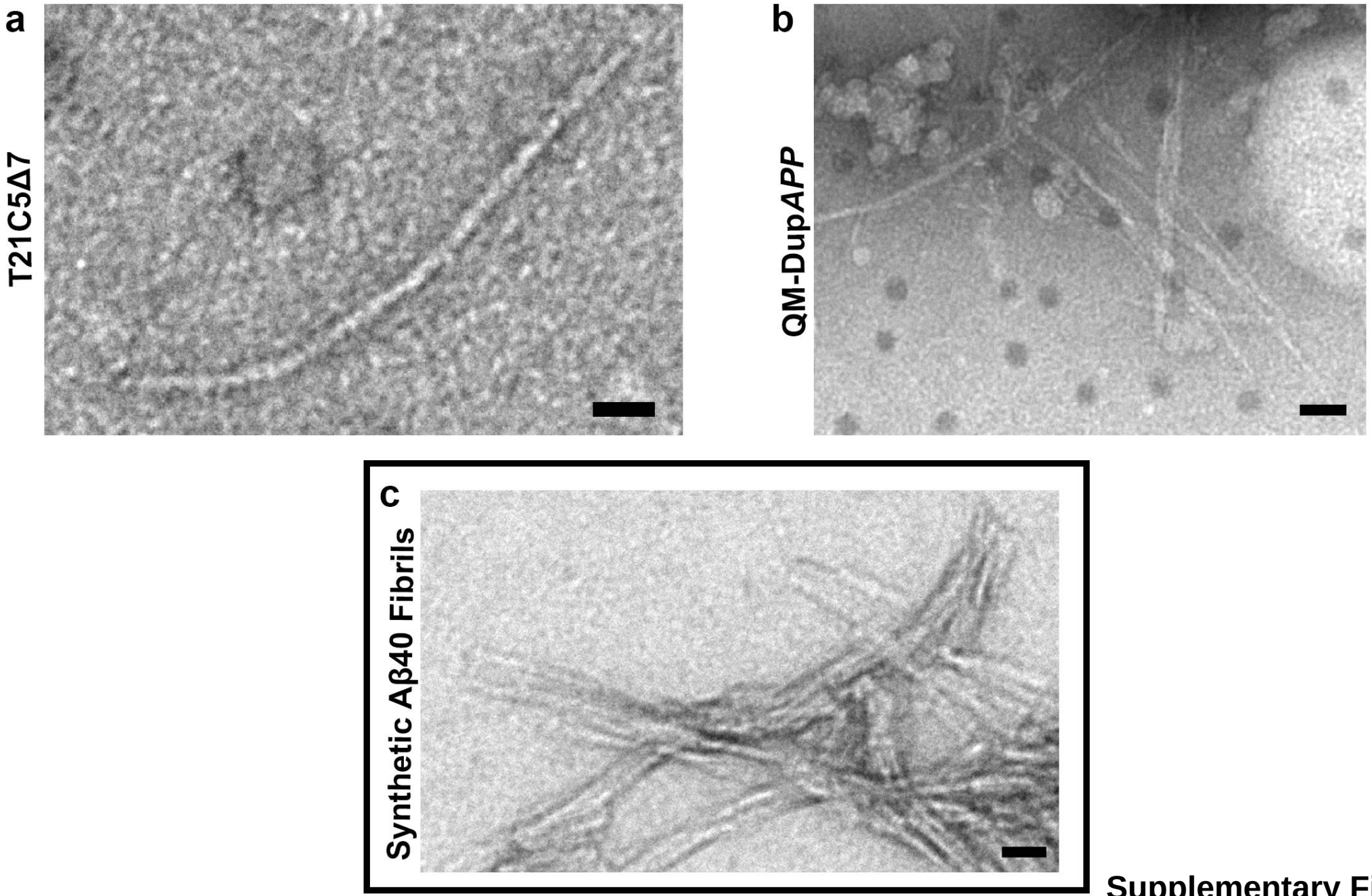

Supplementary Figure 13

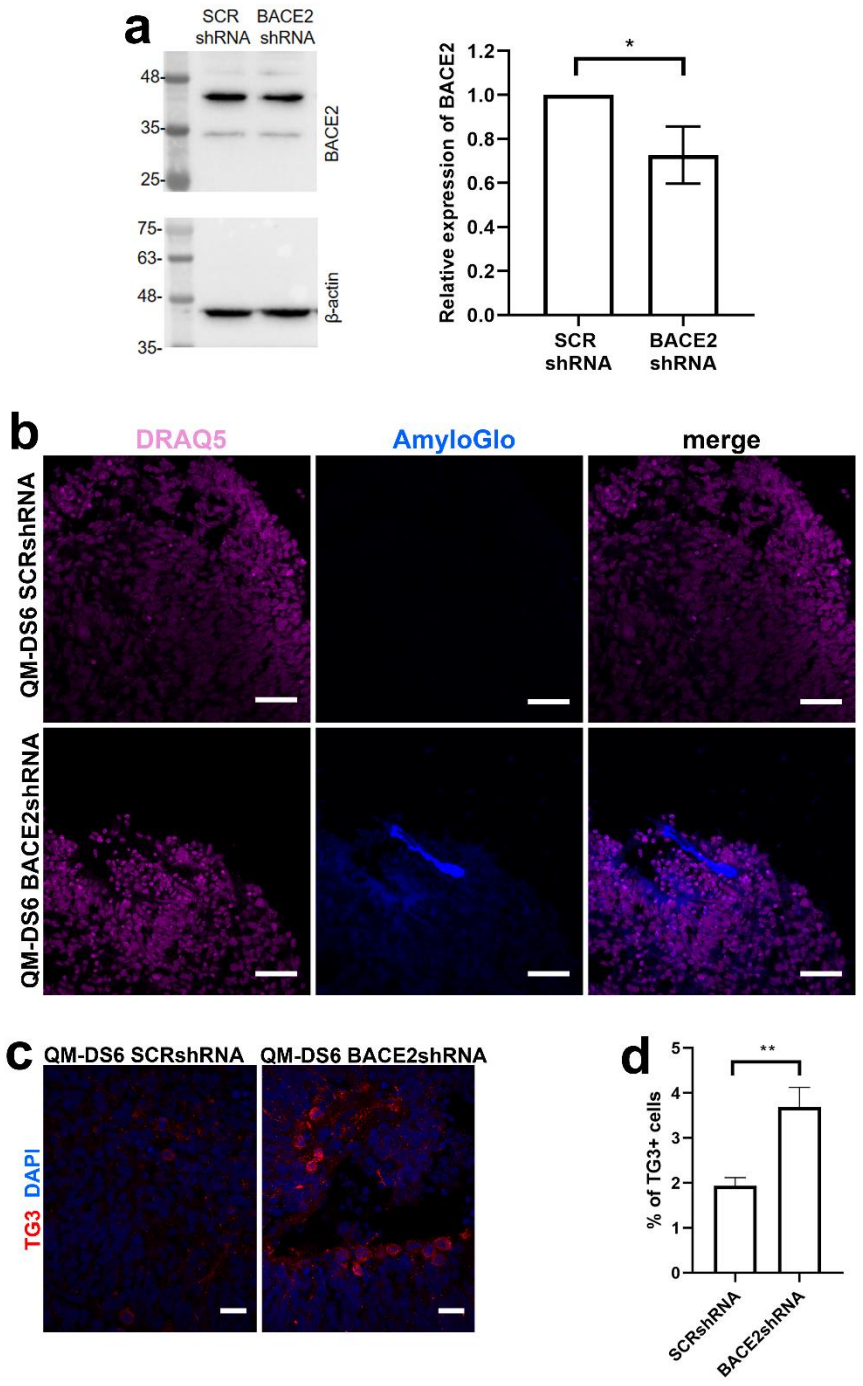

Supplementary Figure 14

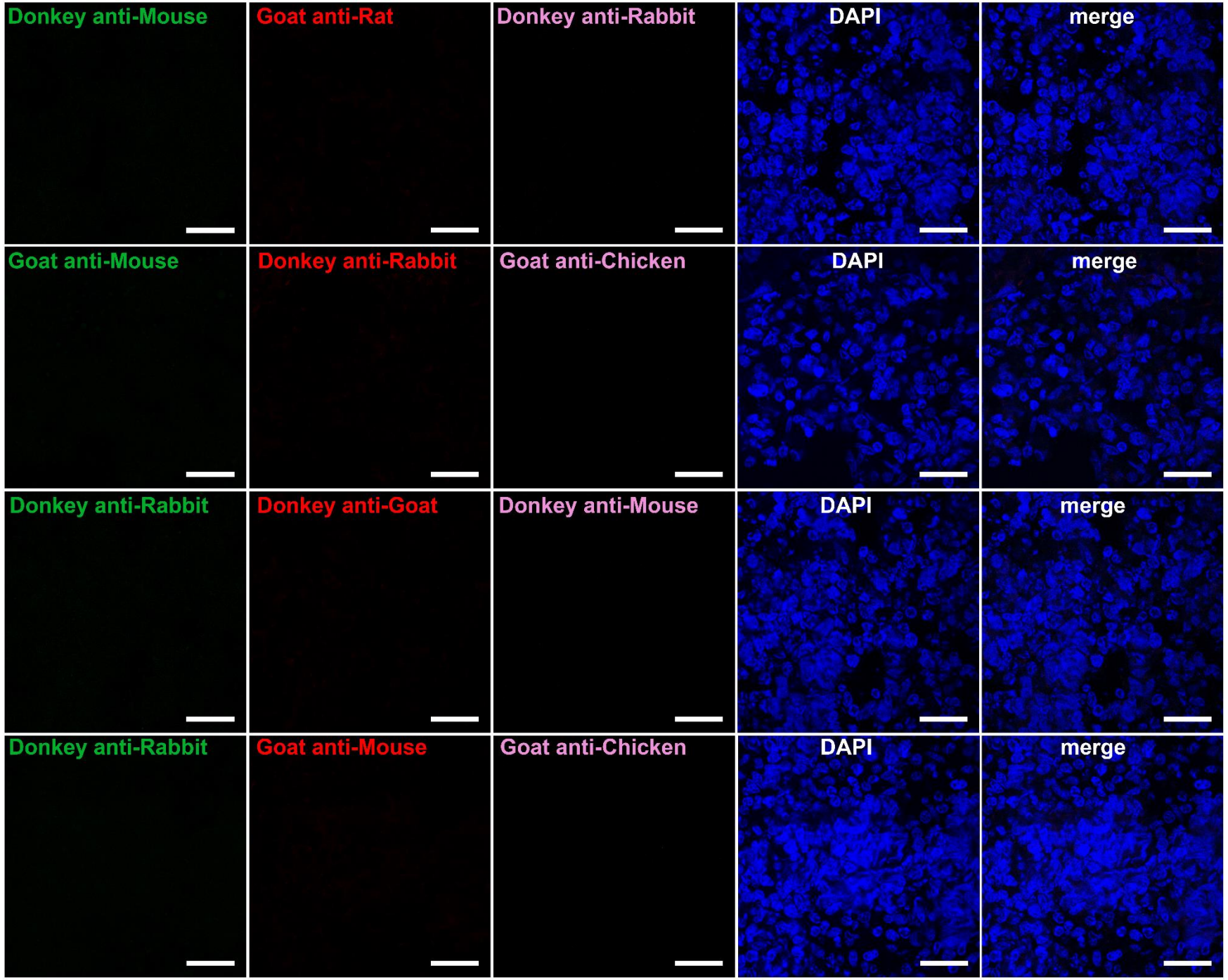

Supplementary Figure 15

Supplementary Information containing Supplementary Figures, Supplementary Tables and Supplementary Data-related to some main Figures.

Supplementary Fig. 1. Cerebral organoids express cortical neuronal layer-specific and astrocyte markers.

Supplementary Fig. 2. Comparison of the proportions of neurons and astrocytes to total cells in cerebral organoids. Isogenic D21 and T21 cerebral organoids generated mostly neurons and a small proportion of astrocytes, with no differences in the proportion of astrocytes or neurons in D21 compared to T21. Similar proportions were also detected in organoids from DupAPP, QM-DS1 and QM-DS2 iPSCs.

Supplementary Fig. 3. SNP arrays confirmed trisomy of chromosome 21 in all the iPSC lines used in this study, or in the case of QM-DupAPP, the partial duplication of a 580kbp segment of chromosome 21.

Supplementary Fig. 4. Quantitative comparison of 100DIV isogenic T21 and D21 organoid "cortical" regions by FISH and I.F.

Supplementary Fig. 5. Simplified schematic representation of APP695 from amino acid 500 to the C-terminal.

Supplementary Fig. 6. Conditioned media from isogenic D21 and T21 organoids was compared by IP-MS and ELISA.

Supplementary Fig. 7. Aβx-34 colocalises with BACE2 much more than with BACE1 in T21 cerebral organoids.

Supplementary Fig. 8. Validation and controls for immunohistochemistry.

Supplementary Fig. 9. Validation of CRISPR-edited iPSCs by SNP array and paralogous-loci-amplification-quantitative pyrosequencing, and that CRISPR-edited cerebral organoids express cortical neuronal layer-specific markers.

Supplementary Fig. 10. CRISPR/SpCas9-HF1-mediated reduction of BACE2 copy number from 3 to 2 in the T21C5 hiPSC line, reduced BACE2 protein expression to disomic levels, but does not alter the level of APP protein.

Supplementary Fig. 11. Staining of extracellular β-amyloid deposits in organoids with two different methods.

Supplementary Fig. 12. Relative quantification of cell death in CRISPR-edited T21C5Δ7 organoids.

Supplementary Fig. 13. Electron micrographs of negatively stained filaments isolated from insoluble fraction of the AD-like pathology containing organoid lysates.

Supplementary Fig. 14. shRNA-mediated knockdown of BACE2 in QM-DS6 reduced protein expression in iPSCs and provoked AD-like pathology.

Supplementary Fig. 15. Secondary antibody alone controls for organoid immunostaining.

Supplementary Table 1. Human Brain Samples:

Supplementary Table 2. Chemicals:

Supplementary Table 3. Primary antibodies:

Supplementary Table 4. Secondary antibodies:

Supplementary Table 5. Primer sequences used for the paralogous-loci-amplification-quantitative pyrosequencing

Supplementary Data:

Related to Fig. 1

Related to Fig. 2

Related to Fig. 3. and Supplementary Fig. 7

Related to Fig. 4

Related to Fig. 5

Supplementary Table 1. Human Brain Samples:

Sample	Region	Sex	Age	PMD(h)	Diagnosis	Braak
DS-AD1	Hippocampus	M	59y	<24	DS & AD	
DS-AD2	Frontal cortex	M	62y	51	DS & AD	V
DS-AD3	Frontal cortex	M	64y	16	DS & AD	V
DS-AD4	Frontal cortex	F	67y	17	DS & AD	VI
DS	Hippocampus	M	28y	<24	DS	
DS	Hippocampus	M	8m		DS	
sAD1	Hippocampus	M	73y	<24	AD	IV/V
sAD2	Hippocampus	F	83y	<48	AD	V
sAD3	Hippocampus	F	69y		AD	
NDC1	Hippocampus	M	42y	4.5	NDC	
NDC2	Hippocampus	F	84y	<24	NDC	
NDC3	Hippocampus	F	81y	<24	NDC	
NDC4	Hippocampus	F	85y	<24	NDC	
NDC5	Hippocampus	M	78y	<24	NDC	I/II

Supplementary Table 2. Chemicals:

Chemical	Source	Cat.No	Dilution/final concentration
AmyloGlo	Biosensis	TR-300-AG	1:100
Beta Secretase Inhibitor IV (βI-IV)	Calbiochem	565788	2.5μM (organoids) 0nM-1μM (FRET)
Compound E (Gamma Secretase Inhibitor XXI)	Millipore	565790	6nM
Dako Fluorescence Medium	DAKO	S3023	N/A
DAPI	Sigma	D9542	1:8000
DAPT (Gamma Secretase Inhibitor)	Merck	565770	0nM-1μM
DMSO	Sigma	D2650	1:117
DRAQ5	Abcam	ab108410	1:1000
Formic acid	Sigma	F0507	87%
Hoechst 33342	Life Technologies	R37605	1:1000
LY2886721 (Beta secretase inhibitor)	Selleckchem	S2156	0nM-0.5μM
Sudan black B	Abcam	ab146284	0.1% in 70% EtOH
Thioflavine S	Sigma	T1892	1:100

Supplementary Table 3. Primary antibodies:

antibody	clone	species	source	Cat.No	dilution		
					Organoids	Brain	WB
Aβx-34	1B5.4	mouse	Ref: *Cabrera E et al. 2018*	NA	1:1000	1:500	
Aβx-40	BA27	mouse IgG2a	Wako	014-26923	1:500	1:250	
Aβx-42 (43)	BC05	mouse IgG1	Wako	010-26903	1:500	1:250	
Aβ	4G8	mouse IgG2b	BioLegend	800701	1:200	1:200	
Aβ-pE3 peptide	D5N5H	rabbit IgG	Cell Signaling	#14975	1:200		
APP	6E10	Mouse IgG1	Biolegend	803001			1:1000
BACE1		rabbit IgG	Abcam	ab2077	1:200	1:200	
BACE2		rabbit IgG	Abcam	ab5670	1:200	1:200	1:500
BACE2		rabbit IgG	Abcam	ab5671	1:200	1:200	1:500
BACE2		rabbit IgG	Abcam	ab8025	1:200	1:200	
Beta-Actin		rabbit IgG	Abcam	ab8227			1:10000
BRN2		goat IgG	Santa Cruz	SC-6029	1:250		
CTIP2	25B6	rat IgG2a	Abcam	ab18465	1:100		
EEA1	C45B10	rabbit IgG	Cell Signaling	#3288	1:200		
Flotillin1		goat IgG	Abcam	ab13493	1:200		
FOXG1		rabbit IgG	Abcam	ab18259	1:400		
GFAP		chicken IgY	Abcam	ab4674	-	1:250	
GFAP	2.2B10	rat IgG2a	ThermoFisher Scientific	13-0300	1:1000	-	
HSC70	1B5	rat IgG2a	Abcam	ab19136	1:200		
LAMP1	D2D11	rabbit IgG	Cell Signaling	#9091	1:200		
LAMP2	GL2A7	rat IgG	ThermoFisher Scientific	MA1-165	1:100	1:100	
LAMP2A		rabbit IgG	Abcam	ab18528	1:200		
LC3A	D50G8	rabbit IgG	Cell Signaling	#4599	1:400		
MAP2		chicken IgY	Abcam	ab5392	1:1000	1:500	
Rab7	EPR7589	rabbit IgG	Abcam	ab137029	1:200		
Rab7	Rab7-117	mouse IgG2b	Abcam	ab50533	1:200		
REELIN	142	mouse IgG1κ	Chemicon (Merck)	mab5366	1:300		
SATB2		IgG	Abcam	ab34735	1:200		
Sortilin		goat IgG	R&D Systems	AF3154	1:200		
Tau (3-repeat isoform RD3)	8E6/C11	mouse	Millipore	#05-803	1:500		1:1000
Tau (hyperphosphorilated)	AT8	mouse IgG	ThermoFisher Scientific	MN1020	1:500		
Tau (filamentous)	AT100	mouse IgG	ThermoFisher Scientific	MN1060	1:1000		
Tau (conformationally altered)	TG3	mouse IgM	From Peter Davies (via Alzforum)	NA	1:100		1:1000
TBR1		rabbit IgG	Abcam	ab31490	1:500		

Supplementary Table 4. Secondary antibodies:

antibody	conjugate	source	Cat.No	dilution
Donkey anti-Mouse IgG (H + L)	Alexa Fluor 488	ThermoFisher Scientific	A-21202	1:1000
Donkey anti-Mouse IgG (H + L)	Alexa Fluor 555	ThermoFisher Scientific	A-31570	1:1000
Donkey anti-Mouse IgG (H + L)	Alexa Fluor 647	ThermoFisher Scientific	A-31571	1:500
Donkey anti-Rabbit IgG (H + L)	Alexa Fluor 488	ThermoFisher Scientific	A-21206	1:1000
Donkey anti-Rabbit IgG (H + L)	Alexa Fluor 555	ThermoFisher Scientific	A-31572	1:1000
Donkey anti-Rabbit IgG (H + L)	Alexa Fluor 647	ThermoFisher Scientific	A-31573	1:500
Donkey anti-Goat IgG (H + L)	Alexa Fluor 555	ThermoFisher Scientific	A-21432	1:1000
Goat anti-Mouse IgG2b (H + L)	Alexa Fluor 488	ThermoFisher Scientific	A-21141	1:500
Goat anti-Mouse IgM (H + L)	Alexa Fluor 568	ThermoFisher Scientific	A-21043	1:500
Goat anti-Rat IgG (H + L)	Alexa Fluor 568	ThermoFisher Scientific	A-11077	1:1000
Goat anti-Chicken IgY (H + L)	Alexa Fluor 633	ThermoFisher Scientific	A-21103	1:500
Goat anti-Rabbit IgG (H + L)	HRP	Abcam	ab97051	1:10000

Goat anti-Mouse IgG (H + L)	HRP	Abcam	Ab97023	1:10000
VECTASTAIN ABC HRP Kit	HRP	Vector	PK-4002	1:200
Double staining Kit	HRP & AP	GBI Labs	DS202A-18	NA

Supplementary Table 5. Primer sequences used for the paralogous-loci-amplification-quantitative pyrosequencing

Gene	F primer (5'-3')	R primer (5'-3')	Sequencing primer (5'-3')	Assay used (ref)
GABPA	b-CTTACTGATAAGGACGCTC	CTCATAGTTCATCGTAGGCT	TCACCAACCCAAGAAA	Deutsch et al 2004
ITSN	ATTTATTGCCATGTACACTT	b-GAATCTTTAAGCCTCACATAG	ACCAAGAAAGATGGTGAC	Deutsch et al 2004

Supplementary Information

Related to Fig. 1:
Fig. 1a: Variability between individual iPSC lines (representing individual re-programming events) was tested by ANOVA in Exp1, where all 3 independent trisomic lines of our isogenic model were used in a single experiment. No significant differences between individual lines were found in any of the calculations shown in Fig. 1, demonstrating that our peptide-ratio-readout parameter is driven by the genotype, and not re-programming artefacts or culture history of the iPSC lines (data did not fit the allowed space, available on request).

As peptide-ratio readouts differed slightly between three independent experiments, we are showing complete data here for each experiment individually. As shown in Fig. 1a, the difference (or the absence of difference) caused by T21 in an isogenic comparison remained stable in each of 3 experiments. In Exp3, for the ratio of 1-19/amyloidogenics, the isogenic comparison of T21 v D21 showed a p=0.027 (2-tailed t-test), which dropped to p=0.0681 after ANOVA comparison with all 5 individual samples.
Also in Exp3, we further performed an analysis by genotype groups. For the AβDP/amyloidogenics ratio, the combined T21 samples (n=3) were significantly higher than D21 (ANOVA p=0.0021), and significantly higher than Dup*APP* (ANOVA p=0.0011), whereas D21 is not significantly different from Dup*APP*. The same result was obtained for the total BACE2/amyloidogenics ratio: combined T21 (n=3) v D21, ANOVA p=0.0138; combined T21 (n=3) v Dup*APP*, ANOVA p=0.0036, and D21 v Dup*APP* shows no significant difference. The comparison of α-site cleavages (1-16&1-17)/amyloidogenics never showed any significant difference irrespective of how the samples were grouped.

Related to Fig. 2:
Fig. 2: The FRET assay positive control was performed using recombinant human BACE2 at 37ºC, pH=3.5 for 2h in the R&D systems assay buffer, as specified in the manufacturer's protocol, using the R&D systems FRET control peptide (ES010). In three technical replicates the blank-subtracted raw fluorescence readings obtained were 13,836(±130 SEM). BACE2 with the new FRET peptide for the AβDP cleavage after aa34 (in the absence of any inhibitors) gave blank-subtracted readings 10,100(±59 SEM). This was taken as the 100% value for the graphs shown in Fig. 2. For comparison, BACE1 incubated with the same FRET peptide, using the manufacturer's assay buffer for BACE1, gave the readings of 522 (±58 SEM) in the same experiment.

Related to Fig. 3 and Supplementary Fig. 7:
We compared the degree of colocalisation between either BACE1 or BACE2, and Aβx-34 clearance product in organoids, along with other markers of intra-neuronal compartments: Flotillin1 (general marker of lipid rafts), Rab7 (late endosome marker), Sortilin (a major ApoE receptor linked to Aβ catabolism), and LAMP2 (one of the lysosomal membrane proteins often used to visualize lysosomes in studies of Aβ-processing).
Both BACE1 and BACE2, as well as Aβx-34 highly colocalised with Flotillin1, suggesting that this type of Aβ degradation takes place in lipid raft containing vesicles (Fig. 3 and Supplementary Fig. 7). However, BACE1 and BACE2 differed in vesicular sub-compartment distribution: BACE1 was highly colocalised (>0.6) with each Sortilin and Rab7 and only weakly with LAMP2 (0.22), whereas BACE2 did not co-localise with Sortilin(<0.1), but colocalised moderately with Rab7 (0.31) and highly with LAMP2 (>0.5) (Supplementary Fig. 7). Interestingly, the localisation of the Aβx-34 fragment closely resembles the pattern of

BACE2, and not of BACE1: (Pearson coefficient of 0.1 with each Sortilin and Rab7, and >0.5 with LAMP2), further supporting the observation of Aβx-34 (>0.5) localisation with BACE2 and less so with BACE1, in both organoids (Fig. 3 and Supplementary Fig. 7) and human brain (Fig. 4). In order to define the compartment with the highest concentration of Aβx-34 within the endo-lysosomal system more precisely, we co-stained the Aβx-34 neo-epitope-specific antibody with other markers associated with Aβ processing: LC3A (macro-autophagosome marker), EEA1 (early endosome marker) and LAMP1 (a classical lysosome marker). Surprisingly, none of these markers showed any colocalisation, demonstrating that Aβx-34 is not present in either early endosomes, macro-autophagosomes, or classical lysosomes (Fig. 3). As Aβx-34 did not colocalise with LAMP1 or LC3A, but colocalised strongly with LAMP2, we tested a colocalisation with the components of an alternative autophagy pathway that would be compatible with this pattern of colocalisations: chaperone-mediated autophagy (CMA). Unexpectedly, we detected an extremely high level of co-localization of Aβx-34 with both HSC70 (chaperone in CMA) and LAMP2A, (the isoform of LAMP2 that is the main protein controlling the levels of CMA activity) (Fig. 3). Some intra-neuronal LAMP2A+ vesicles appear to contain both HSC70 and Aβx-34 (Fig. 3). These data suggest that AβDP activity of BACE2 is linked with the CMA pathway.

Related to Fig. 4:
Fig. 4a-d: As immunofluorescence on brain sections is susceptible to bright and false positive autofluorescent signals from lipofuscin granules, we confirmed the colocalisation of Aβx-34 and BACE2 using non-fluorescent, chromogenic dual labelled immunohistochemistry (Supplementary Fig. 8b), where the specificity of the BACE2 antibody was further verified by pre-absorption control with the immunogenic peptide (Supplementary Fig. 8c). This method confirmed the intra-neuronal co-localization of Aβx-34 and BACE2 signals.

Related to Fig. 5:
The 7bp deletion causes a frameshift at aa157 of BACE2 protein sequence. This introduces a stop codon within the protease cleavage domain at aa197. The potential off-target effects of the CRISPR guide RNA used were tested using two prediction software tools: CCTop and http://crispr.mit.edu/. No target sequences were found with 0, 1 or 2 mismatched nucleotides. No targets, that had three or more mismatches were overlapping between the two software predictions. In CCTop, only two sites with three mismatches, and more sites with four mismatches were found. Top 10 loci from this prediction were amplified with the putative target sequence in the middle, and sequenced in the T21 wt iPSC compared to the Δ7 iPSC line. No off-target effects of the CRISPR/SpCas9-HF1 intervention were detected.